

**A New Silicon-Based Dielectric Waveguide
Technology for
Millimeter-Wave/Terahertz Devices and
Integrated Systems**

by
Aidin Taeb

A thesis
Presented to the University of Waterloo
in fulfillment of the
thesis requirement for the degree of
Doctor of Philosophy
in
Electrical and Computer Engineering

Waterloo, Ontario, Canada, 2014

©Aidin Taeb 2014

AUTHOR'S DECLARATION

I hereby declare that I am the sole author of this thesis. This is a true copy of the thesis, including any required final revisions, as accepted by my examiners.

I understand that my thesis may be made electronically available to the public.

Abstract

In recent decades, the millimeter-Wave (mmWave)/THz band has attracted great attention in the research community. The Terahertz frequency band runs from approximately 300 GHz to 3 THz, an incredible 2700 GHz of bandwidth. The Terahertz frequency range has traditionally been considered as the RF "no man's land", between electronic and optical technologies. Many efforts have been made to extend existing active and passive devices to take advantage of these higher frequencies. The development of a universal technology for integrating various functionalities in the THz region is the ultimate goal of many researchers.

The primary focus of this research is to develop a novel silicon waveguide-based technology for implementing various structures and devices in the mmWave and THz range of frequencies. The structures introduced in this study are designed based on High Resistivity Silicon (HRS). Two technologies are developed and investigated at the Centre for Intelligent Antenna and Radio Systems (CIARS): Silicon-On-Glass (SOG) and Silicon Image Guide (SIG) technologies. The proposed technologies provide a low-cost, highly efficient, and integratable platform for realization a variety of mmWave/THz systems suitable for various applications such as sensing, communication, and imaging. A comprehensive study is conducted for functionality and error analysis of the proposed technologies. Also, a vast range of passive structures such as bends, dividers, and couplers are designed, fabricated and successfully tested with desired performance at the mmWave range of frequencies. Additionally, three types of dielectric waveguide antennas are designed and optimized: parasitic tapered antenna, groove grating antenna, and strip grating antenna.

Another focus of this thesis is to investigate the behavior of resonance structures, operating based on Whispering Gallery Modes (WGMs). The WG mode is a special type of high order mode of a circular shaped resonator, and offers very unique properties, which make it very suitable for sensing applications. In this research, an efficient algorithm is developed for analyzing the WGM resonators. Then, the proposed HRS platforms are used for implementing various WGM resonance configurations. The introduced WGM structures are employed for two major applications: DNA sensing and resonance tuning. The results for

DNA testing are quite impressive in being able to distinguish between different kinds of DNA.

To demonstrate the usefulness of the developed HRS structures, a number of complex systems including, a Butler matrix network, a finger-shaped phase shifter, and tunable WGM resonance structures are designed, optimized, and realized in this report. As part of this research, a novel Microwave-Photonic idea is proposed for sensing purposes. The core of the system is based on the WGM resonance structures implemented on the HRS platforms. The proposed system is tested and promising results are achieved.

Acknowledgements

I am taking this opportunity to express my gratitude to everyone who supported me throughout the course of this research. I am grateful for their guidance, invaluable constructive criticism and friendly advice during the project work. I would like to express my appreciation to all of them, realizing that those whom I owe the most I cannot thank enough, and that the things for which I am most grateful, I cannot put into words.

I would like to thank my supervisor, Prof. Safieddin Safavi-Naeini, and my co-supervisor, Dr. Mohamed Basha, for their guidance and support during my PhD studies. I would especially like to express my deepest gratitude to Prof. Safavi-Naeini for his encouragement, kindness and patience during my PhD studies at the University of Waterloo. My sincere thanks to Prof. Ke Wu from the Polytechnique Montréal (University of Montreal) for accepting to be my external examiner. I am also thankful to the committee members, Prof. Sujeet K. Chaudhuri, Prof. Simarjeet Saini, and Prof. James Martin.

My special thanks to Dr. Suren Gigoyan who encouraged me to start my research in this area and for his invaluable kindness, support, and all the skills that I learned from him. I also would like to thank to Dr. Mungo Marsden from Department of Biology for his valuable help. I express my thanks to all of my colleagues at the Centre for Intelligent and Antenna Radio Systems (CIARS), especially Dr. Gholamreza Z. Rafi for his technical help and friendship. Also, I am thankful to Ms. Chris Schroeder for her help in editing of this thesis.

I would like to also acknowledge National Science and Engineering Research Council of Canada (NSERC) and BlackBerry for funding the research.

I wish to express my gratitude to my beloved family: my father, who taught me how to live, my mother, who taught me how to love, my brother, Ali, and my uncle, Dr. Gh. Khajehnasiry.

Last but not least, I extend my heartfelt appreciation to my stunning wife, Mina, for her patience, endless love, and emotionally support.

Dedication

To my parents, who have supported me all during my life,

to my wife, *Mina*, who has been a great source of love and companionship, and

to my son , *Parsa*, who has been the source of energy and joy.

Contents

AUTHOR'S DECLARATION	ii
Abstract	iii
Acknowledgements	v
Dedication	vi
Contents.....	vii
List of Figures	x
List of Tables.....	xvi
List of Abbreviations.....	xvii
Chapter 1 Introduction.....	1
1.1 Why Terahertz.....	1
1.2 Dielectric Waveguide Technology, Bridging the Microwave to Optics	2
1.2.1 Silicon-Based Dielectric Waveguides: an Optimum Solution.....	7
1.3 Objectives and Research Overview	8
Chapter 2 Silicon Waveguide-Based Technology.....	10
2.1 Silicon Image Guide (SIG) Technology	11
2.1.1 Modal Analysis.....	12
2.1.2 Laser Machining Fabrication Process.....	15
2.1.3 Fabrication and Measurement Error Analysis	16
2.1.4 Measurement Results of the Fabricated SIG Straight Waveguide	21
2.2 Silicon-On-Glass (SOG) Technology.....	23
2.2.1 Suspended Silicon-On-Glass; Basic Idea and Design Analysis	24
2.2.2 Silicon on Corrugated Glass; Simulation and Measurement Results	28
2.3 Conclusion.....	32
Chapter 3 SIG Passive Components: Design, Analysis, and Measurement	34
3.1 Bend.....	34
3.1.1 Measurement Results.....	37
3.2 Y-Junction Power Divider.....	39
3.2.1 Measurement Results.....	40
3.3 Directional Coupler	42
3.3.1 Supported SIG Coupler	46

3.3.2 Multi-Mode Interference (MMI) Coupler	48
3.3.3 Measurement Results.....	49
3.4 Parasitic Tapered Antenna.....	51
3.5 Leaky-wave Antenna.....	54
3.5.1 Groove Grating Antenna	55
3.5.2 Strip Grating Antenna.....	58
3.6 Conclusion.....	61
Chapter 4 Dielectric Waveguide Whispering Gallery Mode (WGM) Sensors	62
4.1 Introduction	62
4.2 An Efficient Analysis Method for Calculating the High Order Resonance Frequencies of a DDR.....	64
4.2.1 Variational-Based Method for Improving the Accuracy	70
4.3 WGM-Based Bio-Sensor Technology.....	71
4.4 Alumina-Based Image WGM Sensor	74
4.4.1 Glucose Sensing	78
4.4.2 DNA Sensing.....	80
4.5 DNA Sensing Using Silicon-on-Insulator (SOI) WGM Sensor	83
4.6 SOG Bio-Sensor	89
4.6.1 DNA Sensing.....	92
4.7 SIG WGM Resonance Structures	94
4.7.1 SIG WGM Resonator in a Curved Configuration	97
4.8 Conclusion.....	99
Chapter 5 Silicon-Based Waveguide Devices	100
5.1 Tunable WGM Resonance Structures	100
5.1.1 Alumina-Based Tunable Image WGM Filter	101
5.1.2 Tunable SOG WGM Resonator.....	104
5.1.2.1 Measurement Results.....	106
5.2 Finger-Shaped SOG Phase Shifter	108
5.2.1 Measurement Results.....	112
5.3 SIG Butler Matrix for Beam Scanning Application	114
5.4 Microwave-Photonic WGM Sensor	124
5.4.1 Experimental Verification	125
5.5 Conclusion.....	127

Chapter 6 Concluding Remarks.....	128
6.1 Summary and Contributions.....	128
6.2 Future Work	129
Appendix A Analysis of a Single-Layer and Double-Layer Image Slab Waveguide.....	132
Appendix B Electromagnetic Fields and Dispersion Equation of a Circular Dielectric Waveguide....	135
Appendix C Asymptotic Values and Cut-Off Conditions of a Dielectric Cylinder.....	141
Appendix D Electromagnetic Field for an Image Dielectric Disc Resonator Based on Marcatili's Method	144
Appendix E Applying the Variational Method to an Image Disc Resonator Using the Marcatili's Solution	146
Appendix F Deep Reactive Ion Etching (DRIE) Technique for SOG Fabrication	149
Appendix G The Developed Recipe for Laser Machining the SIG Structures	151
Bibliography.....	153

List of Figures

Fig. 1.1: Common wave guiding technologies for mmWave and THz range of frequencies.....	2
Fig. 2.1: The general configuration of the Silicon Image Guide (SIG) structure.	11
Fig. 2.2: Dispersion curves and modal behavior of the SIG structure over 50 to 250 GHz.	14
Fig. 2.3: The simulated S-parameters of the SIG with the tapered sections, placed on a perfect conductor.....	15
Fig. 2.4: The simulated S-parameters of the 24 mm tapered SIG, on an aluminum ground plane.....	17
Fig. 2.5: The tapering tip width effect on the simulated S-parameters of the SIG structure.	18
Fig. 2.6: The possible measurement errors for a SIG structure.	19
Fig. 2.7: Measurement setup unwanted air gap effect on the simulated S-parameters of the SIG.	20
Fig. 2.8: The ground slit effect on the simulated S-parameters of the SIG structure.	20
Fig. 2.9: The lateral misalignment investigation on the Simulated S-parameters of the SIG.....	21
Fig. 2.10: (a) The straight SIG structures fabricated by the laser machining process (two different lengths: 24 and 34 mm). (b) The measurement setup.	22
Fig. 2.11: The measurement results for two different lengths of the fabricated straight waveguide (SW) SIG structures, compared to the simulation result of a 24 mm SW-SIG.....	23
Fig. 2.12: The absorption loss of Pyrex.....	24
Fig. 2.13: The proposed SDWG structure (a) 3-D view, and (b) the cross view.....	25
Fig. 2.14: The Fourier transform of the E_x field along the dielectric waveguide at 400 GHz.	27
Fig. 2.15: The total electric field distribution of the proposed Suspended SOG structure at 400 GHz.	28
Fig. 2.16: The simulated S-parameters of the Suspended SOG in the range of 350-500 GHz.....	28
Fig. 2.17: The proposed Silicon on Corrugated Glass configuration.	29
Fig. 2.18: Dispersion curves and mode behavior of the SOG structure over G-band.	30
Fig. 2.19: The simulated transmission and return loss of the Silicon On Corrugated Glass over G-band.....	30
Fig. 2.20: (a) The measurement setup for the fabricated Silicon On corrugated Glass, (b) measured S-parameters of the fabricated SOG structure over G-band.	31
Fig. 2.21: (a) The experiment for verifying the low-loss behavior of the silicon waveguide, and (b) the measured S-parameters of the detached silicon waveguide, which is placed between two metallic waveguide ports.	32

Fig. 3.1: The general schematic of two back-to-back bends: (a) without offset, and (b) with offset. . .	35
Fig. 3.2: The simulated insertion loss of the back-to-back bend for different (a) bending angles, and (b) different bending radii. (c) The electric field distribution of the bends with $R= 2$ mm, $\theta=90^\circ$ at $f=150$ GHz (top view).	36
Fig. 3.3: The effect of bending offset on the simulated insertion loss.	36
Fig. 3.4: The fabricated bends, using the developed laser machining technique.	37
Fig. 3.5: The measured S-parameters for the fabricated bends with (a) different radii, and (b) different bending angles. (c) The comparison between the simulated and measured S_{21} for $\theta=90^\circ$	38
Fig. 3.6: The general schematic of 3-dB Y-junction power divider.	40
Fig. 3.7: The simulated insertion loss of the 3-dB in-phase Y-junction power divider for different branching angles.	40
Fig. 3.8: (a) The measurement setup and fabricated back-to-back divider ($R=2$ mm, $2\theta=60^\circ$). (b) NIR illumination experiment.	41
Fig. 3.9: The measured results of S-parameters for the back-to-back divider by means of NIR illumination ($R=2$ mm, $2\theta=60^\circ$, and the total length=34 mm).	41
Fig. 3.10: The general configuration of (a) an SIG directional coupler, and (b) a supported SIG coupler.	42
Fig. 3.11: The simulated outputs power ratios at different frequencies: (a) directed power ratio for $G=180$ μm and varying L , (b) coupled power ratio for $G=180$ μm and varying L , and (c) coupled power ratio for $L=1$ mm and varying G	44
Fig. 3.12: (a) The effect of G on the transmission responses for the fixed L , (b) The effect of L on the transmission responses for the fixed G , and (c) the output phase differences for different values of L and G . (d) The electric field distribution for the SIG coupler at 150 GHz ($G=180$ μm , $L=1$ mm).	45
Fig. 3.13: (a) The effects of G and L on the transmission responses of the supported coupler, (b) the output phase differences for different sets of L and G for the supported coupler.	46
Fig. 3.14: (a) The effects of G and L on the transmission responses of the offset supported coupler, and (b) the output phase differences for different values of L and G for the offset supported coupler.	47
Fig. 3.15: The general configuration of the MMI-based coupler.	48
Fig. 3.16: (a) The effects of W_2 and L on the transmission responses ($S=0.45$ mm) of the MMI coupler, and (b) the output phase differences investigation.	49

Fig. 3.17: (a) The laser machined supported 3-dB coupler and the measurement setup, and (b) the measured S-parameters of the fabricated 3-dB coupler.	50
Fig. 3.18: 3-D configuration of the proposed parasitic tapered antenna [70].	52
Fig. 3.19: The laser machined parasitic tapered antenna: a) 3D views. b) Top view [70].	52
Fig. 3.20: (a) Simulated 3-D pattern of the parasitic tapered antenna at 90 GHz, (b) the simulated gain pattern for the $\phi=90^\circ$ cut, and (c) the simulated gain pattern for the $\theta=60^\circ$ cut [70].	53
Fig. 3.21: (a) The general configuration of the antenna with explanation of the applied EDC technique, (b) the electric field distribution at 160 GHz at the cross section of the antenna before the grooves, and (c) the design parameters.	56
Fig. 3.22: (a) Simulated 3-D gain pattern of the designed grating antenna at 155 GHz, (b) the simulated S_{11} of the antenna, and (c) the simulated gain patterns for the $\phi=90^\circ$ cut [78].	57
Fig. 3.23: The laser machined groove grating antenna sample [78].	58
Fig. 3.24: (a) The general configuration of the proposed strip grating antenna. (b) The simulated 3-D gain pattern at 155 GHz, and (c) the design values.	59
Fig. 3.25: (a) The simulated S_{11} of the strip grating antenna, (b) the simulated gain patterns for the $\theta_r=3^\circ$ cut, and (c) the simulated gain patterns for the $\phi=90^\circ$ cut [79].	60
Fig. 3.26: The laser machined strip grating antenna [79].	60
Fig. 4.1: (a) General configuration of a dielectric insulated image resonator, and (b) general configuration of a dielectric image resonator.	65
Fig. 4.2: (a) The cross section of an image resonator with (b) the equivalent single-layer slab waveguide for calculating the axial dispersion equation, and (c) the equivalent model for calculating the radial dispersion equation.	66
Fig. 4.3: The developed algorithm for obtaining the radial dispersion curve of an image resonator. ...	69
Fig. 4.4: The cross section view of a grounded DDR used in the variation method.	70
Fig. 4.5: The general configuration of the alumina-based WGM resonance structure [124].	74
Fig. 4.6: Modal analysis of the DIG using the EDC technique [124].	75
Fig. 4.7: (a) The axial and radial dispersion curves of the DDR. (b) Normalized E_z field component in the DDR for WGH_{700} mode in the xy -plane. (c) Normalized electric field components in the DDR for WGH_{700} mode in the xy -plane.	76
Fig. 4.8: Effect of gap on the resonance response of DIG-DDR (simulation).	77
Fig. 4.9: (a) Measurement setup and the fabricated sensor device. (b) Comparison between the measured (dashed) and simulated (solid) scattering parameters.	78

Fig. 4.10: (a) Measurement results of the 5 μl glucose solution samples with a concentration of 1.65 g/100 μl . (b) Comparison of resonance responses of the sensor loaded with two different glucose solution samples [124].	79
Fig. 4.11: The measurement results of the alumina sensor loaded with two different single-stranded DNA: (a) EB3 (b) ILK.	82
Fig. 4.12: The measurement results of the alumina sensor loaded with forward-stranded and double-stranded DNA.	83
Fig. 4.13: (a) The SOI sensor configuration. (b) The cross section of a general insulated DDR [132].	84
Fig. 4.14: (a) The SOI measurement setup, and (b) the comparison between the S_{21} obtained from measurement with that of simulation [132].	86
Fig. 4.15: The measured resonance frequency shifts for single-stranded (SS) and double-stranded (DS) DNA samples on SOI technology. The repeatability is validated for each sample.	88
Fig. 4.16: The general configuration of the proposed Silicon on Corrugated Glass sensor.	90
Fig. 4.17: The simulated S-parameters of SOG disc resonator coupled to the dielectric waveguide at G-Band [52].	91
Fig. 4.18: (a) The measurement setup, and (b) two SOG dielectric waveguide structures under test: dielectric waveguide coupled to WGM disc resonator, and dielectric waveguide coupled to WGM ring resonator.	91
Fig. 4.19: The measured S-parameters of (a) the disc resonator on SOG technology over G-band, and (b) the ring resonator on SOG technology over G-band [52].	92
Fig. 4.20: The measured resonance frequency shifts for single-stranded oligos, Forward (FDNA) and Reverse (RDNA) samples, along with the result for double-stranded (DDNA) samples on SOG technology.	93
Fig. 4.21: Resonance frequency error analysis of the SOG sensor, used for sensing different DNA samples. Each test was repeated five times.	94
Fig. 4.22: The general configurations of SIG WGM resonance structures, implemented (a) by a straight waveguide segment, or (b) by a curved waveguide segment.	95
Fig. 4.23: (a) The simulated transmission response (S_{21}) of the straight SIG resonance structure ($R=930 \mu\text{m}$, $Gap=220 \mu\text{m}$). The effects of the Gap and R on the resonance frequencies of (b) the WGH_{500} mode, and (c) the WGH_{600} mode.	96
Fig. 4.24: (a) The laser machined SIG WGM structure. (b) The measured S-parameters for the resonator with $R=920 \mu\text{m}$ and $Gap=220 \mu\text{m}$.	97

Fig. 4.25: (a) The simulated transmission response (S_{21}) of the curved SIG resonance structure with $Gap=200 \mu\text{m}$ and two radii of $R=930 \mu\text{m}$ and $R=940 \mu\text{m}$. The effects of the Gap and R on the resonance frequencies of (b) the WGH_{500} mode, and (c) the WGH_{600} mode.	98
Fig. 4.26: (a) The laser machined curved SIG structure. (b) The measured S-parameters for three different resonators.	98
Fig. 5.1: (a) The general configuration of the proposed tunable alumina WGM resonance structure. (b) The fabricated prototype alumina WGM structure [142].	102
Fig. 5.2: The simulated effect of the metallic bar on the resonance frequency.	102
Fig. 5.3: (a) The measurement setup for the alumina WGM tunable structure. The measured effects of the metallic bar position on (b) the resonance frequency of the system, and (c) the S_{21} phase [142].	103
Fig. 5.4: The general configuration of the proposed tunable SOG-based resonance structure [142].	104
Fig. 5.5: The simulated effect of the metallic cylinder movement on the resonance frequencies of the SOG WGM structure for (a) WGH_{600} mode, and (b) WGH_{700} mode.	105
Fig. 5.6: The measurement setup for testing the tunable SOG WGM structure at	106
Fig. 5.7: The effect of the metallic cylinder on the measured S_{21} of the tunable SOG WGM structure for (a) WGH_{600} mode, and (b) WGH_{700} mode.	107
Fig. 5.8: The general configuration of the proposed finger-shaped phase shifter based on the SOG technology.	110
Fig. 5.9: The simulated transmission loss of the finger-shaped phase shifter, with the total length of $L=16 \text{ mm}$ and $L_2=3 \text{ mm}$	111
Fig. 5.10: The simulated phase shift of the finger-shaped phase shifter for the total finger structure length of $L_2=3 \text{ mm}$. The reference phase is defined for the case $\Delta x=-200 \mu\text{m}$	111
Fig. 5.11: (a) The laser machined movable part of the finger-shaped phase shifter, and (b) the measurement setup.	112
Fig. 5.12: The measured transmission loss of the finger-shaped phase shifter, with the total length of $L=16 \text{ mm}$ and $L_2=3 \text{ mm}$	113
Fig. 5.13: The measured phase shift of the finger-shaped phase shifter for the total finger structure length of $L_2=3 \text{ mm}$. The reference phase is defined for the case $\Delta x=-200 \mu\text{m}$	113
Fig. 5.14: Block diagram of a general 4×4 butler matrix network.	114
Fig. 5.15: The general schematic of the proposed SIG butler matrix network.	116
Fig. 5.16: (a) The designed cross-over electric field distribution at 150 GHz. (b) The S-parameters of the cross-over.	116

Fig. 5.17: (a) The simulated transmission coefficients of the butler matrix network, excited at port-1. (b) The difference between the phases of the output ports and port-5, when the network is excited at port-1.....	117
Fig. 5.18: (a) The simulated transmission coefficients of the butler matrix network, excited at port-2. (b) The difference between the phases of the output ports and port-5, when the network is excited at port-2.....	118
Fig. 5.19: The electric field distributions over the butler matrix network at 150 GHz, when the network is excited at (a) port-1, and (b) port-2.	119
Fig. 5.20: The general schematic of the proposed monolithic SIG butler matrix connected to groove grating antenna array.....	120
Fig. 5.21: (a) The simulated transmission coefficients of the monolithic butler matrix network, excited at port-1. (b) The difference between the phases of the output ports and port-5, when the network is excited at port-1.	121
Fig. 5.22: (a) The simulated transmission coefficients of the monolithic butler matrix network, excited at port-2. (b) The difference between the phases of the output ports and port-5, when the network is excited at port-2.	121
Fig. 5.23: 3-D gain pattern of 1×4 groove grating antenna array, excited by the 4×4 butler matrix network, at 156 GHz.	122
Fig. 5.24: The laser machined monolithic butler matrix network, operating at 156 GHz.	123
Fig. 5.25: The proposed Microwave-Photonic sensing mechanism.	124
Fig. 5.26: (a) The Microwave-Photonic measurement setup for sensing application using WGM curved-SIG structure. (b) The setup for testing the sensor for two different milk samples.	125
Fig. 5.27: The transmission response of the structure at WGH_{600} resonance, for different NIR illumination intensities.	126
Fig. 5.28: The NIR illumination effect on the resonance responses of two different milk samples....	127

List of Tables

Table 2.1: The fabricated SIG dimensions values	22
Table 2.2: The design parameter values of the suspended SOG.	27
Table 2.3: The design parameter values of the Silicon on Corrugated Glass.....	29
Table 2.4: Overall Comparison of SIG and SOG technologies.....	33
Table 3.1: The design parameter values of the Y-junction 3-dB power divider.	39
Table 3.2: Optimal design values of the parasitic tapered antenna.	52
Table 4.1: Design parameters of the sensor at D-band.....	75
Table 4.2: A comparison between the calculated resonance frequency by the developed algorithm, and the full-wave simulation for D-band design.....	77
Table 4.3: A comparison between different methods, employed to find the WGM resonance frequencies of the SOI structure.....	85
Table 4.4. The design parameter values for the SOG sensor.....	90
Table 5.1: Design parameter values for the proposed finger-shaped SOG phase shifter at G-band. .	110
Table 5.2: Design parameter values for the SIG butler matrix.....	117
Table 5.3: The simulated gain pattern data of the butler matrix system over 154-158 GHz.....	123

List of Abbreviations

CIARS: Centre for Integrated Antenna and Systems
CMOS: Complementary Metal Oxide Semiconductors
CNC: Computer Numerical Control
CPW: Co-Planar Waveguide
DDR: Dielectric Disc Resonator
DIG: Dielectric Image Guide
DNA: Deoxyribonucleic Acid
DRIE: Deep Reactive Ion Etching
DWM: Dielectric Waveguide Model
EDC: Effective Dielectric Constant
EDTA: Ethylenediaminetetraacetic Acid
FS: Forward-Stranded
FSR: Free Spectral Range
GaAs: Gallium Arsenide
HCS: High Conductivity Silicon
HIS: High Impedance Surface
HRS: High Resistivity Silicon
IC: Integrated Circuit
InP: Indium Phosphide
LC: Liquid Crystal
LED: Light-Emitting Diode
LTCC: Low Temperature Co-fired Ceramic
MEMS: Micro-Electro-Mechanical Switches
MMI: Multi-Mode Interference
mmWave: Millimeter Wave
MWG: Metallic Wave-Guide
NIR: Near Infra-Red
NRD: Non-Radiative Dielectric
PML: Perfect Magnetic Layer
RNA: Ribonucleic acid
SIG: Silicon Image Guide

SiGe: Silicon Germanium
SIIG: Substrate Integrated Image Guide
SIW: Substrate Integrated Waveguide
SOG: Silicon-On-Glass
SOI: Silicon-On-Insulator
SS: Single-stranded
TE: Transverse Electric
TEM: Transverse Electro-Magnetic
THz: Terahertz
TL: Transmission Line
TM: Transverse Magnetic
TMAH: Tetra Methyl Ammonium Hydroxide
UV: Ultraviolet
WGM: Whispering Gallery Mode

Chapter 1

Introduction

1.1 Why Terahertz

The terahertz (THz) region of electromagnetic spectrum has been subject to extensive research activities due to its unique advantages for a vast number of applications in wireless communication, radar, physics, chemistry, imaging, biology, radio astronomy, and medicine [1], [2], [3], [4], [5]. Although there are various definitions for the THz band, based on the IEEE 802.15 standard (Terahertz Interest group) [6], the THz frequency band lies in the interval from 300 GHz to 3 THz. The THz is the least explored part of the electromagnetic spectrum. Usually, this band is referred to as the “THz Gap”, because of the relatively small amount of information gained in this area in the previous decades. The challenges of working in the THz band are attributed to the signal generation, transmission, and detection as well as the reliability, cost, and complexity of the measurement facilities. However, due to recent developments in device technologies, research and commercial interest in the Millimeter-Wave (mmWave) and THz are rapidly growing.

In addition to spectroscopy and imaging, the THz range of frequencies is very appropriate for biological and pharmaceutical sensing [7]. The primary reason is that many important molecules in these applications have significant vibrational resonances in the THz band. Also, THz offers a viable and non-destructive solution for contact-free sensing and imaging of an opaque non-metallic package interior [8], since THz quanta have much less energy as compared to those of x-ray, preventing biological tissue ionization. The first attempt at THz imaging was made in 1995 [9]. Afterwards, many research groups were encouraged to work on THz imaging for applications ranging from biomedical diagnosis to security purposes [10], [11].

Located between the mmWave and optics, THz frequencies can be used for interfacing between optical and electronic systems. In short, the future belongs to THz. THz technologies open new market opportunities for a vast range of applications [12]. Furthermore, the THz has the ability to be robust, relatively inexpensive, and commercially available for a wide range of applications from security screening to biochemical material

detection. Finally, the universe and the cosmic background are inherently surrounded by Terahertz radiation and that is why THz has received much attention for investigation of our galaxy and the Big Bang [13]. THz has therefore become the most exciting area of research and development in RF technologies with exciting promises for many future generation systems and emerging applications.

1.2 Dielectric Waveguide Technology, Bridging the Microwave to Optics

There has always been a question of “which transmission line or wave guiding technology is suitable for THz applications?” To answer this question, it is desirable to have an overview of the available wave guiding technologies over the entire range of frequencies from microwave to optics, with particular emphasis on the state-of-the-art THz transmission structure technologies.

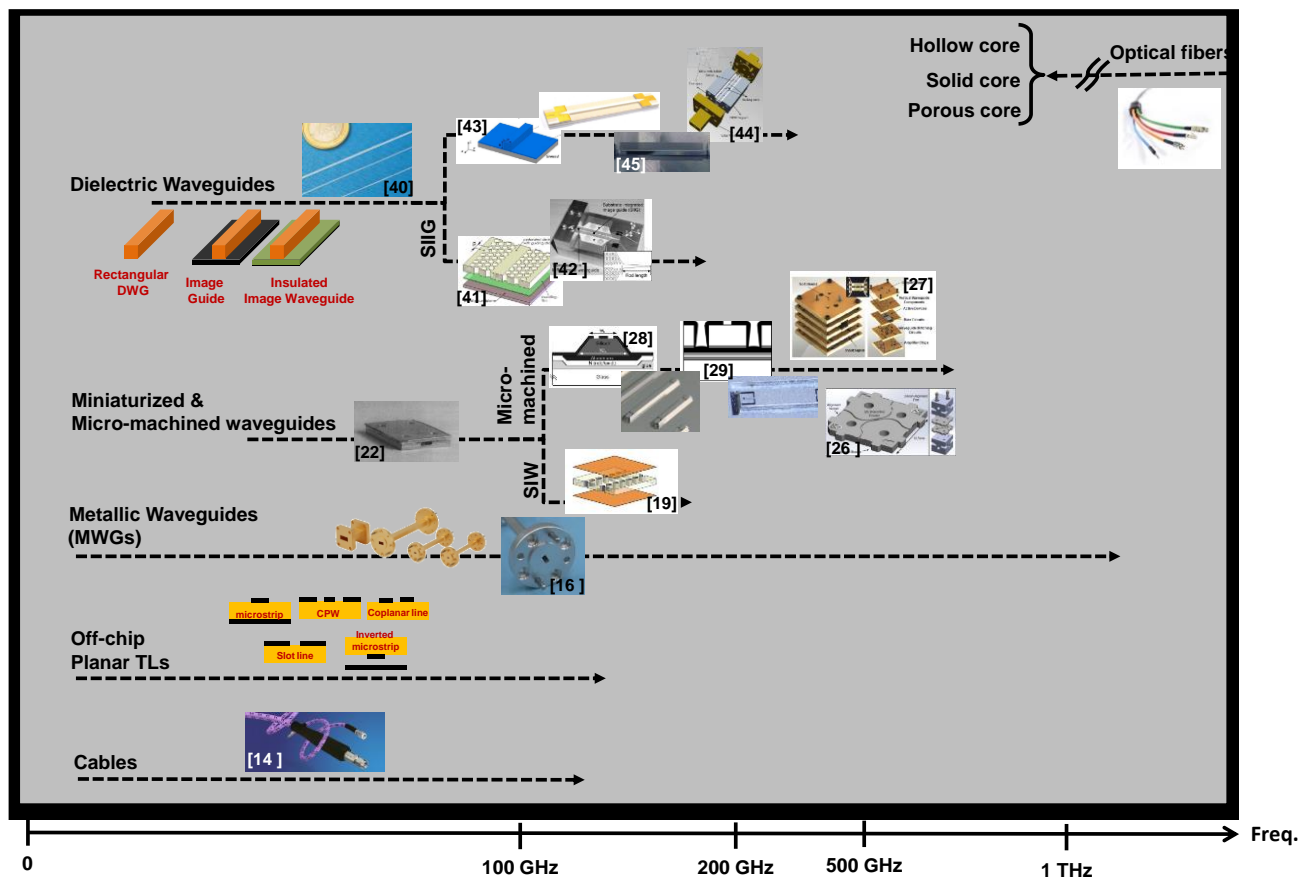


Fig. 1.1: Common wave guiding technologies for mmWave and THz range of frequencies.

TEM transmission lines (TLs), such as coaxial lines, are the oldest and the most common types of TLs for transporting the signal up to a few meters in the microwave range of frequencies. They can operate from very low frequency ranges up to 110 GHz [14]. The main operational frequency limits of the coaxial lines are the loss and fabrication challenges.

Planar multi-layer metallic TLs (both TEM and quasi-TEM types), are the most widely used TLs for realization of RF/microwave/mmWave hybrid and Integrated Circuits (ICs). Co-Planar Waveguide (CPW), microstrip, inverted microstrip, suspended strip line, etc. [15]. are the conventional types of planar TLs, which can be easily used for realization of wide ranges of planar devices in the microwave region. Beyond 200 GHz, the application of planar metallic TLs is often limited to on-chip configurations, such as Complementary Metal Oxide Semiconductor (CMOS), SiGe, and InP. On the other hand, implementation of high performance passive transmission structures, devices, and antennas at the sub-mmWave and THz range of frequencies can be performed only in off-chip configuration. The off-chip planar metallic TLs seriously suffer from ohmic losses and dispersion at the THz range of frequencies. In the category of quasi-planar, the non-TEM fin line offers low loss characteristics as compared to the planar structures at the mmWave range of frequencies. However, due to the geometry of fin line, which includes a metallic waveguide, they are not appropriate for integrated system configurations. Also, fin line realization at the THz range of frequencies encounters difficulties in fabrication.

Metallic waveguide technology and its alternatives are still used in the microwave and mmWave range of frequencies. Metallic waveguides are convenient structures for high power transmission applications. The metallic waveguide dimensions are determined by the wavelength of the dominant mode propagating wave. Metallic waveguides have always been the most trusted candidates for realization of mmWave systems, due to their low-insertion loss and simple design models. However, the accuracy of waveguide dimensions and inner surface roughness are important parameters in determining the performance of this class of TLs. Although these days, the metallic waveguides are realized up to the THz range of frequencies [16], they suffer from conductor loss, dimensional inaccuracies, and complexity of high performance interconnects at higher frequencies. In addition, an important bottleneck of metallic waveguides is their large and bulky 3-D geometries, which make them inappropriate for integration purposes.

To overcome the geometrical issues of the metallic waveguides, the idea of laminated waveguide structures [17] and, more recently, Substrate Integrated Waveguides (SIWs) [18], [19], [20] have been introduced. A SIW structure is formed by a dielectric slab sandwiched between two metal plates from top and bottom, with the sidewalls realized by being metallized via fence. A SIW can be considered as a reduced height waveguide structure that can dominantly support TM modes. The main advantages of SIW structures over the metallic waveguides are their relative ease of fabrication and integration capability with planar circuits. However, realization of SIWs beyond 150 GHz are quite challenging, mainly due to the fabrication limitation in manufacturing via hole arrays. Also, SIWs generally present higher losses as compared to the conventional metallic waveguides. The highest reported operational frequency for an SIW structure is 140 GHz [21].

A considerable amount of research has been conducted to realize compact and miniaturized alternatives for metallic waveguides in the sub-mmWave and THz range of frequencies. Thanks to the technological advancement in micro-machining and lithography fabrication, a new generation of waveguides for carrying mmWave/THz signals has been introduced. As an early work, an air-filled waveguide was realized inside a dielectric medium, by means of SU-8 fabrication process [22], [23], [24], and it was tested up to 320 GHz with minimum loss of 1.1 dB/ λ [25]. In another test, a micro-machining technique was proposed for forming an air channel metallized waveguide inside a silicon substrate, and the design concept was employed for realization of multi-level integrated systems, working up to 1.1 THz range of frequencies [26], [27]. Difficulty in accurate alignment of different parts of the micro-machined waveguide and presenting high insertion loss are the main drawbacks of the introduced micro-machined TLs. The next version of miniaturized waveguides can be classified as micro-fabricated dielectric filled waveguides. So far, this class of waveguides has been fabricated either by means of substrate transfer technique [28], or by Deep Reactive Ion Etching (DRIE) [29] technique. In the work reported in [28], a silicon filled waveguide with a trapezoidal cross section was measured up to 100 GHz, with insertion loss of 0.3 dB/mm. In [29], a rectangular shaped silicon filled waveguide was introduced for operating up to 110 GHz, with insertion loss around 0.122 dB/mm. The major problem of the aforementioned miniaturized waveguides are the multi-level fabrication challenges, the metallic loss of the walls, and realization of complicated passive structures, in the

sub-mmWave and THz range of frequencies. Although, the metallic waveguide structures and their micro-machined alternatives have shown their capabilities in the THz range of frequencies, they are not final solutions.

Dielectric waveguides are strong competitors for metallic waveguides and their alternatives. Dielectric waveguides are simple in geometry and high in electromagnetic performance. By choosing a proper dielectric material, the dielectric waveguide structures can present extremely low-loss performance. Similar to the metallic waveguides, dielectric waveguide dimensions are determined by the wavelength of the propagating signal. Therefore, they can have reasonable dimensions in the mmWave and THz range of frequencies. Studying dielectric waveguides goes back to 1910, when a cylindrical rod was analyzed for the first time [30]. In the 1930s and 1940s, tremendous efforts were conducted for experimentally investigating the rod type of dielectric waveguides [31]. Later on, in the 1950s, the first planar dielectric waveguide, image guide, was proposed and comprehensively studied by various researchers [32], [33], [34], [35]. Dielectric waveguides have been extensively used in optics, where they are known as optical dielectric waveguides. A variety of optical dielectric waveguides, such as strip guides, embedded strip guides, rib waveguides, and ridge waveguides, are used for guiding the light over short distances. In the microwave and mmWave range of frequencies a much simpler version of the optical waveguide, which is a rectangular dielectric waveguide, can be realized. Although the general concept of the mmWave dielectric waveguide is similar to the optical dielectric waveguide, there is one distinct difference: in optics, the dielectric constant of the core channel is close to the one(s) of the surrounding medium(s) [36]. Therefore, in single mode operation, the dimension of the core channel can be on the order of a few wavelengths. In contrast, for a mmWave dielectric waveguide, the dielectric constant of the main channel is usually chosen to be high as to increase the field confinement and reduce the radiation loss. A number of general configurations of dielectric waveguides in the microwave and mmWave range of frequencies are: image guide, suspended waveguide (rectangular waveguide), and insulated waveguide. The investigation of dielectric waveguide structures for the mmWave range of frequencies started in 1959 [35] and was rapidly increased in the 1960s and 1970s [37], [38]. Theoretically, a very thin dielectric waveguide surrounded by air is the lowest loss medium for guiding the signal; however, this structure suffers greatly from the radiation loss due to

any discontinuity and curvature. In 1981, a new generation of dielectric waveguides, called Non-Radiative Dielectric (NRD), was introduced [39]. NRD structures can suppress the radiation by using parallel metallic plates, placed on the top and bottom sides of the dielectric waveguide. The main drawback of NRD structures are their non-integratable configuration.

The invention of IC transistors and advancements in chip technologies made the progress of dielectric waveguide technologies slow. However, over the last decades, by increasing the demand for a low-loss and low-cost TL in the mmWave range of frequencies, a wide range of studies have started to investigate dielectric waveguides. In [40], realization of a polyethylene rectangular dielectric waveguide, operating up to 600 GHz, was reported. But the measured attenuation at 600 GHz was as high as 19 dB/mm. After that, a new class of dielectric waveguides, Substrate Integrated Image Guide (SIIG), was proposed for mmWave applications [41], [42]. The first generation of SIIG structures was realized by a dielectric channel surrounded by air holes at both sides. The major challenges regarding the proposed SIIG structure are fabrication difficulties in making the holes, and realization of high performance and complicated passive structures at the sub-mmWave and THz range of frequencies. Later on, another version of SIIG structures was proposed, by means of Low Temperature Co-fired Ceramic (LTCC) technology [43]. Again, the main drawback of this type of SIIG structure is fabrication challenges in frequency scaling up.

In a recent work [44], a silicon suspended dielectric waveguide was introduced for operating within the 140 to 220 GHz range of frequencies. The average insertion loss of the structure with a total length of 15 mm was reported as approximately 1.5 dB. However, the proposed structure uses holding arms, which makes the structure fragile, relatively large in size, and not appropriate for realization of a practical advanced system. In another work [45], silicon-On-Insulator (SOI) technology was used for implementing an insulated image guide, operating within the 50 to 75 GHz range of frequencies with the average loss of 3.2 dB.

In the end, it is worth mentioning that a number of research groups are following the optical fiber concept for introducing another class of THz TLs, which can be divided into three categories: Hollow Core, Solid Core, and Porous Core TLs [46]. It is beyond the scope of this review section to explain all these types of cylindrical core-based TLs. The main

drawback of cylindrical core-based TLs is their poor capability in integration with conventional planar mmWave/THz systems.

1.2.1 Silicon-Based Dielectric Waveguides: an Optimum Solution

In recent years mmWave technologies have progressed on many fronts, including semiconductor devices. A wide variety of packaged and unpackaged active electronic devices are available in the mmWave range of frequencies. Obviously, the material selection is essential for designing almost any integrated mmWave system. Among the available compound semiconductor devices, silicon-based devices are dominantly utilized in a wide range of applications from digital to high frequency circuits. Different active elements can be realized on the doped silicon substrate. However, due to the substrate losses in most of the conventional planar on-chip technologies, such as CMOS, SiGe, etc., the realization of high performance passive components and TLs is quite challenging. The on-chip antennas are quite inefficient in the mmWave/THz range of frequencies. Therefore, developing a low-cost technology for passive off-chip transmission structures and devices is inevitable. As mentioned in the previous section, dielectric waveguides are highly promising transmission structures for realization of almost any off-chip systems at the mmWave and THz range of frequencies. Generally, dielectric waveguides offer the combined advantages of low-loss, light weight, and ease of fabrication. Also, dielectric waveguide-based devices provide a unique possibility for integration with planar circuits. Among possible candidates, High Resistivity Silicon (HRS) is the most promising material, for the following reasons:

- **Endless resource:** Silicon is one of the most abundant elements within the Earth's crust. Silicon wafers are commercially available at a low cost.
- **Potentially integratable:** Silicon provides a compatible platform for integration with the Silicon-based on-chip system technologies, such as CMOS. This characteristic can lead us to realize an in-package THz system.
- **Low-loss characteristics:** A low-cost HRS wafer has a resistivity better than 10 k Ω .cm, which provides a very low-loss platform for a wide range of applications.
- **Mature fabrication technology:** There are a variety of well-developed and mature technologies for the processing and fabrication of silicon.

In conclusion, to obtain an integrated system operating in the THz range of frequencies, a silicon-based dielectric waveguide is the most optimal candidate. It provides an efficient technology to be integrated with either mmWave planar circuits or optical devices.

1.3 Objectives and Research Overview

In this research, two novel silicon waveguide technologies, Silicon Image Guide (SIG) and Silicon-On-Glass (SOG), are introduced, analyzed, and experimentally verified. The main objective of this research is to demonstrate the capability of the proposed silicon waveguide technologies in realization of a variety of low-cost, integrated, and high performance passive components in the mmWave and THz range of frequencies. A number of new applications, including highly sensitive bio-sensors, are analytically and experimentally studied and proof-of-concept structures are implemented. The bio-sensors under investigation in this research are primarily intended for sensing different types of biological samples such as DNA, proteins, and RNA. Additionally, a number of novel silicon-based device concepts, such as phase shifters and tunable resonators, are designed, fabricated, and successfully tested. To demonstrate the potential of the proposed silicon technologies in the implementation of an integrated mmWave/THz system, a novel monolithic Butler matrix network is realized based on the developed SIG technology.

The chapters of this thesis are organized as follows:

In Chapter 2, extensive design and error analysis are conducted to evaluate the performance of two developed silicon waveguide technologies, SIG and SOG. SIG and SOG structures can be treated as dielectric image guides and suspended waveguides, respectively. The single mode operations of both technologies are investigated through the modal analysis. The SOG platform is realized by a lithography/DRIE fabrication process, and the SIG platform is manufactured by a novel, mask-free, and fast laser machining process. The possible fabrication and measurement setup errors/uncertainties of the proposed silicon technologies are extensively studied. Also, the loss characteristics of both proposed technologies are experimentally assessed.

In Chapter 3, a number of building-block mmWave/THz passive components based on SIG technology are designed, fabricated, and tested. Bend is the first component, which is studied in detail. After that, a Y-junction power divider is designed and optimized, and the

corresponding measurement results are presented. A directional coupler is the next component, which is developed based on the SIG technology. An innovative technique is utilized for implementation of a monolithic coupler. Realizing a system without an antenna can not be imagined, so, the final part of the chapter focuses on the design and optimization of three types of SIG antennas: parasitic tapered antenna, groove grating antenna, and strip grating antenna. The proposed parasitic tapered antenna is a travelling wave antenna with very high gain and low-side lobe levels. The other two antennas are categorized as leaky-wave antennas, with frequency scanning capabilities.

Chapter 4 focuses on specific types of planar resonance structures, based on the Whispering Gallery Modes (WGMs). An efficient analysis approach, which is a combination of Effective Dielectric Constant (EDC) technique and Dielectric Waveguide Model (DWM), is developed for initial design and optimization of the resonance structures. The accuracy of the analysis method is improved by employing the variational method. A number of WGM structures based on the newly developed silicon technologies are designed, fabricated, and tested. The designed WGM structures are used for bio-sensing applications, specifically for DNA sensing. Distinguishing between denatured (single-stranded) DNA and hybridized (double-stranded) DNA is of particular interest for a medical diagnosis and scientific research and an application focus in this research. This facilitates the determination of genome sequence, gene discovery, and gene expression. A number of measurement tests are conducted for verifying the functionality of the WGM sensors in distinguishing between different DNA samples.

In Chapter 5, a number of advanced devices for mmWave applications are designed and implemented based on the previously developed silicon components. The SOG WGM structure is employed for proposing a new idea of tunable resonance structure. The next device is a mmWave phase shifter, which is based on SOG technology. To prove the performance of the SIG technology, an integrated beam forming butler matrix with grating antenna elements, is designed and optimized at the mmWave range of frequencies. The last but not least examined device in this research is a Microwave-Photonic WGM sensor. A low-cost and innovative idea is employed for controlling the resonance behavior of a silicon waveguide resonator by optical illumination.

Chapter 2

Silicon Waveguide-Based Technology

In this chapter, two silicon waveguide technologies are introduced: Silicon Image Guide (SIG) and Silicon-On-Glass (SOG), which are used for implementation of a variety of mmWave/THz guiding structures and devices in this research. High Resistivity Silicon (HRS) is chosen as a core dielectric material in this research, mainly due to its unique properties, which are explained in detail in Chapter 1.

Straight waveguide is considered as a building-block of any dielectric waveguide-based structure. A novel and efficient laser machining process, for fabricating the SIG sample structures, is introduced in this chapter. Also, the analysis and characterization of the SIG technology is presented. More specifically described:

- Modal analysis
- The effect of transitions from metallic waveguide to dielectric waveguide on the performance of the system
- Fabrication and measurement error analysis

Performing the aforementioned investigations assist with the optimal design and fabrication of the SIG and SOG devices which meet more realistic requirements. After extensive research on the SIG technology, a straight waveguide segment, operating over 110-170 GHz, is fabricated using the developed laser machining process and the measurement results are reported.

Then, a more advanced silicon-based technology, the SOG platform, is introduced. The SOG technology is potentially a high performance technology for realizing the next generation of THz integrated devices. Two variations of the SOG technology are explained and analyzed. A straight waveguide sample, based on the SOG technology, is fabricated and the measurement results are shown in the range of 140-220 GHz.

2.1 Silicon Image Guide (SIG) Technology

Different types of dielectric waveguides have been introduced and studied for mmWave applications. Dielectric image guide is one of the most common configurations of dielectric waveguides. Among different configurations of image guides, the rectangular one is the simplest type in terms of fabrication and realization. Fig. 2.1 shows the general configuration of an SIG structure along with the tapered sections, which will be discussed shortly. The rectangular image guide structure is supported by a metallic ground, which also acts as a supporting fixture. The grounding plate can be shared with the DC ground of an active circuit, integrated with the image guide structure. In fact, an image guide is a planar dielectric waveguide structure, suitable for integration purposes. One of the unique advantages of rectangular image guide structures over the rod waveguide is that the image guide structure does not suffer from the mode degeneracy issue. Wide varieties of techniques, ranging from rigorous to approximate methods, exist for analyzing this type of waveguide.

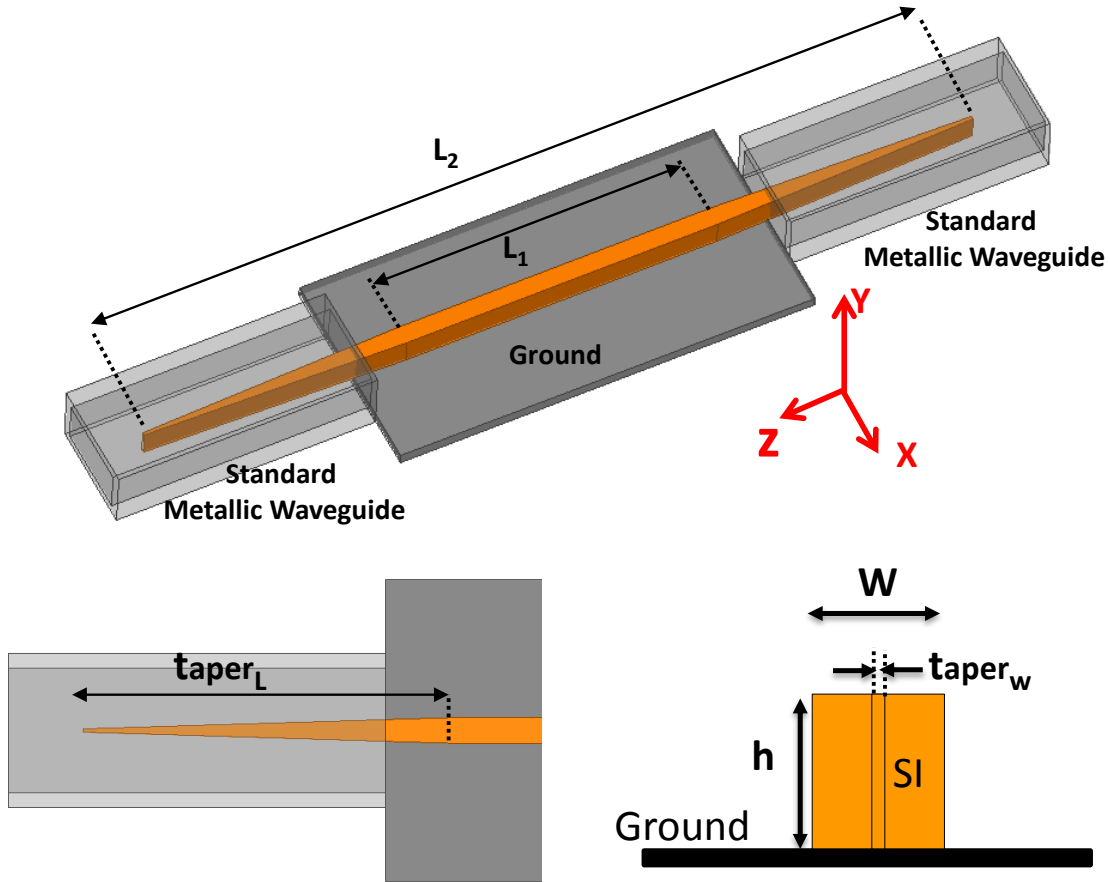


Fig. 2.1: The general configuration of the Silicon Image Guide (SIG) structure.

Different low-loss dielectrics can be used for realization of image guide structures. Ceramic dielectrics, such as alumina, and polymer materials, such as RT duroides, are the two main categories, which are used in image guide devices. However, these materials are not suitable for direct integration with active devices, which are mainly implemented in semiconductors. HRS is a good candidate to achieve an integrated waveguide-based structure with a planar active device. The HRS material used in this research has a resistivity of 10-20 K Ω .cm.

2.1.1 Modal Analysis

Modal analysis determines the behavior of the electromagnetic field inside and surrounding the dielectric waveguide regions over a certain frequency band. Modal analysis provides us valuable information about the cut-off frequencies, propagation characteristics, loss, and field confinement. In metallic waveguides, a cut-off frequency is defined as a frequency below which there is absolutely no wave propagation. In contrast to metallic waveguides, dielectric waveguides do not have a distinct and sharp cut-off frequency. Therefore, instead of defining a cut-off frequency it is more desirable to look at the mode shape and the corresponding propagation loss.

One of the analytical methods for finding the dispersion curves of a dielectric waveguide is the Effective Dielectric Constant (EDC) method. The EDC technique provides reasonable results for the structures with confined modes. The detail of the EDC method, applicable to an image guide structure, is explained in [47]. Two kinds of dominant modes, $TM_Y^{mn}(E_Y^{mn})$ and $TE_Y^{mn}(E_X^{mn})$, potentially can be supported by an image guide structure. Image guide dimensions determine the corresponding dominant mode. The image guide thickness, which is equal to the HRS wafer thickness, is chosen as 500 μ m. This standard HRS wafer can support SIG structures for operating below the 300 GHz frequency range. For the sake of clarity, the D-band range of frequencies (110-170 GHz) is chosen for implementing the SIG structures and devices in the rest of this thesis. The width of SIG (W) is chosen to be smaller than its height (h) to support TM_Y^{11} , as a dominant mode. Since the height of the waveguide is fixed (500 μ m), the waveguide width is the only design parameter for determining the desired mode(s) operational bandwidth. The SIG structures are preferred to have thinner widths for coupling applications, which will be discussed in upcoming chapters. However,

the higher order modes of a thin waveguide are not finely confined and can be radiated easily. Therefore, designing a thin waveguide is a trade-off between single mode operational bandwidth and higher radiation loss.

Fig. 2.2 shows the full-wave simulated dispersion curves of an HRS image guide with the cross section of $500 \times 250 \mu\text{m}^2$, over 50 to 250 GHz. The plots show that the dominant mode of the waveguide is $TM_Y^{11}(E_Y^{11})$. The next two modes, $TM_Y^{21}(E_Y^{21})$ and $TE_Y^{11}(E_X^{11})$, have N_{eff} close to 1 over the D-band range of frequencies. Therefore, these modes can be considered as non-propagating modes. In fact, those modes are too lossy to propagate along the SIG structure. The conductivity and permittivity of simulated silicon structures are considered to be $20 \text{ K}\Omega\text{-cm}$ and 11.8, respectively.

In order to test the SIG structure, a metallic waveguide excitation with the TE^{10} mode, compatible with the measurement setup, was chosen. Different techniques are reported for providing a low-loss transition from the metallic waveguide to a dielectric waveguide structure. In one method, the metallic waveguide is flared out to form a horn for impedance matching points of view [48]. In other works, the dielectric waveguide is tapered in both the E and H planes and inserted into a reduced height metallic waveguide [49]. However, these approaches need complex fabrication processes. Therefore, a simple E -plane dielectric tapered transition, inserted into the metallic waveguide, is designed for carrying out the measurements, effectively, and to keep the total loss low. The tapered length and the position of the tapered are optimized for gradual conversion of modes, from the metallic waveguide mode (TE^{10}) to dielectric waveguide mode (E_Y^{11}). Fig. 2.3 shows the simulated S-parameters of the SIG structure, tapered inside WR-06 standard metallic waveguide ports.

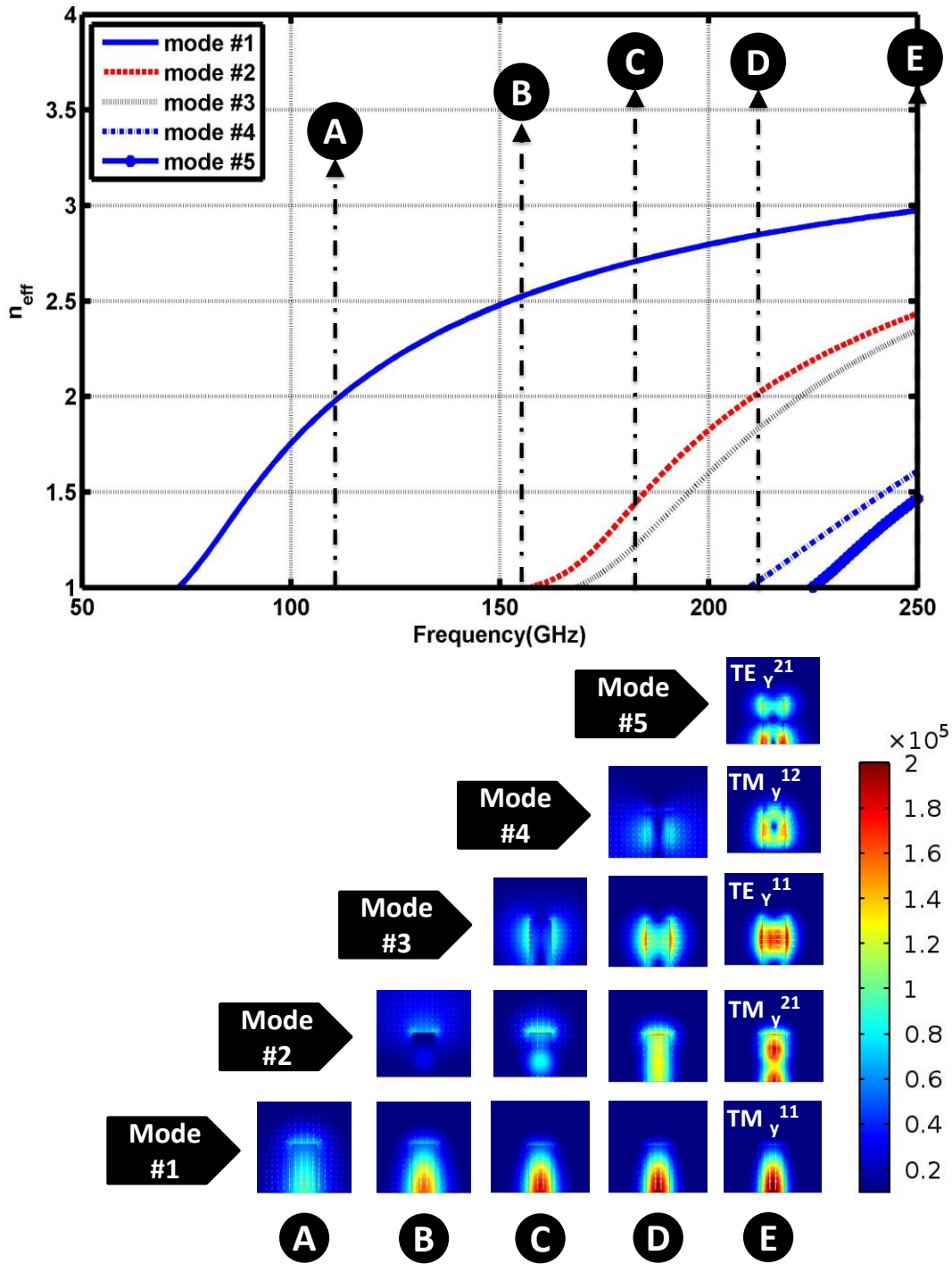


Fig. 2.2: Dispersion curves and modal behavior of the SIG structure over 50 to 250 GHz.

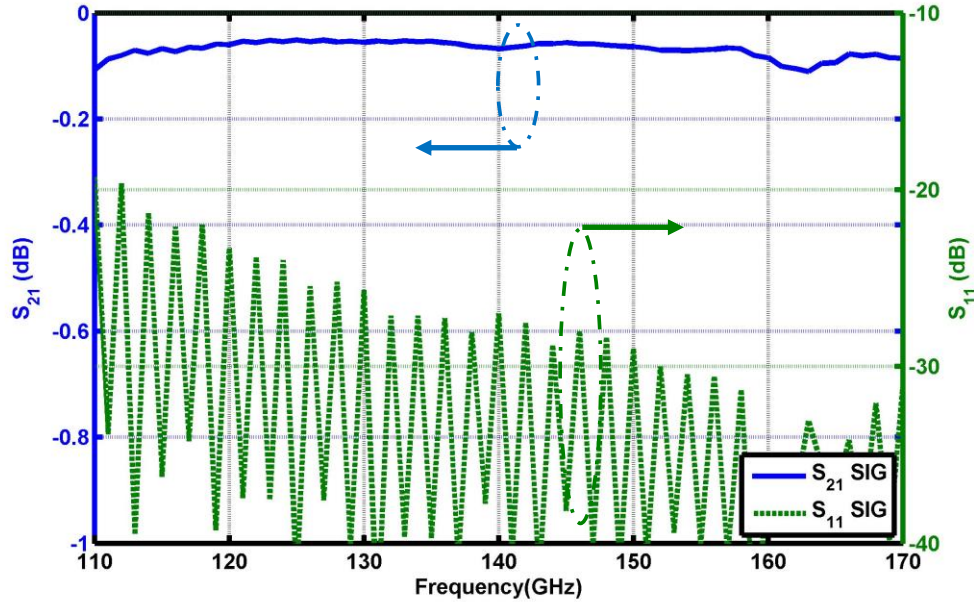


Fig. 2.3: The simulated S-parameters of the SIG with the tapered sections, placed on a perfect conductor.

The simulated insertion loss is compared to that of SIG with no tapering sections. The taper length inside the metallic waveguide is 7 mm and the total length of each taper section and the SIG structure are 9 mm and 24 mm, respectively. The results are obtained for an ideal case when the ground is a perfect conductor. As can be seen, the taper transition has negligible effect on the insertion loss. The sharpness of the taper tip has significant effect on the reflection response of the SIG structure and it will be investigated in this chapter. One of the advantages of exciting the SIG structures with the metallic waveguide, as shown in Fig. 2.1, is to suppress the x -polarized modes; although, in the proposed SIG structure the higher order modes are potentially non-propagating modes over the desired frequency band.

2.1.2 Laser Machining Fabrication Process

All the introduced dielectric image guide structures in this research are fabricated using the laser machining technique. Although, the Deep Reactive Ion Etching (DRIE) technique is capable of fabricating very precise structures, and this degree of precision is only needed for the structures for which micrometer accuracy is needed. On the other hand, laser machining fabrication error is in the range, which is often acceptable for the structures operating at the sub-mmWave and THz range of frequencies. There are distinct advantages for the laser fabrication process over the conventional DRIE fabrication technique; laser machining is a

mask-free, chemical-free, fast, and low-cost process. The detail of developed recipe for machining the SIG structure is discussed in Appendix G.

The developed recipe results in a rectangular dielectric waveguide whose side walls form right angles with the accuracy of $<1^\circ$. Unfortunately, even the lowest power level of the laser beam forms a thin amorphous layer of silicon at the surface, where the laser ablation occurs. Transformation to an amorphous state from a crystalline state, even in the scale of a few hundred nanometers, considerably increases the silicon waveguide insertion loss. Forming a thin layer of oxide at the laser cutting face is another source of loss in the fabricated SIG structure. A number of investigations and tests are conducted to solve this problem. It is understood that Tetra Methyl Ammonium Hydroxide (TMAH) etchant is one of the most effective solutions for cleaning the fabricated HRS waveguides. In fact, immersing a HRS waveguide in TMAH etchant for a few minutes (a 25% TMAH solution) etches the silicon at the rate of $\sim 0.8 \mu\text{m}/\text{min}$ at 80°C . The developed laser machining process recipe enables the realization of all required passive SIG structures. One of the most useful capabilities offered by the laser fabrication process is the possibility of making pockets inside a SIG structure. In other words, multi-level fabrication is now feasible with laser machining. In the next chapter, this capability is used for fabricating the grating antennas.

2.1.3 Fabrication and Measurement Error Analysis

Measurement at the mmWave/THz range of frequencies is very challenging. Preparing an ideal measurement setup with minimum errors is a key step to reach the expected experimental results with sufficient accuracy. Precise measurement error analysis leads us to assess the performance of the system in a real measurement environment. Fabrication and measurement errors/uncertainties are two main categories of the errors. These errors are not completely independent of each other. To conduct experiments with more accuracy the following factors must be taken into consideration:

- The conductivity of the ground
- The sharpness of the tip of the dielectric waveguide tapered section in the transition region
- The mechanical fixture and measurement errors/inaccuracies

Although the dominant mode is highly confined inside the image guide, the attenuation constant of the image guide is increased by an imperfect conductive ground. Fig. 2.4 shows the insertion loss of the SIG structure, placed on an aluminum fixture. The results show that the aluminum plate adds around 0.15 dB loss to the total insertion loss of the 24 mm SIG structure.

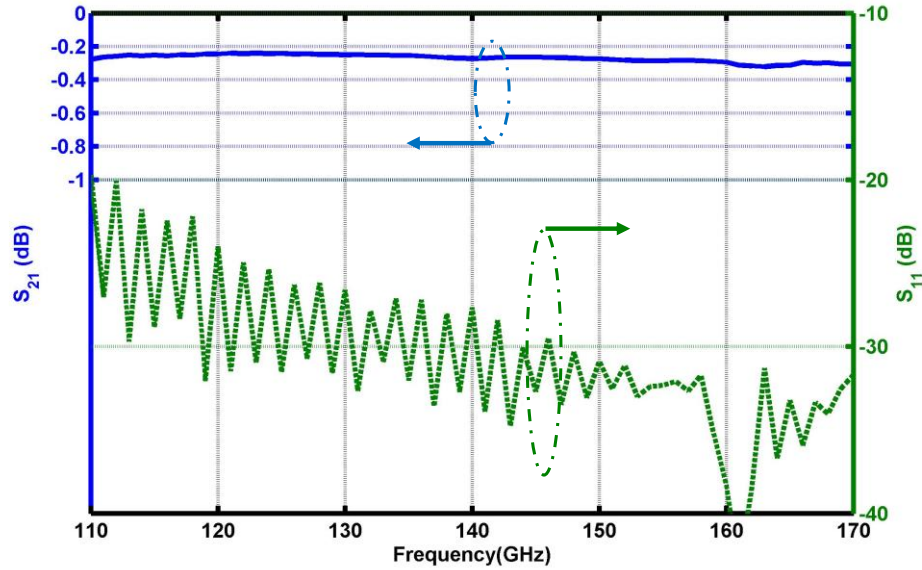


Fig. 2.4: The simulated S-parameters of the 24 mm tapered SIG, on an aluminum ground plane.

Tapered transition has a significant effect on the return loss of a dielectric waveguide-based structure. The sharper the tip, the lower the return loss. Achieving a very sharp tip is not practically feasible with the laser machine fabrication technique. To examine the effect of tip width on the S-parameters, a tapered SIG with three different tip widths, 10 μm , 20 μm , and 50 μm , are simulated. The total length of all simulated SIG structures, including the tapered sections, is 24 mm. The results in Fig. 2.5 show that the tips with the widths of 10 μm and 20 μm have negligible effect on the insertion loss. However, the 20 μm tip width causes larger ripples on the reflection response of the SIG. By increasing the tip width to 50 μm , the SIG loss and reflection increases and the operational frequency bandwidth of SIG structure is decreased.

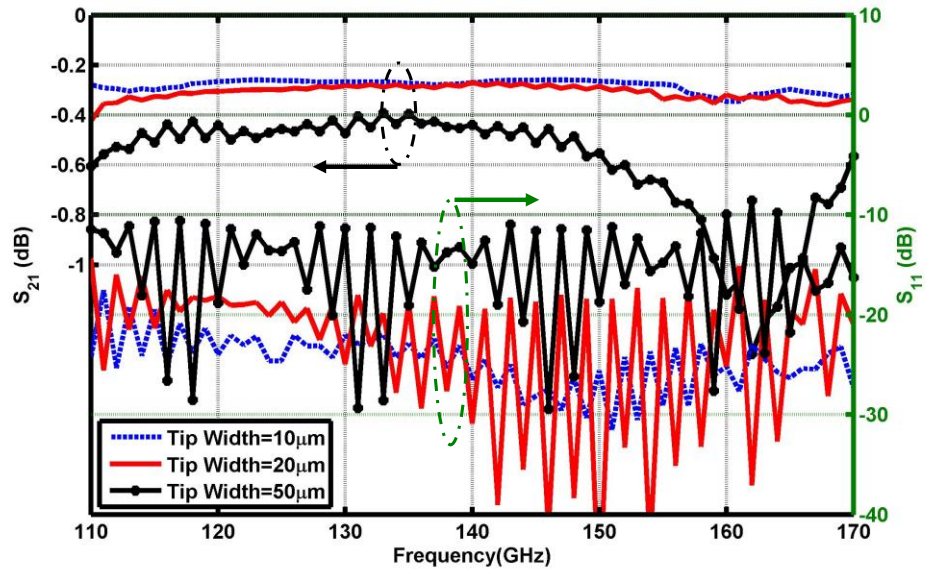


Fig. 2.5: The tapering tip width effect on the simulated S-parameters of the SIG structure.

In order to conduct the experimental measurements, various metallic fixture prototypes are designed and fabricated. The metallic fixtures are manufactured either by Computer Numerical Control (CNC) machinery or wire cutting technique. Due to the fabrication errors, none of the manufactured fixtures are perfect. The fabrication/measurement errors can appear in different geometric formats as follows (refer to Fig. 2.6):

- Existence of the unwanted air gap between the dielectric waveguide and the ground plane:
 - a. Unwanted air gap between the tapered dielectric section and metallic waveguide ground
 - b. Unwanted air gap between the dielectric waveguide and the test fixture ground
 - c. Both the aforementioned cases
- Existence of a slit at the interface of metallic waveguide ports and the metallic fixture
- Lateral misalignment error, due to the centre positioning of the SIG inside the metallic waveguide ports

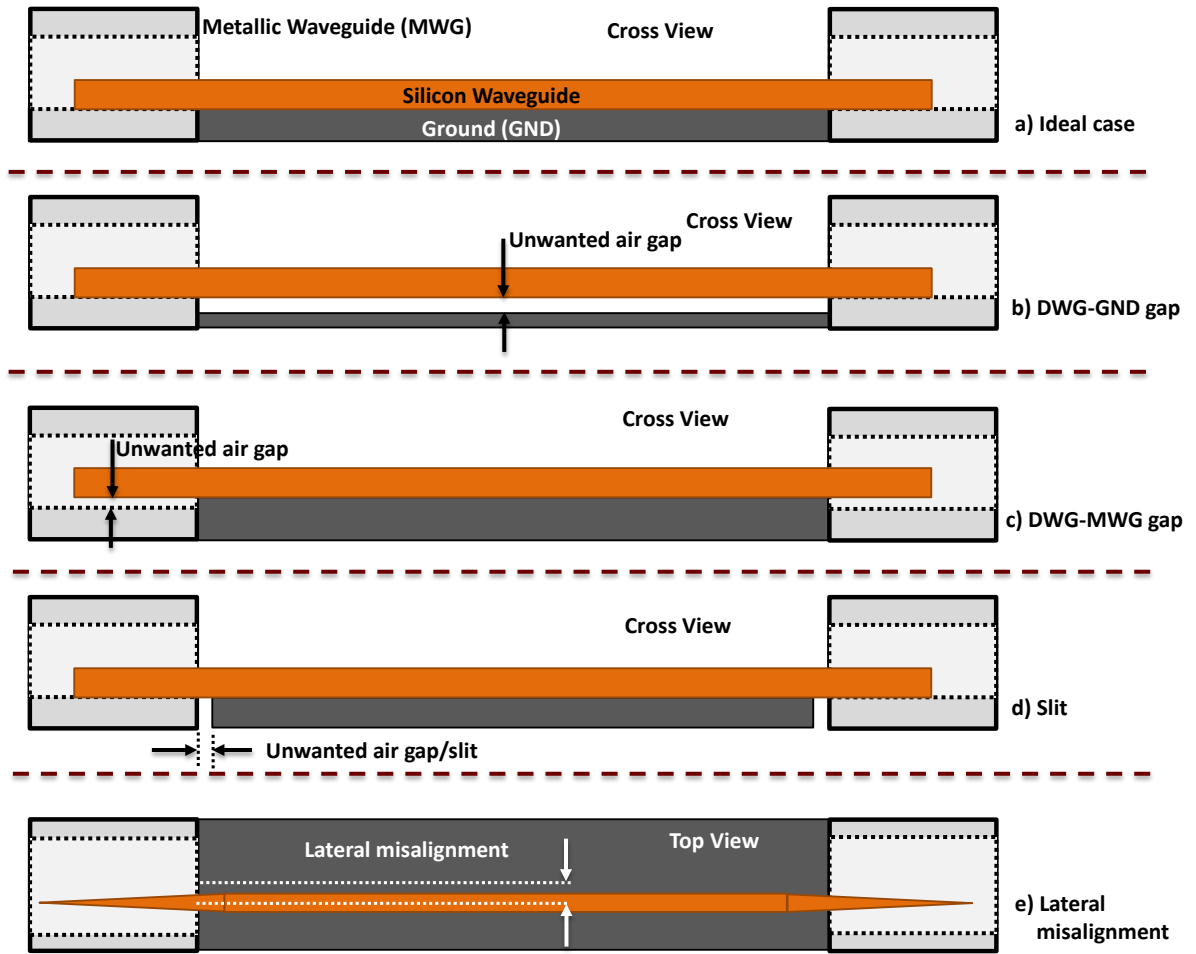


Fig. 2.6: The possible measurement errors for a SIG structure.

Mechanical fabrication tolerance can cause maximum $10\ \mu\text{m}$ misalignment between the test fixture ground and the metallic waveguide ground in two forms, Fig. 2.6(b) and Fig. 2.6(c). Fig. 2.7 shows the simulated unwanted air gap effect on the S-parameter responses of the SIG. Based on the simulation results, the added loss due to the configuration in Fig. 2.6(b) is higher than the one in Fig. 2.6(c).

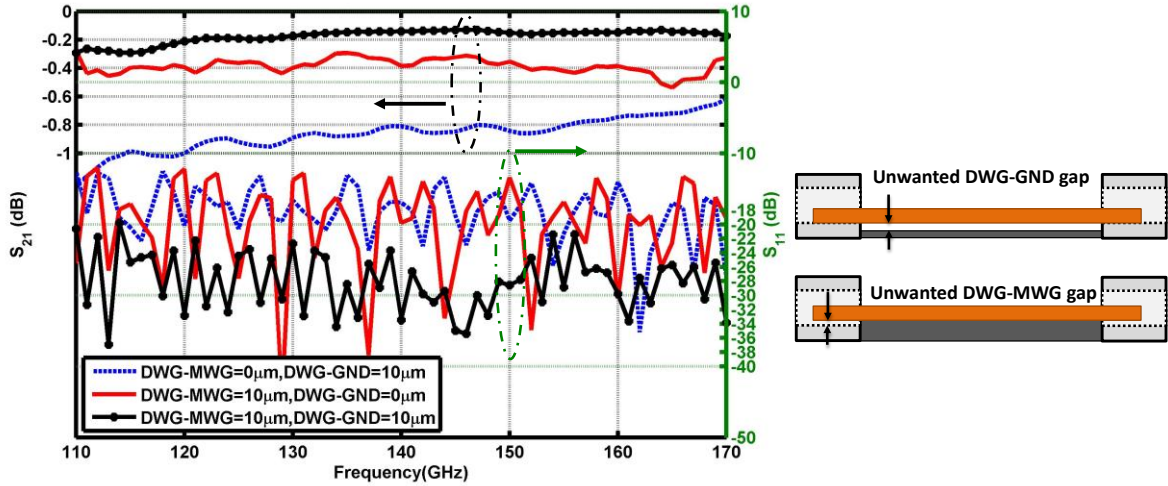


Fig. 2.7: Measurement setup unwanted air gap effect on the simulated S-parameters of the SIG.

In the next step, the effect of a slit, at the interface of fixture and metallic waveguide, on S-parameters is studied. The simulation results for two different slit widths, 10 μm and 50 μm , are shown in Fig. 2.8. It is observed that this fabrication/measurement-setup error has the major effect in increasing the insertion loss as compared to the previously discussed errors. A slit of 10 μm width adds at least 0.5 dB loss to the system. Also, it significantly affects the return loss.

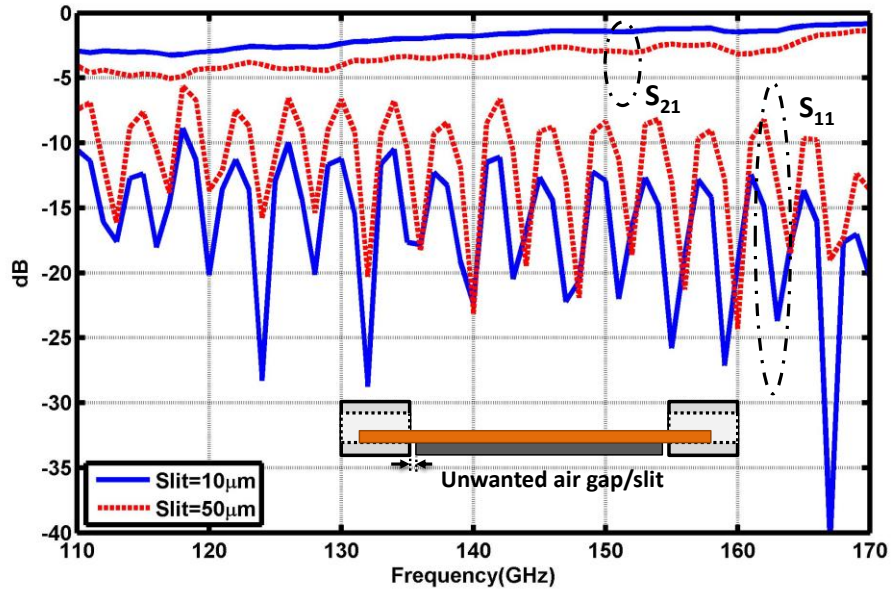


Fig. 2.8: The ground slit effect on the simulated S-parameters of the SIG structure.

Finally, the effect of SIG alignment with respect to the centre of metallic waveguide ports is investigated. Two different lateral misalignments, 100 μm and 300 μm , are simulated and the results are shown in Fig. 2.9. Interestingly, this type of error has the least effect on the S-parameters of the SIG structure. This is important in the case that the SIG is manually positioned between the ports.

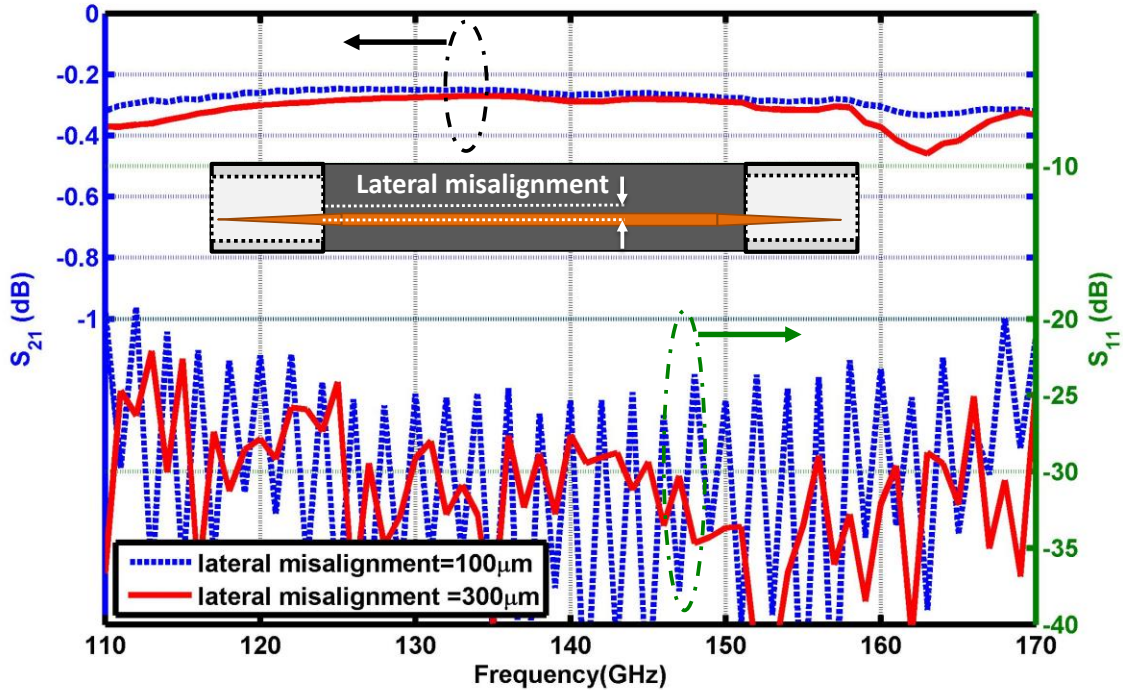


Fig. 2.9: The lateral misalignment investigation on the Simulated S-parameters of the SIG.

2.1.4 Measurement Results of the Fabricated SIG Straight Waveguide

Two different lengths of the HRS straight waveguide segments, 24 mm and 34 mm, are fabricated using the laser machining technique. The structures are fabricated based on the dimensions listed in Table 2.1. Both structures have identical tapered sections with identical 9 mm length. The fabricated SIG structures are measured using an Agilent network analyzer armed with two frequency extender modules, working over 110-170 GHz (refer to Fig. 2.10). Each of the frequency extender modules are placed on a customized positioner, with a 5-axis degree of freedom. The positioners enable us to adjust the extender modules with respect to each other and with respect to the metallic fixture along the five axes; x , y , z , θ , and ϕ . The obtained S-parameters for two different lengths of straight SIGs are plotted in Fig. 2.11.

The measurement results show that the insertion loss for the 34 mm waveguide varies in the range of 0.7 to 1.9 dB. This loss includes the tapered section loss, radiation loss, and metallic loss due to the aluminum ground. The insertion loss for the shorter waveguide, 24 mm, fluctuates between 0.4 to 1.5 dB. The achieved results may include all discussed measurement setup errors. The measured data indicates that the fabricated HRS image guide has the average loss of 0.035 dB/mm, over the range of 110-170 GHz, on an aluminum plate with conductivity of $\sigma \sim 30 \times 10^6$ S/m.

Table 2.1: The fabricated SIG dimensions values.

Parameter	Value	Parameter	Value
L	24 mm	$Taper_L$	9 mm
L_I	6 mm	$Taper_w$	20 μm
W	250 μm	h	~ 500 μm

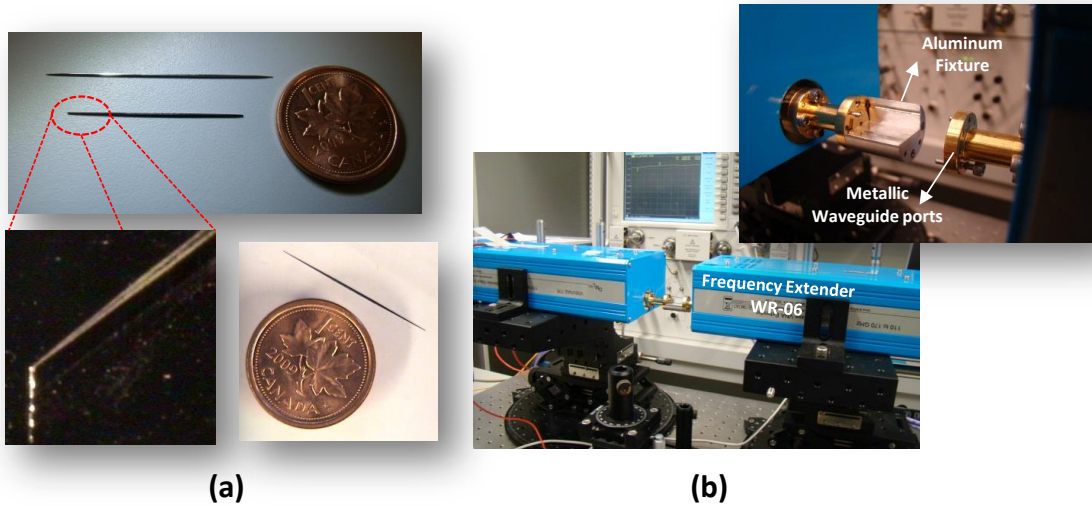


Fig. 2.10: (a) The straight SIG structures fabricated by the laser machining process (two different lengths: 24 and 34 mm). (b) The measurement setup.

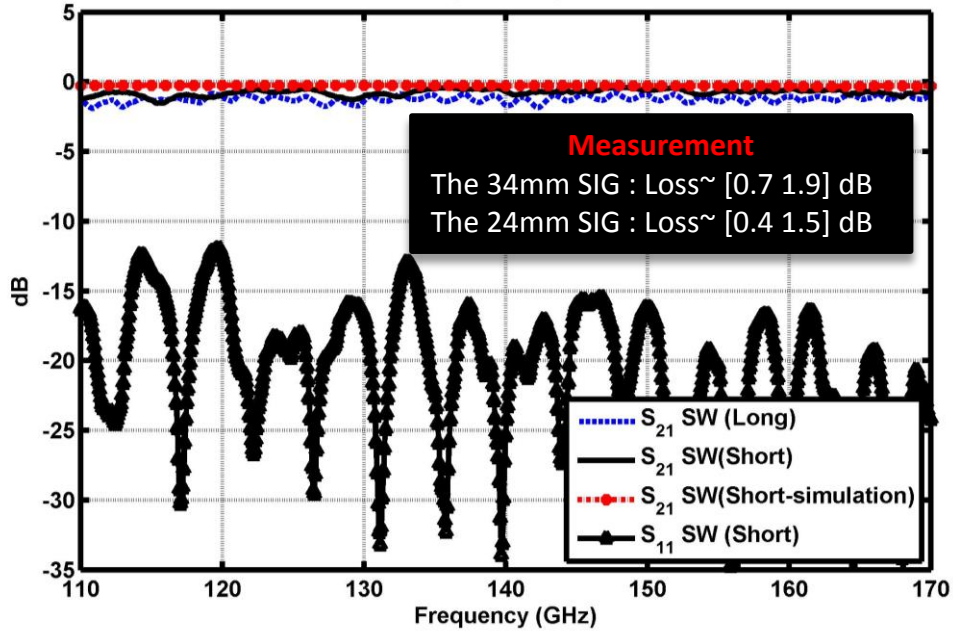


Fig. 2.11: The measurement results for two different lengths of the fabricated straight waveguide (SW) SIG structures, compared to the simulation result of a 24 mm SW-SIG.

2.2 Silicon-On-Glass (SOG) Technology

By increasing the operational frequency of an image guide system, the conductor loss becomes the major source of loss. Also, due to the size shrinkage of passive devices at higher frequencies, a handle-layer is required for holding the HRS waveguide-based devices. The handle-layer must not increase the cost of the system, significantly. The main factors in the total cost of the system are attributed to the substrate materials and the fabrication cost respectively. Secondly, the handle-layer must tolerate different kinds of processing and micro-machining. More importantly, the handle layer should provide a minimum contribution to the total loss of the system.

Glass (Pyrex) is a promising choice. A reasonably priced glass wafer is suitable for low-cost fabrication methods and components. A thick glass substrate eliminates the effect of the ground plate loss. Due to the high contrast between the glass and the silicon, the modes are strongly confined inside the silicon waveguide up to a few hundred gigahertz. Additionally, the glass can be employed in an efficient manner to suppress unwanted modes inside the dielectric waveguide structure. Different methods have been proposed for bonding the glass to silicon, including anodic bonding which is a high quality process. To implement the SOG

structures, the DRIE fabrication process is developed in the Centre for Intelligent Antenna and Radio Systems (CIARS) group. The details of the two-mask DRIE process are explained in Appendix F.

In the following sections, two major developed SOG configurations are discussed: Suspended Silicon-On-Glass, and Silicon on Corrugated Glass. Both technologies can be designed for two possible x - or y - polarizations. Both technologies are similar in terms of modal behaviors. A y -polarized straight waveguide segment based on the Silicon on Corrugated Glass technology, is designed, fabricated, and tested over the G-band range of frequencies (140-220 GHz).

2.2.1 Suspended Silicon-On-Glass; Basic Idea and Design Analysis

The Simplest configuration for a SOG structure is to place the glass (Pyrex) substrate directly underneath the HRS rectangular waveguide, which is called insulated image guide configuration. However, the main issue is the effect of the lossy glass substrate on the total insertion loss of the system, especially at higher frequencies. Fig. 2.12 shows the absorption loss plot of the Pyrex, derived according to [50].

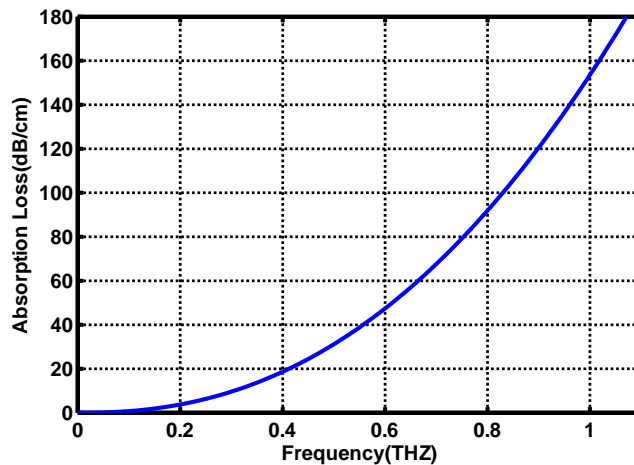


Fig. 2.12: The absorption loss of Pyrex.

The preliminary simulations, conducted at CIARS [51], signify that the Pyrex underneath a rectangular silicon waveguide causes a relatively substantial loss beyond the 100 GHz. This problem is solved by a simple and novel idea, as depicted in Fig. 2.13. An empty channel with the proper depth is designed under the silicon and inside the Pyrex. The depth and width of this cavity channel depend on the propagating mode. With this technique, the penetration

of the desired silicon field inside the Pyrex is negligible. Obviously, to suspend the waveguide, a kind of support mechanism is needed above the cavity. The support structure should not have significant effect on the modal behavior of the HRS waveguide. Therefore, a set of narrow arms are used to connect the HRS waveguide to the sides and suspend the waveguide. The arms are firmly fixed to the Pyrex by square legs. It is found that the arms do not change the electric field distribution inside the waveguide, as long as the width of the supporting arms are less than 1/10 of the waveguide width. By using this novel structure, the Pyrex loss is almost eliminated.

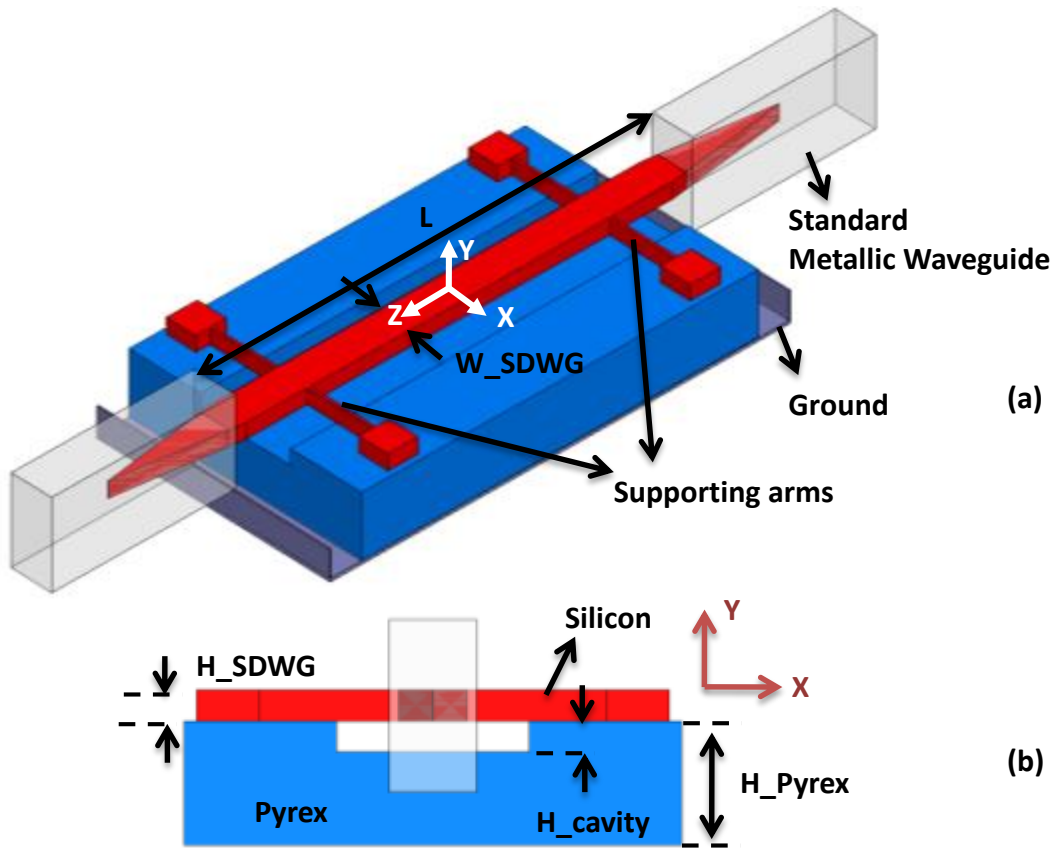


Fig. 2.13: The proposed SDWG structure (a) 3-D view, and (b) the cross view.

The proposed suspended SOG structure potentially can be designed to operate dominantly either in y polarization or x polarization, suppressing non-desirable modes. To have a y -polarized suspended SOG structure, the width of silicon waveguide should be wider than its height, and the reverse for the x -polarized structure. Obviously, the appropriate excitation configuration should be chosen based on the desired polarization in the SOG structure. In

both types of excitation, the silicon waveguide should be placed symmetrically at the middle of the metallic waveguide. One of the main advantages of having x -polarized excitation is to reach a better coupling from metallic waveguide mode to dielectric waveguide mode. Consequently, a shorter taper can be designed for the suspended SOG structures.

To design the SOG structures, the thickness of the HRS waveguides is pivotal in determining the operation frequency range. A comprehensive study was performed at CIARS to find the minimum number of required silicon wafers with corresponding thicknesses to cover the required range from 50 GHz to 1.1 THz. After an extensive study and characterization effort by CIARS researchers, optimal HRS wafer thicknesses for various ranges of frequencies, for both polarization configurations, have been obtained, and a general design guideline has been developed for future designs to facilitate new designs and to decrease the overall cost of the systems. After tabulating the appropriate thicknesses for the corresponding range of frequencies, the optimum thickness can be selected for a certain design. For instance, the 100 μm standard silicon wafer is found to be the optimum thickness for the range of 370-470 GHz for an x -polarized suspended SOG structure. Although for proof of concept, a suspended SOG structure is designed at that specific range of frequency, the idea can be applied to the entire mmWave/THz range of frequencies.

The waveguide is designed to operate in single mode over the chosen band. The dominant mode of the dielectric waveguide with the cross section of $100 \times 220 \mu\text{m}^2$ is $TE_Y^{11}(E_X^{11})$. Table 2.2 lists the design parameters of the structure. The structure is excited with an x -polarized WR-2.2 metallic waveguide. In order to verify the single mode propagation inside the silicon waveguide a spatial Fast Fourier Transform (FFT) test is performed. To determine the correct number of modes, the field is sampled along the line on which the maximum possible modes contribute (it is specified with a dot in Fig. 2.14), and then spatial FFT with respect to a variable, representing the direction of wave propagation along the waveguide, is performed. Fig. 2.14 shows the FFT result of the E_x field, extracted from a full-wave simulation at 400 GHz, along the line from $[x_1= W_SDWG/2, y_1= - H_SDWG/4, z_1= - L/2]$ to $[x_2= W_SDWG/2, y_2= - H_SDWG/4, z_2= L/2]$. Accordingly, the effective index of the waveguide is derived as $n_{eff} = \lambda_g/\lambda_0 \approx 2.21$. The propagation constant, obtained from this technique, is almost the same as the one calculated analytically.

Table 2.2: The design parameter values of the suspended SOG.

Parameter	Value	Parameter	Value
Total length of the structure	10 mm	H_{SDWG}	100 μm
W	220 μm	H_{Pyrex}	400 μm
L	5 mm	H_{Cavity}	100 μm

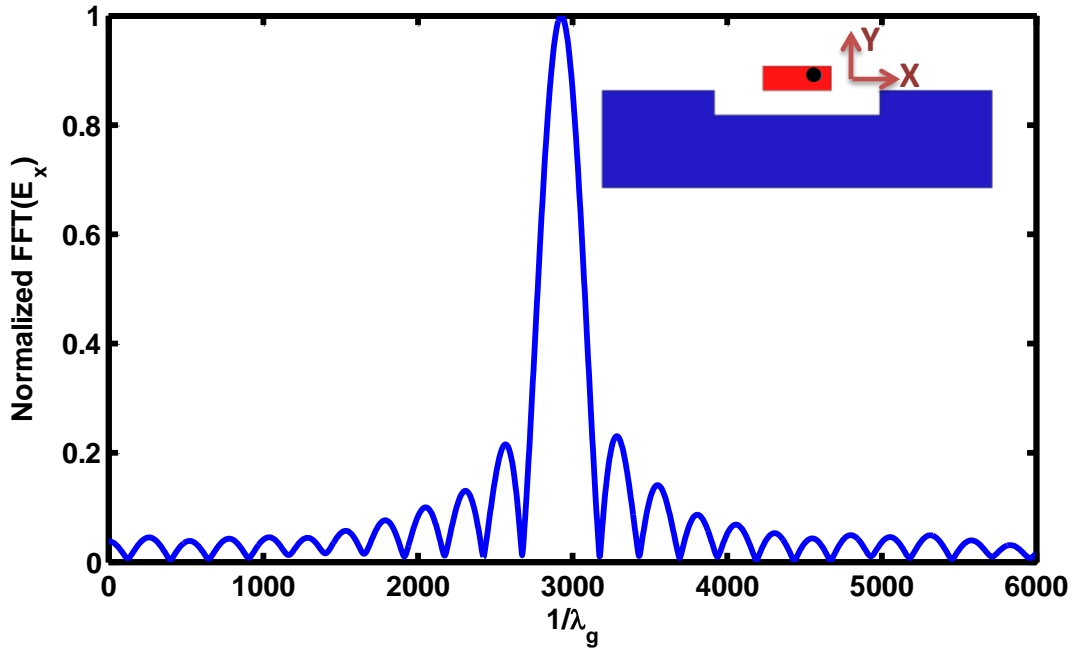


Fig. 2.14: The Fourier transform of the E_x field along the dielectric waveguide at 400 GHz.

Fig. 2.16 denotes the transmission loss of the entire structure with an overall length of 10 mm, including all the transitions. The effect of supporting beams in the transmission response is negligible. According to the simulated results, it is found that the proposed waveguide has a maximum insertion loss of 0.5 dB, and a return loss better than -15 dB over the 370-470 GHz.

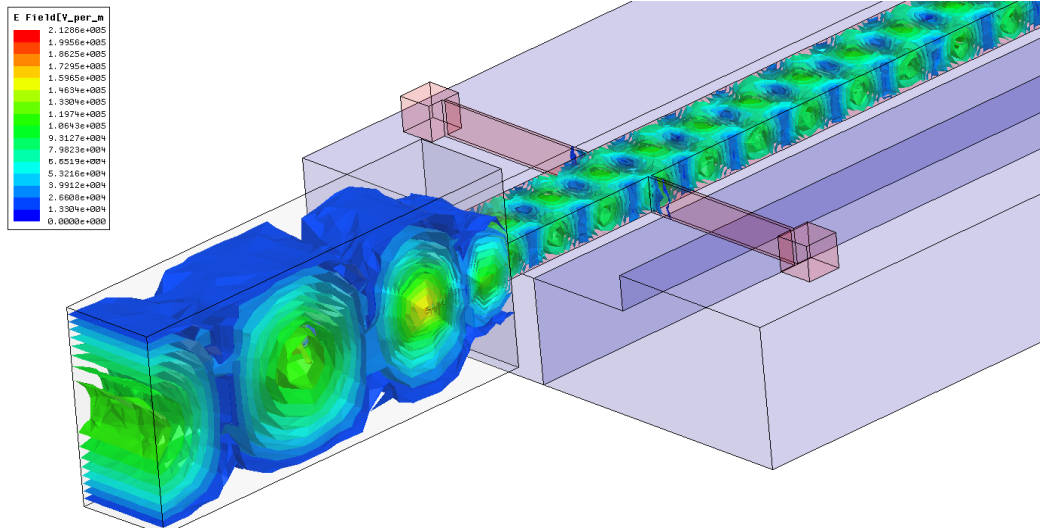


Fig. 2.15: The total electric field distribution of the proposed Suspended SOG structure at 400 GHz.

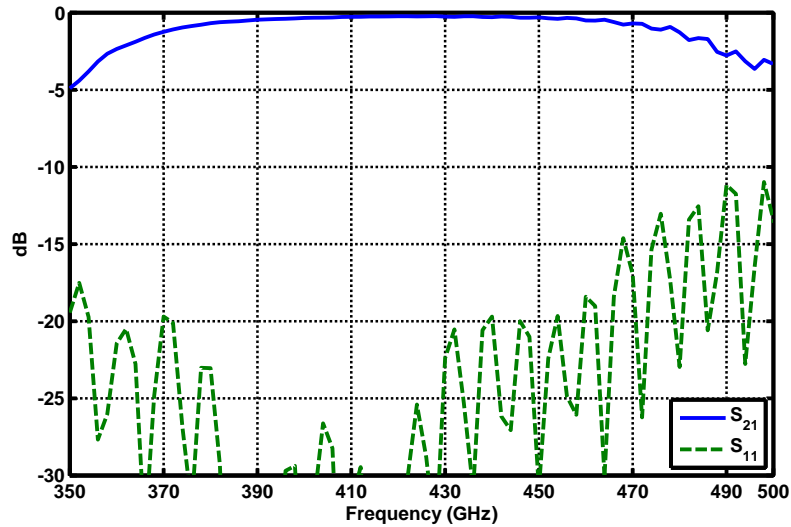


Fig. 2.16: The simulated S-parameters of the Suspended SOG in the range of 350-500 GHz.

2.2.2 Silicon on Corrugated Glass; Simulation and Measurement Results

The introduced suspended SOG technology is not an optimized configuration for advanced devices, especially when a coupling structure is required. Also, the fragile support beams occupy, relatively, a large area. Therefore, a modified version of the Suspended SOG technology is developed in CIARS [52], [53]. In the new SOG configuration, HRS waveguide is held on top of an array of narrow glass bridges (refer to Fig. 2.17). The

corrugation is designed in such a way that it does not disturb the field, significantly. The proposed technology can be reconfigured to support either x - or y - polarized field.

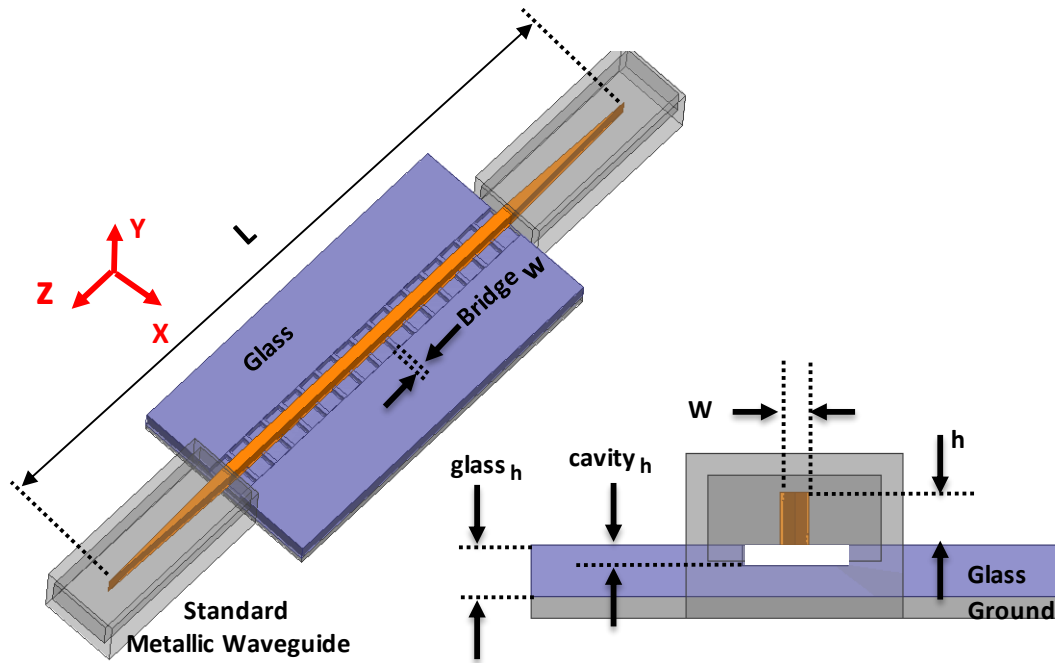


Fig. 2.17: The proposed Silicon on Corrugated Glass configuration.

Although designing a SOG structure at a higher range of frequencies is more attractive, it requires less fabrication tolerances and a greater measurement expertise. Moreover, the design ideas can be verified at lower frequencies with a lower risk. The silicon wafer with a 500 μm thickness is chosen to cover the 140-220 GHz standard frequency band for design of a y -polarized Silicon on Corrugated Glass waveguide. The design parameters, optimized for the structure to operate in single mode, are listed in Table 2.3. The performance of the SOG structure is investigated via the simulated dispersion curves (refer to Fig. 2.18). The transmission and reflection losses of the finalized structure, achieved by the full-wave simulations, are shown in Fig. 2.19.

Table 2.3: The design parameter values of the Silicon on Corrugated Glass.

Parameter	Value	Parameter	Value
L	16 mm	$Glass_h$	500 μm
W	300 μm	$Cavity_h$	100 μm
h	500 μm	$Bridge_w$	30 μm

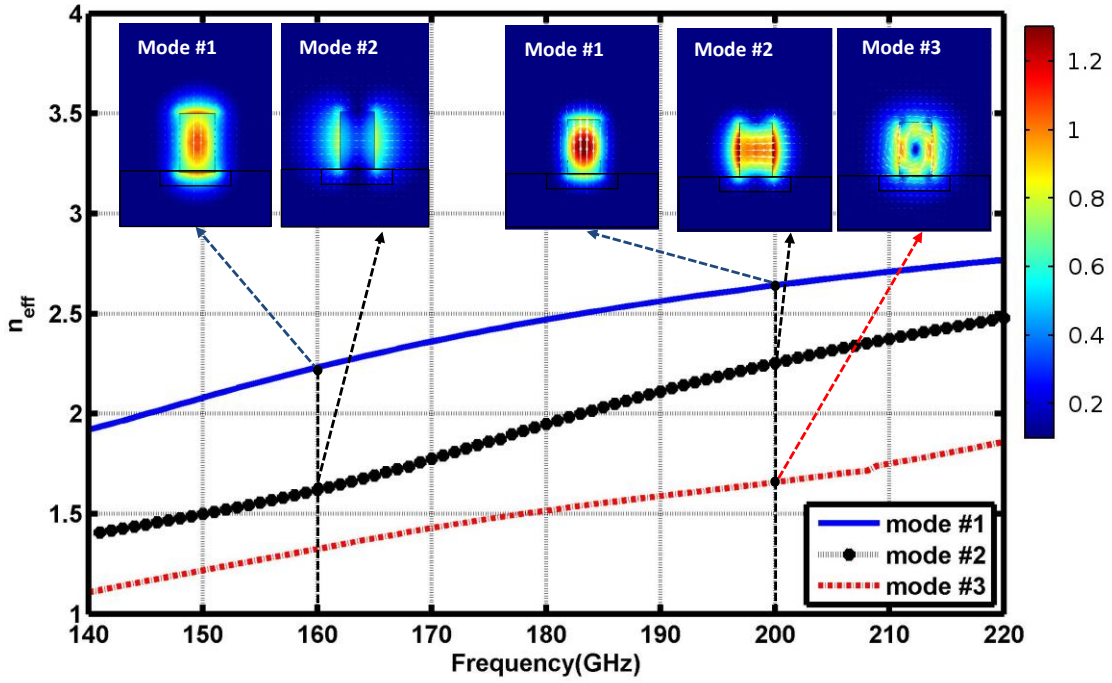


Fig. 2.18: Dispersion curves and mode behavior of the SOG structure over G-band.

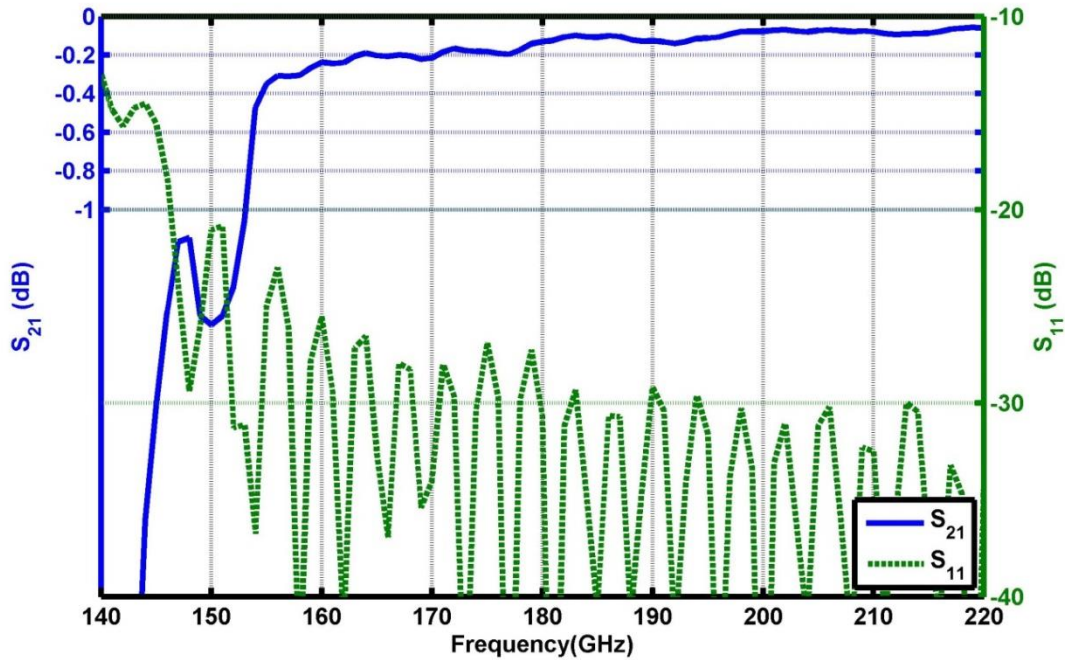


Fig. 2.19: The simulated transmission and return loss of the Silicon On Corrugated Glass over G-band.

The fabricated straight waveguide sample is tested, and the measured results are shown in Fig. 2.20(b). The obtained average insertion loss, over the range of 150-200 GHz, is approximately 2.5 dB, with a minimum of 0.2 dB. The measured loss of the whole structure is more than what was predicted by the simulation. The major reason for this discrepancy is due to the fabrication and the measurement setup errors, part of which are mechanical fixture errors. These errors are generally similar to those which are explained in Section 2.1.3. The main error factor is the roughness of the fixture. Also, the fabrication errors in realizing the cavity channel and the bridges are another source of errors.

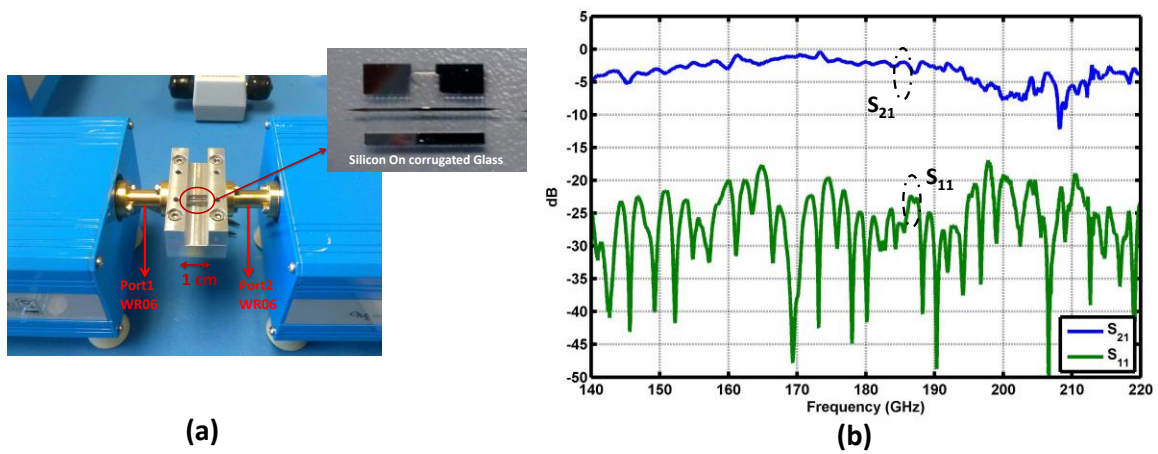


Fig. 2.20: (a) The measurement setup for the fabricated Silicon On corrugated Glass, (b) measured S-parameters of the fabricated SOG structure over G-band.

An innovative experiment is performed for verifying the low-loss behavior of the HRS waveguide. In this test, the dielectric waveguide is detached from the glass and inserted directly inside the metallic waveguide, as shown in Fig. 2.21(inset). In fact, the silicon waveguide is suspended in air, while the tapered sections are held by metallic waveguide ports. Although the propagation mode in this case is different from that in SOG configuration, the S-parameter measurements provide a good insight about the inherent loss of HRS waveguide. The measured S-parameters are plotted in Fig. 2.21. It is observed that in a small range of frequencies the insertion loss drops to its minimum value which is less than 0.25 dB.

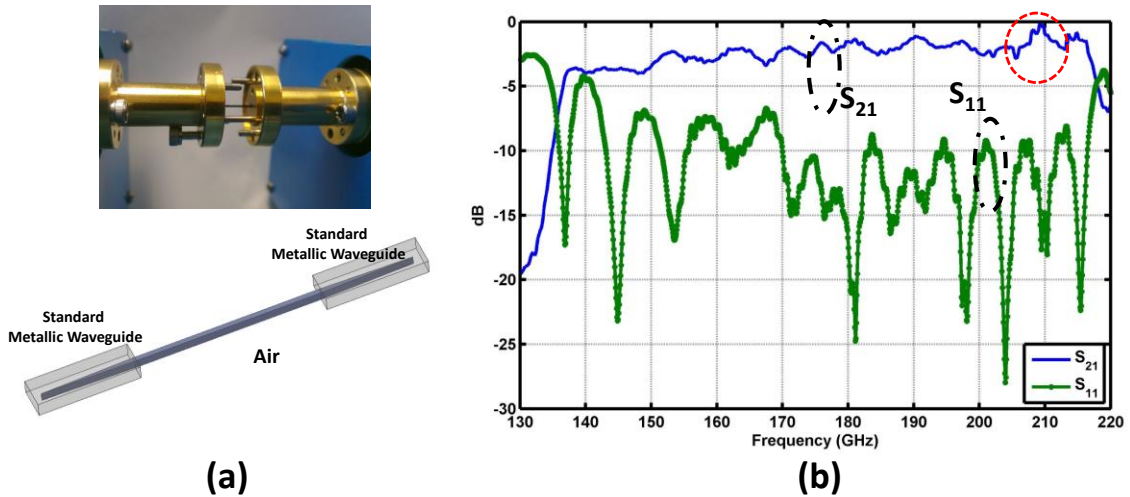


Fig. 2.21: (a) The experiment for verifying the low-loss behavior of the silicon waveguide, and (b) the measured S-parameters of the detached silicon waveguide, which is placed between two metallic waveguide ports.

2.3 Conclusion

In this chapter, the performance of both technologies was extensively investigated through the modal analysis and full-wave simulations. Moreover, the effects of all possible errors, due to the measurement setup imperfections and fabrication inaccuracies/uncertainties, on the performance of the newly developed devices were studied. Then, the waveguide samples, in both technologies, were fabricated and tested. In addition to the lithography/DRIE fabrication technique, which was mainly used for SOG structures, an efficient and fast laser machining process was developed for realization of the prototype SIG structures and devices. The introduced laser machining fabrication technique is a chemical and mask-free process, which was utilized for shaping the silicon structures with the capability of making a pocket inside the silicon wafer. The technique provides micrometer fabrication accuracy which is required for device prototyping at the mmWave and THz range of frequencies. The experimental results confirmed that the SIG can potentially be a highly low-loss (less than 0.035 dB/mm) transmission structure over the D-band (110-170 GHz) range of frequencies. The measured results were obtained for a straight waveguide segment on SIG technology with aluminum ground. The fabricated SOG waveguide, operating over the G-band (140-220 GHz) range of

frequencies, showed the minimum insertion loss of 0.2 dB for the total length of 16 mm, including the tapered sections.

The introduced SOG technology in this chapter can be extended to high THz frequencies due to SOG low-loss characteristic and ease-to-handle geometry. Indeed, SOG technology is a promising technology for implementing THz devices. However, the proposed SIG technology offers more cost-effective and ease-to-fabricate devices at mmWave range of frequencies, where the ohmic loss due to the ground can be tolerated.

In the next chapter, several SIG passive structures are designed and implemented.

Table 2.4: Overall Comparison of SIG and SOG technologies.

Technology	Propagation Loss	Fabrication	Fragility	Transition to Metallic Waveguide	Single Mode Operation Bandwidth
SIG	Low < 350 GHz	Laser machining or DRIE(Minimum one mask)	High	Easy	Wider than SOG
SOG	Low, even at high THz frequencies (Less than SIG)	DRIE (Minimum two masks)	Less than SIG	Moderate (More complex metallic fixture than the one for SIG)	Moderate

Chapter 3

SIG Passive Components: Design, Analysis, and Measurement

In order to implement an integrated dielectric waveguide-based system, various key components are required. This chapter introduces a number of developed passive structures based on the SIG technology. The design ideas can be easily extended to the SOG technology; however, as a starting point it is easier to work with SIG structures from the fabrication and measurement points of view. The designed passive elements are formed and developed based on the topologies and ideas originated in the optics and the microwave range of frequencies. The design analysis and the measurement results of the proposed components are presented.

3.1 Bend

Bends are essential components in implementation of various integrated systems. The bends are necessary for realizing in-package systems, where the size is an important parameter. In optics, designing bends and curvatures have always been a challenge due to fundamental limitations including very small contrast between the waveguide core and surrounding medium [54]. Having a bend with a small radius and a wide angle comes at the cost of higher radiation loss, due to the radiation from the curved parts. Extensive works have been performed in optics to reduce the bending/radiation loss. Using a metal sheet at the curvature section is one method for reducing the bending loss in optical wavelengths. Radiation loss can be less problematic in the mmWave/THz range of frequencies by using the HRS waveguide-based technology. The highly confined field inside the HRS waveguide has much less radiation loss at the bends.

The waveguide bends can be implemented by both the SIG and SOG technologies. Fig. 3.1 shows the general configuration of two back-to-back SIG bends. The bends are often described by two main parameters: bending radius, and bending angle. The radiation loss decreases with an increase in operational frequency and waveguide width, because the propagation mode becomes more confined inside the waveguide. The SIG waveguide dimensions are the same as the one for the straight waveguide segment ($500 \times 250 \mu\text{m}^2$), explained in Chapter 2. The first set of simulations is based on the configuration in

Fig. 3.1(a), which consists of two back-to-back identical bends, placed on a perfect ground plane. Fig. 3.2(a) illustrates the effect of bending angle on the insertion loss, for the fixed curvature radius ($R=1$ mm). Also, the influence of different radii of curvature for a fixed bending angle ($\theta=90^\circ$) is shown in Fig. 3.2(b). As can be observed, the bends with $R<1$ mm and $\theta>90^\circ$ are affected more in terms of radiation loss and frequency bandwidth. However, for a bend with the radius of $R>1$ mm, the effect of bending angle is negligible.

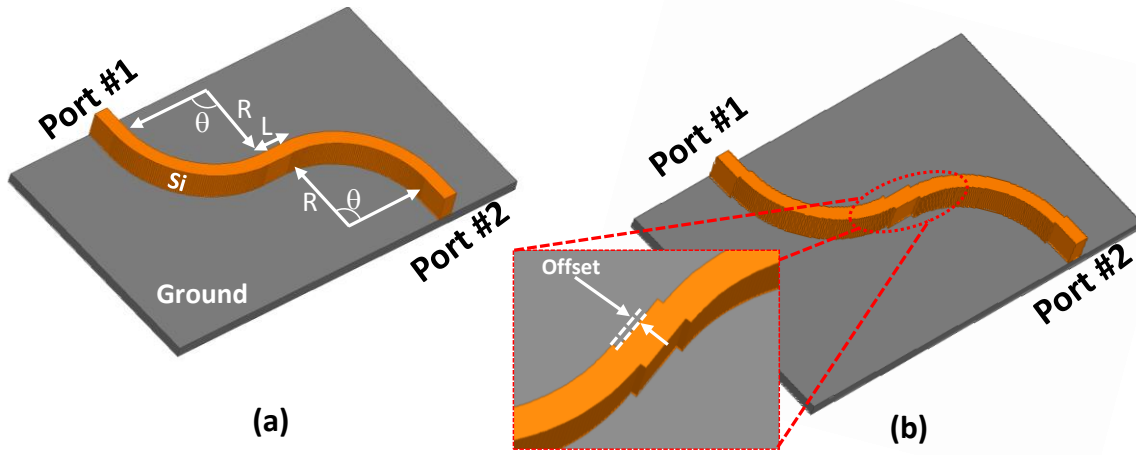


Fig. 3.1: The general schematic of two back-to-back bends: (a) without offset, and (b) with offset.

The simulations show that for two different bending radii, $R=1$ mm and $R=2$ mm, the bending loss at 150 GHz is around 0.11 dB/90°. Also, the curvatures with $\theta>90^\circ$ and $R<1$ mm suffer significantly from the radiation loss.

One way to reduce the radiation loss is to use an offset at the bends interface, as illustrated in Fig. 3.1(b) [55]. The propagation field tries to escape outward; however, the bend offset pushes the field inwards with respect to the bend. The insertion losses of a bend with $R=1$ mm and $\theta=90^\circ$, in three different offset cases, are shown in Fig. 3.3. The simulated results show that the optimum bending offset is 50 μm .

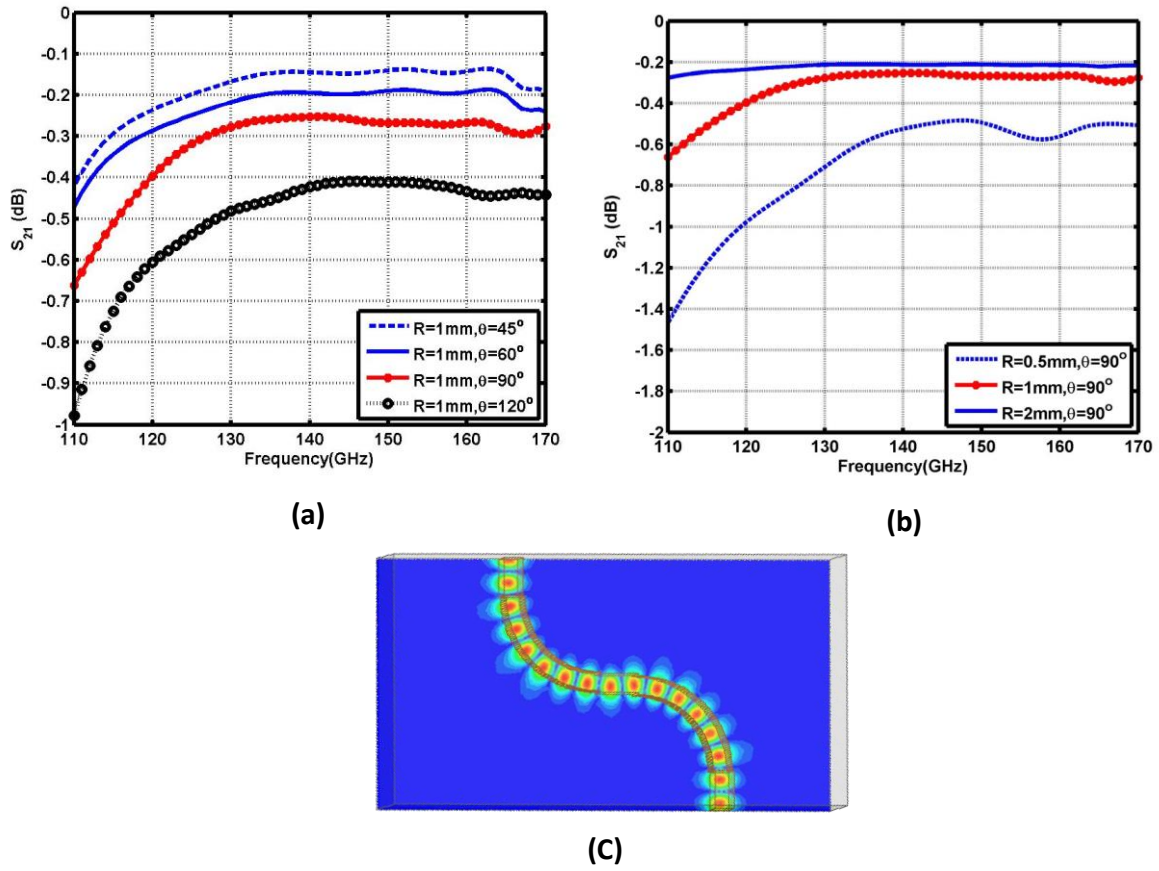


Fig. 3.2: The simulated insertion loss of the back-to-back bend for different (a) bending angles, and (b) different bending radii. (c) The electric field distribution of the bends with $R=2\text{ mm}$, $\theta=90^\circ$ at $f=150\text{ GHz}$ (top view).

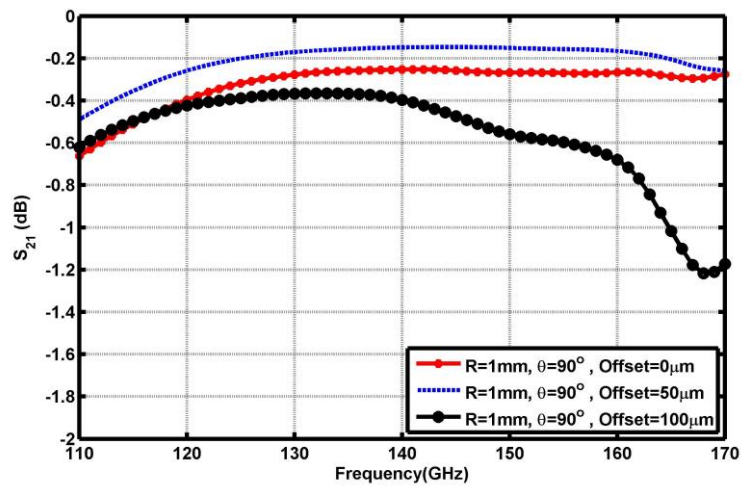


Fig. 3.3: The effect of bending offset on the simulated insertion loss.

3.1.1 Measurement Results

For proof of concept, a few SIG bends with different parameters are fabricated using the laser machining technique. The fabricated bends are shown in Fig. 3.4, and the corresponding measured results are shown in Fig. 3.5. All the fabricated bends consist of four identical bend sections, in order to have the input and output waveguides in the same level. Also, as discussed before, 9 mm tapered sections are used for providing the smooth transition between the metallic waveguide and SIG structures. The total lengths of the structures, shown in Fig. 3.4, with radii of $R=1$ mm and $R=2$ mm are $L=24$ mm and $L=34$ mm, respectively. Analyzing the results shows that a bend with the fixed radius of $R=1$ mm, has the loss of approximately 0.55 dB/ 90° at 150 GHz, while a bend with the fixed radius of $R=2$ mm, has the minimum loss of 0.25 dB/ 90° , which is quite a promising result for a bend.

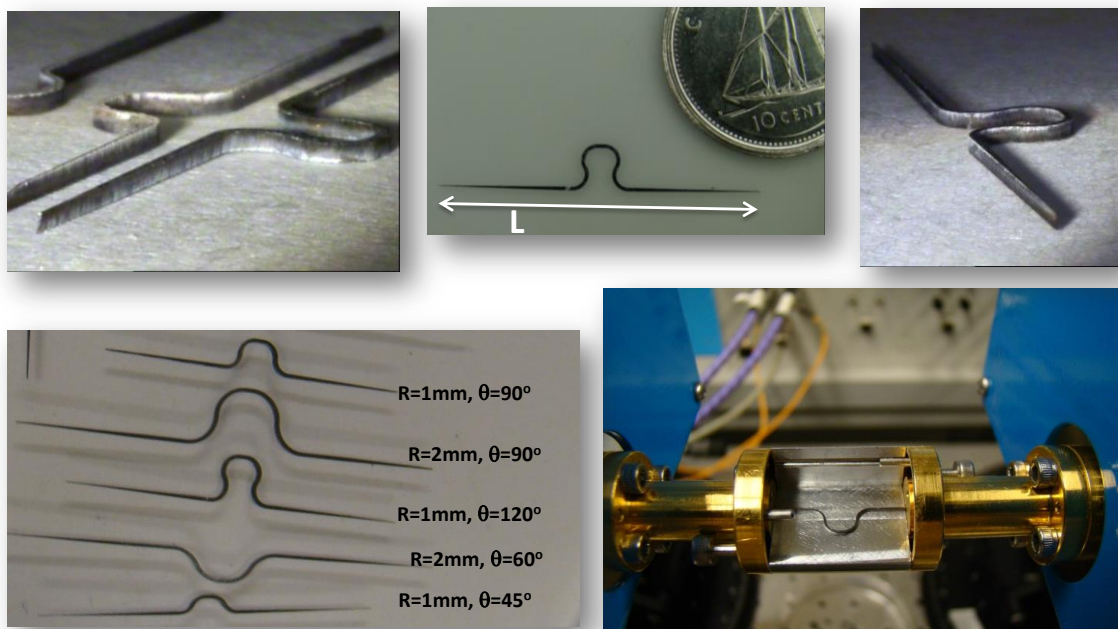
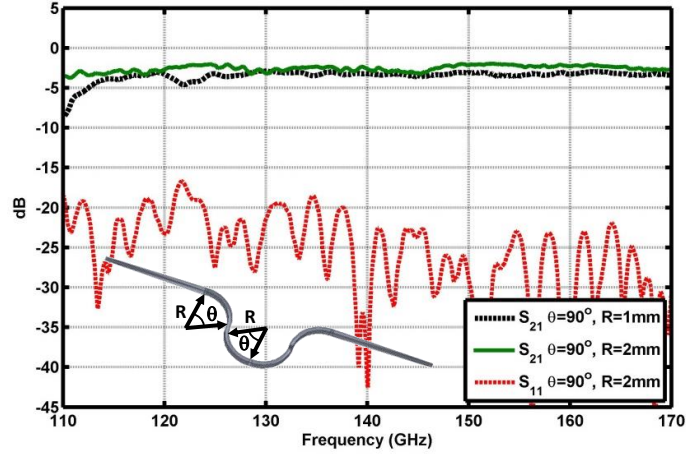
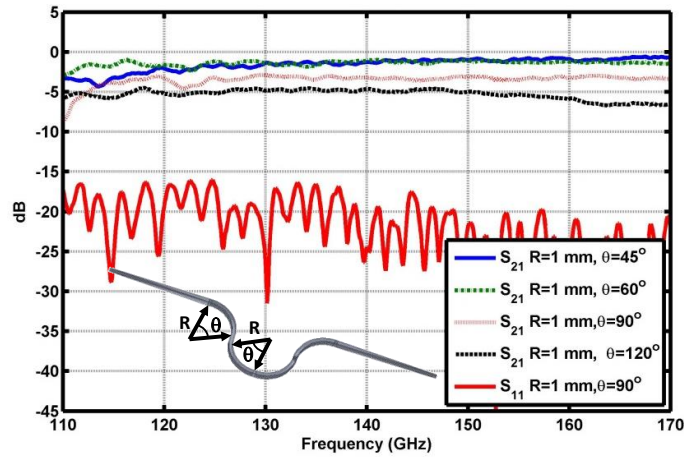


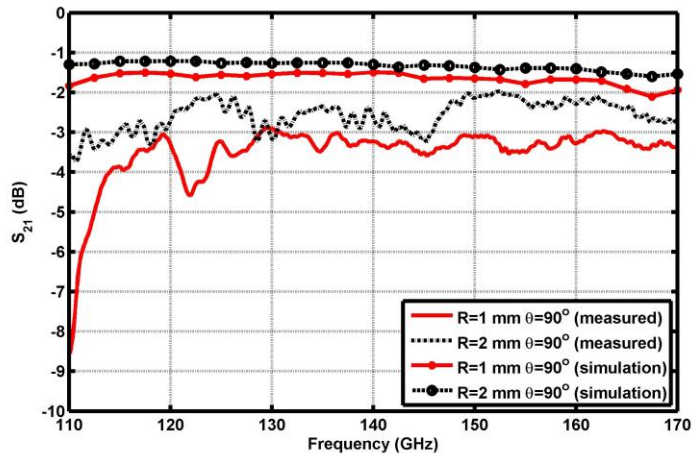
Fig. 3.4: The fabricated bends, using the developed laser machining technique.



(a)



(b)



(c)

Fig. 3.5: The measured S-parameters for the fabricated bends with (a) different radii, and (b) different bending angles. (c) The comparison between the simulated and measured S_{21} for $\theta=90^\circ$.

3.2 Y-Junction Power Divider

The power divider is another important passive building-block, which is required for realization of almost any mmWave integrated circuits. Although Y-junction power dividers are widely studied and implemented in the optical range [56], [57], the dielectric waveguide power dividers have not been extensively reported at the mmWave range of frequencies, except for lower mmWave range of frequencies [58].

A symmetric dielectric Y-junction power divider can be realized by various approaches. Fig. 3.6 shows the general configuration of a dielectric waveguide 3-dB Y-junction power divider. The input and output waveguides are designed for operating in single mode. The single mode dielectric waveguide is divided into two separate output dielectric waveguides through a transition waveguide section. The output waveguides make an angle of 2θ at the branching point. The total return loss of the system is mainly determined by this angle, while the wider angles result in higher radiation loss. However, due to the high contrast between the silicon and air, the achievable Y-junction angles are much larger than those in the traditional dividers in the optical range of frequencies, wherein the branching angle is often less than 10° [56]. Various techniques have been proposed in optics to decrease the return loss caused by a junction discontinuity. Most of them employ a matching section to compensate the phase-front mismatch. However, they require a more complex fabrication process. In the proposed power divider, the transition section and the bends are optimized to reduce the return loss, while the insertion loss is kept low. The inner sections of the bends, as shown in Fig. 3.6, have bending angles of θ and the radii of R_1 and R_2 . The divider is designed and optimized to operate within the D-band (110-170 GHz) range of frequencies. The design parameters are listed in Table 3.1.

Table 3.1: The design parameter values of the Y-junction 3-dB power divider.

Parameter	Value	Parameter	Value
L_1	10 mm	R_1	1 mm
W_1	250 μm	R_2	2 mm
W_2	510 μm	θ	30°

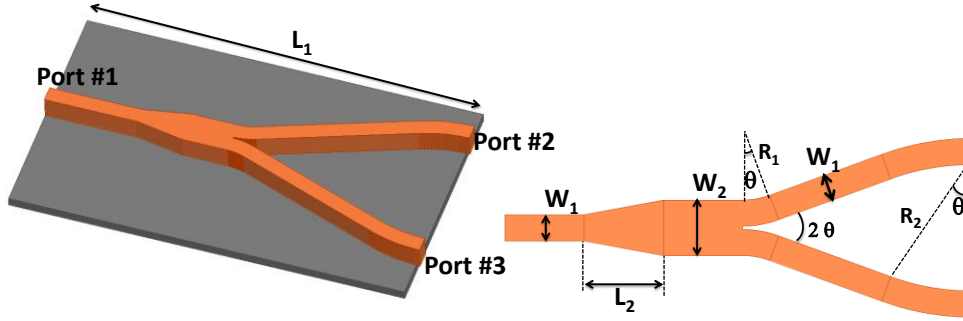


Fig. 3.6: The general schematic of 3-dB Y-junction power divider.

Fig. 3.7 shows the simulated S-parameters of the 3-dB in-phase Y-junction power divider obtained from HFSS full-wave simulation. The results are achieved for three different branching angles, while the R_1 is 2 mm. The total loss observed in each output port is less than 0.3 dB for $\theta=30^\circ$ and $\theta=60^\circ$ over 120-170 GHz band.

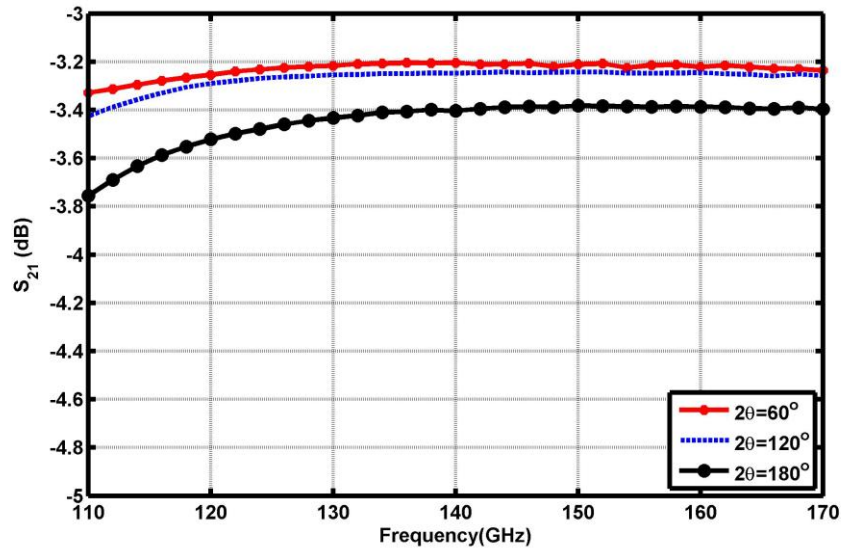
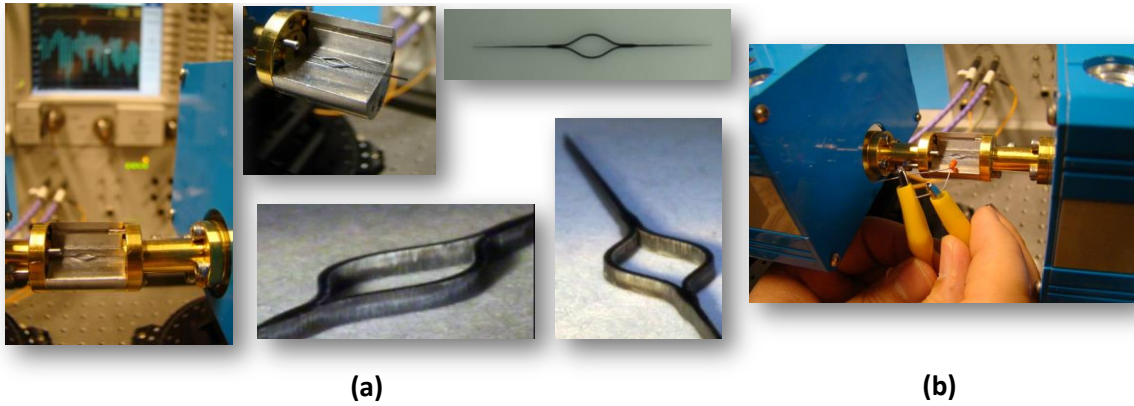


Fig. 3.7: The simulated insertion loss of the 3-dB in-phase Y-junction power divider for different branching angles.

3.2.1 Measurement Results

Due to measurement setup challenges for testing a 3-port power divider, two identical dividers are connected back-to-back, to form a symmetric two port structure. The back-to-back power divider sample is fabricated using the developed laser machining technique. The fabricated structure has a total length of 34 mm, including the tapered sections. The bends have $R_1 = R_2 = 2$ mm and $\theta = 30^\circ$. Fig. 3.8 shows the fabricated divider from different views

along with the measurement setup. To verify the dividing performance of the divider, a Near Infra-Red (NIR) Light Emitting Diode (LED), operating at 960 nm, is used. In fact, the illumination of HRS structure increases the conductivity of the silicon and causes substantial loss in the propagating signal. First, the total insertion loss of the system is measured, and the average insertion loss is 1 dB (refer to Fig. 3.9). Then, the main guiding channel labelled as the “main line” in Fig. 3.9(b), is illuminated by a very low power NIR signal ($<5 \mu\text{W}$). The results show that S_{21} drops approximately 9 to 11 dB. In the next step, each Y-junction branch is illuminated one at a time and the changes in the S_{21} are recorded. The measured data, which are plotted in Fig. 3.9, show that the S_{21} drops by 3.5 dB, on average.



**Fig. 3.8: (a) The measurement setup and fabricated back-to-back divider ($R=2 \text{ mm}$, $2\theta=60^\circ$).
(b) NIR illumination experiment.**

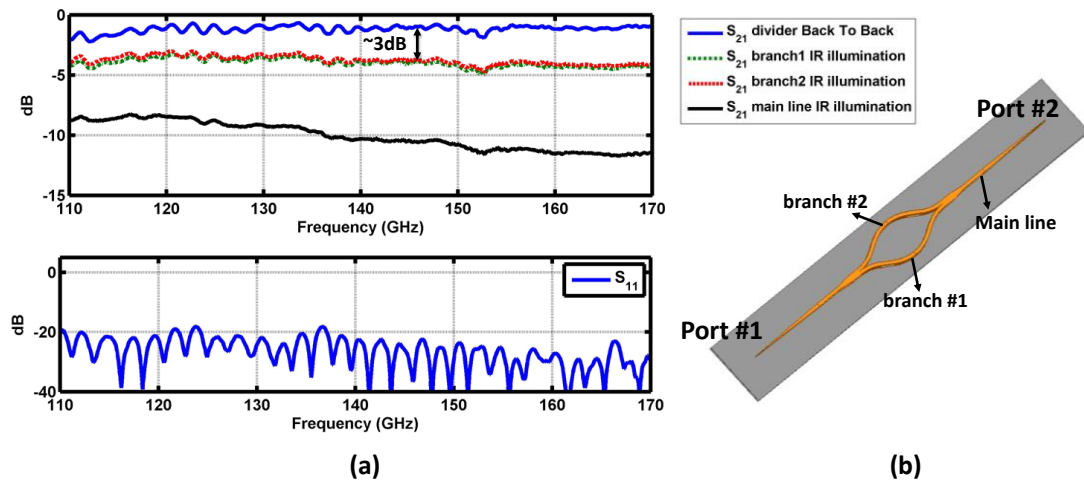


Fig. 3.9: The measured results of S-parameters for the back-to-back divider by means of NIR illumination ($R=2 \text{ mm}$, $2\theta=60^\circ$, and the total length=34 mm).

3.3 Directional Coupler

Directional couplers are used in several applications, such as signal combining, power splitting, mixing, and switching. In microwave frequency ranges, where we can still use the planar circuits, plenty of coupler ideas such as the branch coupler, rat-race coupler, and directional coupler have already been introduced [59]. The metallic waveguide-based couplers, such as the Beth-hole coupler, are another group of couplers in the microwave range [59]. On the other hand, dielectric waveguide couplers have been studied and implemented extensively at optical wavelengths [60], where the couplers play important roles in formation of almost any optical systems from communication to imaging applications. Implementing the dielectric waveguide-based couplers in the mmWave/THz range of frequencies, where realization of planar circuits and metallic waveguides are challenging, is a significant step towards development of high performance integrated systems [61]. The coupled field is triggered and transformed in the secondary waveguide, which is placed in close vicinity of the primary waveguide, by the tail (decaying part) of the field in the first channel. The coupler structure, which consists of two coupled dielectric waveguides, can be studied using the even and odd mode theory. Fig. 3.10 shows the geometry of a directional dielectric waveguide coupler, while the G and L are the gap and the length of the coupling section, respectively. For a reasonably chosen G , the L determines the coupling power ratio as well as the operational frequency.

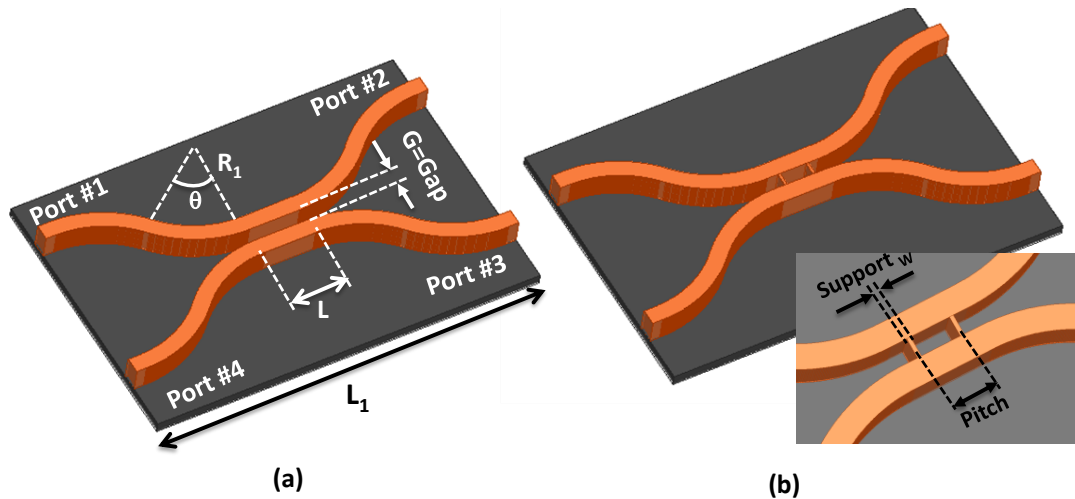


Fig. 3.10: The general configuration of (a) an SIG directional coupler, and (b) a supported SIG coupler.

To find the initial value of L , the EDC method is used in order to calculate the even and odd propagation constants of the structure. Then the coupling power ratio, direct power ratio, and the coupling length (L_{eff}), over which the signal is completely coupled to the adjacent waveguide, are calculated using the following formulas [60], [61]:

$$L_{eff} = \frac{\pi}{\beta_e - \beta_o} \quad (3-1)$$

$$\frac{P_2}{P_1} = \left(\cos \left(\frac{\pi}{\beta_e - \beta_o} L \right) \right)^2 \quad (3-2)$$

$$\frac{P_3}{P_1} = \left(\sin \left(\frac{\pi}{\beta_e - \beta_o} L \right) \right)^2 \quad (3-3)$$

where β_e and β_o are the even and odd propagation constants of the coupler. The input and output waveguides are separated by the optimized bends. To facilitate the measurements, the bends are added at both sides of the coupled section. Separating the waveguides by smooth bends helps to increase the frequency bandwidth. As discussed in Section 3.1, the bends should be carefully designed in order to have negligible radiation loss. Additionally, the coupler bends contribute to the coupling ratio. Therefore, the actual effective coupling length is larger than L due to the bending parts, which are part of the coupling mechanism. The coupler waveguides have the same cross sections as those of SIGs in the previous designs. The calculated even and odd propagation constants for the $G=180 \mu\text{m}$ at 150 GHz are $\beta_e=8112 \text{ rad/m}$, $\beta_o=7339 \text{ rad/m}$. The coupling length is calculated as $L_{eff}=4.06 \text{ mm}$, using (3-1). All the bends have radius and angle of $R=2 \text{ mm}$, $\theta=90^\circ$, respectively. The coupler can be designed for providing any desired coupling ratio. Fig. 3.11 shows the effect of G and L on the coupled (P_3/P_1) and directed (P_2/P_1) power ratios at different frequencies. In order to have a 3-dB coupler, the optimized coupler parameters are obtained as $G=180 \mu\text{m}$ and $L=1 \text{ mm}$. The simulated data shows that, an increase in the gap (G) or decrease in the coupling length (L) results in the reduction of the frequency, at which the structure acts as a 3-dB coupler (refer to Fig. 3.12(a) and Fig. 3.12(b)). The phase differences between the coupling port (port #3) and the direct port (port #2) are within the 90-93 degree over 140-155 GHz (refer to Fig. 3.12(c)). The 1-dB bandwidth of the 3-dB coupler, over which the maximum imbalance between the signals at the output ports reaches 1 dB is approximately 6 GHz.

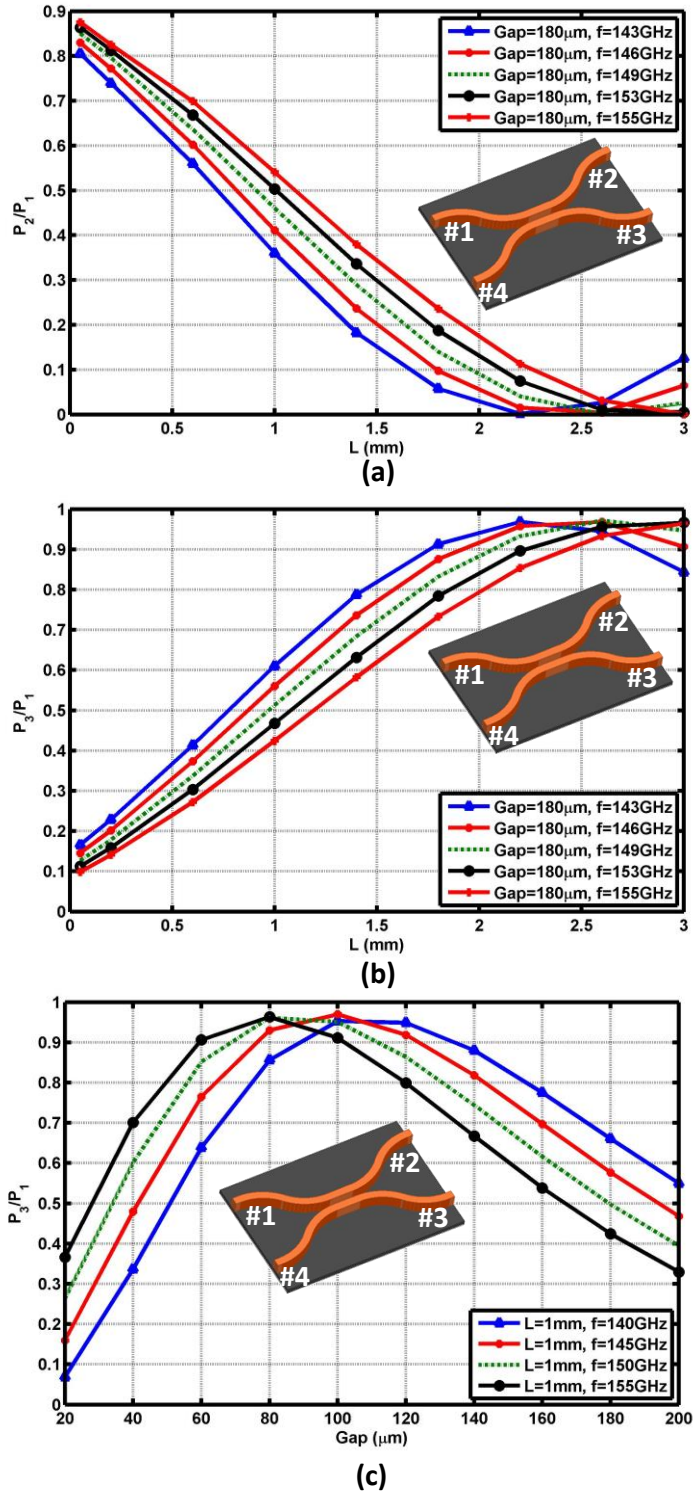


Fig. 3.11: The simulated outputs power ratios at different frequencies: (a) directed power ratio for $G=180\ \mu\text{m}$ and varying L , (b) coupled power ratio for $G=180\ \mu\text{m}$ and varying L , and (c) coupled power ratio for $L=1$ mm and varying G .

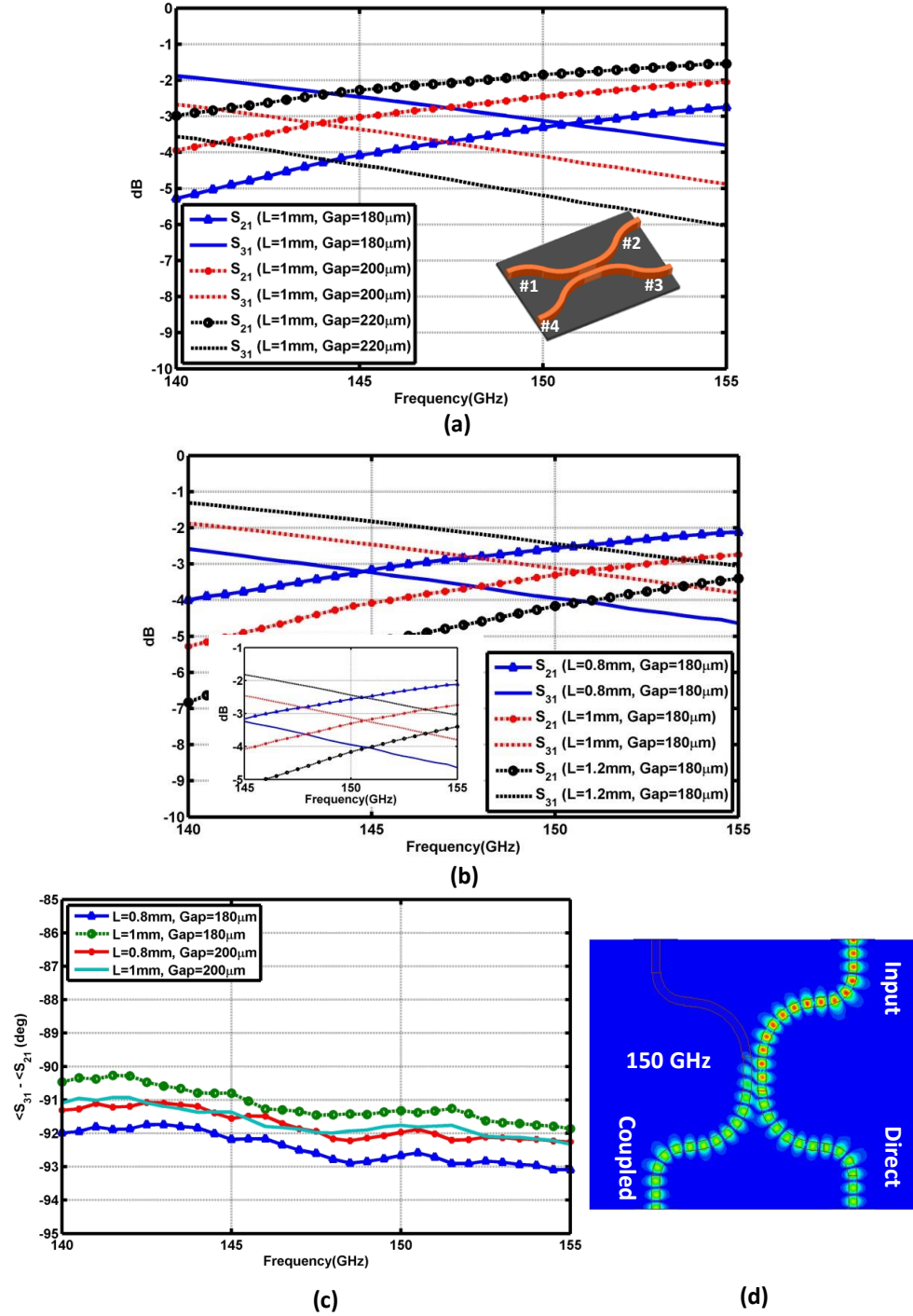


Fig. 3.12: (a) The effect of G on the transmission responses for the fixed L , (b) The effect of L on the transmission responses for the fixed G , and (c) the output phase differences for different values of L and G . (d) The electric field distribution for the SIG coupler at 150 GHz ($G=180 \mu\text{m}$, $L=1 \text{ mm}$).

3.3.1 Supported SIG Coupler

As it is obvious from the simulation results, the gap (G) plays a significant role in determining the coupling ratio. However, the guiding channels of the coupler are detached from each other. Therefore, a precise manual positioning of the waveguide channels is required, which is practically impossible. To avoid this issue, the idea of supported beams is introduced and shown in Fig. 3.10(b). For reaching a monolithic coupler, two narrow beams connect the waveguides at the coupling region. The supporting beams are separated from each other with $500\ \mu\text{m}$ pitch and they have identical $30\ \mu\text{m}$ width.

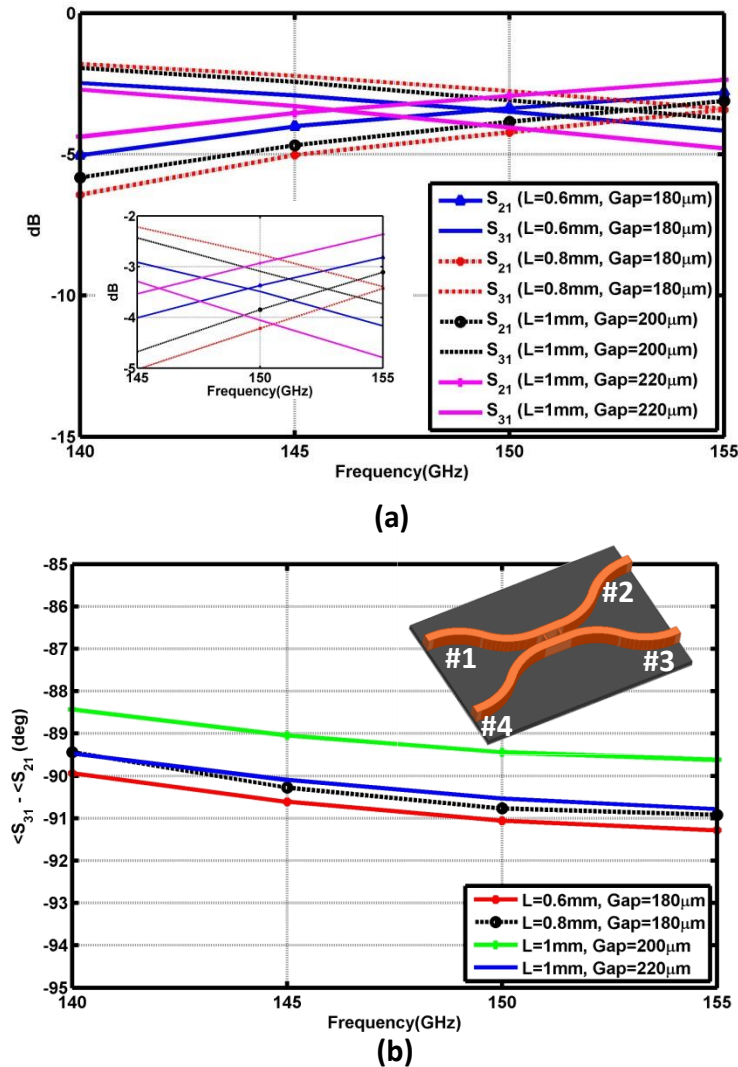


Fig. 3.13: (a) The effects of G and L on the transmission responses of the supported coupler, (b) the output phase differences for different sets of L and G for the supported coupler.

The supporting beams mainly affect the coupling ratio. The simulated results for different gaps and coupling lengths are shown in Fig. 3.13. It is found that for having a 3-dB coupler operating over the same frequency range as the one for the original coupler, the coupling gap and length should be set to $G=180\ \mu\text{m}$ and $L=0.6\ \text{mm}$, respectively.

As previously discussed, the idea of offset positioning at the bend interfaces can be used to reduce the radiation loss at the bends. The simulated results for the supported coupler with offset= $50\ \mu\text{m}$ are shown in Fig. 3.14. The variations of the output ports phases over the entire range are smaller as compared to the previous case with no supports.

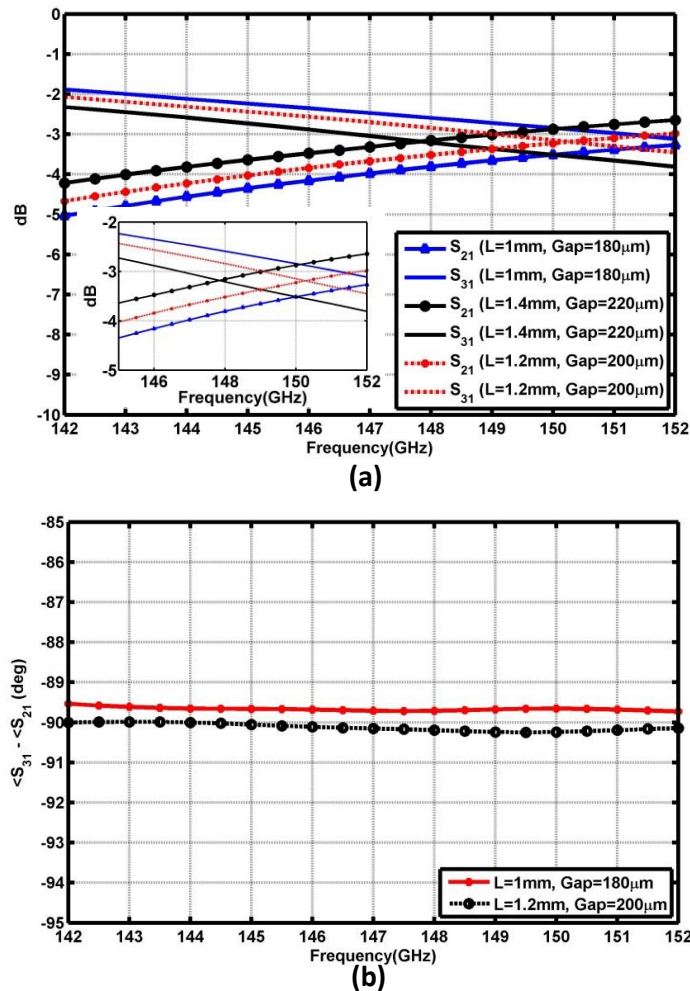


Fig. 3.14: (a) The effects of G and L on the transmission responses of the offset supported coupler, and (b) the output phase differences for different values of L and G for the offset supported coupler.

3.3.2 Multi-Mode Interference (MMI) Coupler

The MMI concept can also be used to realize a coupler. MMI structure is a known component at optics for dividing, coupling, and switching purposes [60]. The general configuration of the proposed MMI-based coupler is shown in Fig. 3.16(a). The middle section acts as a multimode medium, where the entering single mode field is converted to several modes. A 3-dB coupler can be achieved by placing the output ports at the position of two-fold images, at the distance of [60], [62], [63]:

$$L_{3dB} \sim 1.5 \frac{n_{eff} W_2}{\lambda_o} \quad (3-4)$$

The calculated n_{eff} , for $W_2=950 \mu\text{m}$, is 2.34. Therefore the theoretical obtained L_{3dB} is $730 \mu\text{m}$, and its optimized value is $700 \mu\text{m}$ for the operational frequency of 157 GHz. The simulated results for the optimized MMI-based 3-dB hybrid coupler, while the separating distance between the ports is $S=450 \mu\text{m}$, and the bends have $R=2 \text{ mm}$, $\theta=90^\circ$, is plotted in Fig. 3.16(b). One challenge in implementation of the MMI-based couplers is the sensitivity of the output phases to the design parameters (refer to Fig. 3.16(c)). Also, the smallest fabrication tolerance in positioning the ports with respect to each other results in noticeable errors in the coupling ratio.

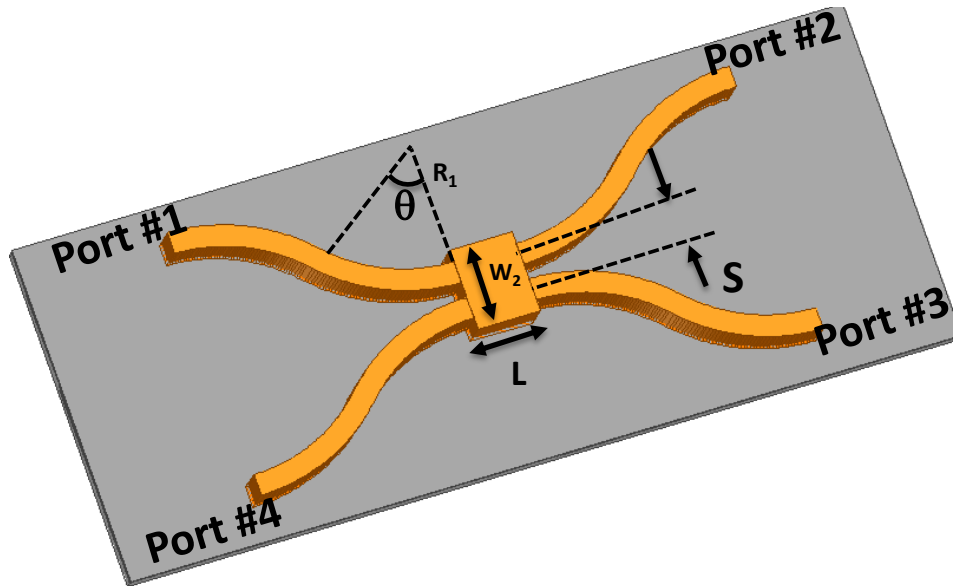
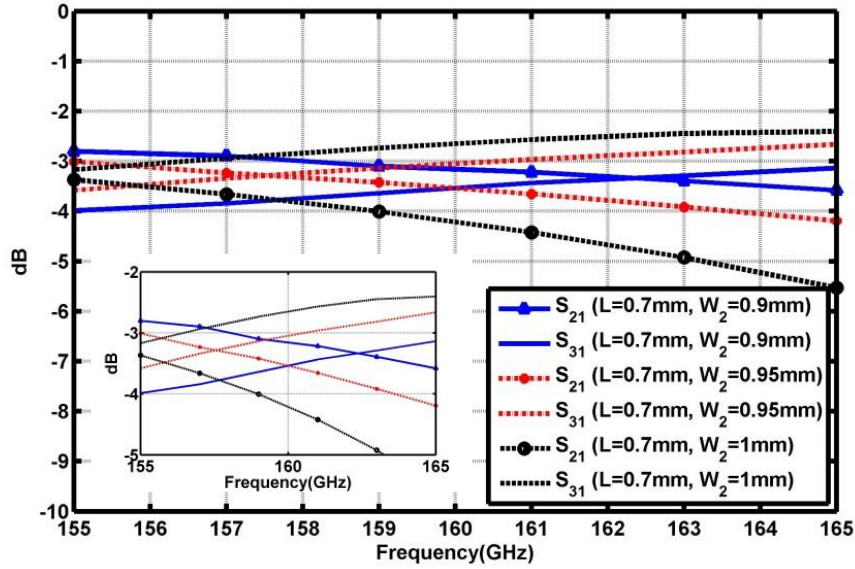
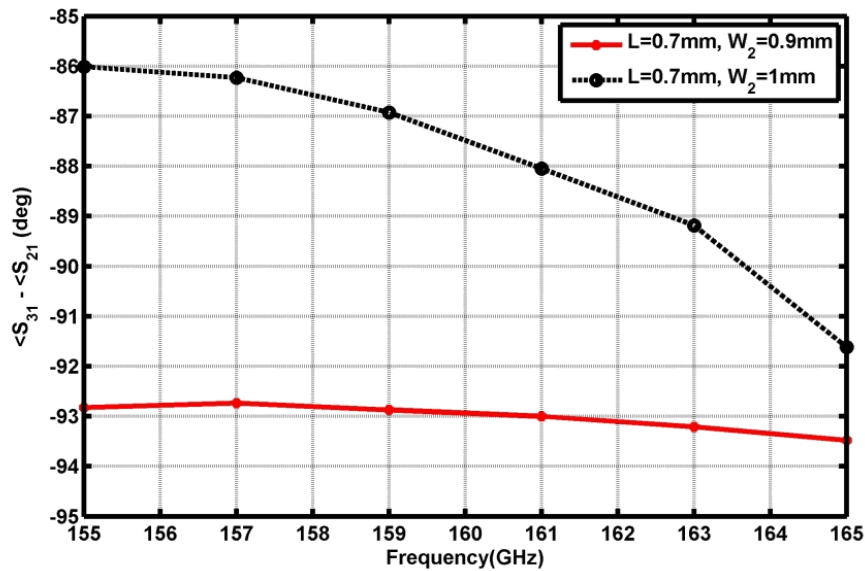


Fig. 3.15: The general configuration of the MMI-based coupler.



(a)



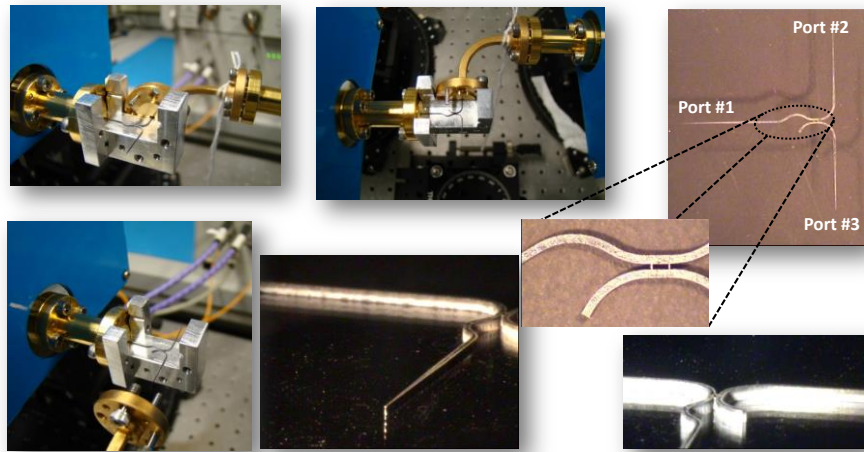
(b)

Fig. 3.16: (a) The effects of W_2 and L on the transmission responses ($S=0.45$ mm) of the MMI coupler, and (b) the output phase differences investigation.

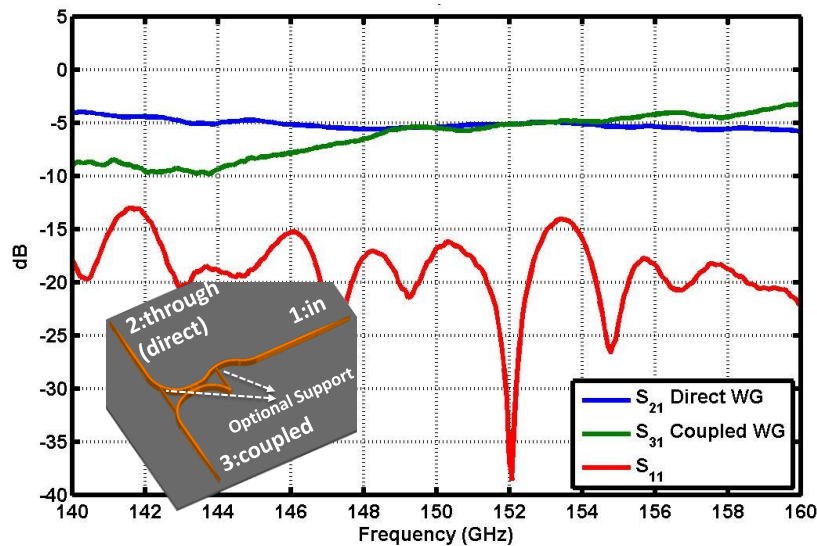
3.3.3 Measurement Results

For experimental validation of the proposed coupler structures, the supported coupler, shown in Fig. 3.10(b) with $L=0.8$ mm and $Gap=180$ μm , is chosen to be fabricated. The laser machined coupler is shown in Fig. 3.17(a). The two additional supported labeled as “optional supports”, as shown in the inset picture (refer to Fig. 3.17(b)), can be used for enhancing the

stability of the structure at the cost of higher loss and higher phase errors. The output ports are separated by a 180 degree angle from each other. A 90° right-angle metallic waveguide is used to connect the measurement setup extender modules to the metallic fixture. The corresponding insertion loss of the metallic waveguide bend was measured at 0.5 dB. The measured results of the coupled and through transmission coefficients, which are separately measured, are shown in Fig. 3.17(b). The total loss of the coupler structure with the $f_c=152$ GHz is approximately 1.7 dB, including the radiation losses, the tapered section losses, and the fixture losses.



(a)



(b)

Fig. 3.17: (a) The laser machined supported 3-dB coupler and the measurement setup, and (b) the measured S-parameters of the fabricated 3-dB coupler.

3.4 Parasitic Tapered Antenna

The antenna is a critical element for realization of any RF-end system. Dielectric waveguide-based antennas are of interest to many designers in the mmWave range of frequencies. SIG technology provides a low-cost platform for realizing high performance beam-steering systems at the mmWave range of frequencies. Low-cost, highly-efficient, and integratable antenna systems are key enabling technologies for the mass market emerging mmWave/sub-mmWave communication systems. The advantage of using image guide antennas is that the ground plate blocks the down-going signals and redirects all the energy to the upper space.

Tapered antennas are the simplest type of dielectric antenna from the design perspective, in addition to their natural wide radiation and matching bandwidth. The tapered antennas are categorized as travelling-wave radiators, where any discontinuity causes radiation of the trapped field inside the waveguide. In fact, the radiation in the tapered section happens due to changes in the propagation constant of the field, which decreases to $\beta_z = k_0$ at the tapered section. Different configurations of tapered antennas, such as rod antennas [64], [65], NRD antennas [66], [67], and image guide antennas [68], [69], were implemented at the microwave and mmWave range of frequencies. The length of the tapered section defines the gain and side-lobe levels. So, the main drawback of these antennas is their lengthy size. To overcome this issue the tapered section should be shortened at the cost of higher side-lobe levels. To keep the side-lobe levels low as well as increasing the gain, the parasitic elements can be employed. The geometry of the proposed antenna is shown in Fig. 3.18 [70]. The SIG antenna consists of a tapered antenna coupled to two parasitic tapered sections. The parasitic elements are connected to the main part of the antenna through narrow supportive beams with 30 μm width. The supportive beams are important from the mechanical stability point of view. Also, the supportive beams precisely locate the parasitic elements at the desired distance (g). The antenna is placed on a finite metallic plane. The antenna input port is tapered in order to provide a smooth transition from the rectangular metallic waveguide (WR-10) to the antenna for operating at 75-110 GHz. The optimal design values, for which the gain and the side-lobe levels are maximized, are listed in Table 3.2.

Table 3.2: Optimal design values of the parasitic tapered antenna.

Parameter	a	b	L_1	L_2	L_3	W_1	W_2	W_3	g
(mm)	16	6	13	3	3	0.33	0.1	0.030	0.13

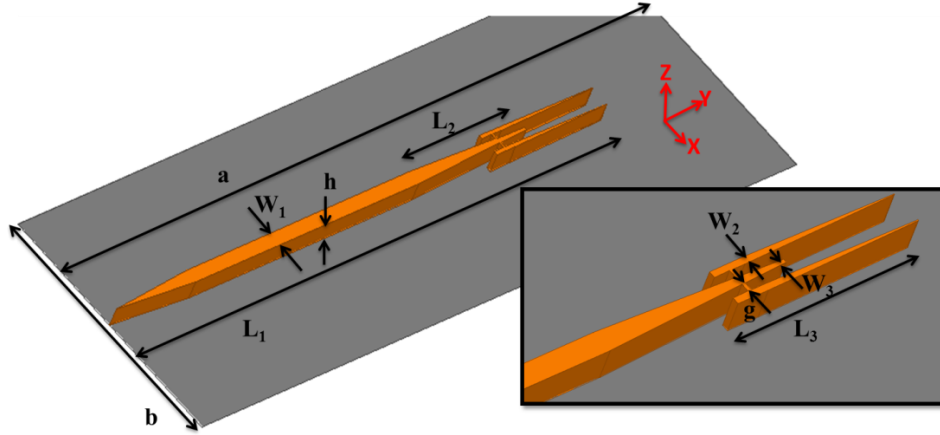


Fig. 3.18: 3-D configuration of the proposed parasitic tapered antenna [70].

The width of the dielectric waveguide is calculated in such a way to operate as a single mode within the desired operational frequency. The total length of the antenna is approximately 3.7 wavelengths (the radiating part has approximately 5 mm length).

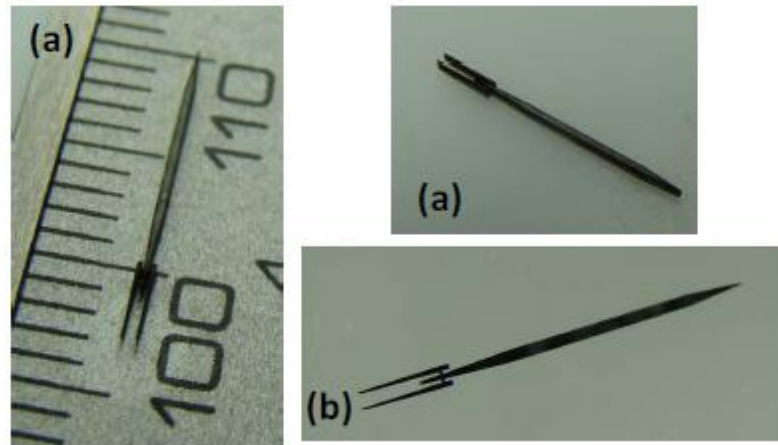
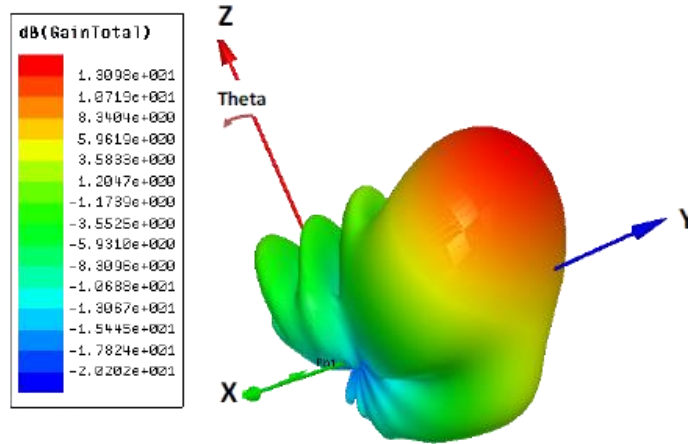
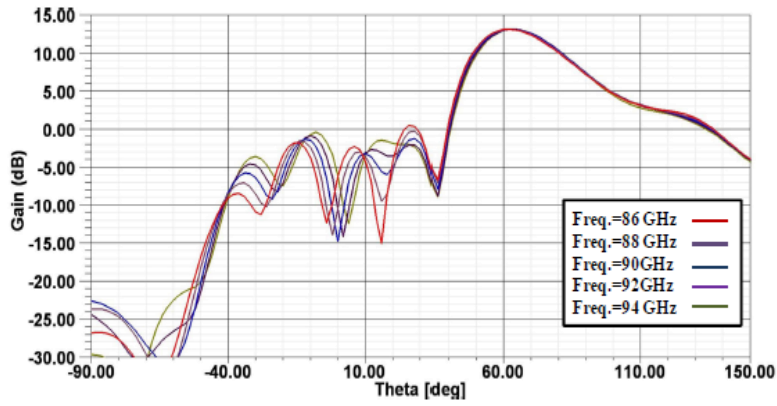


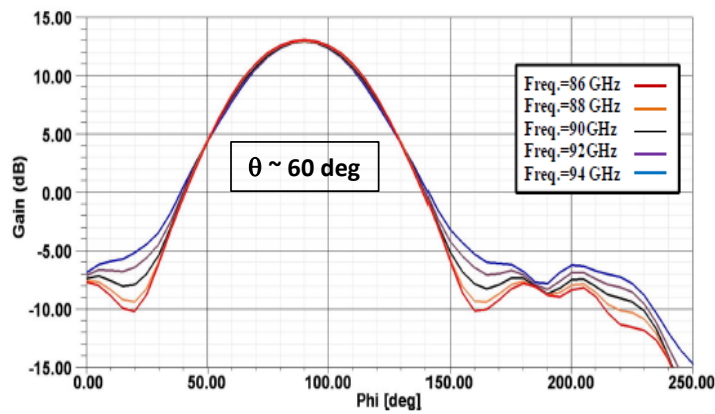
Fig. 3.19: The laser machined parasitic tapered antenna: a) 3D views. b) Top view [70].



(a)



(b)



(c)

Fig. 3.20: (a) Simulated 3-D pattern of the parasitic tapered antenna at 90 GHz, (b) the simulated gain pattern for the $\phi=90^\circ$ cut, and (c) the simulated gain pattern for the $\theta=60^\circ$ cut [70].

The 3-D gain pattern of the antenna at 90 GHz is shown in Fig. 3.20(a). The maximum gain is approximately 13.1 dBi and the beam is 60° tilted with respect to the z -axis. Also, the total gain of the antenna for different frequencies at the yz -plane is shown in Fig. 3.20(b). Within the range of 86 GHz to 94 GHz the antenna gain pattern is almost constant and all the side-lobe levels are better than 13 dB. Fig. 3.20(c) shows the total gain of the antenna in $\theta=60^\circ$ plane. The parasitic elements increase the gain to approximately 1.7 dB while enhancing the side-lobe levels by at least 4 dB as compared to the antenna without the parasitic elements.

3.5 Leaky-wave Antenna

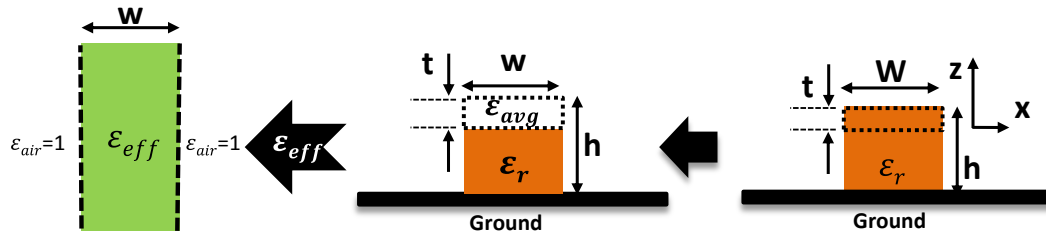
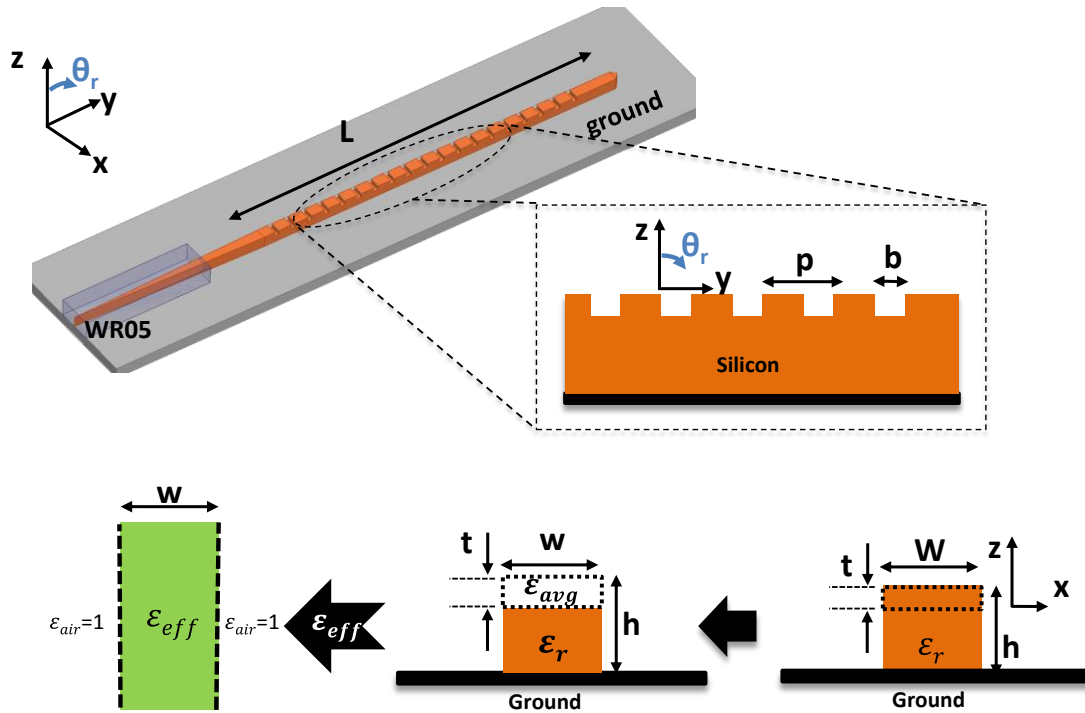
Leaky-wave antennas are among the most cost-effective techniques for implementing beam-steering systems at the mmWave range of frequency. Leaky-wave antennas are suitable for the systems required to radiate at the sector of sideward direction or at the broad-side direction. Additionally, leaky-wave antennas provide unique advantages such as low profile, ease to fabricate, narrow beam, frequency scanning, and high efficiency for any mmWave system [71]. A wide variety of leaky-wave antennas have been investigated and developed for microwave/mmWave applications [71]. Planar printed leaky-wave antennas are among the popular techniques for the microwave range of frequencies [72], [73]. As mentioned earlier, conductor loss and difficulty of fabrication are the major drawbacks of such configurations in the mmWave range of frequencies. Dielectric waveguide-based leaky-wave antennas are good candidates for mmWave applications [74], [75], [76], [77]. Leaky-wave antennas are divided into three groups: linear, quasi-linear, and periodic leaky-wave antennas. The linear and quasi-linear antennas are traditionally realized by a slit on the surface of a metallic waveguide, in which fast wave mode is propagating [71]. On the other hand, periodic leaky-wave antennas are realized using the periodic mechanism for perturbing a propagating field inside a dielectric structure, which carries slow-wave mode. The periodic perturbation transforms the slow-wave modes to the radiating spatial fast-wave modes. In fact, the propagating wave at any discontinuity starts to partially radiate and the wave decays exponentially along the structure. The most common type of the periodic leaky-wave antennas are the metallic strip and groove grating antennas. In the following sections two types of SIG grating antennas, strip grating and grooved grating antennas are

discussed and the design steps, for operating over D-band (110-170 GHz) range of frequencies, are explained.

3.5.1 Groove Grating Antenna

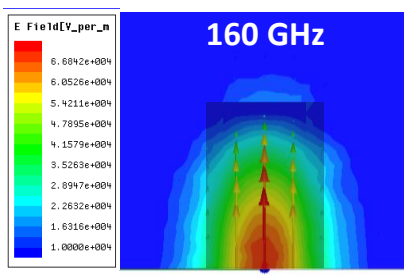
The proposed grating antenna, [78], acts as a fast wave structure excited by a surface-wave/slow-wave of the SIG straight waveguide segment. The first design step is to determine the width of the antenna in Fig. 3.21(a). The SIG width, W , defines the modal behavior of the structure. It also affects the beam-width and side-lobe levels. The optimal value of the waveguide width and input tapering length, obtained from computational simulations, are 450 μm and 9 mm, respectively. The wider width of the waveguide in comparison to the previously implemented SIG passive structures is due to the highly confined field requirements of the antenna. In fact, a narrower width of waveguide results in higher side-lobe levels and lower gain. Exciting the antenna by a metallic waveguide guarantees the single mode operation of the antenna.

The next step is to find the grating parameters. The grating period, p , has an important role in determination of the radiation beam angle, which can be calculated as $\sin(\theta) = \frac{\beta_n}{k_0} = \left(\frac{\beta_y}{k_0} + \frac{n\lambda_0}{p}\right)$, obtained from the theory of the Floquet mode [71]. k_0 and λ_0 are free space wavenumber and wavelength, respectively. Also, n is the space harmonic order which is desired to set $n=-1$. The other important parameter is β_n , Floquet mode phase constant of the fast wave structure. β_y is the phase constant of the equivalent unperturbed waveguide. Furthermore, in a grating leaky-wave antenna, groove depth, t , defines the amount of radiation leakage, which should ensure that the largest portion of the input power to the grating antenna is radiated before reaching the end of the structure. For initial design, the EDC method, as schematically illustrated in Fig. 3.21(a), is used to determine the grating parameters [74].



$$\beta_y = \sqrt{(k_0^2 \epsilon_{eff} - \beta_x^2)}$$

(a)



(b)

Parameter	L	W	h	t	p	b
(mm)	17	0.45	0.5	0.22	0.78	0.18

(c)

Fig. 3.21: (a) The general configuration of the antenna with explanation of the applied EDC technique, (b) the electric field distribution at 160 GHz at the cross section of the antenna before the grooves, and (c) the design parameters.

Once the initial design is completed, all SIG and grating parameters are finely adjusted and optimized using full-wave simulations in order to provide maximum gain while keeping the side-lobe levels low. For the particular design example reported here, the optimized groove depth is obtained as $t=220 \mu\text{m}$ and $\beta_y/k_0 = 2.92$. In the EDC method (refer to Fig. 3.21(a)), ϵ_{avg} is the volume average permittivity of the grooves which is $\epsilon_{avg} = 9.38$, for the aspect ratio of $b/p=0.23$. The optimal value $p=0.78$ comes from the fact that the radiation angle is

desired to be approximately $\theta_r = 30^\circ$ at centre frequency. Another important effect of p is on the number of spatial modes. The chosen P guarantees to have only $n=-1$ spatial fast-wave mode. The total length of antenna is calculated using the $L = -\frac{1}{2\alpha} \ln(1 - \eta)$ term, in which α is the attenuation constant of the antenna, and η is the efficiency of the antenna which is set at >0.95 . The total number of grooves is set to 20 for providing acceptable gain and beam-width.

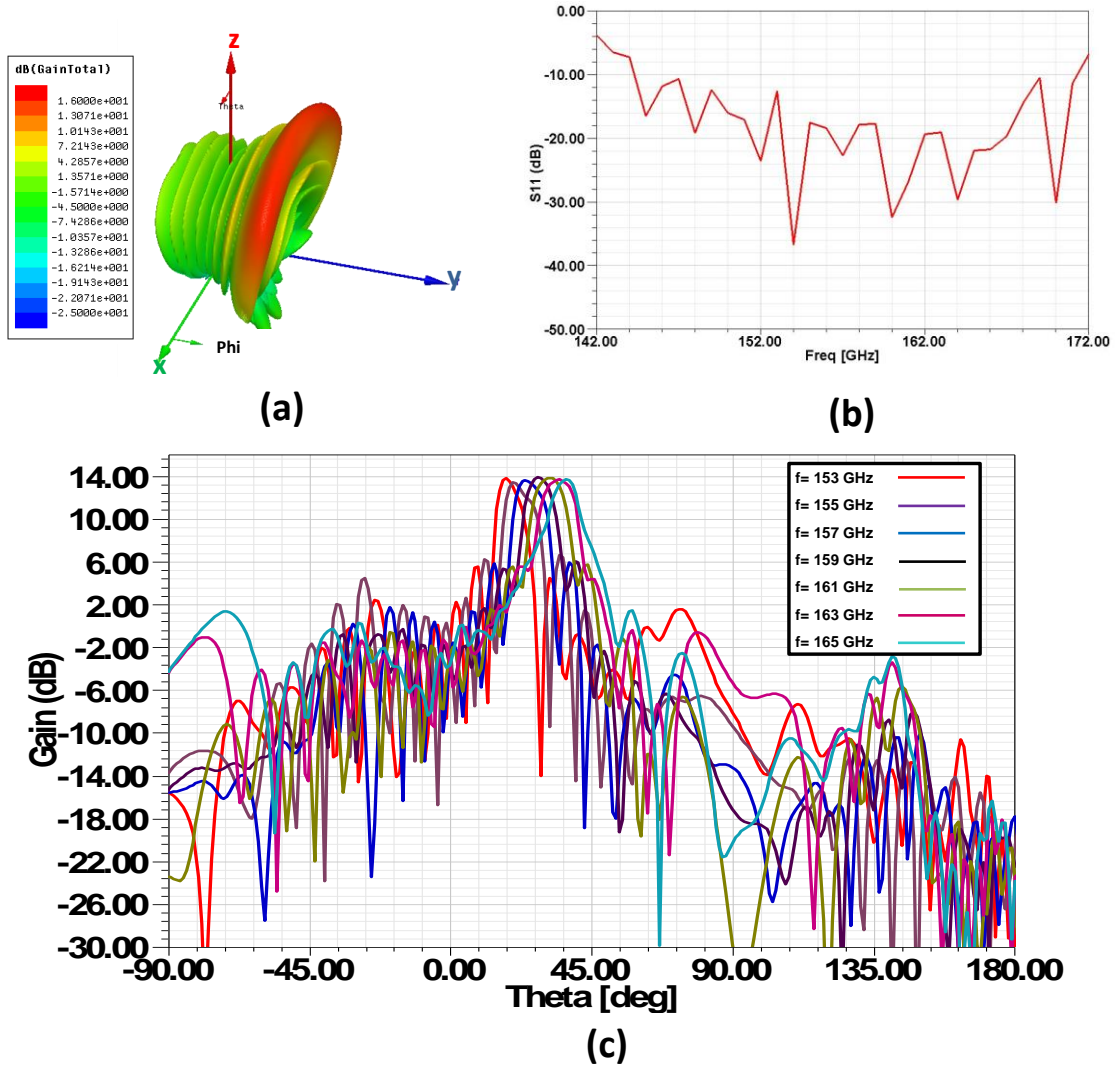


Fig. 3.22: (a) Simulated 3-D gain pattern of the designed grating antenna at 155 GHz, (b) the simulated S_{11} of the antenna, and (c) the simulated gain patterns for the $\phi=90^\circ$ cut [78].

A simulated 3-D pattern of the designed antenna at $f=155$ GHz is shown in Fig. 3.22(a). The simulated reflection response of the antenna over the G-band range of frequencies is

depicted in Fig. 3.22(b). To obtain more insight about the antenna behavior and gain, Fig. 3.22(c) shows the simulated gain plots of the designed antenna at $\phi=0^\circ$ for various scan angles. Almost a flat gain, with less than 0.5 dB fluctuation over the entire angular scanning range is achieved. The simulated radiation efficiency of the antenna is better than 92%, which demonstrates the significant advantage of using silicon as the main substrate.

The designed antenna is fabricated using a developed laser machining technique. The capability of the laser technique for making a pocket inside the dielectric structure is an important feature, which discriminates this technique from the DRIE fabrication method. Comprehensive experiments are conducted to find the optimized values of the laser process for making desired groove depths with the minimum surface roughness. The fabrication tests prove that the roughness of a groove with 200 μm depth is $\pm 5 \mu\text{m}$. Moreover, the simulations show that $\pm 5 \mu\text{m}$ roughness inside the grooves causes less than 0.5 dB changes in the maximum gains of the antenna. The fabricated grating antenna sample is shown in Fig. 3.23.

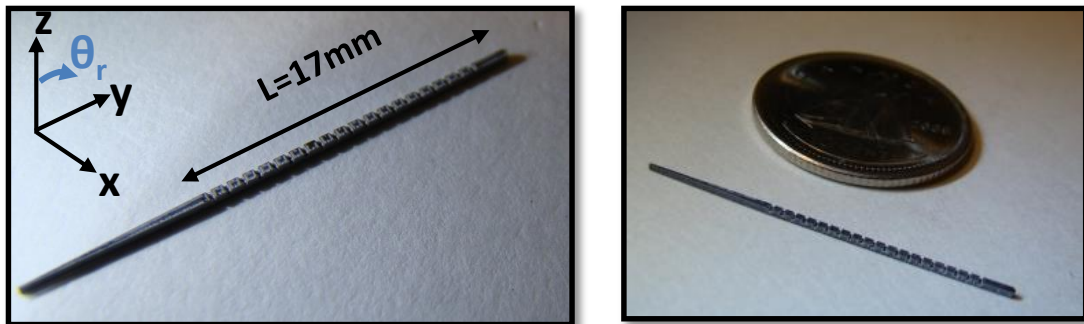


Fig. 3.23: The laser machined groove grating antenna sample [78].

3.5.2 Strip Grating Antenna

The theory of the strip grating dielectric waveguide antenna is similar to the one for the groove grating antenna. Regarding the grating parameters, the width and the periodicity of the strips should be determined in such a way to provide the desired antenna radiation characteristics. The proposed strip grating SIG antenna, [79], is shown in Fig. 3.24(a), where the period of strips determine the radiation angle, and the ratio of b/p introduces the amount of power leakage. The optimized design values for the antenna for operating over 145-160 GHz are listed in the table in Fig. 3.24(c). The simulated 3-D gain pattern of the

antenna at 155 GHz is plotted in Fig. 3.24(b). The radiation pattern of the strip grating antenna is closer to the broad-side angle in comparison to the groove grating antenna.

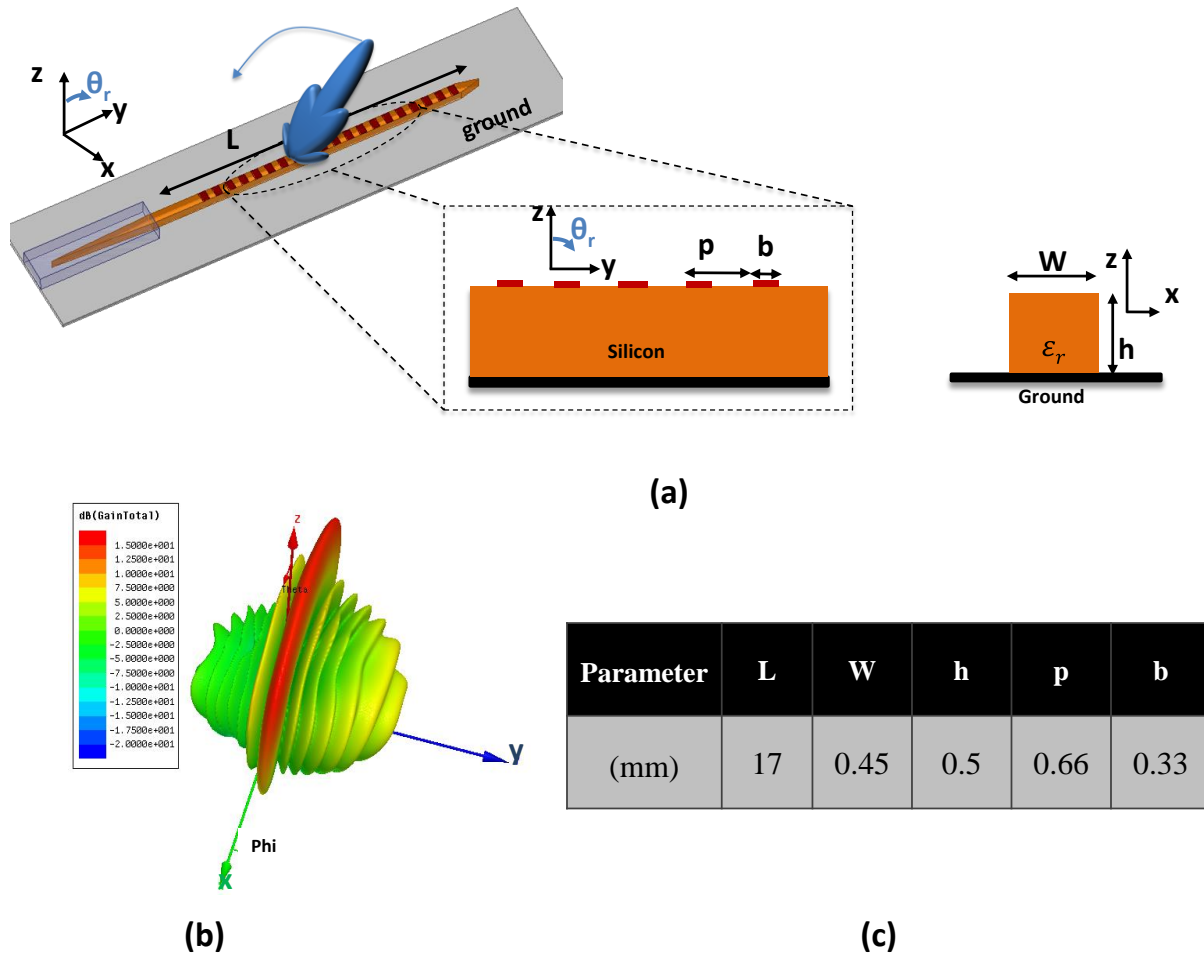


Fig. 3.24: (a) The general configuration of the proposed strip grating antenna. (b) The simulated 3-D gain pattern at 155 GHz, and (c) the design values.

The simulated reflection response and gain pattern for the $\phi=90^\circ$ cut, are shown in Fig. 3.25(a)-(b), for different angular scanning, over the 145-160 GHz range. The maximum simulated gain of 14.9 dBi, with reasonable flatness over the whole range, is achieved for the antenna length of $L=17$ mm. The side-lobe levels are less than 9 dB. The antenna efficiency is better than 92%.

The fabricated strip grating antenna by means of the laser machining process is shown in Fig. 3.26. For this reason, first the HRS wafer is coated with a few microns of copper, and

then the laser machine is optimized to pattern the copper. The laser speed is increased to avoid any unwanted damage to the surface of the silicon waveguide.

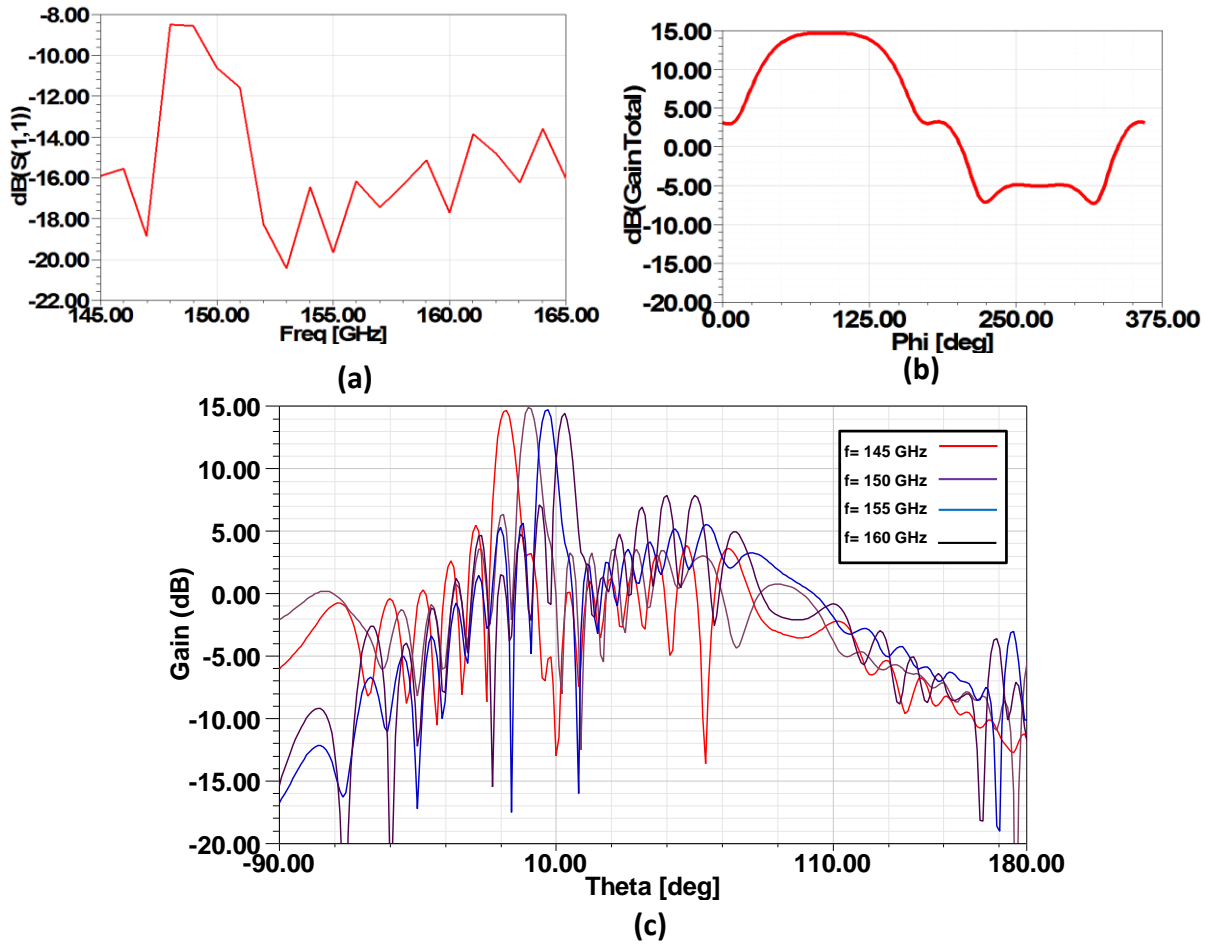


Fig. 3.25: (a) The simulated S_{11} of the strip grating antenna, (b) the simulated gain patterns for the $\theta_r = 3^\circ$ cut, and (c) the simulated gain patterns for the $\phi = 90^\circ$ cut [79].

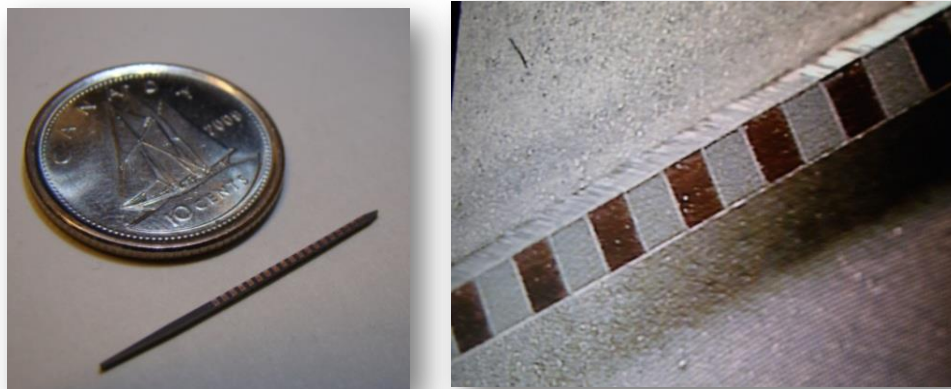


Fig. 3.26: The laser machined strip grating antenna [79].

3.6 Conclusion

In this chapter, the newly developed SIG technology was used for implementing various passive structures, operating over the D-band (110-170 GHz) range of frequencies. A number of designed bends were extensively studied and designed. The measured results demonstrated that a bend with the radius of $R=2$ mm has the minimum bending loss of 0.25 dB/ 90° . Then, a 3-dB Y-junction power divider was designed, and fabricated using the laser machining process. A back-to-back version of the divider was fabricated and successfully tested, by means of an optical method. The next introduced component was a directional coupler, which was extensively studied and designed. The idea of supporting beams was used for reaching a monolithic coupler. Also, the MMI version of coupler was designed and simulated. Finally, a 3-dB supported directional coupler was fabricated and successfully tested. The coupler sample was tested at $f_c=152$ GHz with the additional loss of 1.7 dB.

The last two sections of the chapter introduced three types of SIG antennas: 1) parasitic tapered antenna, 2) groove grating antenna, and 3) strip grating antenna. The design procedures along with the simulation results were discussed in detail. The main advantage of the proposed parasitic tapered antenna, operating from 86 GHz to 94 GHz, was its relatively high gain, 13 dBi, in comparison to a conventional tapered antenna. Then, two highly-efficient and low-cost grating antennas, groove grating and strip grating antennas, designed and optimized for the D-band applications with the boresight beam scanning capabilities, were discussed. The results indicated almost a flat gain of 14.2 dBi over the 153–165 GHz scanning range for a 17 mm long groove grating antenna. Also, the proposed strip grating antenna has a flat gain of about 14.9 dBi over the 145-160 GHz range of frequencies. All the antennas were realized by a fast and newly developed laser machining process.

Chapter 4

Dielectric Waveguide Whispering Gallery Mode (WGM) Sensors

Resonance structures are commonly used over the entire electromagnetic spectrum for designing a variety of devices, such as filters, sensors, and oscillators. In this chapter, an efficient and fast analysis method is developed for finding the resonance frequencies of the planar resonators, operating in higher order modes. This method is used for initial design and optimization of several Whispering Gallery Mode (WGM) resonators, realized on different technologies, mainly on silicon-based platforms. The designed resonance structures are fully simulated, fabricated, and tested. The introduced WGM resonance structures are employed for bio-sensing applications with the focus on DNA sensing.

4.1 Introduction

The WGM was first conceptualized by Lord Rayleigh who found that a high frequency sound wave can propagate on a concave surface [80]. Then, the WGM idea was adopted for studying wave propagation in atmospheric layers around the earth [81]. Since then, many efforts have been made to analyze dielectric resonators operating in the WG mode [82], [83], [84]. The main characteristics offered by WGM-based dielectric resonators are described below:

- They present a unique field distribution. WGMs are special modes of resonators close to the cylindrical boundary. Therefore, most of the energy is confined between the outer boundary and an inner radius, called the *caustic radius*.
- They offer oversized dimensions as compared to that of lower order modes. This property makes the WGM resonator a perfect candidate for mmWave applications. This characteristic reduces the effect of the fabrication error.
- They present high Q-factor resonances.

Several WGM-based applications have been reported in optics, mmWave, and even sub-mmWave electronic systems. In optics, the WGM spherical resonator is well-known for sensing applications [85], which will be discussed in Section 4.3. The planar type of WGM resonators are widely used in microwave devices such as filters, antennas, and power

dividers [86], [87]. WGM resonators are appealing because of their unique electromagnetic behavior. However, due to the various computational and theoretical challenges, not many WGM-based devices are implemented in the mmWave range of frequencies.

A WGM resonator can play an important role in realizing different mmWave integrated devices. The coupled WGM resonator can be used for various applications that require a confined field inside the resonator. These modes are extremely sensitive to any perturbation. Two types of WGMs can be excited inside a resonator: 1) standing wave WGM, and 2) travelling wave WGM. In the standing wave WGM, in contrast with the travelling wave WGM, the peak location of the field distribution does not change over time. A system composed of a dielectric waveguide coupled to a WGM resonator can be used as a common structure for a number of applications in sensing and mmWave signal processing (filtering, phase-shifting, etc.).

WGMs can be categorized as the high order modes, with rapid circumferential (azimuthal) variation, of a cylindrical waveguide. As it is known, a dielectric cylinder waveguide can support hybrid modes. WG modes are classified, depending on the polarization and the spatial distribution of the electromagnetic fields, as WGE_{nml} and WGH_{nml} . For WGE modes, the electric field is essentially transverse, whereas for WGH modes, the electric field is essentially axial. Each mode is denoted by three mode numbers: n , m , and l , describing the number of field cycles of variations along the azimuthal, radial, and axial directions, respectively [88].

In a Dielectric Disc Resonator (DDR), WG modes, with a small axial propagation constant, travels azimuthally close to the resonator boundary [84]. The excitation type and the resonator's physical parameters determine the type of the WGM inside the resonator. Among different types of WG modes, the WGE_{n00} and WGH_{n00} modes are desirable, because they provide a highly confined and sensitive field inside the resonator. In the WGE_{n00} mode, the predominant component is the axial H field, in contrast to the axial E field in the WGH_{n00} mode. WG modes with higher order numbers exhibit less radiation loss as compared to lower order modes [89].

4.2 An Efficient Analysis Method for Calculating the High Order Resonance Frequencies of a DDR

Rigorous full-wave analysis of a system, consisting of a dielectric waveguide coupled to a planar WGM-DDR, takes a long time. Therefore, developing a fast analytic method for doing initial design, which usually requires running many cycles, is required. Additionally, the developed analytic method is used for optimization the WGM resonator, in terms of resonance frequency. Calculating the resonance frequency of a DDR operating in higher order modes is not easy, mathematically. Various methods have been developed to find the resonance frequency of a dielectric resonator [90], [91], [92]. Obviously, the numerical methods offer a better accuracy at the cost of computational complexity. The majority of analytic solutions are based on a simple assumption that the modes are either quasi- TE (when E_z is zero) or quasi- TM (when H_z is zero). Other approaches, introduced to find the low order modes of a dielectric resonator consider a Perfect Magnetic Layer (PML) boundary for a resonator in order to simplify the resonance frequency calculations [93]. However, these simplifications reduce accuracy of the resonance frequency calculation.

The general structure under investigation is a DDR, placed on the grounded substrate, which is called an insulated image resonator (refer to Fig. 4.1(a)). In the following, an efficient and fast analysis method is developed for calculating the WGM resonance frequency of a DDR. The developed analysis method helps in initial design, sensitivity analysis, and optimization of the resonance structures. To calculate the higher order mode resonance frequencies of a DDR, the approach introduced in [92], which is a combination of the EDC method and Dielectric Waveguide Model (DWM) [92], [94], [95], [96], [97], [98] is adopted and developed. For the sake of simplicity and with the knowledge that the majority of the structures in this study are formed by an image resonator, the developed analysis method is described for an image resonator (refer to Fig. 4.1(b)). However, the developed analysis method is general and can be applied to any configuration of dielectric waveguide, for finding the high order resonance frequencies. The method can be described in four steps as follows:

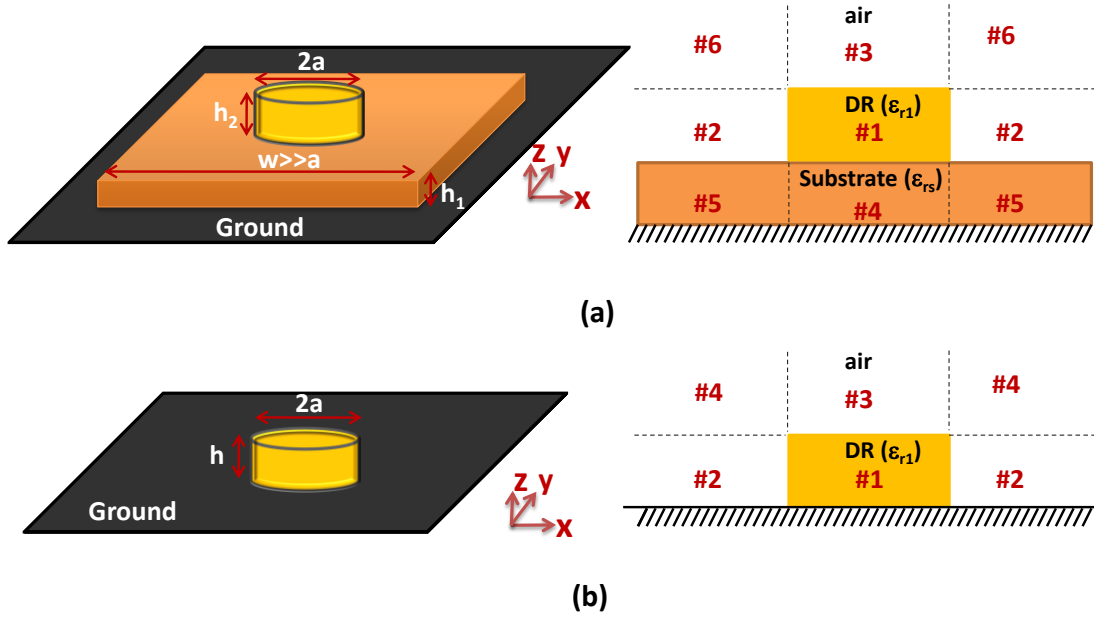


Fig. 4.1: (a) General configuration of a dielectric insulated image resonator, and (b) general configuration of a dielectric image resonator.

Step-1 (Applying EDC-DWM): To calculate the resonance frequency of an image resonator, all the propagation and attenuation constants of the structure in all the sub-regions should be found, using EDC-DWM method. In EDC-DWM technique, the critical assumption is that the fields in sub-region 4 are much smaller than their neighbors, and can be ignored. This assumption is valid if a strongly confined field exists inside the resonator. Applying the EDC-DWM to the image resonator, two sets of dispersion equations are obtained: 1) the axial dispersion equations, which are derived by field matching at $z=0$, $z=h$ surfaces, and 2) the radial dispersion equations, which are derived by field matching at $x=a$ surface. By solving the obtained dispersion equations simultaneously, the resonance frequency of the DDR is derived. Fig. 4.2 illustrates how an image resonator can be analyzed using the EDC-DWM method.

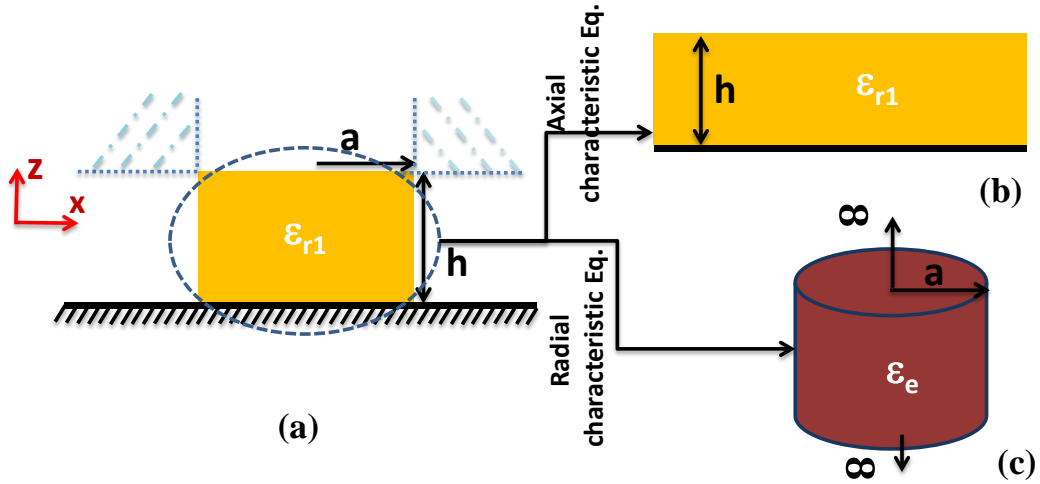


Fig. 4.2: (a) The cross section of an image resonator with (b) the equivalent single-layer slab waveguide for calculating the axial dispersion equation, and (c) the equivalent model for calculating the radial dispersion equation.

The dispersion equations of a single-layer slab, for both possible polarizations are obtained as (Appendix A):

$$\begin{cases} \frac{\epsilon_{r1}\alpha_z}{k_z} = \tan(k_z h) & TM \text{ mode} \\ -\frac{\alpha_z}{k_z} = \cot(k_z h) & TE \text{ mode} \end{cases} \quad (4-1)$$

where k_z and α_z are the axial propagation and the axial attenuation constants, respectively, and they are related by

$$\alpha_z^2 = k_0^2(\epsilon_{r1} - 1) - k_z^2 \quad (4-2)$$

$$k_x^2 = k_0^2\epsilon_{r1} - k_z^2 \quad (4-3)$$

To obtain the radial dispersion equation, Maxwell equations are solved for an infinite dielectric cylinder. Appendix B describes how the dispersion equation of an infinite dielectric cylinder is derived by matching the tangential components of the E and H fields at the boundaries. The obtained dispersion equation for an infinite dielectric cylinder is

$$\left[\frac{J'_n(k_\rho a)}{(k_\rho a)J_n(k_\rho a)} + \frac{K'_n(\alpha_\rho a)}{(\alpha a)K_n(\alpha_\rho a)} \right] \times \left[\frac{J'_n(k_\rho a)}{(k_\rho a)J_n(k_\rho a)} + \frac{1}{\varepsilon_{r1}} \frac{K'_n(\alpha_\rho a)}{(\alpha_\rho a)K_n(\alpha_\rho a)} \right] = \left[n(\varepsilon_{r1} - 1) \frac{k_{z'} k_0}{k_\rho^2} \right] \quad (4-4)$$

where

$$\alpha_\rho^2 + k_\rho^2 = k_0^2(\varepsilon_{r1} - 1) \quad (4-5)$$

$$k_\rho^2 = k_0^2 \varepsilon_{r1} - k_{z'}^2 \quad (4-6)$$

$k_{z'}$ is the axial propagation constant of an infinite dielectric cylinder. By solving (4-4)-(4-6), at different frequencies and for a specific mode number, n , the corresponding dispersion curve of a dielectric cylinder is acquired.

Step-2 (Solving the radial dispersion equation): In the following, an efficient and fast algorithm is introduced to solve (4-4)-(4-6), in order to find the radial dispersion curve. The main difficulty to solve these highly nonlinear equations, to find the required WGM dispersion curve, is the existence of unwanted modes in the vicinity of the objective mode.

As a starting point, ε_{r1} is set to one, which corresponds to a weakly guided mode [99]. The corresponding propagation constants are derived via the following decoupled equations (Appendix B):

$$-\frac{J_{n+1}(k_\rho a)}{k_\rho a J_n(k_\rho a)} = \frac{K_{n+1}(\alpha_\rho a)}{\alpha_\rho a K_n(\alpha_\rho a)} \quad EH_{nm} \quad (4-7)$$

$$\frac{J_{n-1}(k_\rho a)}{k_\rho a J_n(k_\rho a)} = \frac{K_{n-1}(\alpha_\rho a)}{\alpha_\rho a K_n(\alpha_\rho a)} \quad HE_{nm} \quad (4-8)$$

Then, the new value of ε_{r1} is updated via (4-4) repeatedly, as α_ρ is decreased by a small amount, Δ . The procedure of incrementally reducing the α_ρ continues until the $\delta \triangleq \varepsilon_{r1(updated)} - \varepsilon_{r1(real)}$ reaches to the acceptable tolerance, which is define by us.

In order to calculate the radial dispersion equation, it is required to have an estimation of the k_ρ searching interval to avoid interfering with any unwanted mode. In other words, the modes of a dielectric cylinder are separated from each other by small differences in the radial propagation constants, k_ρ . Therefore, the asymptotic values of (4-4) are used for defining the

searching intervals. The employed asymptotic expressions to determine the required intervals of k_ρ for both the HE and EH modes are given below (Appendix C).

HE_{nm} mode:

$$(\varepsilon_{r1} + 1)J_{n-1}(k_\rho^{min}a) = \frac{k_\rho^{min}a}{n-1}J_n(k_\rho^{min}a) \quad (4-9)$$

$$J_{n-1}(k_\rho^{max}a) = 0 \quad (4-10)$$

EH_{nm} mode:

$$J_n(k_\rho^{min}a) = 0, \quad k_\rho^{min}a \neq 0 \quad (4-11)$$

$$J_{n+1}(k_\rho^{max}a) = 0 \quad (4-12)$$

Step-3 (Bottom ground plane correction): In the next step, the effect of ground plane is incorporated in the calculation of the radial dispersion equation, for the purpose of increasing the EDC-DWM analysis accuracy. For the sake of generalization, Fig. 4.1(a) configuration is considered. Then, (4-4) is solved for the modified dielectric constant $\varepsilon_{r1} = \varepsilon_{eff}$, in which ε_{eff} is defined as [100]

$$\varepsilon_{eff} = \begin{cases} \frac{1}{2}(\varepsilon_{r1} - (\varepsilon_{r1} - \varepsilon_{eff_0})\frac{h_1}{a}) + \frac{\varepsilon_{eff_0}}{2} & h_1/a \leq 1 \\ \varepsilon_{eff_0} & h_1/a > 1 \end{cases} \quad (4-13)$$

where ε_{eff_0} is the effective dielectric constant of an infinite dielectric cylinder ($\varepsilon_{eff_0} = \frac{k_\rho^2}{k_0^2}$).

In the case of a suspended resonator, ε_{eff} is reduced to ε_{eff_0} . The diagram in Fig. 4.3 explains the algorithm for obtaining the radial dispersion curve of an image resonator.

Step-4 (Resonance frequency calculation): In the last step, the resonance frequency is calculated. The resonance frequency of the DDR is the frequency at which $k_z = k_{z'} = k_{z''}$. Graphically, the intent is to find the intersection point of the calculated axial and radial dispersion curves.

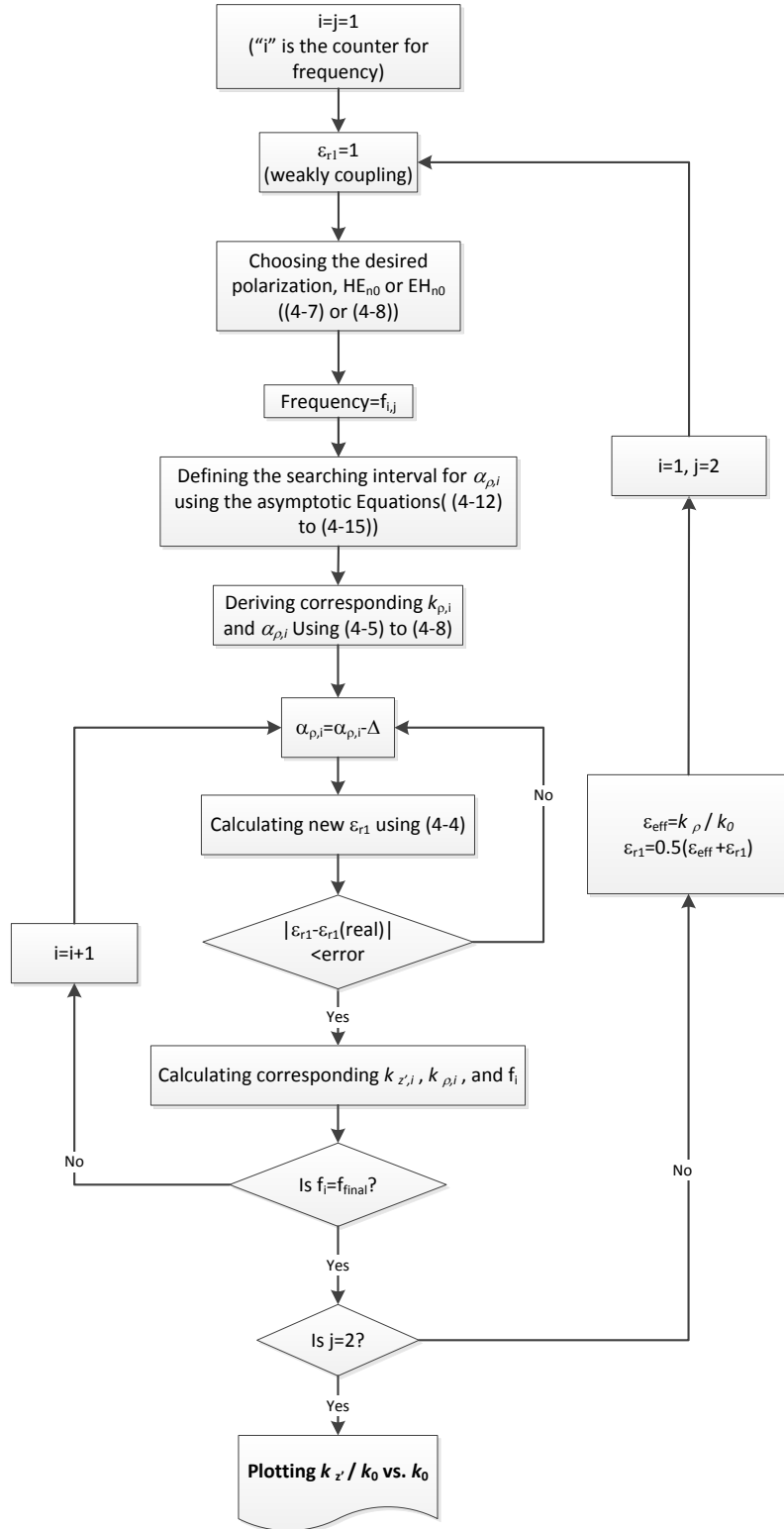


Fig. 4.3: The developed algorithm for obtaining the radial dispersion curve of an image resonator.

4.2.1 Variational-Based Method for Improving the Accuracy

Nature is full of optimal configurations. Consequently, researchers try to find the optimal systems that have small and minimal variations. The variational principle is to find a function to damp a variation. From a mathematical point of view, the variational method is used for improving and optimizing the characteristic values of a system.

Among different methods, introduced to solve the system of differential equations of an electromagnetic structure, the variational and perturbation methods are efficient and accurate approximate approaches [101], [102]. In contrast to the perturbation method, which is the way to find the effect of small changes, a variational method is an approach to refine an obtained value. The important application of the variational method is to amend the resonance frequency of a certain electromagnetic configuration. The variational method is an optimization technique applied to a stationary problem to improve the initial solution. The key in employing the variational method is to define an appropriate formula. It should be stationary with respect to the parameter which is going to be calculated. This stationary formula is not unique.

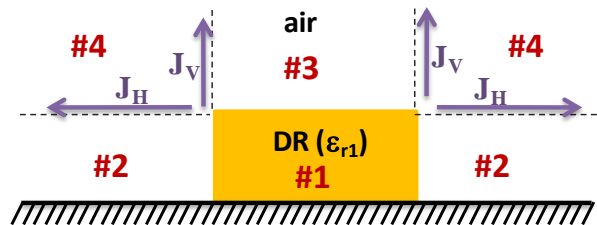


Fig. 4.4: The cross section view of a grounded DDR used in the variation method.

In the case of dielectric resonators, the variational technique is used to improve the accuracy of the resonance frequency when a reasonably accurate estimate of the field distribution in the resonator is known. The stationary formula should be defined such that minor inaccuracies in the field pattern do not significantly affect the resonance frequency. Most all of the stationary formulas are expressed as a ratio between different types of the stored energies in the sub-regions. Among different equations proposed to find the resonance frequency of a resonator, shown in Fig. 4.4, the one, which is based on the self-reaction principle [103], [104] is utilized here. The resultant stationary equation is based only on the electric field terms. The stationary formula is:

$$\omega_r^2 = \frac{\iiint_v E^* \cdot \left(\nabla \times \frac{1}{\mu} \nabla \times E \right) \cdot dv - \iint_s (n \times E) \cdot \left(\frac{\nabla \times E^*}{\mu} \right) \cdot ds}{\iiint_v \varepsilon E \cdot E^* \cdot dv} \quad (4-14)$$

For an image dielectric resonator, the surface integral in the numerator of (4-14) originates from the surface electric currents, J_V and J_H , shown in Fig. 4.4. The volume integral in (4-14) should apply to the sub-regions, denoted as 1 to 3 in Fig. 4.4 (the fields in the sub-region 4 are assumed to be zero similar to the described structure in the previous section). To derive the field distribution inside the resonator and in the neighboring sub-regions, the Marcattili's solution is employed [105]. By understanding the fact that fields satisfy the Helmholtz equation, the volume integral in nominator can be simplified as

$$\iiint_v E^* \cdot \left(\nabla \times \frac{1}{\mu} \nabla \times E \right) \cdot dv \xrightarrow{k^2 = \omega^2 \varepsilon \mu \text{ \& Helmholtz equation}} \omega^2 \cdot \iiint_v \varepsilon E \cdot E^* \cdot dv \quad (4-15)$$

Eventually, (4-14) can be written as follows:

$$\omega_r^2 = \frac{\omega^2 \cdot \iiint_v \varepsilon E \cdot E^* \cdot dv - \iint_s (n \times E) \cdot \left(\frac{\nabla \times E^*}{\mu} \right) \cdot ds}{\iiint_v \varepsilon E \cdot E^* \cdot dv} = \omega^2 \left(1 - \frac{\sum N_s}{\sum D_v} \right) \quad (4-16)$$

where N_s and D_v denotes the numerator surface integral and dominator volume integral, respectively. The detailed calculation of the volume and surface integrals of the structure in Fig. 4.4 are explained in Appendix E.

4.3 WGM-Based Bio-Sensor Technology

Various methods, mostly in optics, have been proposed for sensing and analyzing biological materials such as antibodies, tissues, nucleic acids, and DNA [3], [106], [107], [108]. There are various sensing methods, and the important ones are categorized as: electrochemical, photometric, and ion channel switching approaches. Among these techniques, the photometric method (an inherent marker-free sensing method) is more efficient. It is based on the electromagnetic characteristics of materials. The photometric methods are divided into various types. Resonance-based sensing is the most popular approach [109]. Resonator-based structures are the basis of many optical bio-sensors [110], [111], [112] Micro-ring, micro-sphere, surface plasmon, photonic crystal cavities, and planar resonators are some examples from this category [113], [114], [115] The operating principle of these devices can be explained by the concept of evanescent field interaction. Resonance-

based sensing is classified into two major groups of techniques: those based on absorption measurement and those based on refractive index measurement.

In the absorption-based method, the electromagnetic absorption factor of the material in proximity of the sensor changes the resonator loaded Q-factor. This technique is commonly used to distinguish between the different types of molecules. In the refractive index measurement approach, any change in the dielectric constant of a material leads to a shift in the resonance frequency. The selectivity and sensitivity of this method depends on the electromagnetic properties of the sensor resonator. Numerous investigations have been performed on the refractive index method [55]. In addition, the refractive index measurement is the basis of operation of another type of sensor, called the evanescent wave sensor.

Although remarkable results have been accomplished by introducing bio-sensor devices in the THz frequency range, continual efforts are required to improve sensor characteristics such as sensitivity, reusability, portability, and selectivity, as well as decreasing fabrication costs. It is extremely difficult, if not impossible, to build such a sensor that can meet all of the aforementioned criteria.

Among the resonator-based sensors, the ones that use WGM are of great interest. This is mainly due to the fact that the WGM resonator can provide a highly sensitive and a low cost technology for sensing applications. The WGM-based resonator can be used as a highly effective sensing element in many bio-sensing applications such as the detection of proteins, toxin molecules, and DNA [85]. Very few WGM-based devices are introduced at the mmWave range of frequencies for sensing application such as nano-litre liquid sensing [116]. On the other hand, the WGM technique has been well recognized for sensing applications in the optical range of frequencies [85]. Blair and Chen's [117] pioneering work demonstrated how the WGM-based resonator can be used as a cavity sensor to enhance the sensitivity, and to reduce the sample size. Another group utilized the WGM-based resonator to investigate protein materials [118]. Several researchers have focused on the extraction of the complex permittivity of different materials, such as alumina, bulk GaAs, and ceramic in the lower range of the mmWave band [119], [120], [121]. Additionally, others have reported the detection of a small volume of liquid samples at 40 GHz by using a WGM-based resonator as an evanescent wave technique [116]. Following the same approach, the detection of the small

variation in the material concentration can be performed. In these techniques, a small volume of the solution sample, placed on the top of a DDR, can be modelled by equivalent surface impedance. This surface impedance depends on the electromagnetic characteristics and the thickness of the deposited material. Accordingly, the resonance condition inside the resonator is altered and the resonance peak is shifted. The value of the resonance shift is directly related to the variation of the sample concentration.

Many factors can contribute to the portable system errors and therefore must be taken into consideration. Important ones are listed below:

- The measurement system setup errors.
- High sensitivity of the measurement setup to the environmental conditions.

In this research, different reasonably accurate WGM sensors have been designed and fabricated at the mmWave range of frequencies from 75 to 240 GHz, where vibrations of bounded molecules of biological samples are greater in THz region than the ones in optics and microwave. Furthermore, thanks to technological advancement in measurement instruments, the THz region now is a suitable band for material characterization and bio-sensing. Although the aforementioned errors exist in this range of frequency, the safe margin, which is required for cancelling the errors, is large enough.

In the following sections, first, the design procedure of an alumina-based WGM sensor, operating at D-band (11-170 GHz), is explained. The WGM resonance behavior is analyzed using the developed algorithm and the results are modified using the introduced variational method. Then, the whole resonance structure is simulated and the results are compared to the ones obtained from the measurement. The alumina sensor is tested for sensing the sugar and water solution. Also, the sensor is utilized to distinguish between different types of DNA. In the next step, a Silicon-On-Insulator (SOI)-based WGM structure is employed for DNA sensing purpose. As a last set of sensing experiments, the SOG structure is tested for distinguishing between different DNA samples. Finally, the SIG technology is used for designing two WGM-based resonance configurations.

4.4 Alumina-Based Image WGM Sensor

Alumina is chosen for fabricating the first prototype of WGM resonance sensor structure. Alumina is a fairly low-loss, easy-to-fabricate, and low-cost material. Historically, the author's first implemented WGM structure was a low-cost and high-power mmWave oscillator based on a direct coupling of a Gunn diode to an alumina WGM resonator, working at 40 GHz [122]. Following that, the author designed several alumina WGM sensors, operating at the mmWave range of frequencies from 75 to 220 GHz [123], [124]. The alumina WGM sensor, designed over the D-band (110-170 GHz) range of frequencies, is shown in Fig. 4.5. The structure consists of metallic input/output rectangular waveguides (WR-06) and the Dielectric Image Guide (DIG), which is tapered at the ends.

The DIG is designed in such a way that the structure supports dominant mode operation in our desired frequency band. The modal analysis of the DIG is performed by using the EDC method. The dispersion plots for different modes are depicted in Fig. 4.5 for the design parameters given in Table 4.1. The dominant mode is the E_z^{11} mode. Due to exciting the structure by means of a metallic waveguide, the E_x^{11} mode, which potentially can be excited inside DIG, is not triggered. As before, the tapered sections are designed in a manner so that the minimum insertion loss is achieved.

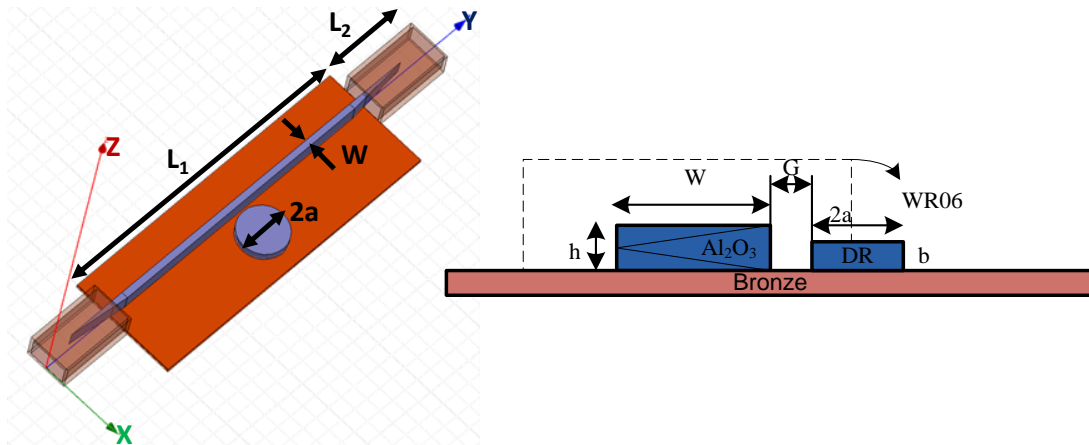


Fig. 4.5: The general configuration of the alumina-based WGM resonance structure [124].

Table 4.1: Design parameters of the sensor at D-band.

Parameter	L_1	L_2	W	Gap	a	b	h
(mm)	20	5	0.47	0.13	1.36	0.65	0.55

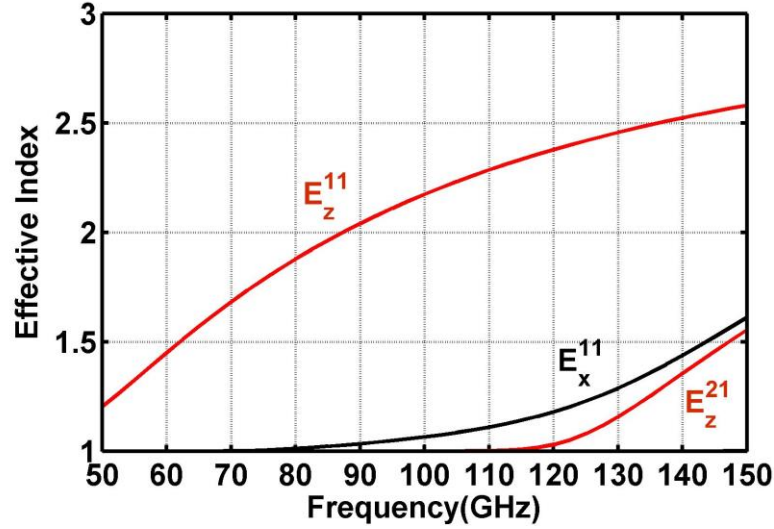


Fig. 4.6: Modal analysis of the DIG using the EDC technique [124].

The most critical part is the design of the DDR. Following the same procedure, explained in Section 4.2, the resonator is investigated in terms of WGM resonance behavior. The DDR is designed such that, it supports desired WGM resonances in the frequency range of interest. Choosing the mode number as a designed parameter, is crucial. The low-order modes ($n < 5$) are radiating with low Q-factor, and very-high-order modes ($n > 10$) are not at all suitable for sensing applications [125]. The reason is that the relatively higher-order modes need a larger size of DDR for operating in the same desired range of frequency. In addition, the higher-order modes ($n > 10$) are very confined, and are not suitable for sensing, as higher-order modes have very small evanescent field tail, which is necessary to sense the external perturbation, outside of DDR. Another important design parameter is the radius of the DDR. Relatively large radius, related to high-order modes within the desired range of frequencies, increases the loss and dictates a small gap between DDR and DIG. The type of WGM is determined by the polarization of the excitation and physical parameters of the DDR.

The gap distance between the DDR and DIG is determined to maximize the sensitivity. Although critical coupling increases the sensitivity of the system on one hand, the sensor

would become sensitive to environmental variations including temperature and moisture. Therefore, practically the DDR should not be placed in the critical coupling.

To calculate the approximate resonance frequency of the unloaded resonator, two dispersion equation sets, axial and radial dispersion equations, are solved simultaneously. The corresponding resonance frequency is calculated as 123.40 GHz, as shown in Fig. 4.7(a). Different components of the electrical field are plotted in different cross sections, as observed in Fig. 4.7(b)-(c). The excited resonance mode inside the resonator is WGH_{700} . The analytical calculation is verified by the eigen-mode solution, obtained from two commercial full-wave simulators, Ansoft HFSS and Comsol.

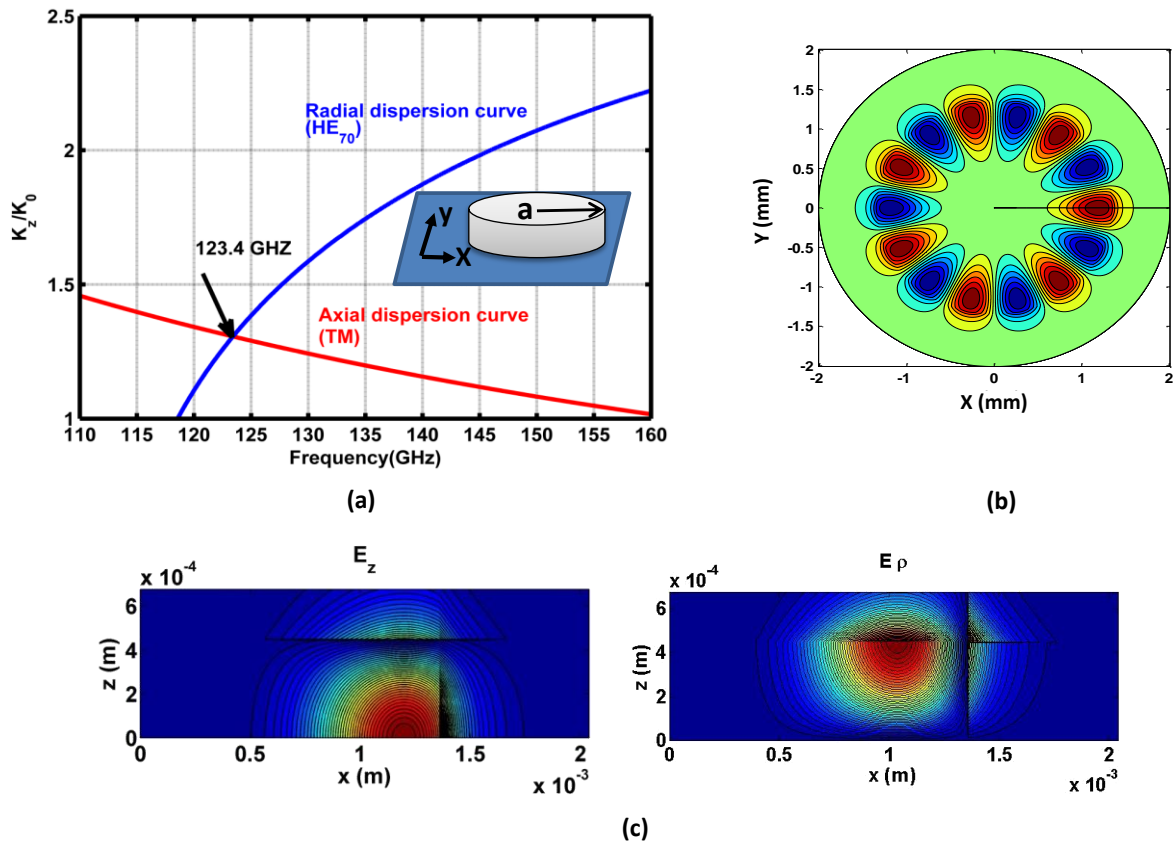


Fig. 4.7: (a) The axial and radial dispersion curves of the DDR. (b) Normalized E_z field component in the DDR for WGH_{700} mode in the xy -plane. (c) Normalized electric field components in the DDR for WGH_{700} mode in the xy -plane.

Table 4.2: A comparison between the calculated resonance frequency by the developed algorithm, and the full-wave simulation for D-band design.

Mode	Resonance frequency from the proposed algorithm (GHz)	Resonance frequency after applying the variation method (GHz)	Resonance frequency from the full-wave simulation (HFSS) (GHz)	Error between the full-wave and EDC-DWM (%)	Error between the full-wave and the variational method (%)
<i>WGH₇₀₀</i>	123.4	124.36	124.65	1.00	0.23
<i>WGH₈₀₀</i>	134.9	135.95	136.35	1.06	0.29

The variational method, described in Section 4.2.1, is applied to the problem to reduce the resonance frequency calculation error, as a result of ignoring the fields in the corner sub-regions. The modified resonance frequency after using the variational method is found to be 124.34 GHz, when compared with the initial value of 123.4 GHz. The accurate resonance frequency obtained from the full-wave simulation is 124.65 GHz. Table 4.2 compares two sets of resonance frequencies, obtained from the proposed technique and the full-wave simulation, for the D-band design. The depth of resonance is directly related to the DDR distance from the DIG. Choosing a proper resonance depth (Q-factor), the system sensitivity to the environmental conditions can be decreased at the cost of decreasing the selectivity margin of the sensor. Hence, a trade-off should be taken into account to choose the appropriate gap between the DIG and DDR. Fig. 4.8 demonstrates the effect of the gap on the resonance response.

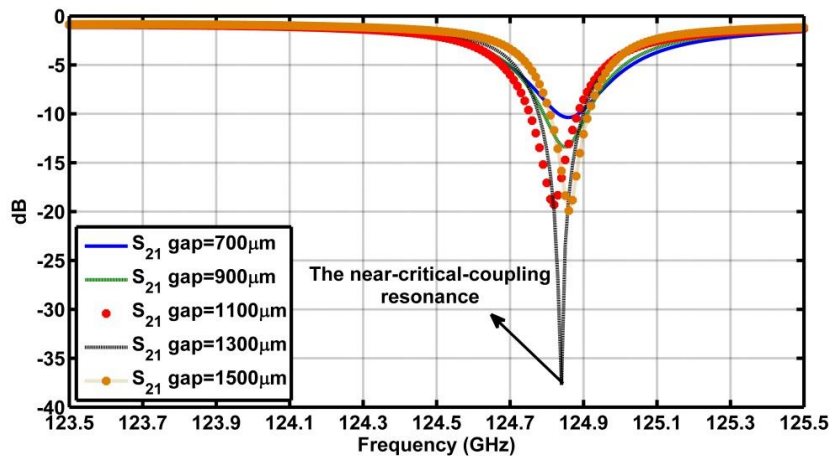


Fig. 4.8: Effect of gap on the resonance response of DIG-DDR (simulation).

The prototype structure was made and tested as shown in Fig. 4.9. To fix the position of the DIG and the DDR over the metallic base, a low-loss epoxy glue was used. Although small drops of epoxy glue were used, the loss increment, due to the presence of the glue, is inevitable. Considering the fact that the desired mode inside the DIG is almost confined in the centre, fixing the waveguide from the sides with glue drops has no significant effect on the field distribution. Since the resonator field is sensitive to any perturbation, fixing the DDR with glue should be handled with care. To eliminate this undesired effect, the bottom of the DDR is metalized. The overall functionality of the sensor is verified by using the full-wave simulation. Fig. 4.9 illustrates the experimental setup, consisting of a network analyzer, two harmonic mixers at D-band, and the proposed sensor device.

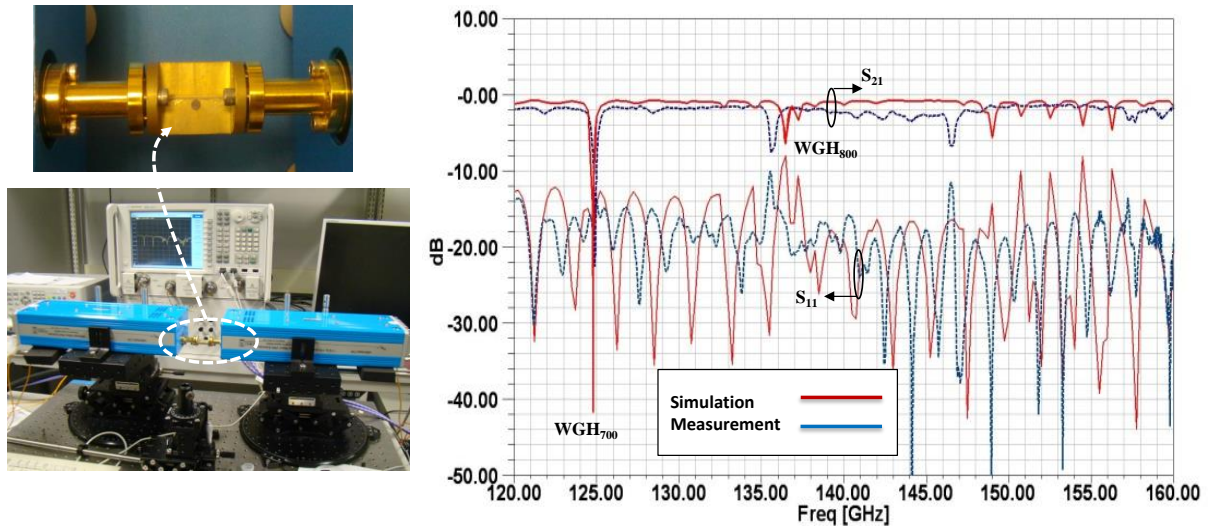


Fig. 4.9: (a) Measurement setup and the fabricated sensor device. (b) Comparison between the measured (dashed) and simulated (solid) scattering parameters.

4.4.1 Glucose Sensing

Determining the accurate amount of glucose in blood has been the subject of extensive research on sensing techniques [126], [127]. Most of the existing approaches for glucose detection are based on electro-chemical methods. To test the sensor, described in the previous section, two different concentrations of glucose in the water solution were prepared: 1 g/100 μ l (60 mol/l) and 1.65 g/100 μ l (99 mol/l) diluted glucose. The glucose and water solution sample is chosen to investigate the functionality of the implemented bio-sensor device. Eventually, the obtained data will help us to optimize the system including the sensor

and the measurement setup for our main goal, which is DNA sensing. In each trial, a constant volume of the solution ($5 \mu\text{l}$) is placed on top of the DDR, and the changes in the resonance frequency and Q-factor are recorded after the water evaporates. The repeatability of the measurement results is a key factor that should be examined carefully. Thus, for each concentration, the measurement is repeated several times. Undoubtedly, an accurate measurement is dependent on a precise calibration. An intensive effort was made to ensure an accurate calibration in order to reduce the transmission loss measurement error to less than 0.02 dB over the entire range of frequency. Additionally, the temperature was controlled at $23 \pm 1^\circ$. This small fluctuation in temperature does not have a significant effect on the resonance characteristics (less than $\pm 2 \text{ MHz}$ shift in the resonance frequency). It is because the temperature expansion of alumina is very low. For verification of the data, all the measurements were repeated several times. Also, after removing each sample, the response of the sensor was verified to be identical to the initial state. The sensor was tested for two different concentrations of the glucose solution, $1.65 \text{ g}/100 \mu\text{l}$ and $1 \text{ g}/100 \mu\text{l}$.

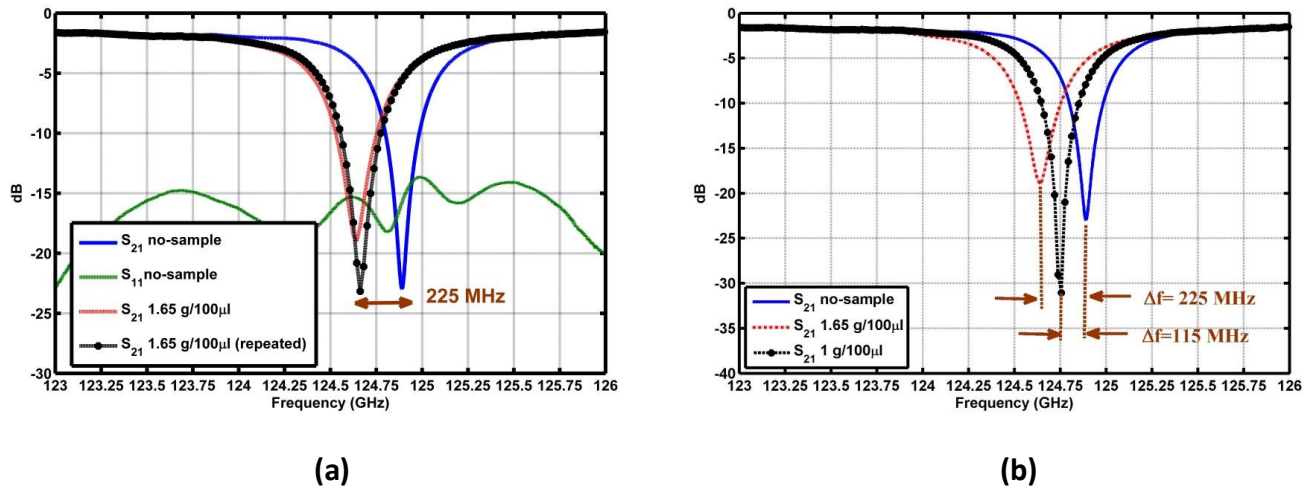


Fig. 4.10: (a) Measurement results of the $5 \mu\text{l}$ glucose solution samples with a concentration of $1.65 \text{ g}/100 \mu\text{l}$. (b) Comparison of resonance responses of the sensor loaded with two different glucose solution samples [124].

Fig. 4.10 shows the measurement results for the concentration of $1.65 \text{ g}/100 \mu\text{l}$. It is observed that a 225 MHz shift in the resonance frequency is achieved. For the second set of

the samples, with the concentration of 1g/100 μ l, the smaller resonance frequency shift is obtained. It is interesting to note that in this case, the resonance frequency shows higher Q-factor as compared with the no-sample case. The reason is that, the thin layer of sample increases the attenuation loss inside the DDR, and consequently the coupling state becomes closer to the condition of critical coupling. The results for all the cases are compared in Fig. 4.10

4.4.2 DNA Sensing

The description of an individual genetic background (DNA and RNA) has become a powerful tool in the diagnosis of diseases, genetic disorders and pathogen infection. The recent discovery that most cancers have widely varying genetic backgrounds indicates that successful intervention may require individualized therapeutic strategies [128]. The present technology, used to evaluate one's individual genetic makeup, is based on the ability of an immobilized single-stranded DNA to hybridize to a complementary sequence forming a double-stranded structure, which is then detected via an optical method [129]. Until now this has required time-consuming modification, fluorescent labeling and enzymatic amplification of the sample being analyzed. While these techniques have proven to be sensitive, they run the risk of experimental bias as well as the cost and complicated methodology beyond the scope of local healthcare providers. The development of an integrated, cost-effective, and ultra-high sensitivity bio-sensor holds the promise of quick and effective healthcare practices that are tailored to individuals.

Recent improvements in many label free microwave/optic DNA detectors have been achieved based on the fact that, different DNA segments can be distinguished by their differences in the dielectric constants. Resonator-based techniques have been introduced as efficient and accurate methods for DNA labelling [130]. Most of the achievements in DNA sensing are obtained in the optics by using highly sensitive micro-spherical resonator structures. However, the micro-spherical resonator is a 3-D structure, decreasing the inerrability of the system. Additionally, the fabrication of this kind of resonator is difficult. Thus, varieties of planar structures, including corrugated parallel resonators and quarter wavelength resonators, have been proposed and used for DNA sensing [131]. A WGM-based DDR is essentially a planar structure approach, which is practical and suitable for the

integration. In terms of measurement sensitivity, WGM-based techniques have considerable advantages in comparison with other sensing methods.

The alumina WGM-based structure, designed in the previous section, is employed for the DNA sensing. The measurement setup is the same as the one in Fig. 4.9(a). The test procedure is conducted as follows: first, the resonator is completely washed by distilled water and allowed to dry completely. Then, the transmission loss of the uncovered structure is measured. In the next step, the DNA sample, either in single-stranded or double-stranded form, is deposited simply by pipetting 5 μl from an aqueous solution onto the WGM DDR. After the water evaporates, the DNA forms a thin film with a thickness of only a few tens of nanometers. Again, the response is measured. Next, the surface of the resonator is washed by using the distilled water several times. After a specific time, 20 minutes, the resonance frequency is again measured. To stabilize the resonance frequency, the data are compared with that initially recorded. This process is repeated several times, for each sample, to check the repeatability of the measurement.

In the first round of measurements, two different single-stranded DNA solutions, labelled as EB3 and ILK, are selected. These denatured DNA samples are different from each other, in sequence, by almost 70%. Each sample consists of a denatured DNA oligo at a concentration of 1 g/l in distilled H_2O . By using the explained procedure, each DNA oligo is loaded on the top of the DDR, and the observed resonance frequency shift is recorded.

Fig. 4.11 shows the results for two samples, EB3 and ILK. The two DNA samples are distinguishable from each other by a 6.5 MHz difference in the resonance frequency shift.

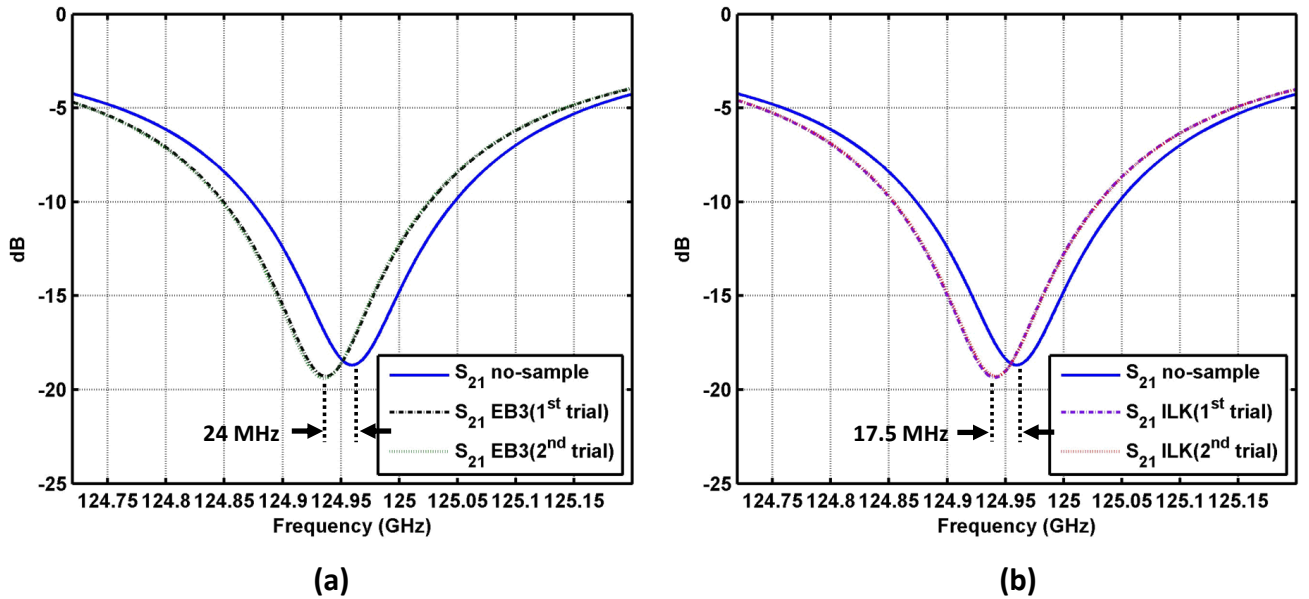


Fig. 4.11: The measurement results of the alumina sensor loaded with two different single-stranded DNA: (a) EB3 (b) ILK.

In the second experiment, a denatured DNA (forward-stranded DNA) and a hybridized DNA (double-stranded DNA) are chosen. A hybridized DNA has an inherently higher dielectric constant and absorption factor than a denatured DNA. The difference in the dielectric constants causes a larger shift in the resonance frequency. Following the same measurement procedure for differentiating between two single-stranded DNA, a new set of results are achieved for both the single and double DNA samples. Fig. 4.12 shows the results from the unloaded resonator, and from the resonator, loaded by a new denatured DNA (forward-stranded) and double-stranded samples. The experiment tests are repeated to verify the reproducibility of the setup. It is known that the resonance frequency shift is larger for the material with a higher refractive index. The sensor is evaluated by comparing the results of both the denatured and the hybridized DNA experiments. Fig. 4.12 demonstrates that the hybridized DNA, clearly generates a larger shift, 305 MHz, in the resonance frequency compared to the denatured DNA, which causes only a 170 MHz shift.

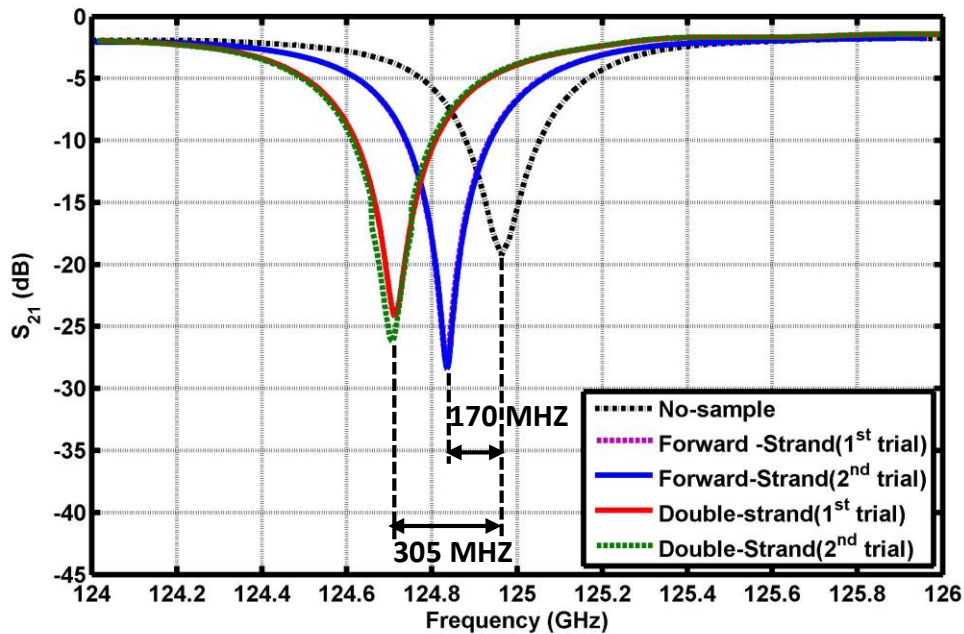


Fig. 4.12: The measurement results of the alumina sensor loaded with forward-stranded and double-stranded DNA.

4.5 DNA Sensing Using Silicon-on-Insulator (SOI) WGM Sensor

Difficulty in integration with other available IC technologies was the main drawback of the previous introduced structure, the alumina-based sensor. On the other hand, SOI technology is very convenient for introducing a potentially integrated mmWave system. HRS technology enables us to design a low-loss, and consequently a high Q-factor resonator. Accordingly, a fast, low-cost, reliable, and highly sensitive sensor is feasible. In this section, a SOI WGM sensor is employed for distinguishing between different DNA oligos, after evaporation of the buffer solution [132]. The system is particularly realized in a HRS SOI technology, which was originally introduced in [133], as a liquid ring resonator sensor. The SOI technology allows us to have accurate control on the gap size between the disc and the waveguide, which is a critical parameter in determining the performance of the sensor.

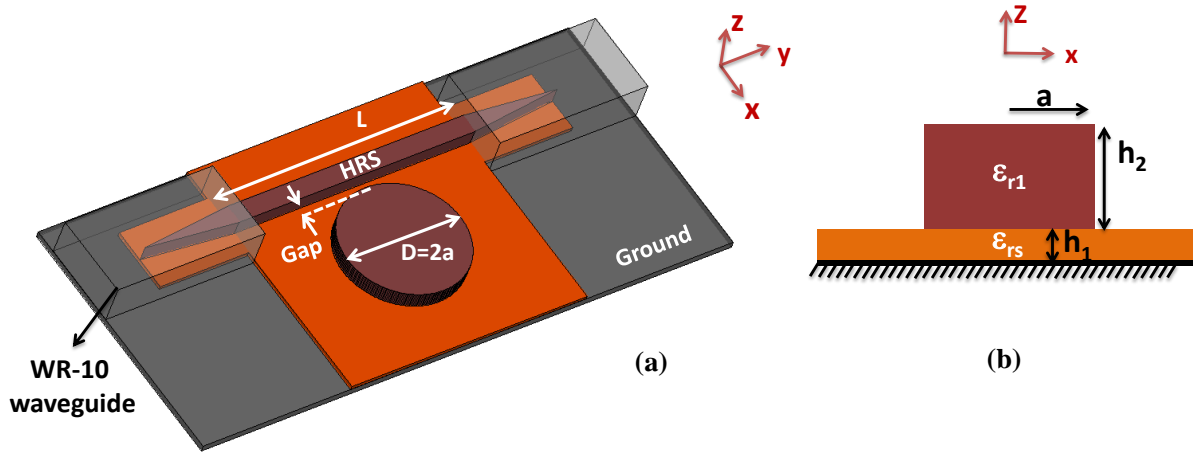


Fig. 4.13: (a) The SOI sensor configuration. (b) The cross section of a general insulated DDR [132].

Fig. 4.13 shows the schematic of the proposed sensor. The sensor consists of a dielectric waveguide coupled to a DDR. The device supports, WGH mode in which E_z is the dominant mode. The top layer of the SOI-based wafer has a thickness of approximately $500 \mu\text{m}$ while the handle wafer has a thickness of $130 \mu\text{m}$. The buried oxide layers has a thickness of $1\sim 2 \mu\text{m}$. The fabrication process is a simple single-mask process similar to the one explained in [133]. The dielectric waveguide is excited by the standard rectangular metallic waveguide (WR-10). The dielectric waveguide is linearly tapered at both ends for smooth transition to the rectangular metallic waveguide. The total length of the dielectric structure is 20 mm . The dielectric waveguide is designed to support a single mode operation (E_z^{11}). The dielectric waveguide channel has a cross section of $0.5 \times 0.6 \text{ mm}^2$. The DDR has a radius of 1.91 mm , which supports four distinct WGH modes within the range of $75\text{-}110 \text{ GHz}$. The disc surface area is suitable for placing the exact $10 \mu\text{l}$ DNA sample. In addition, the designed DDR provides the non-radiative WG modes ($n > 6$) within the desired frequency range.

The analysis method, explained in Section 4.2, is employed for finding the resonance frequency and optimization of the SOI structure. In the case of an insulated resonator, the radial dispersion equation is the same as (4-4), while the axial dispersion equation for TM^z mode of a double-layered image slab waveguide is as follow:

$$\left[1 + \left(\frac{\alpha_1}{k_z}\right)\left(\frac{\varepsilon_{r1}}{\varepsilon_{rs}}\right)\tan h(\alpha_1 h_1)\tan(k_z h_2)\right] + \left(\frac{k_z}{\alpha_0 \varepsilon_{r1}}\right)\left[-\tan(k_z h_2) + \left(\frac{\alpha_1}{k_z}\right)\left(\frac{\varepsilon_{r1}}{\varepsilon_{rs}}\right)\tan h(\alpha_1 h_1)\right] = 0 \quad (4-17)$$

where α_0 and α_1 are the axial attenuation constants in air and in the substrate, respectively. k_z is the axial wavenumber. The parameters α_0 , α_1 , and k_z are related to each other through the following equations:

$$\alpha_0^2 = [k_0^2(\varepsilon_{r1} - 1) - k_z^2] \quad (4-18)$$

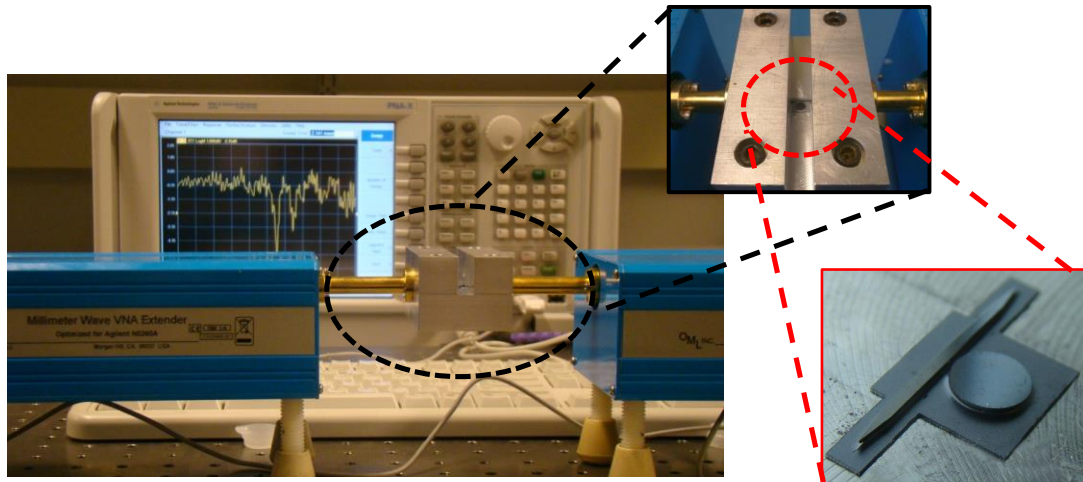
$$\alpha_1^2 = [k_0^2(\varepsilon_{r1} - \varepsilon_{rs}) - k_z^2]$$

The achieved results are approximate ones due to the assumption of zero-field at the corner regions of the DDR. The accuracy of the calculated values can be improved by using a variational expression for the resonance frequency.

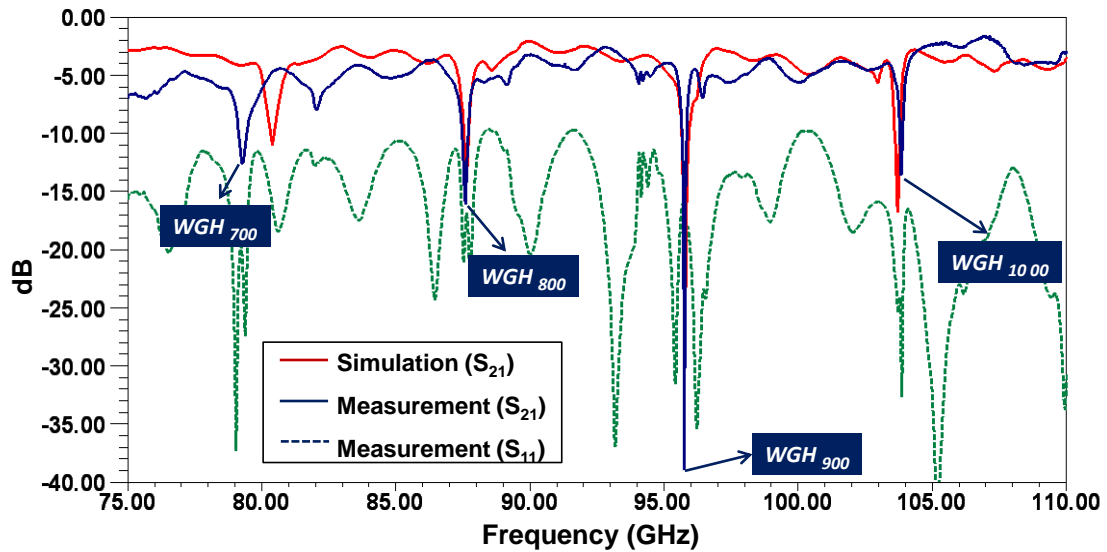
Table 4.3: A comparison between different methods, employed to find the WGM resonance frequencies of the SOI structure.

Mode	Resonance frequency EDC method (GHz)	Resonance frequency after applying the variation method (GHz)	Resonance frequency from the full-wave simulation (HFSS) (GHz)	Error between the full-wave and EDC-DWM (%)	Error between the full-wave and the variational method (%)
<i>WGH</i> ₈₀₀	86.61	87.12	87.52	1.04	0.45
<i>WGH</i> ₉₀₀	94.31	95.35	95.75	1.50	0.42

The resonance characteristics of the DDR for different WGM resonances are obtained from the full-wave eigen-mode simulation, performed by HFSS, and compared to those calculated by the EDC and variational method (Table 4.3). Obviously, a good agreement is achieved between the results. However, the developed numeric method is much faster than the HFSS simulator.



(a)



(b)

Fig. 4.14: (a) The SOI measurement setup, and (b) the comparison between the S_{21} obtained from measurement with that of simulation [132].

To examine the capabilities, sensitivity, and selectivity of the sensor a number of DNA samples were prepared. Complementary 38 base pair synthetic oligonucleotides (short and single-stranded DNA molecules), were obtained from Sigma Genosys Canada.

Oligo #1: 5`- GGT GCT ACA GTT GCT CAT GAG CTG GGG CAC AAC TTG GG-3`

Oligo #2: 5`- CCC AAG TTG TGC CCC AGC TCA TGA GCA ACT GTA GCA CC-3`

The individual oligonucleotides used for single-stranded DNA tests were denatured at 95°C for 3 minutes in annealing buffer (10 mM Tris, pH 7.5, 50 mM NaCl, 1 mM EDTA) and then rapidly cooled on ice. A double-stranded DNA was generated by combining oligonucleotide 1 and 2 at equimolar concentration. The samples were denatured at 95°C for 3 minutes in a heat block. The block was then allowed to cool to room temperature over one hour. Annealed oligos were stored on ice. Single and double-stranded oligos were tested at equal molar concentrations, 20 nmol. The prototype sensor was tested with the similar measurement setup as before, a Network Analyzer, equipped with two external mixer modules. The fabricated HRS waveguide has a length (L) of 13 mm and two 3 mm tapered sections. To provide a high Q-factor resonant for WGH_{900} mode, the gap between the DDR and DWG is 160 μm . The measurement setup including the sensor device is illustrated in Fig. 4.14(a). The measured transmission and reflection responses of the device within the range of 75-110 GHz are plotted in Fig. 4.14(b), and compared with the simulated ones. A strong agreement is achieved between the measurement and the simulation results. The higher loss, observed in the measured results, is due to the misalignment and metallic fixture issues. The related Free Spectral Range (FSR) for this structure is around 8.15 GHz.

Q-factor is an important measure of the quality of a resonance mode. One method to determine the loaded Q-factor of a reaction-type resonator is to analyze the S_{21} contour in the smith chart [134]. The loaded quality factor of the resonator can be calculated based on the coupling coefficient, k , and total attenuation of the resonator, α :

$$Q_L = \frac{n\pi}{\sqrt{1 - k^2}e^{-\alpha}} \sqrt{\frac{1 + (1 - k^2)e^{-2\alpha}}{2}} \quad (4-19)$$

α and k are obtained by the expressions given in [135]. Interestingly, the calculated k for the mode WGH_{900} is approximately 0.94, which is close to critical coupling value. The calculated loaded quality factor for this mode is approximately 1100. Therefore, the unloaded Q-factor is $Q_0 = Q_L(1 + k) = 2134$.

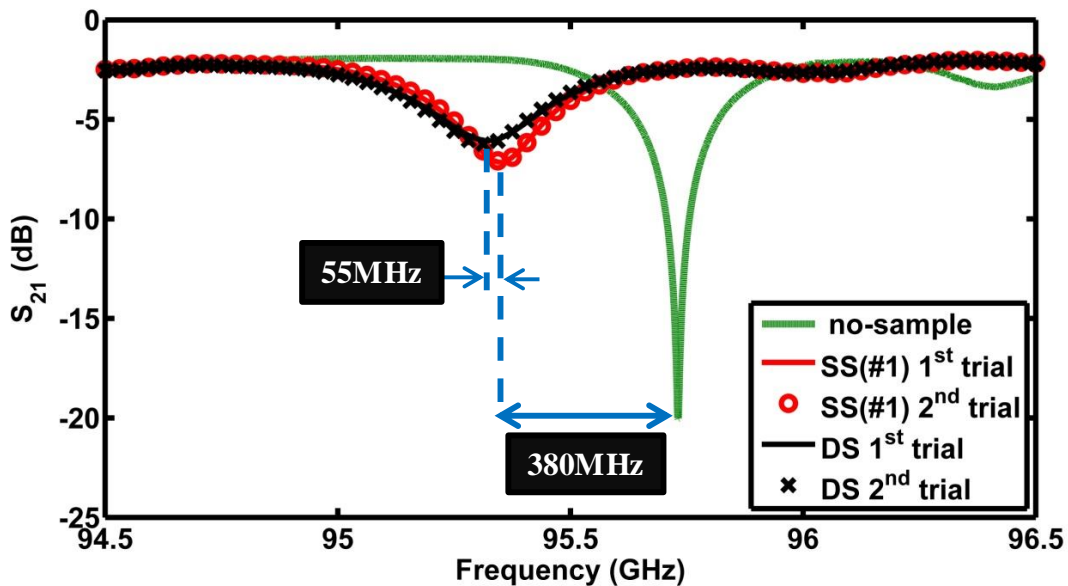


Fig. 4.15: The measured resonance frequency shifts for single-stranded (SS) and double-stranded (DS) DNA samples on SOI technology. The repeatability is validated for each sample.

In order to coat the DDR with DNA, approximately 10 μl of the oligonucleotide in annealed buffer is pipetted on the top surface of the DDR. The liquid is evaporated, resulting in a thin layer (~ 250 nm) of DNA. The DNA samples can be modeled as a thin dielectric layer, with specific permittivity, placed on top of the DDR [100]. In the first set of experiments, two DNA oligonucleotides of the same length but with different base pair order are used. Fig. 4.15 shows changes in the resonance frequency of the transmission response after loading the DDR with oligo #1. A 380 MHz resonance frequency shift is achieved. The same measurement procedure is followed for oligo #2, resulting in a 390 MHz shift. These results describe a distinct 10 MHz difference in resonance frequency shift for the two DNA oligos. To ensure repeatability, multiple trials of each test are conducted. After each measurement, the resonator is completely washed using distilled water. The resonance frequency and its depth are re-checked with the reference point before evaluating the subsequent DNA sample.

Next, the author evaluated the ability to distinguish between single and double-stranded DNA. Equimolar amounts of the double-stranded DNA resulting from the annealing of oligo#1 and oligo#2 are placed on top of the DDR and the changes in the transmission response are recorded. For comparison, the results obtained from double-stranded DNA is

overlaid on the results of single-stranded DNA (refer to Fig. 4.15). A significantly higher 55 MHz shift in the resonance frequency is achieved. This was expected as double-stranded DNA has higher equivalent permittivity compare to single-stranded DNA. Also, a stronger damping, which is related to lower Q-factor, is noticed in the resonance frequency for the double-stranded DNA. This is due to the fact that double-stranded DNA has higher absorption loss.

4.6 SOG Bio-Sensor

In this section a new innovative WGM sensor based on the Silicon on Corrugated Glass technology, which was introduced in Section 2.2.2, is developed and implemented [52]. The proposed sensor is shown in Fig. 4.16. The structure consists of a dielectric rectangular waveguide, tapered at the ends, coupled to a DDR, placed on a small round Glass membrane. Due to the field confinement close to the circumference of the DDR, the membrane does not perturb the field. The dielectric waveguide is designed for dominant E_y^{11} mode. The detail design parameters and modal analysis of the straight waveguide segment were discussed in Section 2.2.2. Since E_y^{11} is vertically polarized, the resonator is designed such that it operates in WGH mode, in which the magnetic field is mainly in a transverse direction.

Applying the EDC-DWM technique, the suspended dielectric resonator can be formulated in terms of the radial and the axial dispersion equations. The radial dispersion equation for a disc with $r=a$, is the same as (4-4) . The resonator in vertical direction can be considered as a suspended disc. Consequently, the axial dispersion equation for a symmetric slab waveguide in TM_y mode can be written as:

$$\tan(k_y h) = \epsilon_{r1} \frac{2k_y h \alpha_y}{k_y^2 - \epsilon_{r1} \alpha_y^2} \quad (4-20)$$

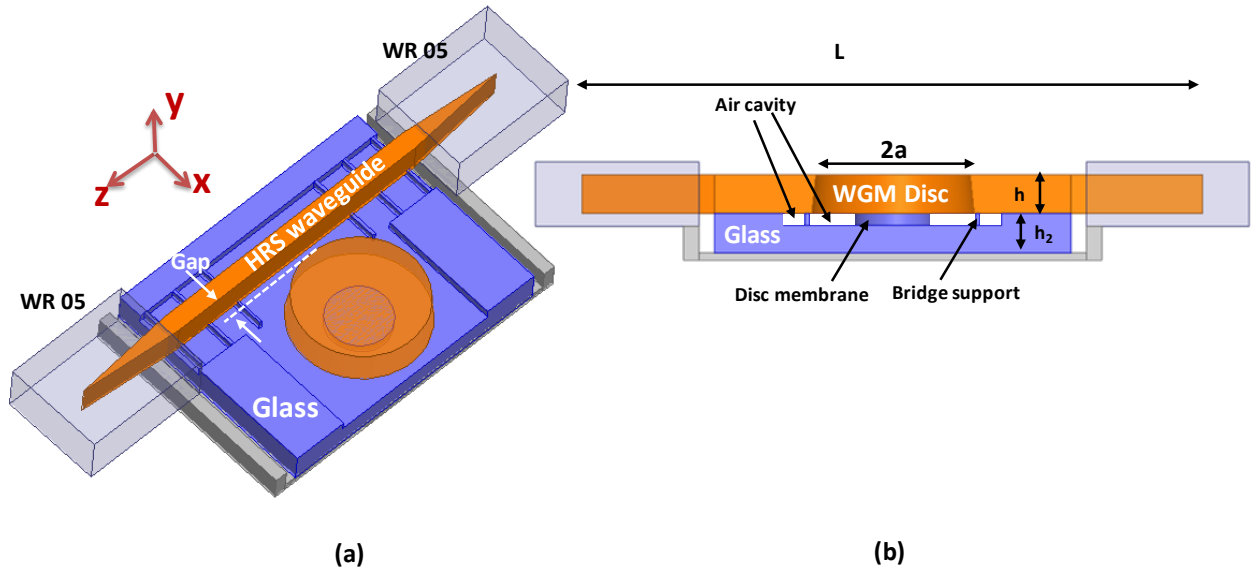


Fig. 4.16: The general configuration of the proposed Silicon on Corrugated Glass sensor.

The WGM resonance frequencies of the SOG disc resonator are calculated by solving the axial and radial dispersion equations, simultaneously, using the efficient algorithm, which was explained before. The initial design parameters of the SOG sensor is optimized and re-tuned using the full-wave simulation. The design parameter values, for operating over G-band frequency range (140-220 GHz), are listed in Table 4.4. The radius of the resonator is primarily determined such that the minimum mode number of WGM is larger than 6 over the desired range of frequency. The simulated S-parameters of the final structure are plotted in Fig. 4.17. Four distinct resonance modes are observed in this figure.

Table 4.4. The design parameter values for the SOG sensor.

Parameter	L	h	h_2	a	W	Gap
(mm)	16	0.5	0.5	0.9	0.3	0.16

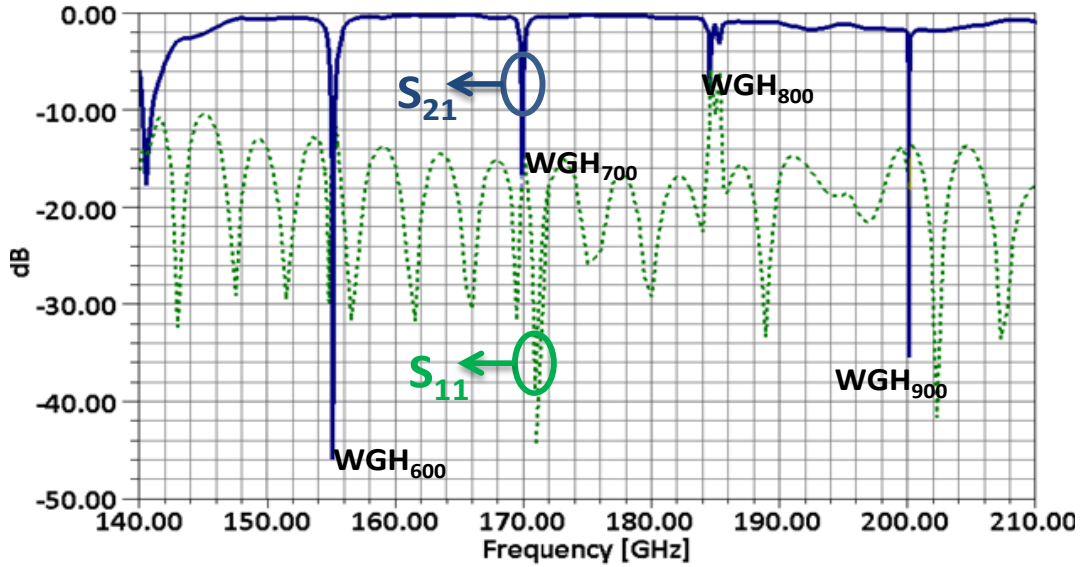


Fig. 4.17: The simulated S-parameters of SOG disc resonator coupled to the dielectric waveguide at G-Band [52].

Two types of resonator structures are fabricated using the DRIE technique, and tested over the G-band; 1) a dielectric waveguide, coupled to a DDR, and 2) a dielectric waveguide, coupled to a ring resonator. The radius of the ring resonator is the same as the disc resonator and its inner radius is 400 μm . The side-wall of the disc resonator is tilted 2 degrees, with the respect to the vertical axis, after the fabrication process. The sample structures, placed on a customized aluminum fixture, are measured using the test setup, which is shown in Fig. 4.18.

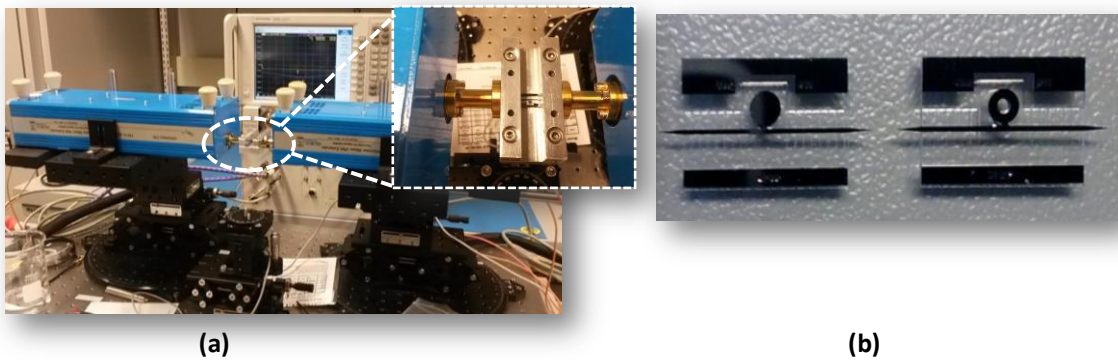


Fig. 4.18: (a) The measurement setup, and (b) two SOG dielectric waveguide structures under test: dielectric waveguide coupled to WGM disc resonator, and dielectric waveguide coupled to WGM ring resonator.

The measured S-parameters of the two resonator structures are plotted in Fig. 4.19. As can be seen, the ring resonator modes behave as travelling waves. Furthermore, the main advantages of the ring resonator compared to the disc resonator are to suppress the potential unwanted modes. The obtained measurement result for the disc resonator shows higher loss than the simulation one. This discrepancy was explained in Section 2.2.2.

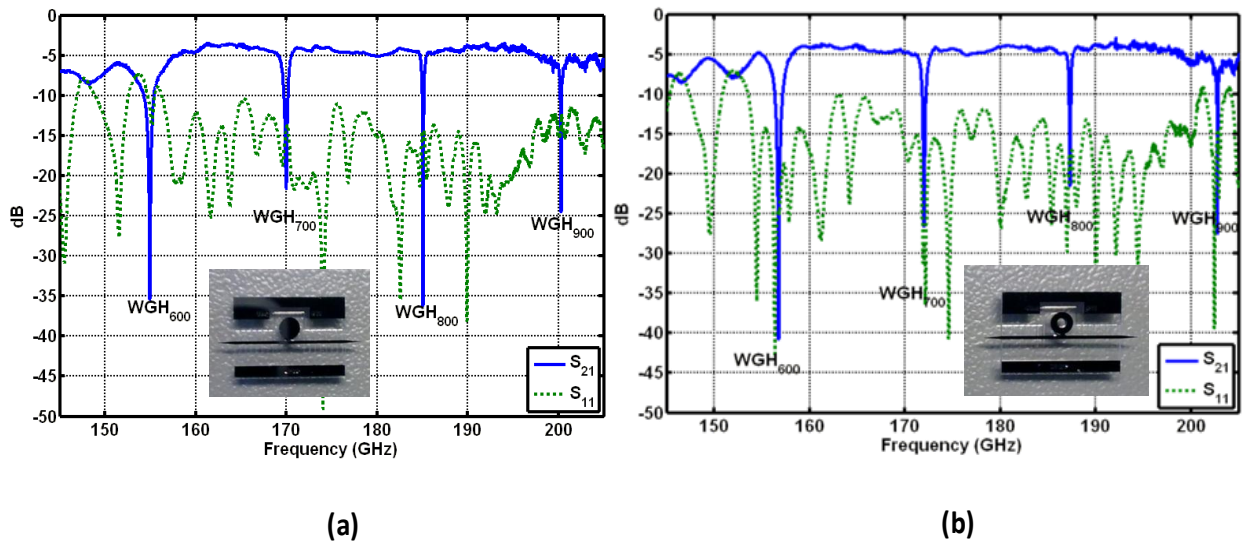


Fig. 4.19: The measured S-parameters of (a) the disc resonator on SOG technology over G-band, and (b) the ring resonator on SOG technology over G-band [52].

4.6.1 DNA Sensing

The implemented SOG disc resonator structure is used for DNA sensing. All the measurement steps and sample preparation are the same as the previous DNA experiments, conducted on alumina and SOI sensors. The complementary 39 base pair synthetic oligonucleotides, single-stranded DNA molecules, were obtained from Sigma Genosys Canada.

Oligo #1:5`- GCA GTG TTT TGT ATG TGC TGC GTG CTT TCA GCA GTT TCC-3`

Oligo #2:5`-GGA AAA CTG CTG AAA GCA CGC AGC ACA TAC AAA ACA CTG-3`

As before, the individual oligonucleotides used for single-stranded DNA tests were denatured at 95°C for 3 minutes in annealing buffer, and then rapidly cooled on ice. A double-stranded DNA was generated by combining oligonucleotide 1 and 2 at equimolar concentration. The samples were denatured at 95°C for 3 minutes in a heat block. The block

was then allowed to cool to room temperature over one hour. Annealed oligos were stored on ice. Single- and double- stranded oligos were tested at almost equal molar concentrations, 22 nmol.

Approximately 2 μ l of the oligonucleotide in annealed buffer is pipetted onto the top surface of the DDR for covering the DDR completely. The buffer liquid is evaporated and a uniform thin layer of DNA is formed. In the first set of experiments, two DNA oligonucleotides, in forward and reverse DNA sequencing, of the same length and molarity concentration but with different base pair orders are used.

Fig. 4.20 shows changes in the resonance frequency for three different DNA samples. A 233.75 MHz resonance frequency shift is achieved for oligo #1 (FDNA) sample. Repeating the same measurement procedure for oligo #2 (RDNA) results in a 250 MHz shift in the resonance frequency. The difference between two resonance frequency shifts of DNA oligos are >16 MHz. All the experiments are repeated a few times, after washing the resonator with distilled water in each test.

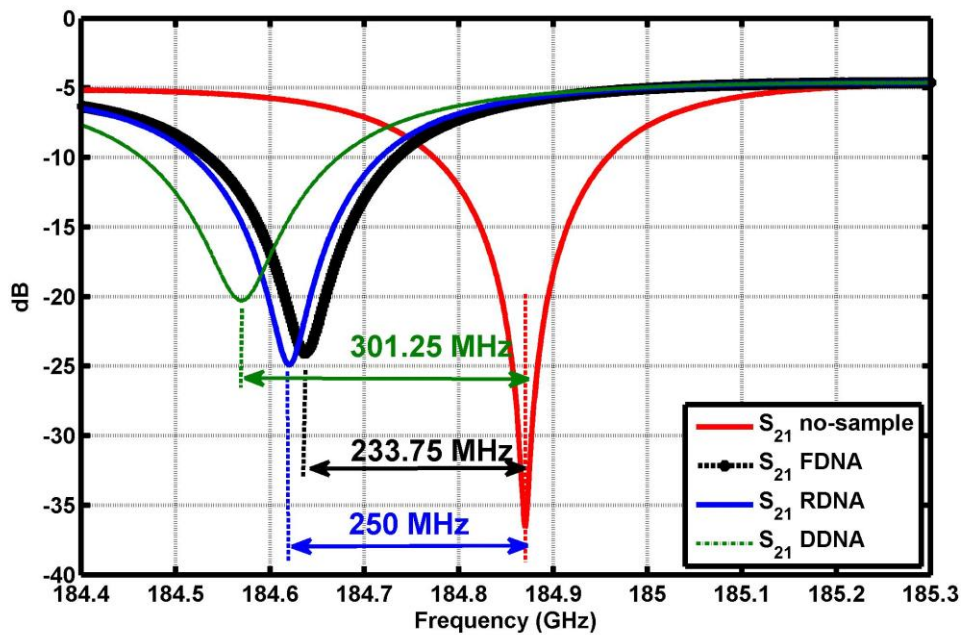


Fig. 4.20: The measured resonance frequency shifts for single-stranded oligos, Forward (FDNA) and Reverse (RDNA) samples, along with the result for double-stranded (DDNA) samples on SOG technology.

In the last experiment, an equimolar amount of the double-stranded DNA, which is achieved by annealing the forward and reverse oligos, is tested. The measured results are plotted in Fig. 4.20. There is a distinct 67.5 MHz difference between the resonance frequency shifts of double-stranded sample and forward oligo. The difference between the resonance frequencies of double-stranded sample and reverse oligo is 51.25 MHz. All the aforementioned experiments are repeated five times for verifying the repeatability of the sensor. The statistical results, which demonstrate the variation of resonance frequencies for each sample, are shown in Fig. 4.21.

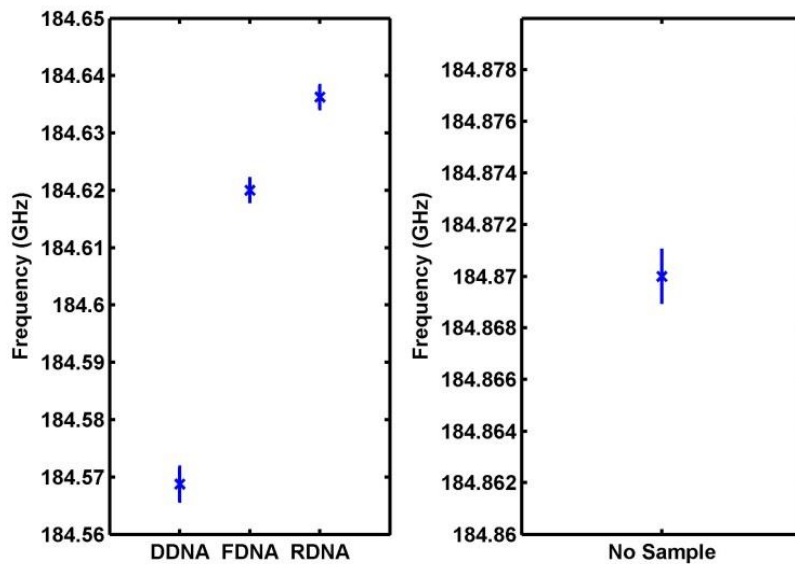


Fig. 4.21: Resonance frequency error analysis of the SOG sensor, used for sensing different DNA samples. Each test was repeated five times.

4.7 SIG WGM Resonance Structures

The SIG technology is used for implementation of two WGM-based resonance structures over the range of 110-170 GHz. The EDC-DWM method, explained in Section 4.2, is employed for initial design and analysis of the image disc resonator. Then the complete structure, consisting of the DDR coupled to the image guide, is optimized using the full-wave simulation. The resonance structures, as shown in Fig. 4.22, are realized either by a straight waveguide or curved waveguide segments, coupled to a WGM resonator. In the previously introduced alumina image guide-based sensor; the waveguide and the resonator were fabricated separately. Then, they were manually placed at the desired coupling distance.

However, the response of the system was strongly influenced by inaccurate positioning of the DDR. To solve this problem, the monolithic SIG resonance structures are realized by means of supporting beams, as it is shown in Fig. 4.22. The main usage of the supporting beam is to position the resonator at the desired distance from the waveguide, leading to a stable resonance behavior of the structures.

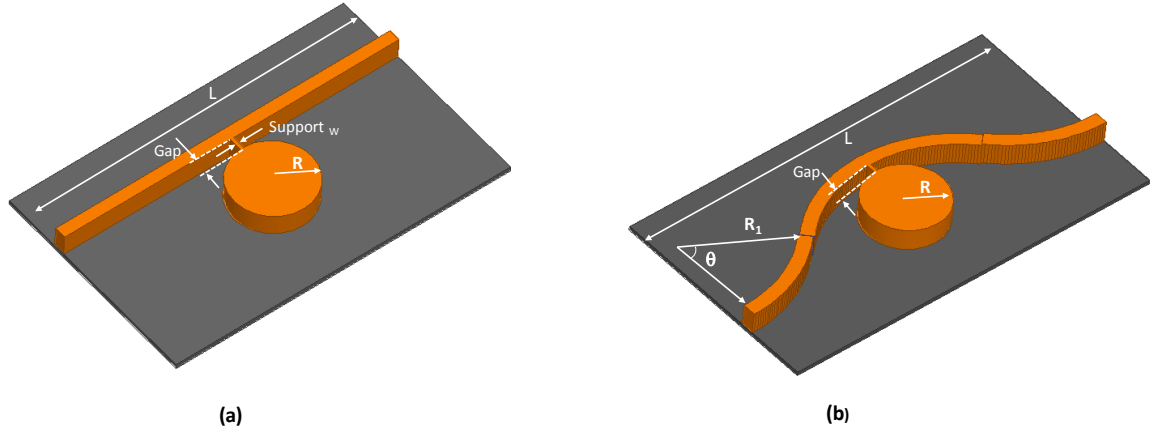


Fig. 4.22: The general configurations of SIG WGM resonance structures, implemented (a) by a straight waveguide segment, or (b) by a curved waveguide segment.

The simplest WGM resonance configuration is the one realized by a straight waveguide segment (refer to Fig. 4.22(a)). The straight waveguide segment has the same cross section dimension as the one described in Section 2.1. The effects of the gap and the radius, on the resonance characteristics, are investigated. Fig. 4.23 (a) shows the S_{21} of the resonator, which has a radius of $930 \mu\text{m}$ and the $Gap=220 \mu\text{m}$. Additionally, Fig. 4.23(b) and Fig. 4.23(c) demonstrate the effects of the radius and the gap on the resonance frequencies of the WGH_{500} and WGH_{600} modes, respectively. In all cases the support beams have a width of $30 \mu\text{m}$. For the sake of simplicity and in order to reduce the simulation time, the tapering sections are removed and the ground plane is considered as a perfect conductor.

A WGM-based resonance structure, with $R=920 \mu\text{m}$ and $Gap=220 \mu\text{m}$, is fabricated using the developed laser machining process (refer to Fig. 4.24(a)). The sample resonator is tested over a customized aluminum fixture, and the measured results are plotted in Fig. 4.24(b). A

small shift less than 1 GHz is observed in the resonance frequencies. That is mainly due to the fabrication imperfections and uncertainty about the dielectric constant of silicon.

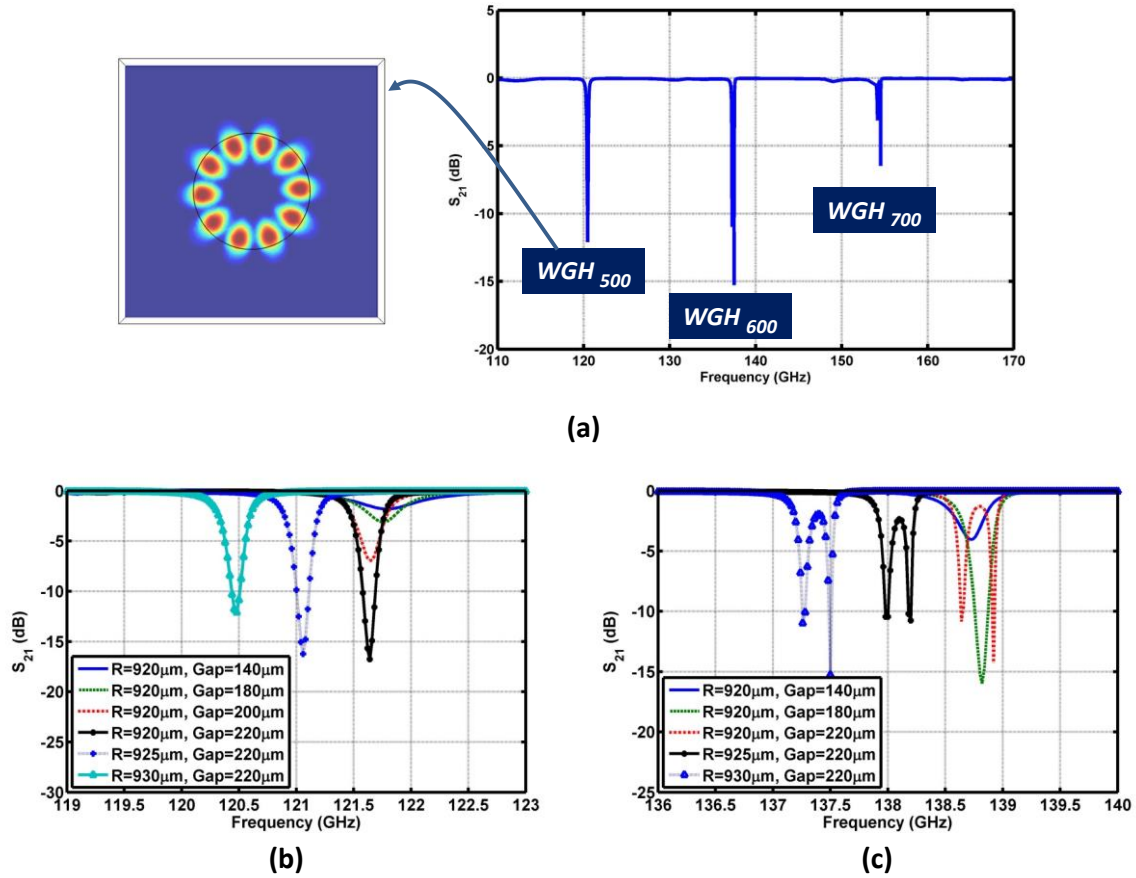


Fig. 4.23: (a) The simulated transmission response (S_{21}) of the straight SIG resonance structure ($R=930\mu\text{m}$, $Gap=220\mu\text{m}$). The effects of the Gap and R on the resonance frequencies of (b) the WGH_{500} mode, and (c) the WGH_{600} mode.

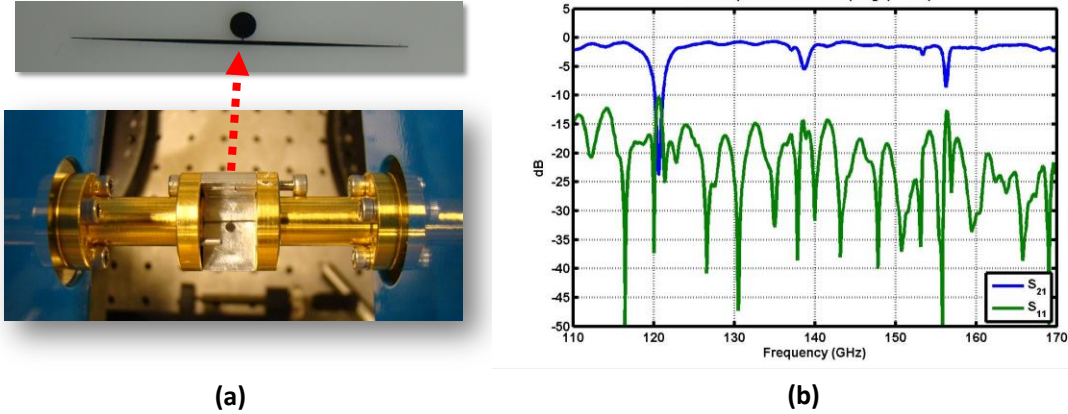


Fig. 4.24: (a) The laser machined SIG WGM structure. (b) The measured S-parameters for the resonator with $R=920 \mu\text{m}$ and $Gap=220 \mu\text{m}$.

4.7.1 SIG WGM Resonator in a Curved Configuration

The simulated and measured results show that the SIG structure potentially supports the unwanted modes. One way to suppress the unwanted modes is to increase the length of the coupling region. The simplest idea is to use a curved waveguides surrounding the resonator, as it is shown in Fig. 4.22(b). Fig. 4.25 shows the S_{21} plots for the curved structure with the $Gap=200 \mu\text{m}$ and for two different resonator radii, $R=930 \mu\text{m}$ and $R=940 \mu\text{m}$. Three distinct WGM resonance frequencies are observed. The measured data shows that the curved configuration results in higher resonance frequencies in comparison to the straight waveguide configuration with identical resonator.

Fig. 4.25(b) and Fig. 4.25(c) illustrate the effects of gap and the radius on the resonance frequencies for the WGH_{500} and WGH_{600} modes, respectively. Three samples with different Gaps and radii are fabricated using the laser machining process. All the structures include four bends with $R_f=3 \text{ mm}$ and $\theta=45^\circ$. The measured results are plotted in Fig. 4.26(b). It is observed that, as compared to the straight waveguide segment, the unwanted modes are significantly less excited in the curved structure.

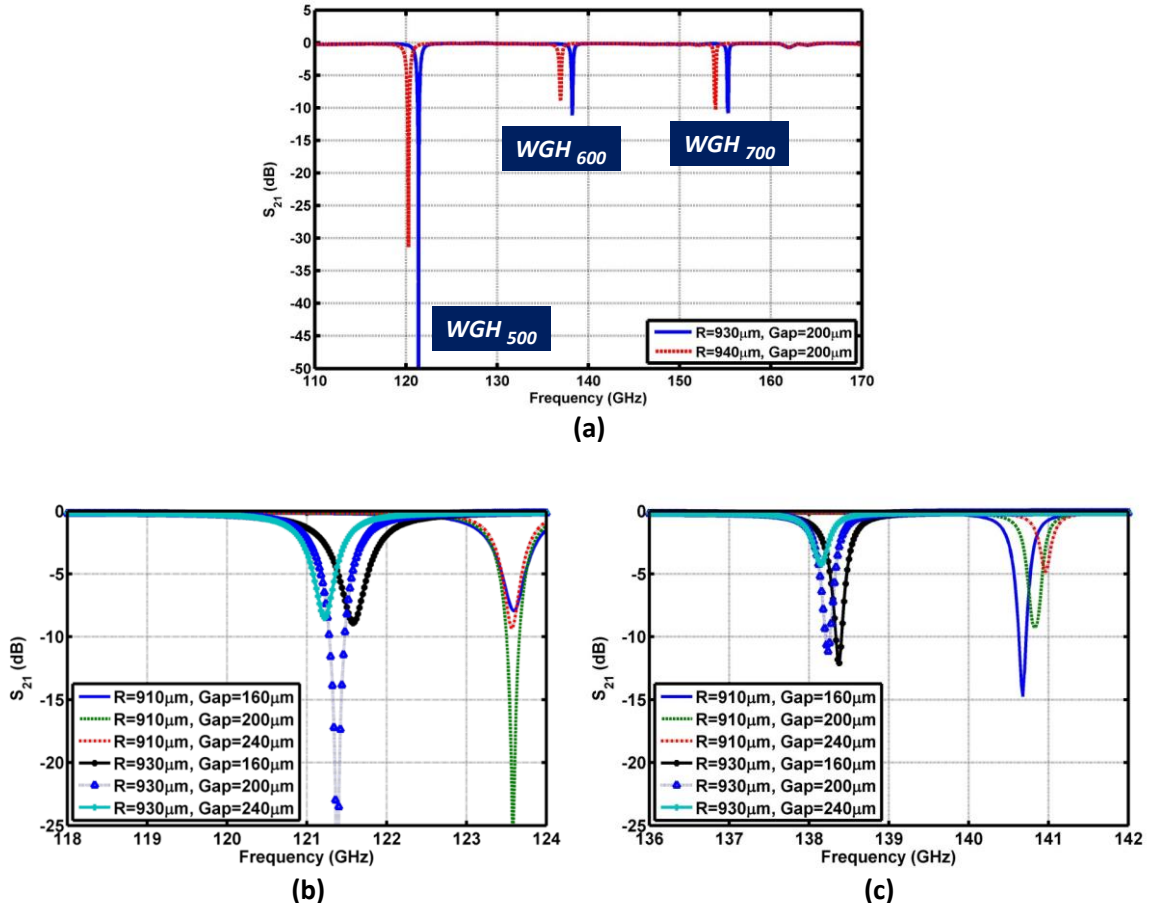


Fig. 4.25: (a) The simulated transmission response (S_{21}) of the curved SIG resonance structure with $Gap=200 \mu\text{m}$ and two radii of $R=930 \mu\text{m}$ and $R=940 \mu\text{m}$. The effects of the Gap and R on the resonance frequencies of (b) the WGH_{500} mode, and (c) the WGH_{600} mode.

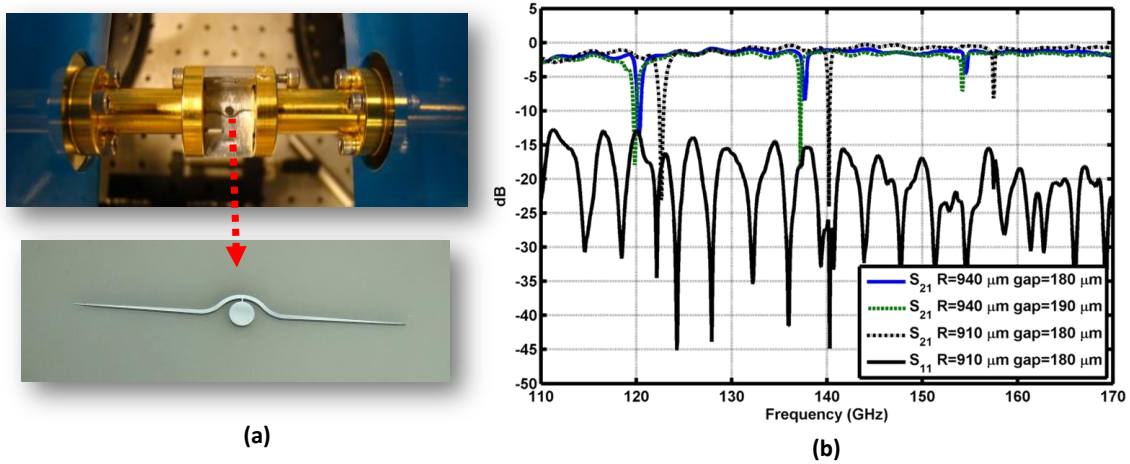


Fig. 4.26: (a) The laser machined curved SIG structure. (b) The measured S-parameters for three different resonators.

4.8 Conclusion

In this chapter, a fast and efficient analysis method, based on the EDC-DWM technique, for finding the resonance frequencies of the WGMs was presented. The alumina WGM structure was employed for two important sensing applications: glucose and DNA sensing. The measurement results showed the capability of the alumina sensor in distinguishing two different single-stranded DNA oligos.

Then, SOG technology was used for design and realization of two WGM resonance structures, at the mmWave/THz range of frequencies (G-Band), where the DNA molecule shows a stronger inter-molecular vibration. Two types of SOG WGM structures, disc and ring resonators, were fabricated and tested. The sample SOG and SOI WGM resonators were tested for DNA sensing. The experiments demonstrated successful differentiation between the reverse-stranded, forward-stranded, and double-stranded DNA samples. The last section of the chapter introduced two configurations of WGM structures on the SIG technology. The introduced resonance structures are monolithic and a high degree of positional accuracy can be realized by means of narrow support beams.

Chapter 5

Silicon-Based Waveguide Devices

Up to this point, two major silicon-based technologies, SIG and SOG, were introduced, and studied. Also, a variety of essential silicon waveguide passive components such as bend, divider, antenna and coupler were discussed in Chapter 3. In Chapter 4, the WGM resonance structures for sensing applications were investigated and a number of prototypes based on various technologies were tested.

The low-loss HRS technologies, SIG and SOG, provide effective solutions for high performance and integrated devices in the sub-mmWave/THz ranges. The proposed silicon waveguide technologies are especially useful to tackle the packaging issues. This chapter, first, introduces two essential mmWave components, tunable resonator and phase shifter. The principle concepts, simulation results, and experimental results are presented. Then, the SIG technology is employed in more complicated configuration for realization of an integrated butler matrix system for beam forming at the mmWave/THz range of frequencies.

Finally, a novel idea is utilized for controlling the resonance behavior of a WGM-based structure, using optical signal.

5.1 Tunable WGM Resonance Structures

Tunable devices, such as tunable filters, add an extra functionality to mmWave system for applications such as electronic scanning radar and intelligent transceivers. Various approaches are utilized for realizing the tunable filters, while each technique has its own advantages and disadvantages. Varactor and Micro-Electro-Mechanical Switches (MEMS) have been widely used for implementing tunable filters in the microwave range [136], [137], [138]. However, these switches often introduce considerable insertion loss in the RF signal path. Voltage tunable materials such as Ferroelectric have shown great potential to realize tunable resonance structures [136]. But, nonlinearity and loss are the main drawbacks of these materials. Also, they can not offer wide tunability. Tunable evanescent mode cavity is another approach for adjusting the resonance frequency [139], [138]. These cavities present high Q-factor resonances, but they are bulky devices. Wide tuning capability of resonance-based structures is very important for reducing the complexity and enhancing the

performance of almost any system. As it was shown in the previous chapter, WGM resonances are highly sensitive to perturbations due to the changes in the physical condition of the surrounding media of the resonator. The tunability of the WGM-based structure has been studied in optics by adjusting the coupling factor which alters the bandwidth and depth of resonance [140], [141]. In this section, a novel approach is introduced for implementing tunable WGM-based resonance structures at the mmWave/THz range of frequencies. The resonance frequencies of the structures are tuned by perturbing the WGM fields of the resonator, using metallic structures. As a proof-of-concept this idea is tested using a micro-positioner. Two WGM-based structures, previously designed in this research, are utilized for implementing the tunable resonators: alumina WGM image guide structure (Section 4.4), and SOG WGM structure (Section 4.6). Alumina WGM structure, which operates at D-band (110-170 GHz), is tuned by a narrow metallic bar, moving in a direction perpendicular to the axis of the WGM resonator. On the other hand, SOG WGM structure, which operates at the G-band (140-220 GHz), is tuned by a metallic cylinder which moves vertically (in a direction parallel to the axis of the WGM resonator). For proof of concept, the designed tunable SOG resonator is designed and tested at the specific range of frequencies with the specific tuning parameters. The same idea can be applied to the entire mmWave/THz range of frequencies.

5.1.1 Alumina-Based Tunable Image WGM Filter

The first tunable structure is an image guide WGM structure made of alumina [142]. The introduced WGM resonator supports *WGH* modes. Fig. 5.1(a) illustrates the proposed tuning mechanism for the image alumina waveguide configuration. A narrow metallic bar, with 1 mm width, is employed to perturb the WGM field and to shift the resonance frequency. The bar is placed 50 μm above the disc resonator and slides horizontally in x -direction over the disc resonator. The total movement of the metallic bar is 200 μm . Indeed, the metallic bar moves between the centre and the edge of the DDR in certain offset steps.

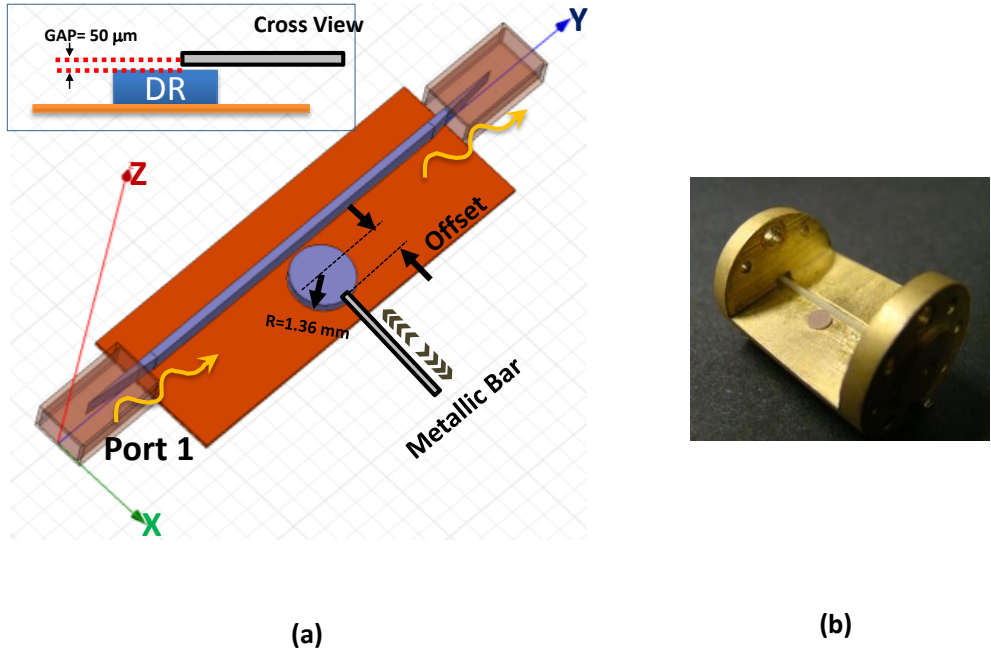


Fig. 5.1: (a) The general configuration of the proposed tunable alumina WGM resonance structure. (b) The fabricated prototype alumina WGM structure [142].

The designed structure is simulated using a full-wave HFSS simulator. The simulated S_{21} versus frequency for WGH_{700} mode and for different offset values are plotted in Fig. 5.2. The results show 100 MHz tunability. Wider range of tunability can be obtained by reducing the gap between the metallic bar and the resonators, with the price of higher loss.

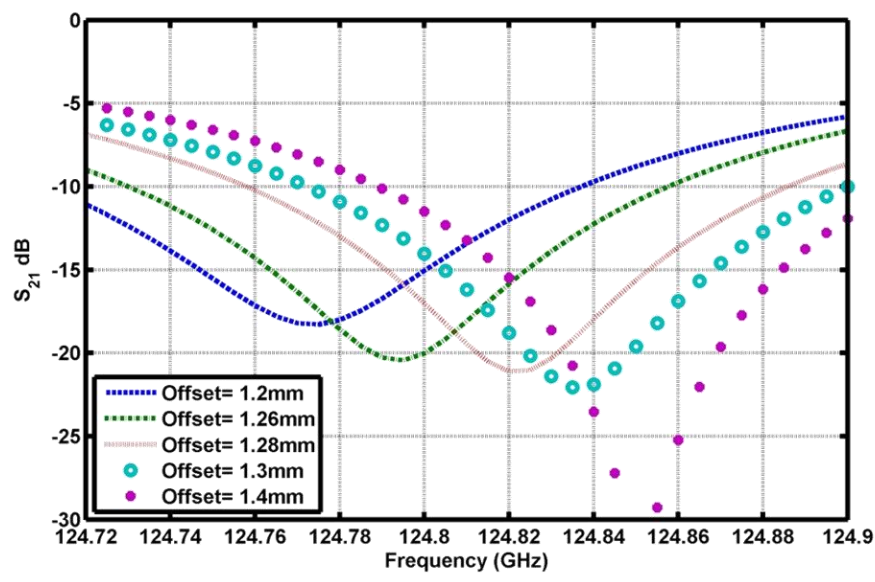


Fig. 5.2: The simulated effect of the metallic bar on the resonance frequency.

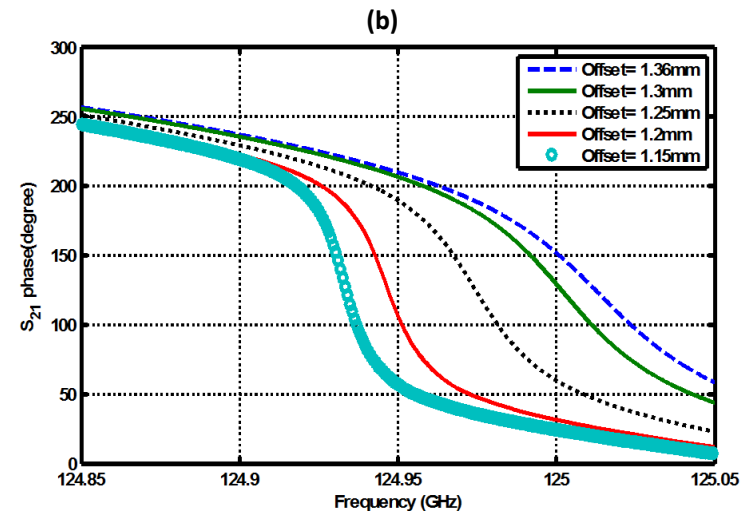
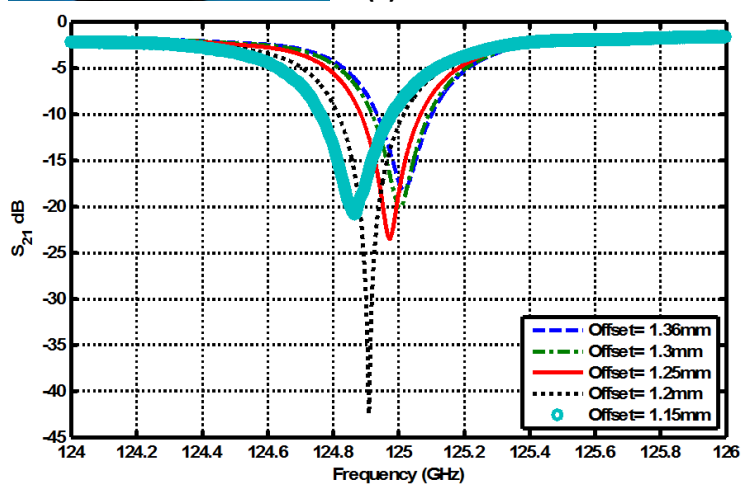
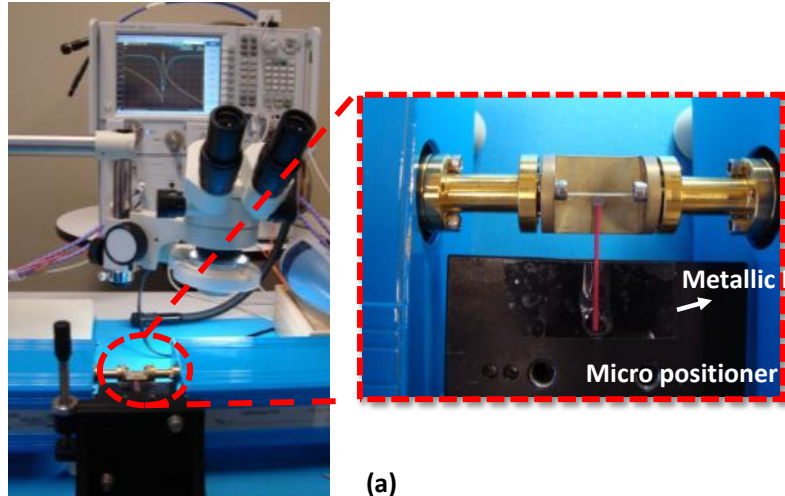


Fig. 5.3: (a) The measurement setup for the alumina WGM tunable structure. The measured effects of the metallic bar position on (b) the resonance frequency of the system, and (c) the S_{21} phase [142].

As a proof-of concept, a measurement setup as shown in Fig. 5.3(a), is used. A manual micro-positioner is used for changing the position of the metallic bar relative to the centre of the resonator. The experimental data are plotted in Fig. 5.3(b) and Fig. 5.3(c). A 140 MHz tunability is accomplished. Also, a maximum phase shift of 150° is achieved at 124.95 GHz. The resonance structure can act as a tunable band-stop filter.

5.1.2 Tunable SOG WGM Resonator

The next tunable resonance structure, as illustrated in Fig. 5.4. [142], is based on the novel SOG WGM structure (Section 4.6). In order to perturb the WGM field more effectively, a metallic cylinder (tuner), with the same diameter as the disc resonator ($a=0.8$ mm), is placed on top of the resonator and moves vertically up and down. The tuner perturbs the field inside and outside the resonator.

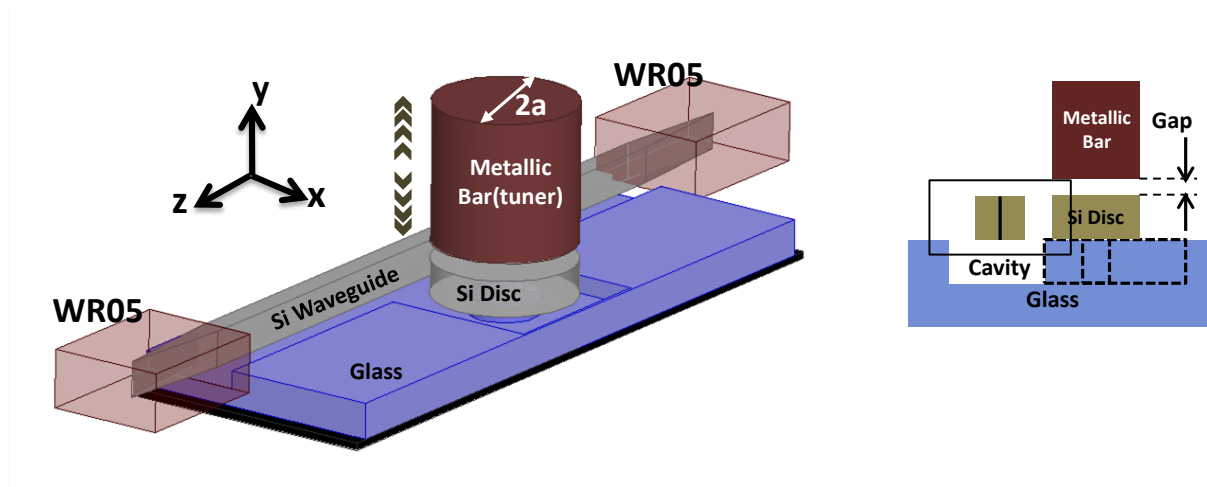
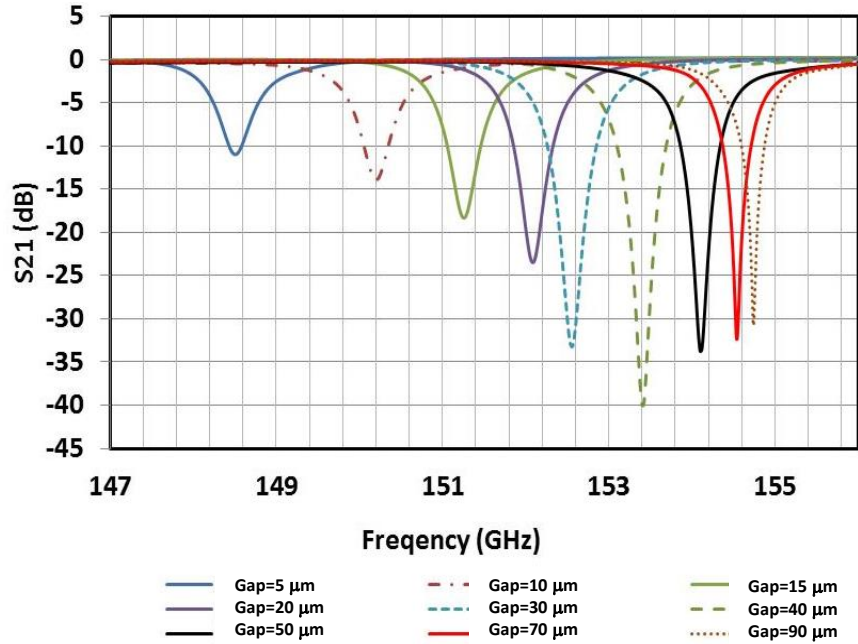
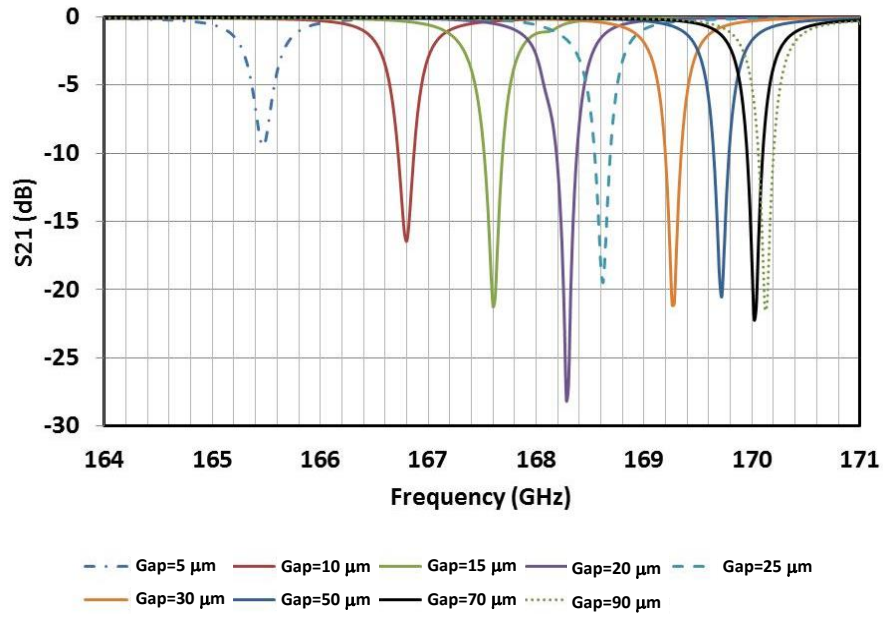


Fig. 5.4: The general configuration of the proposed tunable SOG-based resonance structure [142].

Changing the gap does not affect the mode numbers of WGM fields. However, the gap changes the resonance depth and the resonance frequency. Fig. 5.5(a) shows the simulation results of the S_{21} at WGH_{600} resonance frequency, when the air gap changes from 5 to 90 μm . By decreasing the gap, the system approaches critical coupling. Moreover, the resonance frequency shifts down by moving the tuner closer to the resonator. The simulation results show almost 6 GHz tunability for WGH_{600} resonance. A tunability of almost 4 GHz is obtained for WGH_{700} mode (refer to Fig. 5.5(b)).



(a)



(b)

Fig. 5.5: The simulated effect of the metallic cylinder movement on the resonance frequencies of the SOG WGM structure for (a) WGH_{600} mode, and (b) WGH_{700} mode.

5.1.2.1 Measurement Results

A completely in-house developed measurement setup, shown in Fig. 5.6, is used for testing the tunable SOG WGM structure. The extender modules are placed on top of two individual 5-degrees of freedom positioners. The SOG resonance structure is positioned between the outputs of the extender modules. A metallic cylinder moves up and down on top of the resonator, using an accurate 6-degrees of freedom micro-positioner.

The system is tested at two different WGM modes; WGH_{600} and WGH_{700} . The movement of the metallic cylinder is realized by a manual micro-positioner. The results of resonance frequency shifts, for different *Gap* values at WGH_{600} and WGH_{700} resonances are plotted in Fig. 5.7. In both cases, it is difficult to determine the real gap between the metallic cylinder and the resonator for the zero-state, in which the cylinder is placed at the minimum practical distance to the resonator. Therefore, we consider this starting gap value as ‘*g*’, when $g < 5 \mu\text{m}$. Then, the other next gap steps are accurately determined by micro-positioner.

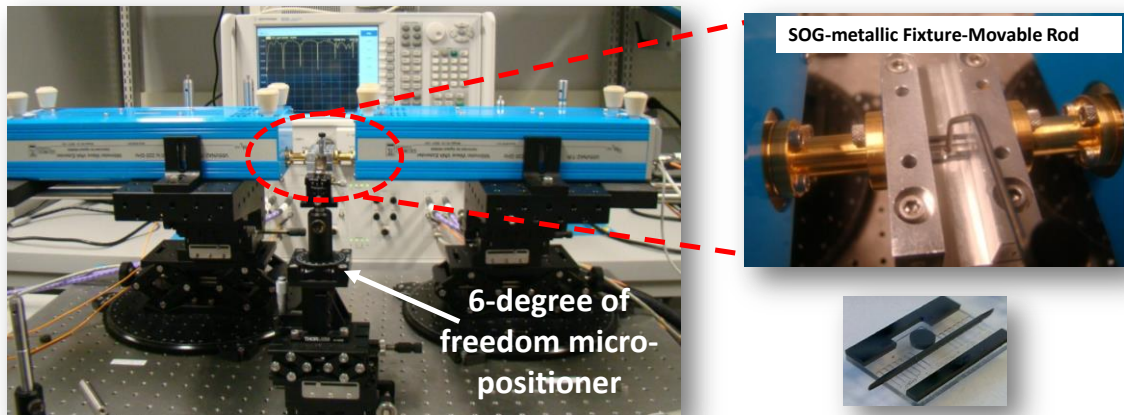


Fig. 5.6: The measurement setup for testing the tunable SOG WGM structure at G-band (140-220 GHz).

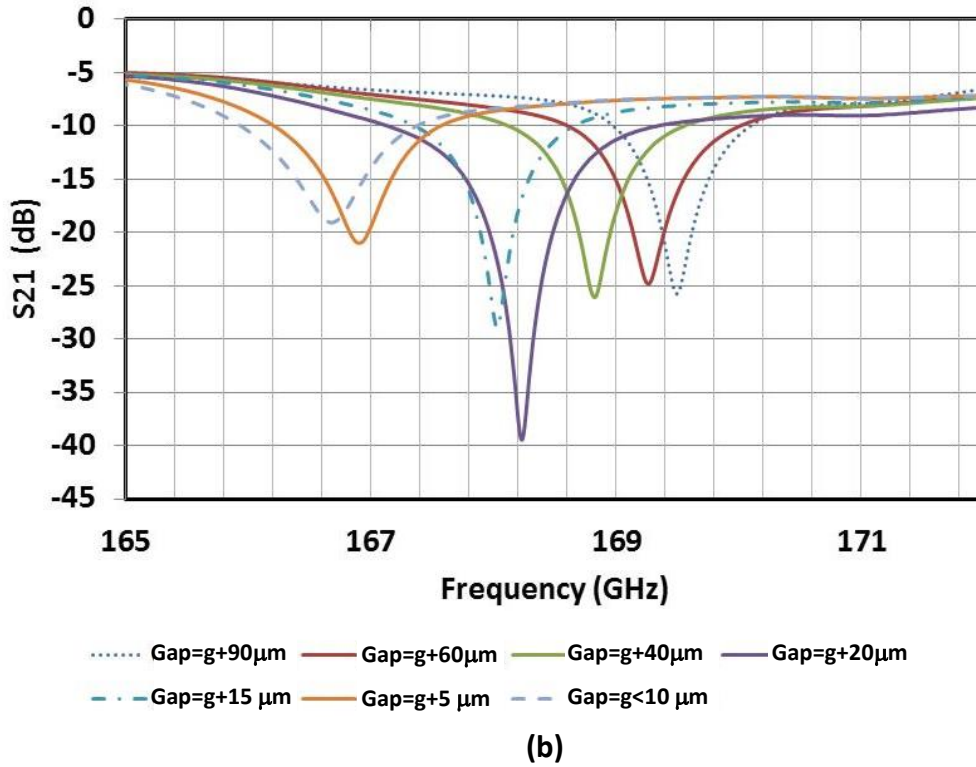
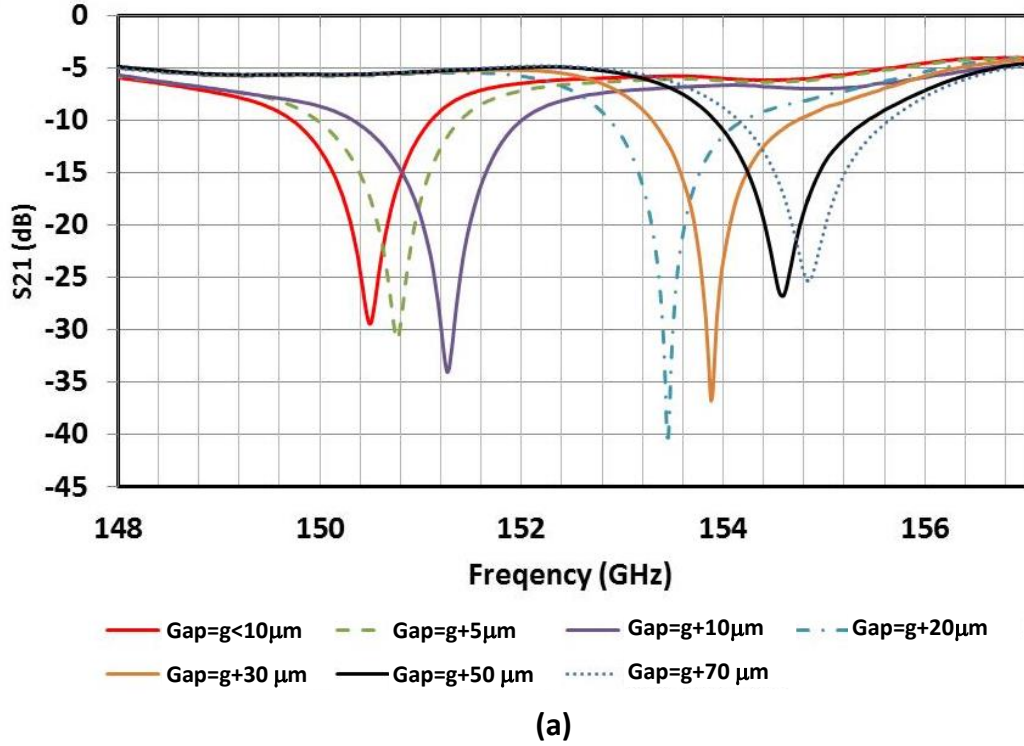


Fig. 5.7: The effect of the metallic cylinder on the measured S_{21} of the tunable SOG WGM structure for (a) WGH_{600} mode, and (b) WGH_{700} mode.

The results show that the tunability of the structure for WGH_{600} and WGH_{700} modes are around 4.5 GHz and 3 GHz, respectively. Since we can not reach the gaps smaller than 5 μm , the measured tunability range is smaller than simulated one.

5.2 Finger-Shaped SOG Phase Shifter

Adjustable phase shifters are required for a wide variety of systems such as smart antenna systems with beam steering capability, measurement equipment, receivers, high data rate optical transceiver front-end, and imaging systems [143], [144]. The key aspects of a desirable phase shifter are low-cost, low-loss, wide bandwidth, low-power consumption, and integration capability. Phase shifters can be broadly classified as active and passive phase shifters. Active phase shifters use active components to compensate for the high insertion loss of the phase shifting elements. The majority of active phase shifters are implemented by advanced semiconductor technologies such as CMOS, SiGe, and GaAs semiconductor devices with/without MEMS structures. Although promising performances have been reported for these types of phase shifter at the mmWave range of frequencies [145], [146], technological limitations make it extremely difficult to extend these techniques to sub-mmWave.

Different passive phase shifting mechanisms, such as variable lumped structures, switched-line architectures, vector modulators, travelling wave structures with tunable loading, reflective types, and materials with tunable parameters such as ferroelectric devices, have been reported. However, these types of phase shifters are prone to a high insertion loss and are relatively large in dimension. Such phase shifters usually exhibit a high loss at mmWave frequencies, e.g. 10 dB at 60 GHz [147]. Liquid Crystal (LC) phase shifters are a new class of phase shifter, which are controlled with voltage, and provide medium insertion loss; however, their responses are slow with high phase-shift dependent insertion loss variation [148].

Decades ago, dielectric waveguides were used in proximity to a mechanically movable metallic sheet to implement the adjustable phase shifters [149], [150], [151]. Recently, in [152] a High-Impedance Surface (HIS) was used to implement a waveguide-based structure for realization of a tunable phase shifter, working up to 110 GHz. However, the HIS still needs to be moved with respect to the waveguide in order to provide the required phase shift.

The results show high insertion loss and low phase shift: $16^\circ/\text{mm}$ at 80 GHz, and the moving mechanism of the HIS seemed to be complex.

Loaded planar transmission line is the basis of another class of tunable phase shifter, in which the traditional planar transmission lines, such as CPW, are loaded by a movable dielectric material on top [153], [154]. This approach is often suitable for lower RF and microwave range of frequencies, where realization of the planar transmission lines is feasible.

The proposed phase shifter in this research, which is called finger-shaped phase shifter and illustrated in Fig 5.8, is essentially a SOG waveguide segment loaded with a moving High Conductivity Silicon (HCS ($\sigma > 10^5 \text{ S.m}^{-1}$)) finger-shaped structure on top. The finger-shaped movable part consists of an array of parallel T-shaped bars and perturbs the modal field of the waveguide. The movable part can be a dielectric material with high dielectric constant. The typical thickness of a movable layer is 300~500 μm . The phase shifter provides a large bandwidth with a reasonable insertion loss, operating at G-band (140-220 GHz).

Typically, the design of a phase shifter is a compromise between the insertion loss and the required phase shift. For maximizing the phase shift for a given insertion loss, extensive simulations were performed to reach an optimized set parameter values. The finger-shaped arms act as a ladder network of series capacitors and shunt inductors. The optimal design parameters are listed in Table 5.1. The gap between the arms and dielectric waveguide is set to 5 μm . The number of arms determines the achievable phase shift range. An example of the structure with 15 arms and the total length of $L_2=3 \text{ mm}$ has been designed, simulated, and optimized. The arms slide in the x -direction from a pre-defined initial state, which is $\Delta x(\text{initial})=-200 \mu\text{m}$.

Table 5.1: Design parameter values for the proposed finger-shaped SOG phase shifter at G-band.

Parameter	Value	Parameter	Value	Parameter	Value
L	16 mm	$finger_h$	500 μm	W_1	170 μm
W	300 μm	$Pitch$	200 μm	W_2	50 μm
L_2	3 mm	Gap	5 μm	L_1	100 μm

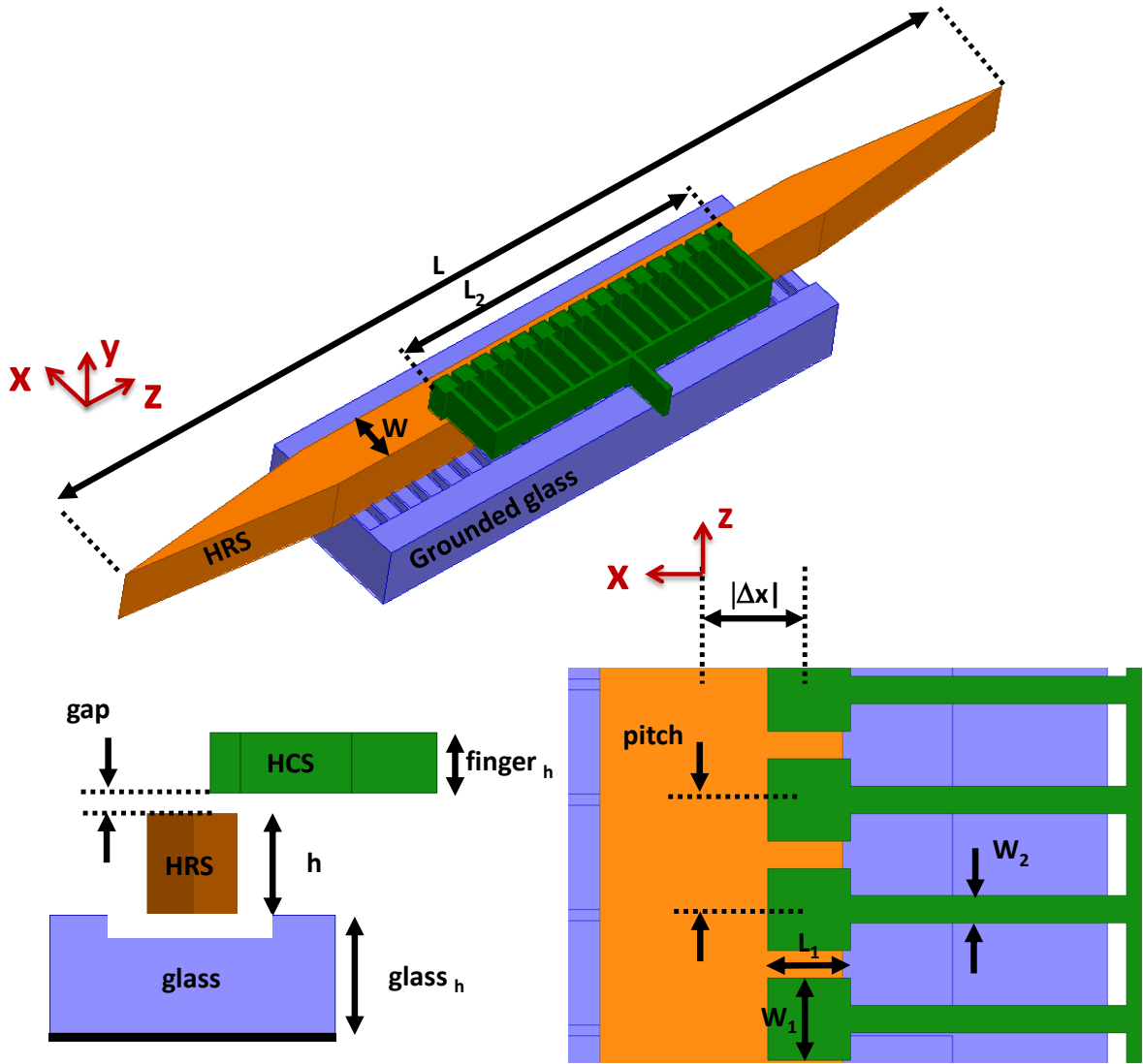


Fig. 5.8: The general configuration of the proposed finger-shaped phase shifter based on the SOG technology.

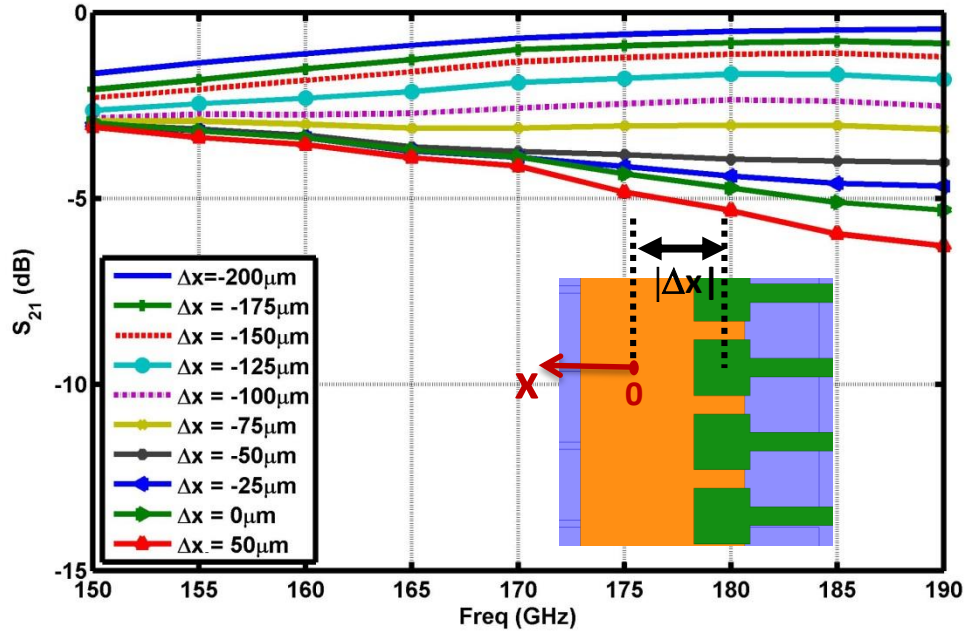


Fig. 5.9: The simulated transmission loss of the finger-shaped phase shifter, with the total length of $L=16$ mm and $L_2=3$ mm.

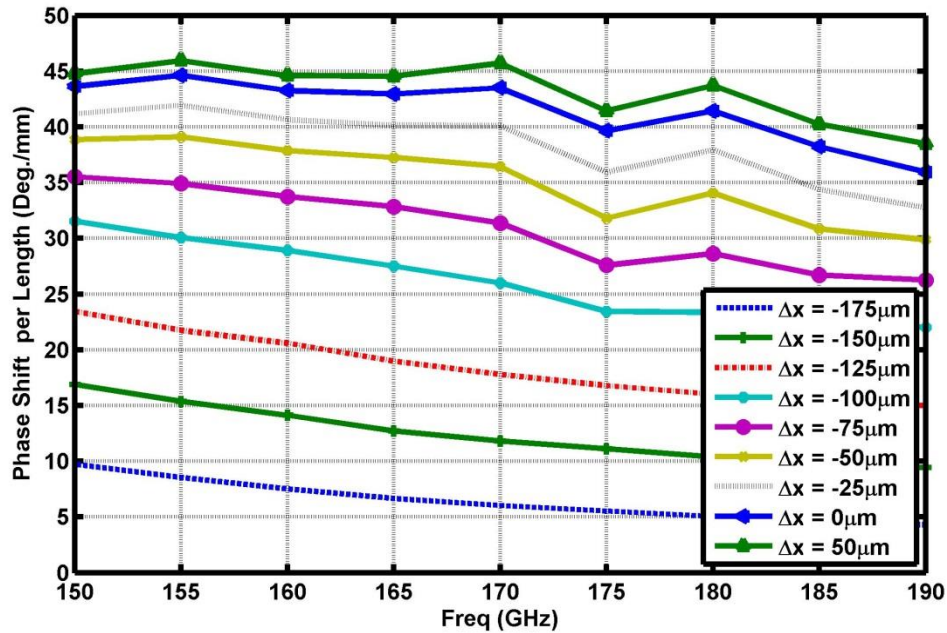


Fig. 5.10: The simulated phase shift of the finger-shaped phase shifter for the total finger structure length of $L_2=3$ mm. The reference phase is defined for the case $\Delta x=-200$ μm .

The simulated total insertion loss of the structure for 250 μm overall movement is shown in Fig. 5.9, for different Δx steps. The total insertion loss of the structure with $L=16$ mm and

$L_2=3$ mm is less than 6 dB, over the range of 150-190 GHz. It is observed that a maximum phase shift of 138 degree (the average of 24.6 degree/ λ) and additional loss of 0.3-1.6 dB/mm are achieved for the designed finger-shaped phase shifter, with the finger structure length of 3 mm, over the range of 150-190 GHz (refer to Fig. 5.10).

5.2.1 Measurement Results

The movable part of the finger-shaped phase shifter is fabricated using the developed laser machining process. The fabricated prototype is shown in Fig. 5.11(a). For proof of the concept, the movable part is attached to a highly accurate micro-positioner, and slides over the previously fabricated SOG straight waveguide segment (see Section 2.2.2). The measured insertion loss and phase shift of the phase shifter, for the finger structure length of 3 mm, are plotted in Fig. 5.12 and Fig. 5.13, respectively.

The measurements show that implemented phase shifter results in maximum of 34 degree/mm phase shift (the average of 15.6 degree/ λ) and additional loss of 0.7-1.7 dB/mm (the average of 1.38 dB/ λ), over the range of 150-190 GHz.

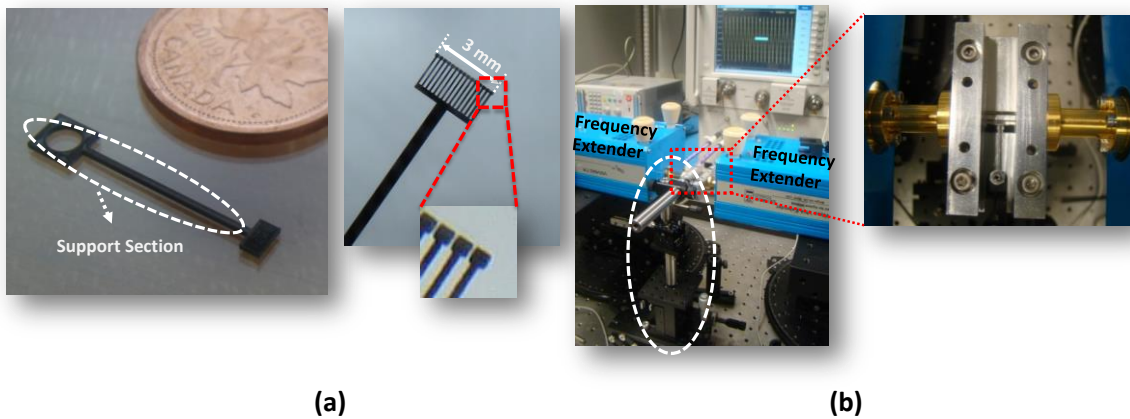


Fig. 5.11: (a) The laser machined movable part of the finger-shaped phase shifter, and (b) the measurement setup.

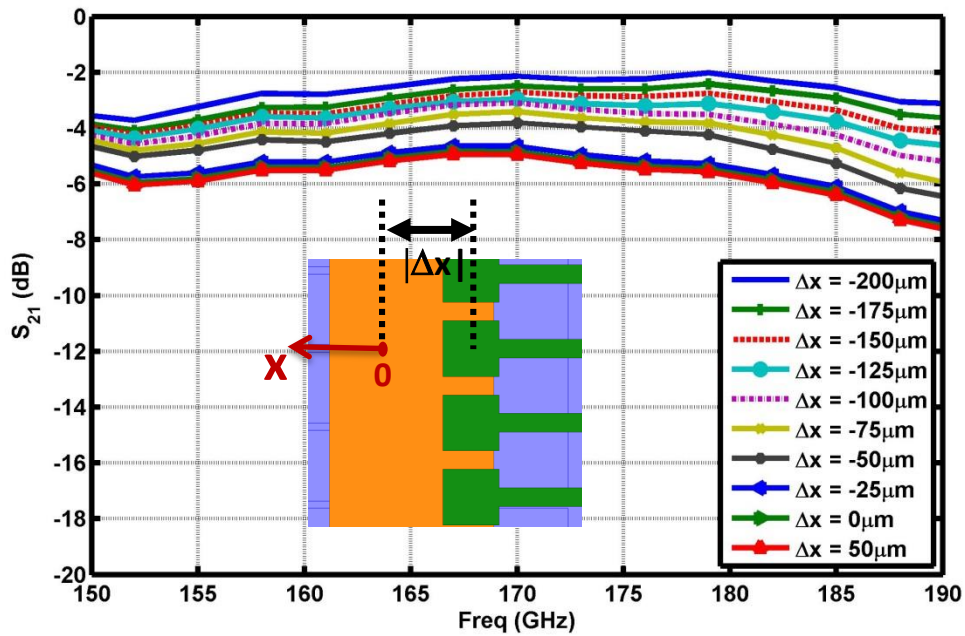


Fig. 5.12: The measured transmission loss of the finger-shaped phase shifter, with the total length of $L=16$ mm and $L_2=3$ mm.

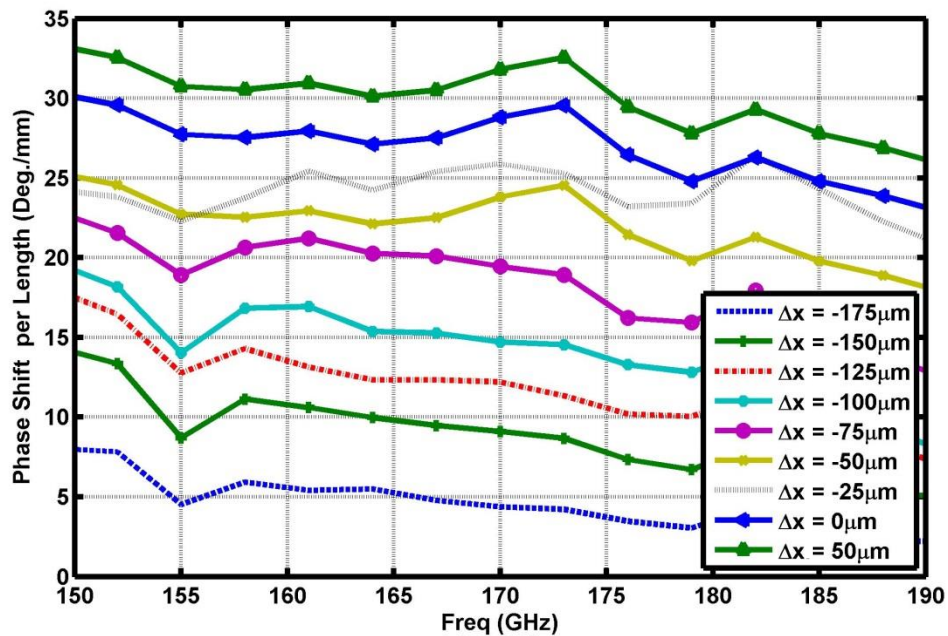


Fig. 5.13: The measured phase shift of the finger-shaped phase shifter for the total finger structure length of $L_2=3$ mm. The reference phase is defined for the case $\Delta x=-200$ μm .

5.3 SIG Butler Matrix for Beam Scanning Application

Nowadays different Beam Forming Networks (BFNs) are employed for a variety of mmWave applications, particularly for communication and wireless purposes. The electronic beam forming can be performed in different schemes including frequency scanning, phase scanning, and time scanning. The phase scanning can be realized either by continuous beam scanning or beam switching techniques. Among different beam switching techniques, such as Blass and Rotman Lens network [155], the cost-effective butler matrix network is chosen to be implemented for this research [156], [157]. The butler matrix circuit was first introduced by Jesse Butler [158]. In the mmWave range of frequencies, most of the butler matrices have been realized either by the traditional planar circuit technologies [159] or SIW technology [160], [161]. However, realization of the butler matrix using those approaches, in higher frequencies, encounters issues such as loss, fabrication challenges, and integration difficulties. Implementation of butler matrix, using a dielectric waveguide technology, has not yet been reported. Although the main drawback of the butler matrix is its relatively large size, the butler matrix network is the simplest and the most cost-effective approach for the cases where the size can be tolerated. Depending on the number of required beam positions, the order of the butler matrix, N , is defined.

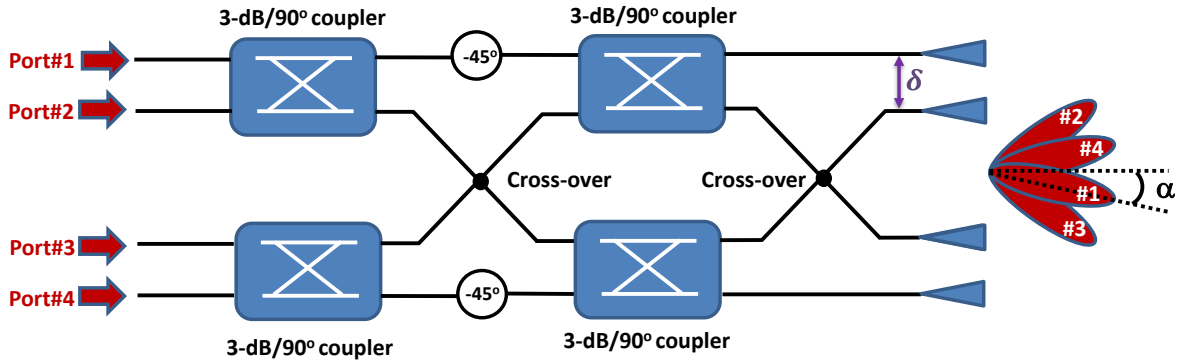


Fig. 5.14: Block diagram of a general 4x4 butler matrix network.

The most common configuration of a 4x4 butler matrix consists of four 3-dB/90° directional couplers, two 45° phase shifters, and two cross-overs. The butler matrix network provides uniform amplitude distribution and constant phase difference between the successive output ports, $\delta = \frac{(-1)^{p+1}(1-2p)\pi}{N}$, when $p=1, 2, \dots, N$. Therefore, the ideal phase difference between the output ports for a 4x4 butler matrix are -45, 135, -135, and 45

degrees, when the network is excited from port-1 to port-4, in sequence. The radiation beams are pointing in α direction, which is determined as follow:

$$\text{Sin}(\alpha) = \frac{\lambda}{2\pi d} \delta \quad (5-1)$$

where d is the separation distance between the output ports.

The proposed 4×4 butler matrix, which is illustrated in Fig. 5.15, is designed to operate over the 145-165 GHz, where the air absorption loss is minimum and makes this range suitable for communication applications. The SIG configuration is chosen for implementing the butler matrix mainly due to its simplicity for the fabrication. The key component in realization of butler matrix is a 3-dB directional coupler whose design was explained in Section 3.3. In addition to the directional coupler, two cross-over components are needed. Two approaches can be employed for implementing the cross-over: 1- connecting two 3-dB/90° coupler back to back, 2- realizing the cross-over by a single 180° coupler. Although the second approach provides smaller cross-over structure, it does not act as a perfect cross, specifically in these two cases: 1- when there are unbalanced signals at the inputs or, 2- when there is a reflected signal at the output. For these reasons, the author designed and re-optimized two 3-dB/90° couplers to be connected back to back for realization of the cross-overs. The simulated results along with the electric field distribution of the optimized cross-over are shown in Fig. 5.16. The input and output branches have the curvatures with radii and the angles of 2 mm and 45 degree, respectively. The rest of design parameters can be found in the Table 2.1.

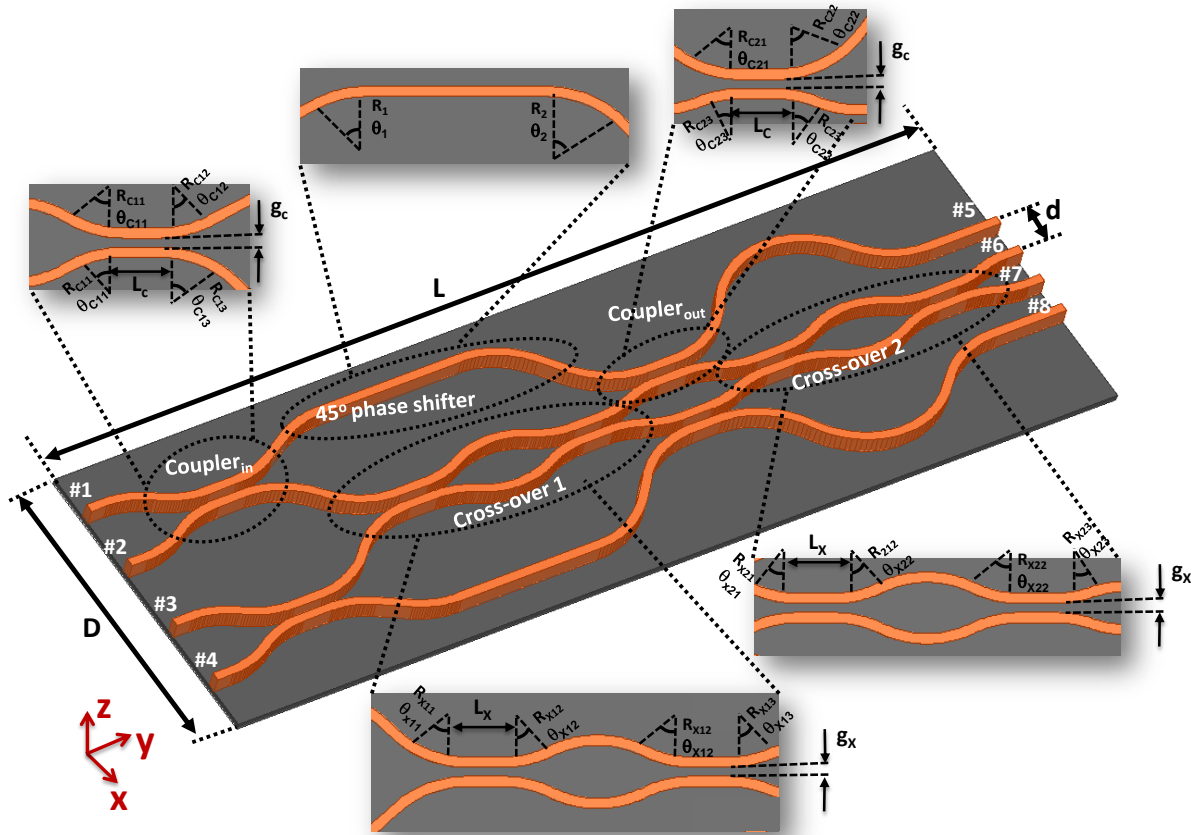


Fig. 5.15: The general schematic of the proposed SIG butler matrix network.

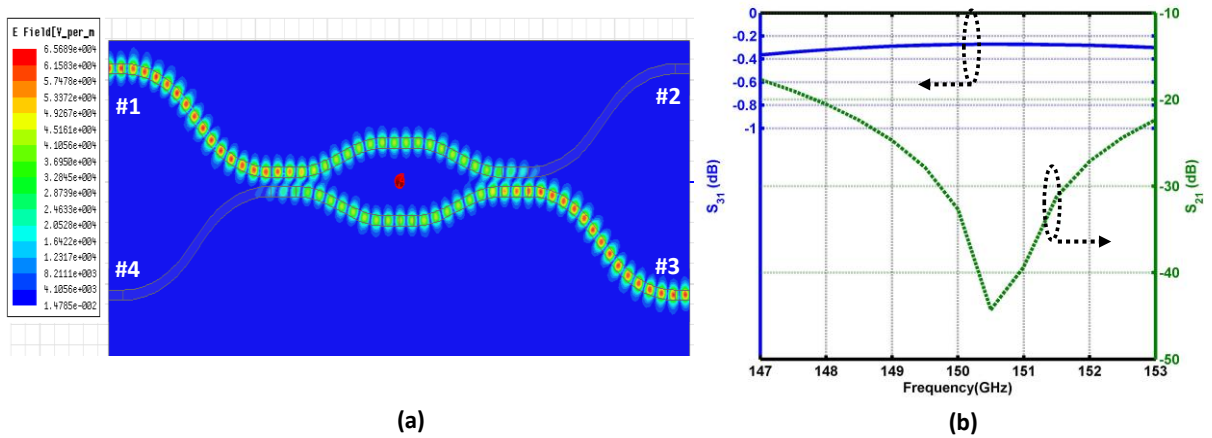


Fig. 5.16: (a) The designed cross-over electric field distribution at 150 GHz. (b) The S-parameters of the cross-over.

The main challenge in design of the butler matrix is to adjust the output phases of the network. Therefore, after positioning all the components, the lengths of the transmission lines and the bends should be adjusted to provide the required fixed phase shifts at the outputs. The optimized design parameter values, which provide the minimum network loss for the desired phase differences between the output ports at 150 GHz, are listed in Table 5.2.

Table 5.2: Design parameter values for the SIG butler matrix.

Parameter	Value	Parameter	Value	Parameter	Value	Parameter	Value	Parameter	Value
L	27.8 mm	R_{C11}	2.5 mm	θ_1	30°	R_{C23}	2.5 mm	θ_{X13}	20°
D	9 mm	θ_{C11}	30°	R_2	2.5 mm	θ_{C23}	20°	R_{X21}	2.5 mm
P	1.2 mm	R_{C12}	2.5 mm	θ_2	48°	R_{X11}	2.5 mm	θ_{X21}	20°
g_X	180 μm	θ_{C12}	28°	R_{C21}	2.5 mm	θ_{X11}	45°	R_{X22}	2.5 mm
L_X	1 mm	R_{C13}	2.5 mm	θ_{C21}	48°	R_{X12}	2.5 mm	θ_{X22}	25°
g_C	180 μm	θ_{C13}	45°	R_{C22}	2.5 mm	θ_{X12}	25°	R_{X23}	2.5 mm
L_C	1 mm	R_1	2.5 mm	θ_{C22}	54.5°	R_{X13}	2.5 mm	θ_{X23}	18°

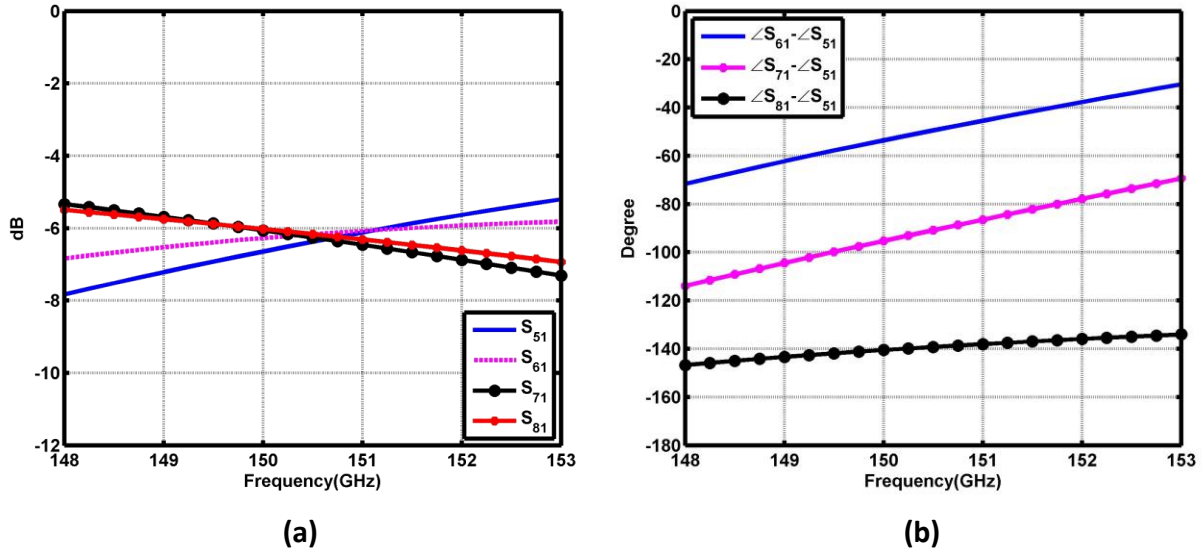


Fig. 5.17: (a) The simulated transmission coefficients of the butler matrix network, excited at port-1. (b) The difference between the phases of the output ports and port-5, when the network is excited at port-1.

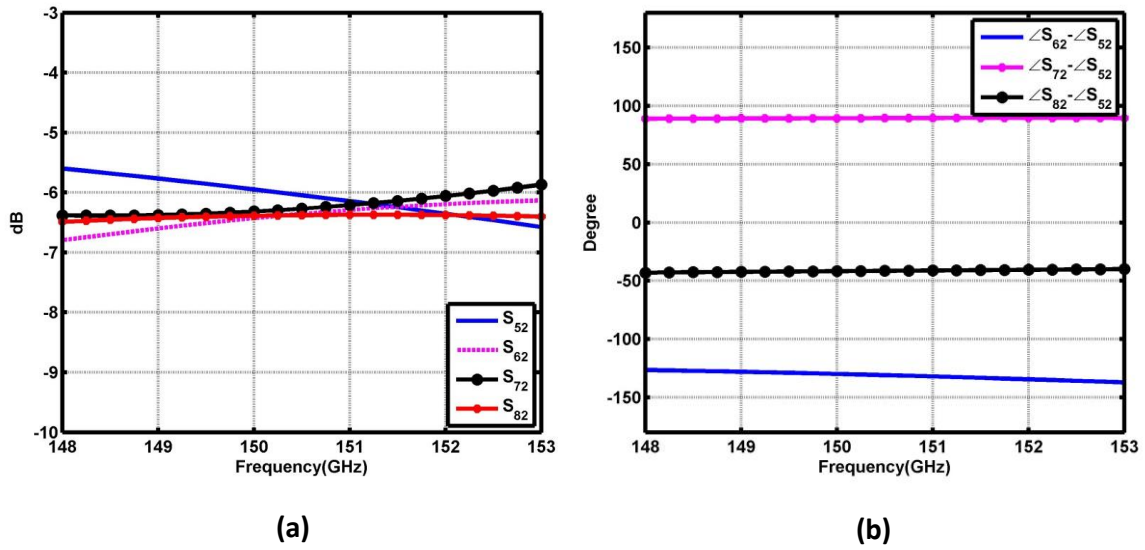


Fig. 5.18: (a) The simulated transmission coefficients of the butler matrix network, excited at port-2. (b) The difference between the phases of the output ports and port-5, when the network is excited at port-2.

The simulated insertion losses and phase differences at the output ports, when the network is excited at port-1, are shown in Fig. 5.17. The simulated network insertion loss exhibits a maximum additional 1.5 dB loss, relative to the theoretical 6 dB loss, from 148.5 to 152.5 GHz. Fig. 5.18 presents the simulated results when the network is excited at port-2. Over 148.5-152.5 GHz, the simulated output amplitude imbalance is less than 1.9 dB when the network is excited at port-1, and is less than 1 dB when the signal is excited at port-2.

The electric field distributions of the network, when port-1 and port-2 are excited, are shown in Fig. 5.19, respectively.

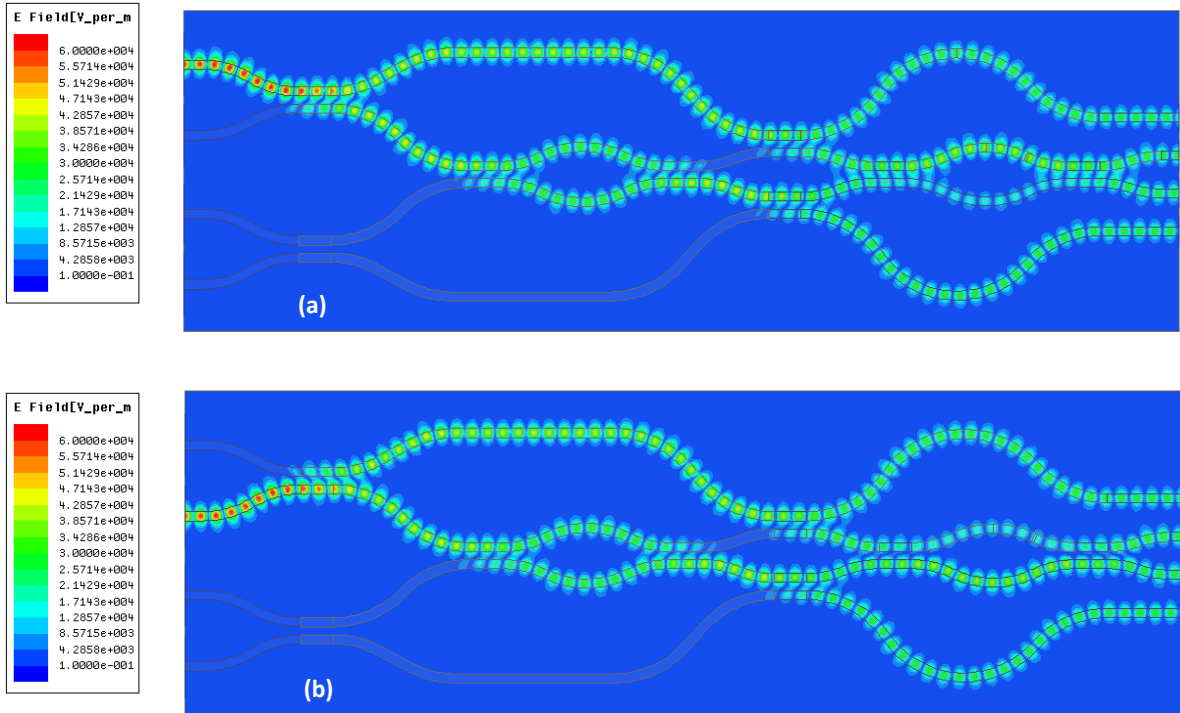


Fig. 5.19: The electric field distributions over the butler matrix network at 150 GHz, when the network is excited at (a) port-1, and (b) port-2.

The network proposed in Fig. 5.15 is not a monolithic network. Therefore, realization of the network needs precise manual positioning, which brings substantial uncertainty to the results. As proposed in Section 3.3, the network can become mechanically stable by using the supporting beams. Due to the existence of supporting beams, a small degree of degradation in frequency bandwidth is inevitable. To compensate for the effect of the supporting beams on changing the frequency bandwidth, and for re-adjusting the output phases, the network has been re-optimized. The final proposed monolithic 4×4 butler matrix is shown in Fig. 5.20, and is operating at the centre frequency of 156 GHz. The corresponding insertion losses and output phases when the network is excited at port-1 and port-2, are shown in Fig. 5.21 and Fig. 5.22, respectively.

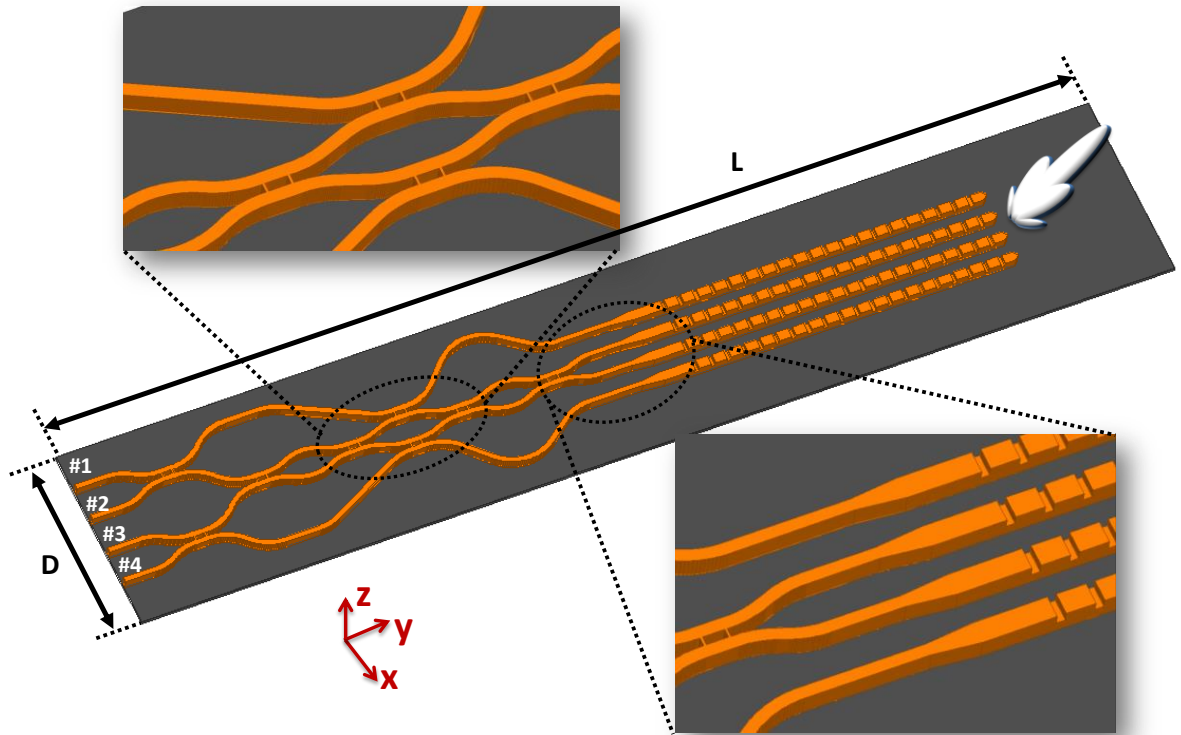


Fig. 5.20: The general schematic of the proposed monolithic SIG butler matrix connected to groove grating antenna array.

The simulated additional insertion loss reaches a maximum of 1.7 dB, relative to the theoretical 6 dB loss, over 154-158 GHz. The simulated output amplitude imbalance is less than 1.7 dB when the network is excited at port-1, and is less than 1.2 dB when the network is excited at port-2. Over 154-158 GHz, the maximum simulated output phase error is 13° when the network is excited at port-1, and is less than 5° when the network is excited at port-2.

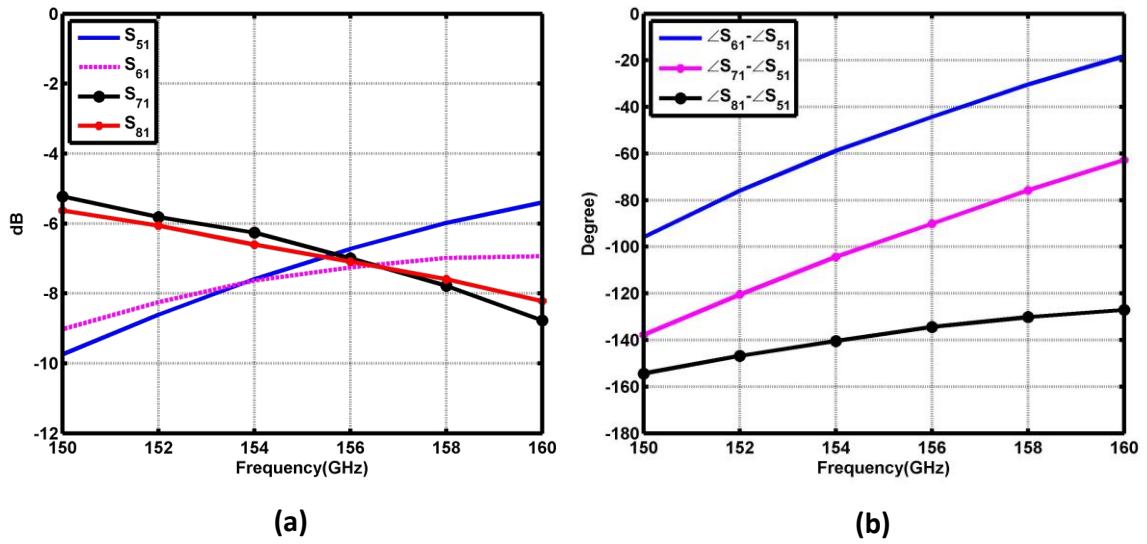


Fig. 5.21: (a) The simulated transmission coefficients of the monolithic butler matrix network, excited at port-1. (b) The difference between the phases of the output ports and port-5, when the network is excited at port-1.

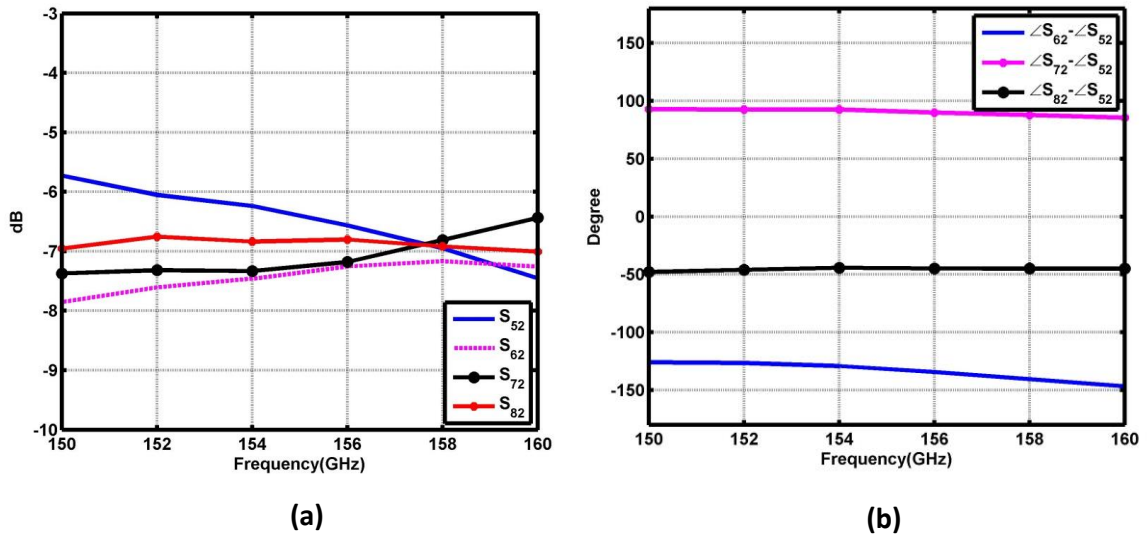


Fig. 5.22: (a) The simulated transmission coefficients of the monolithic butler matrix network, excited at port-2. (b) The difference between the phases of the output ports and port-5, when the network is excited at port-2.

The grooved grating antenna is chosen for integration with the butler matrix network. There are two reasons for choosing the grating antenna, instead of a tapered antenna, as a radiating element: 1-a grating antenna has wide beam in E -plane, and 2- the antenna beam is near boresight radiation. Therefore, the groove grating antenna makes the butler matrix system appropriate for the communication purposes. The separation distance between the antenna elements, which are designed in Section 3.5.1, is about $d=0.6\lambda$. The network beams are theoretically radiating at the angles (α) of 11.5° , -37° , 37° , -11.5° angles, when it is excited from port-1 to port-4, in sequence. The general configuration of the butler system, operating over 154-158 GHz, is shown in Fig. 5.20. The overall dimensions of the ground plane are $L=50$ mm and $D=9$ mm.

Fig. 5.23 shows 3-D simulated gain pattern of the groove grating antenna array, excited by a 4×4 butler matrix at 156 GHz. The maximum achieved gain is 20 dBi, when the network is excited either at port-1 or port-4. There is 1.5 dB gain reduction, when the network is excited either at port-2 or port-3. Table 5.3 lists the simulated gain pattern data for the integrated butler network system, shown in Fig. 5.20, for three different frequencies: 154 GHz, 156 GHz, and 158 GHz.

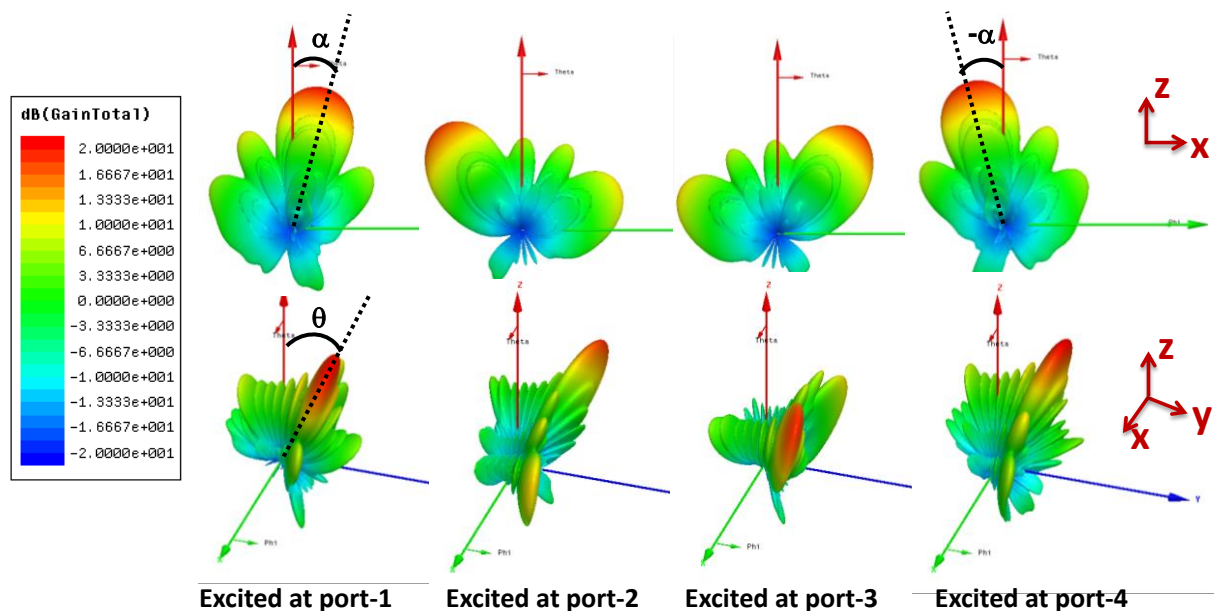


Fig. 5.23: 3-D gain pattern of 1×4 groove grating antenna array, excited by the 4×4 butler matrix network, at 156 GHz.

Table 5.3: The simulated gain pattern data of the butler matrix system over 154-158 GHz.

Frequency	Excited at port-1	Excited at port-2	Excited at port-3	Excited at port-4
154 GHz	$\alpha=13.2^\circ$	$\alpha=-36.1^\circ$	$\alpha=36.1^\circ$	$\alpha=-13.2^\circ$
	$\theta=24.2^\circ$	$\theta=43.5^\circ$	$\theta=43.5^\circ$	$\theta=24.2^\circ$
	gain= 19.9 dBi	gain= 19.4 dBi	gain= 19.4 dBi	gain= 19.9 dBi
156 GHz	$\alpha=11.9^\circ$	$\alpha=-35$	$\alpha=35$	$\alpha=-11.9^\circ$
	$\theta=26^\circ$	$\theta=45^\circ$	$\theta=45^\circ$	$\theta=26^\circ$
	gain= 20 dBi	gain= 19 dBi	gain= 19 dBi	gain= 20 dBi
158 GHz	$\alpha=11.5$	$\alpha=-34.6$	$\alpha=34.6$	$\alpha=-11.5$
	$\theta=28^\circ$	$\theta=46.5^\circ$	$\theta=46.5^\circ$	$\theta=28^\circ$
	gain= 19.7 dBi	gain= 18.5 dBi	gain= 18.5 dBi	gain= 19.7 dBi

• α and θ are defined in Fig. 5.23

The optimal monolithic butler matrix prototype, integrated with the groove grating antenna array, was fabricated using the developed laser machining fabrication process. The fabricated structure is shown in Fig. 5.24. The measurement tests are in progress.

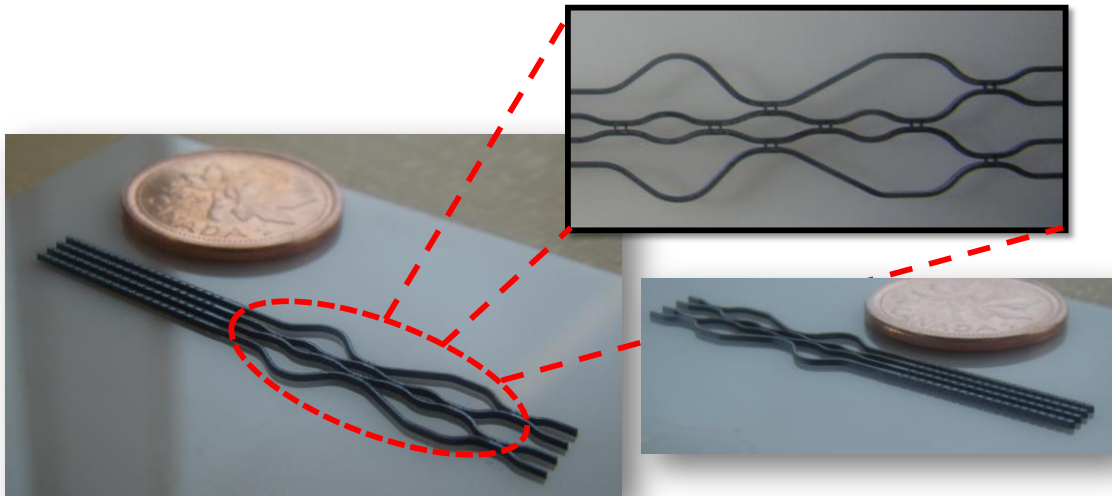


Fig. 5.24: The laser machined monolithic butler matrix network, operating at 156 GHz.

5.4 Microwave-Photonic WGM Sensor

Illumination of an intrinsic silicon structure by an optical source increases the imaginary part of the complex dielectric constant and thereby loss in the silicon substrate. The induced absorption loss can be controlled by the optical light intensity, which forms a thin plasma layer at the surface [162], [163]. The presence of the plasma layer changes the effective dielectric constant (negligible at the mmWave range of frequencies) and the conductive properties of the structure.

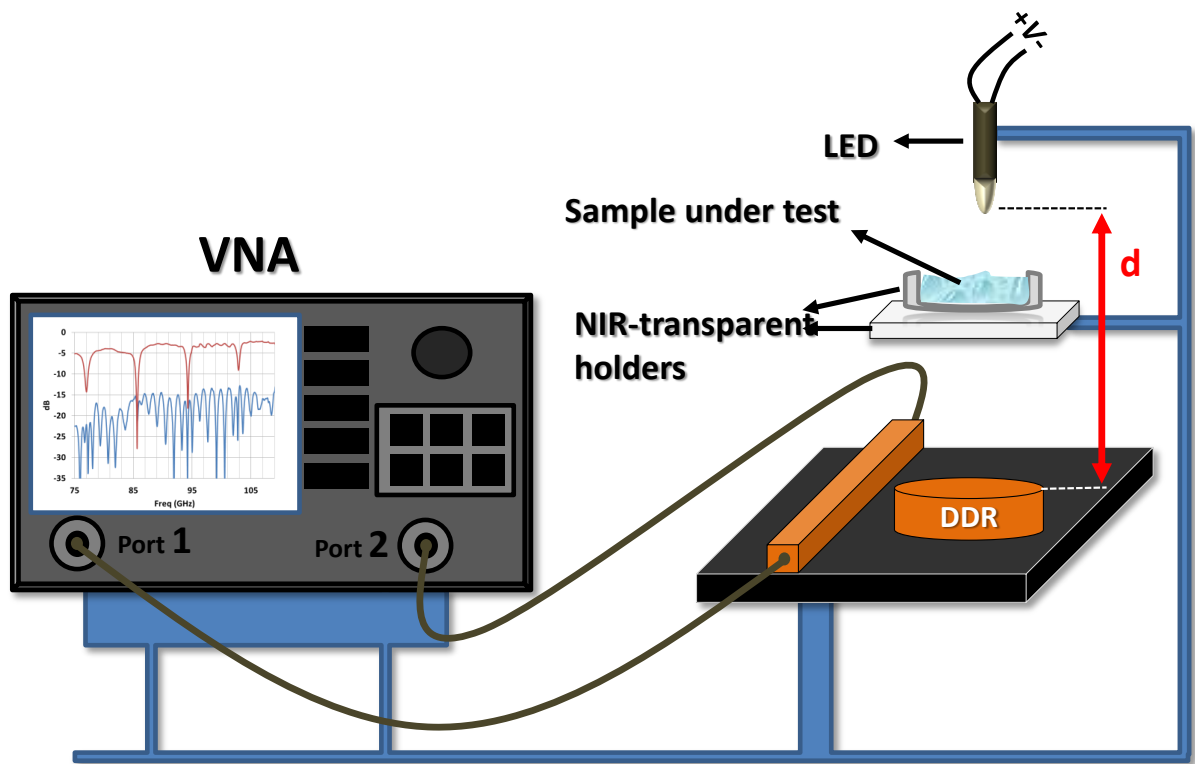


Fig. 5.25: The proposed Microwave-Photonic sensing mechanism.

The introduced concept is utilized for changing and controlling the behavior of the silicon DDR. Therefore, the silicon DDR is illuminated by an optical source, such as a LED, from the top surface, as shown in Fig. 5.25. The intensity and the wavelength of the light determine the depth of the plasma layer, which affects the Q-factor of DDR. As seen in Chapter 4, due to the uncertainty in the conductivity and the dielectric properties of the silicon at the mmWave range of frequencies, as well as fabrication errors, the fabricated

WGM resonance structures always show resonances characteristics and Q-factor, which are different from the simulated ones. The resonance behavior of those structures can be re-tuned by optical illumination. The proposed approach is very effective for sensing applications, when high Q-factor resonances are needed.

5.4.1 Experimental Verification

The proposed SIG WGM configuration, introduced in Section 4.7, is used for realization of a Microwave-Photonic WGM sensor. For the first experiment, the measurement setup, shown in Fig. 5.26(a), is utilized. It consists of the WGM resonator coupled to the curved SIG structure, illuminated from the top, by a 960 nm NIR-LED. The LED is located at exactly 10 cm above the DDR. Fig. 5.27 shows the effect of LED light on the WGH_{600} resonance of the structure. As it can be observed, varying the NIR intensity greatly affects the resonance depth. The critical coupling almost occurs when the LED operates at $V=200$ mV and $I=1.5$ mA. The aforementioned optical technique can be combined with the bio-sensing experiments, described in Chapter 4, for increasing the sensitivity.

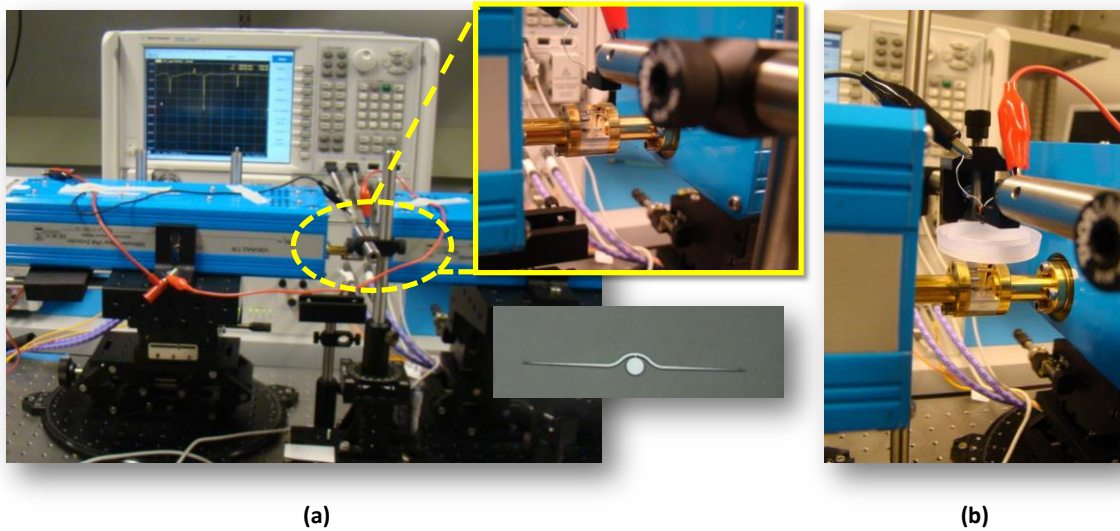


Fig. 5.26: (a) The Microwave-Photonic measurement setup for sensing application using WGM curved-SIG structure. (b) The setup for testing the sensor for two different milk samples.

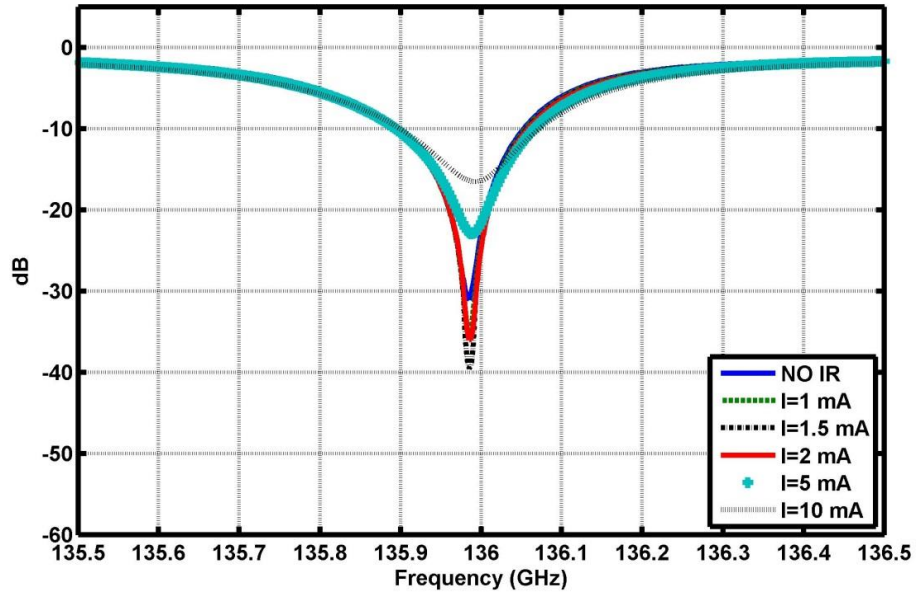


Fig. 5.27: The transmission response of the structure at WGH_{600} resonance, for different NIR illumination intensities.

As a new sensing method, an IR-transparent container is positioned between the DDR and the LED, and it was filled with two different milk samples: 2% and 10%. The measurement setup is shown in Fig. 5.26(b). The container is filled with equal 1 ml of each type of milk, and the experiments are repeated several times for validating the repeatability of the test results. The measured results are depicted in Fig. 5.28. The results show that for 2% milk, the near critical coupling happens when the LED is driven by $I=4.5$ mA, while the coupling reaches to its maximum, for 10% milk, at $I=11$ mA. These results prove that two different milk concentrations can be distinguished from each other by their differences in the resonance responses to the same IR illumination.

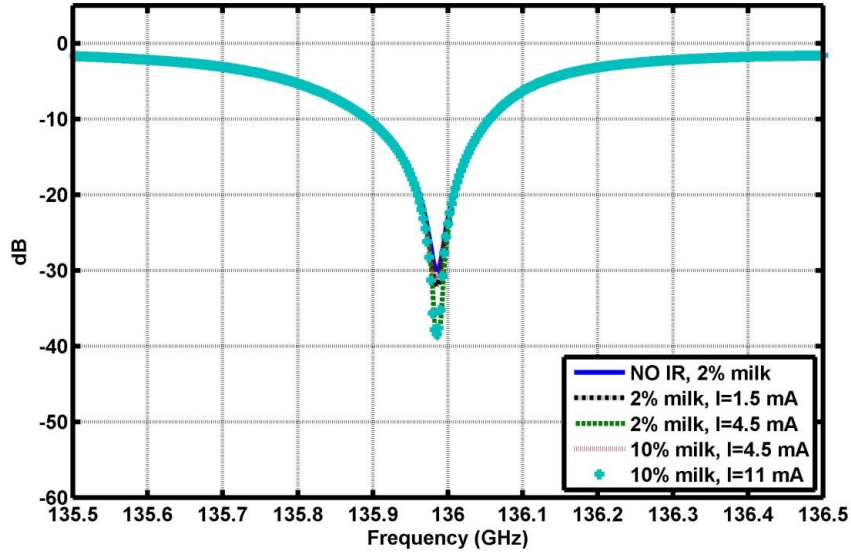


Fig. 5.28: The NIR illumination effect on the resonance responses of two different milk samples.

5.5 Conclusion

This chapter reported several high performance and cost-effective silicon-based advanced devices, working at the mmWave/THz range of frequencies. A tunable resonance structure was the first device, implemented based on the SOG WGM disc resonator. The measurement results indicated that the movable metallic bar on top of the resonator produces 4.5 GHz and 3 GHz tuning bandwidths at $f_c=152$ GHz and $f_c=168$ GHz, respectively. The designed tunable structure can be used for tunable filter and phase shifter applications. The next device was the finger-shaped phase shifter, implemented on SOG technology. The structure demonstrated relatively wide bandwidth, 150-190 GHz, with a measured maximum phase shift of 34 degree/mm, while the added insertion loss was within 0.6-1.5 dB/mm.

As a significant step in realizing large-scale integrated structures, a monolithic butler matrix beam forming network, integrated with a groove grating antenna array, and operating over the 154-158 GHz range of frequencies, was developed. Finally, a novel, simple, and cost-effective Microwave-Photonic device was proposed for refining and tuning the resonance response of a silicon WGM structure. Using a low power LED, the loaded Q-factor of the proposed SIG WGM structure was controlled over the wide range of values. This new Microwave-Photonic WGM device was tested for sensing two different milk samples.

Chapter 6

Concluding Remarks

6.1 Summary and Contributions

In this research, two high performance HRS-based waveguide technologies: Silicon-On-Glass (SOG) and Silicon Image Guide (SIG) were proposed and implemented for low-cost integrated mmWave/THz systems.

In summary, the major contributions of the author can be listed as follows:

- The development of two cost-effective and high performance silicon waveguide technologies (SIG and SOG).
- The development of a fast laser machining process for prototyping the SIG structures.
- The design, implementation, and successful measurement of several essential passive components in the SIG technology, including bend, Y-junction power divider, and directional coupler.
- The design and fabrication of a number of waveguide based antennas, including the parasitic tapered antenna, groove grating antenna, and strip grating antenna, on SIG technology.
- The development of an efficient analysis method for analyzing the planar DDRs, operating in WGMs.
- The design, implementation, and successful measurement of a number of planar silicon-based WGM resonance structures.
- The employment of the low-cost WGM-resonance-based sensors for bio-medical applications, specifically for DNA sensing.
- The implementation and experimental verification of two SOG based devices: tunable WGM resonance structure and finger-shaped phase shifter.
- The design and fabrication of an integrated beam forming antenna consisting of a butler matrix and the antenna elements based on SIG technology.

- Investigation and implementation of a new Microwave-Photonic WGM sensor.

6.2 Future Work

The following are suggested as possible directions for future research work:

- **Scaling up the silicon-based structures to a higher range of frequencies**

The introduced silicon-based technologies, SOG and SIG, were demonstrated up to 240 GHz. Exploring and studying the THz spectrum is needed to refine the proposed structures to perform at higher frequencies. Investigating the general performance factors of the structures, such as loss, and implementation of the structures at a higher range of frequencies are planned to be performed in the future.

- **Design and implementation of more advanced silicon-based passive components**

In Chapter 3, a few passive SIG components were designed and realized. Based on this experience, more advanced components, such as filters, Mach-zender, MMI structures, and attenuators can be developed. This will enable us to realize a complete and high performance mmWave/THz system. Additionally, it is now possible to proceed towards the design and realization of more advanced types of the reduced size silicon-based antennas, which brings unique characteristics to mmWave/THz systems.

- **Qualitative studies of the performances of the WGM sensors**

In Chapter 4, different planar dielectric based WGM sensors were designed and tested. To assess the performance of the implemented sensors, in the next step the sensitivity and selectivity of these structures should be evaluated in a more realistic environment. Additionally, it is desirable to investigate the sensing mechanism of the WGM disc resonators in the presence of samples: more profoundly, by modeling the samples with an impedance layer. This will help to characterize the samples in terms of permittivity and absorption factor, with a simple analytical model.

- **Adding the MEMS capability to the movable structures**

In Chapter 5, two categories of movable structures: tunable resonance structure and finger-shaped phase shifter, were implemented using movable parts and were tested by means of accurate micro-positioners. The next step will be focused on a fully integrated device, using MEM technology to realize moving parts.

- **Design and implementation of an in-package mmWave/THz system**

A cost-effective fully integrated high performance system is a dream for the mmWave/THz community. Packaging and integration are major challenges in realization of a commercial mmWave/THz system. As it was mentioned in Chapter 1, the newly developed silicon technologies empower us to tackle the aforementioned issues. In this thesis, varieties of silicon components and devices were designed and implemented using the aforementioned technologies; however, all of them were designed to be tested by metallic-waveguide-based measuring instruments. To remove this technological limitation from future developments, as an important objective of future research activities, the author plans to extend his current research results to introduce a real in-package and integrated mmWave/THz system. This is an integral part of the current CIARS research strategy in the area of high performance packaging technologies to interconnect planar active circuits with the new silicon technologies [164]. As a particular short term milestone, the author plans to realize an integrated beam forming transceiver incorporating the developed silicon butler matrix system, and planar mmWave active devices, such as those implemented in commercial CMOS technologies.

Appendices

Appendix A

Analysis of a Single-Layer and Double-Layer Image Slab Waveguide

Waveguide

1) Double-Layer Image Slab

For a two horizontal layer slab waveguide, placed over a ground plane (refer to Fig. A-1), the electric fields for each region at the *TM* mode are:

$$E_z(z) = \begin{cases} A \cos(k_{z1}z), & 0 \leq z \leq h_1 \\ B_1 \cos(k_z(z - h_1)) + B_2 \sin(k_z(z - h_1)), & h_1 \leq z \leq h_1 + h_2 \\ C e^{-\alpha_{z2}(z - h_1 - h_2)}, & z \geq h_1 + h_2 \end{cases} \quad (\text{A-1})$$

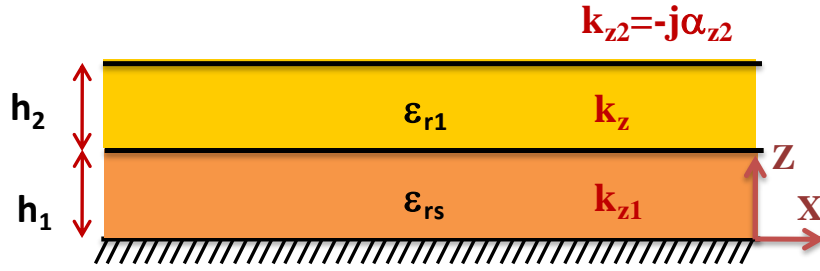


Fig. A-1. A double-layer image slab waveguide.

where

$$k_{z1}^2 = k_z^2 - k_0^2(\epsilon_{r1} - \epsilon_{rs}) \quad (\text{A-2})$$

$$\alpha_{z2}^2 = k_0^2(\epsilon_{r1} - 1) - k_z^2 \quad (\text{A-3})$$

$$k_x^2 = k_0^2 \epsilon_{rs} - k_{z1}^2 = k_0^2 + \alpha_{z2}^2 \quad (\text{A-4})$$

For the *TE* mode, (A-1) is defined for H_z instead of E_z . The propagation constant in each layer can be real or imaginary, depending on whether the solution in each region corresponds to an evanescent or a travelling wave. By matching the tangential electric and magnetic fields

in the boundaries, the unknown constants are derived. The related dispersion equations for both the *TM* and *TE* polarization are:

TM mode:

$$\left[1 - \left(\frac{k_{z1}}{k_z}\right) \left(\frac{\epsilon_{r1}}{\epsilon_{rs}}\right) \tan(k_{z1}h_1) \tan(k_z h_2)\right] - \left(\frac{k_z}{\alpha_{z2}\epsilon_{r1}}\right) \left[\tan(k_z h_2) + \left(\frac{k_{z1}}{k_z}\right) \left(\frac{\epsilon_{r1}}{\epsilon_{rs}}\right) \tan(k_{z1} h_1)\right] = 0 \quad (\text{A-5})$$

TE mode:

$$\left[1 + \left(\frac{\alpha_{z2}}{k_z}\right) \tan(k_z h_2)\right] - \left(\frac{k_z}{k_{z1}}\right) \tan(k_{z1} h_1) \left[\frac{\alpha_{z2}}{k_z} - \tan(k_z h_2)\right] = 0 \quad (\text{A-6})$$

and (A-2) converts to the following equation:

$$\alpha_{z1}^2 = k_0^2(\epsilon_{r1} - \epsilon_{rs}) - k_z^2 \quad (\text{A-7})$$

In the case where slab#2 has a larger dielectric constant than slab#1 ($\epsilon_{r1} > \epsilon_{rs}$), the dispersion equations are modified by substituting $k_{z1} = -j\alpha_{z1}$ in (A-5) and (A-6) as:

TM mode:

$$\left[1 + \left(\frac{\alpha_{z1}}{k_z}\right) \left(\frac{\epsilon_{r1}}{\epsilon_{rs}}\right) \tanh(\alpha_{z1}h_1) \tan(k_z h_2)\right] - \left(\frac{k_z}{\alpha_{z2}\epsilon_{r1}}\right) \left[-\tan(k_z h_2) + \left(\frac{\alpha_{z1}}{k_z}\right) \left(\frac{\epsilon_{r1}}{\epsilon_{rs}}\right) \tanh(\alpha_{z1} h_1)\right] = 0 \quad (\text{A-8})$$

TE mode:

$$\left[1 + \left(\frac{\alpha_{z2}}{k_z}\right) \tan(k_z h_2)\right] + \left(\frac{k_z}{\alpha_{z1}}\right) \tanh(\alpha_{z1} h_1) \left[\frac{\alpha_{z2}}{k_z} - \tan(k_z h_2)\right] = 0 \quad (\text{A-9})$$

2) Single-Layer Image Slab

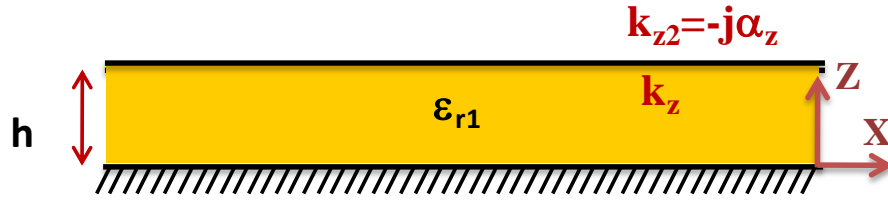


Fig. A-2. A single-layer slab wave guide.

For a single-layer image slab, by setting $\epsilon_{rs} = 1, h_1 = 0, h_2 = h,$ and $\alpha_{z2} = \alpha_z$ in (A-8) and (A-9), the dispersion equations are obtained as:

$$\begin{cases} \frac{\epsilon_{r1}\alpha_z}{k_z} = \tan(k_z h) & TM \text{ mode} \\ -\frac{\alpha_z}{k_z} = \cot(k_z h) & TE \text{ mode} \end{cases} \quad (\text{A-10})$$

where

$$\alpha_z^2 = k_0^2(\epsilon_{r1} - 1) - k_z^2 \quad (\text{A-11})$$

Appendix B

Electromagnetic Fields and Dispersion Equation of a Circular Dielectric Waveguide [165]

The Helmholtz equation in the cylindrical coordinate system is given by

$$\frac{1}{\rho} \frac{\partial}{\partial \rho} \left(\rho \frac{\partial \psi}{\partial \rho} \right) + \frac{1}{\rho^2} \frac{\partial^2 \psi}{\partial \phi^2} + \frac{\partial^2 \psi}{\partial z^2} + k^2 \psi = 0 \quad (\text{B-1})$$

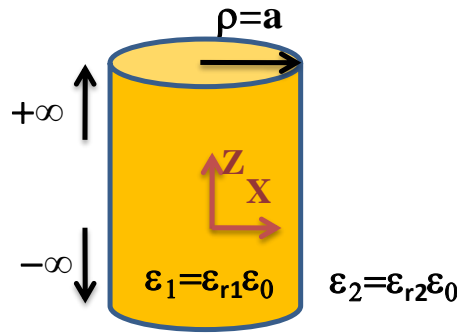


Fig. B-1. An infinite dielectric cylinder.

The electric and magnetic vector potentials for inside a uniform circular dielectric waveguide is defined as

$$\psi_e = A J_n(k_\rho \rho) e^{jn\phi} e^{-jk_z z} \quad (\text{B-2})$$

$$\psi_h = B J_n(k_\rho \rho) e^{jn\phi} e^{-jk_z z} \quad (\text{B-3})$$

where k_ρ and k_z are radial and axial propagation constants, respectively. For the outside of the cylinder, a decaying field is required in the radial direction. Therefore, the electric and magnetic vector potentials for this region are obtained as

$$\psi_{e2} = C K_n(\alpha_\rho \rho) e^{jn\phi} e^{-jk_z z} \quad (\text{B-4})$$

$$\psi_{h2} = DK_n(\alpha_\rho \rho) e^{jn\phi} e^{-jk_z z} \quad (\text{B-5})$$

The electric and magnetic fields are defined in terms of ψ_e and ψ_h as

$$E_\rho = \frac{1}{k_\rho^2} \left(\frac{\partial^2 \psi_e}{\partial \rho \partial z} - \frac{j\omega\mu}{\rho} \frac{\partial \psi_h}{\partial \phi} \right) \quad (\text{B-6})$$

$$E_z = \left(k^2 + \frac{\partial^2}{\partial z^2} \right) \psi_e \quad (\text{B-7})$$

$$E_\phi = \frac{1}{k_\rho^2} \left(\frac{1}{\rho} \frac{\partial^2 \psi_e}{\partial \phi \partial z} + j\omega\mu \frac{\partial \psi_h}{\partial \rho} \right) \quad (\text{B-8})$$

$$H_\rho = \frac{1}{k_\rho^2} \left(\frac{\partial^2 \psi_h}{\partial \rho \partial z} + \frac{j\omega\varepsilon}{\rho} \frac{\partial \psi_e}{\partial \phi} \right) \quad (\text{B-9})$$

$$H_z = \left(k^2 + \frac{\partial^2}{\partial z^2} \right) \psi_h \quad (\text{B-10})$$

$$H_\phi = \frac{1}{k_\rho^2} \left(\frac{1}{\rho} \frac{\partial^2 \psi_h}{\partial \phi \partial z} - j\omega\varepsilon \frac{\partial \psi_e}{\partial \rho} \right) \quad (\text{B-11})$$

By substituting the defined potentials, (B-2)-(B-5), in (B-6)-(B-11), and after mathematic simplifications, the obtained electric and magnetic fields for the inside and outside of the cylinder are as follows

$\rho < a$:

$$E_{\rho 1} = \left[-jk_z k_\rho A J'_n(k_\rho \rho) + \frac{\omega\mu n}{\rho} B J_n(k_\rho \rho) \right] e^{jn\phi} e^{-jk_z z} \quad (\text{B-12})$$

$$E_{\phi 1} = \left[\frac{k_z n}{\rho} A J_n(k_\rho \rho) + j\omega\mu k_\rho B J'_n(k_\rho \rho) \right] e^{jn\phi} e^{-jk_z z} \quad (\text{B-13})$$

$$E_{z 1} = k_\rho^2 A J_n(k_\rho \rho) e^{jn\phi} e^{-jk_z z} \quad (\text{B-14})$$

$$H_{\rho 1} = \left[-\frac{\omega\varepsilon_1 n}{\rho} A J_n(k_\rho \rho) - jk_z k_\rho B J'_n(k_\rho \rho) \right] e^{jn\phi} e^{-jk_z z} \quad (\text{B-15})$$

$$H_{\phi 1} = \left[-j\omega\varepsilon_1 k_\rho A J'_n(k_\rho \rho) + \frac{k_z n}{\rho} B J_n(k_\rho \rho) \right] e^{jn\phi} e^{-jk_z z} \quad (\text{B-16})$$

$$H_{z1} = k_\rho^2 B J_n(k_\rho \rho) e^{jn\phi} e^{-jk_z z} \quad (\text{B-17})$$

$\rho > a$:

$$E_{\rho 2} = \left[-jk_z \alpha_\rho C K_n'(\alpha_\rho \rho) + \frac{\omega \mu n}{\rho} D K_n(\alpha_\rho \rho) \right] e^{jn\phi} e^{-jk_z z} \quad (\text{B-18})$$

$$E_{\phi 2} = \left[\frac{k_z n}{\rho} C K_n(\alpha_\rho \rho) + j\omega \mu \alpha_\rho D K_n'(\alpha_\rho \rho) \right] e^{jn\phi} e^{-jk_z z} \quad (\text{B-19})$$

$$E_{z2} = -\alpha_\rho^2 C K_n(\alpha_\rho \rho) e^{jn\phi} e^{-jk_z z} \quad (\text{B-20})$$

$$H_{\rho 2} = \left[-\frac{\omega \varepsilon_2 n}{\rho} C K_n(\alpha_\rho \rho) - jk_z \alpha_\rho D K_n'(\alpha_\rho \rho) \right] e^{jn\phi} e^{-jk_z z} \quad (\text{B-21})$$

$$H_{\phi 2} = \left[-j\omega \varepsilon_2 \alpha_\rho C K_n'(\alpha_\rho \rho) + \frac{k_z n}{\rho} D K_n(\alpha_\rho \rho) \right] e^{jn\phi} e^{-jk_z z} \quad (\text{B-22})$$

$$H_{z2} = -\alpha_\rho^2 D K_n(\alpha_\rho \rho) e^{jn\phi} e^{-jk_z z} \quad (\text{B-23})$$

where

$$\alpha_\rho^2 + k_\rho^2 = \omega^2 \mu (\varepsilon_1 - \varepsilon_2) \quad (\text{B-24})$$

$$k_\rho^2 = k_0^2 \varepsilon_{r1} - k_z^2 \quad (\text{B-25})$$

Defining $u \triangleq k_\rho a$, $w \triangleq \alpha_\rho a$, and $v \triangleq \omega a \sqrt{\mu (\varepsilon_1 - \varepsilon_2)}$, the following term is obtained

$$u^2 + w^2 = v^2 \quad (\text{B-26})$$

In general, the cylindrical dielectric waveguide provides the hybrid mode of HE_{nm} and EH_{nm} . The subscripts of n and m denote, respectively, the number of azimuthal variations and the number of radial variations. By applying the boundary conditions at the boundaries of the tangential E and H fields, the following matrix expression for the dielectric cylindrical waveguide is achieved as

$$\begin{bmatrix} K_\rho^2 J_n(k_\rho a) & 0 & \alpha_\rho^2 K_n(\alpha_\rho a) & 0 \\ 0 & K_\rho^2 J_n(k_\rho a) & 0 & \alpha_\rho^2 K_n(\alpha_\rho a) \\ \frac{k_z n}{a} J_n(k_\rho a) & j\omega\mu k_\rho J_n'(k_\rho a) & -\frac{k_z n}{a} K_n(\alpha_\rho a) & -j\omega\mu\alpha_\rho K_n'(\alpha_\rho a) \\ j\omega\varepsilon_1 k_\rho J_n'(k_\rho a) & \frac{k_z n}{a} J_n(k_\rho a) & -j\omega\varepsilon_2\alpha_\rho K_n'(\alpha_\rho a) & -\frac{k_z n}{a} K_n(\alpha_\rho a) \end{bmatrix} \begin{bmatrix} A \\ B \\ C \\ D \end{bmatrix} = 0 \quad (\text{B-27})$$

The dispersion equation is obtained by setting the matrix determinant equal to zero

$$\begin{aligned} & \left[\frac{\varepsilon_1 J_n'(k_\rho a)}{(k_\rho a) J_n(k_\rho a)} + \frac{\varepsilon_2 K_n'(\alpha_\rho a)}{(\alpha_\rho a) K_n(\alpha_\rho a)} \right] \times \left[\frac{\mu J_n'(k_\rho a)}{(k_\rho a) J_n(k_\rho a)} + \frac{\mu K_n'(\alpha_\rho a)}{(\alpha_\rho a) K_n(\alpha_\rho a)} \right] \\ & = \frac{n^2 k_z^2}{\omega^2} \left[\frac{1}{(k_\rho a)^2} + \frac{1}{(\alpha_\rho a)^2} \right] \end{aligned} \quad (\text{B-28})$$

Equation (B-28) is represented as below

$$\begin{aligned} & \left[\frac{J_n'(k_\rho a)}{(k_\rho a) J_n(k_\rho a)} + \frac{K_n'(\alpha_\rho a)}{(\alpha_\rho a) K_n(\alpha_\rho a)} \right] \times \left[\frac{J_n'(k_\rho a)}{(k_\rho a) J_n(k_\rho a)} + \frac{1}{\varepsilon_{r1}} \frac{K_n'(\alpha_\rho a)}{(\alpha_\rho a) K_n(\alpha_\rho a)} \right] \\ & = \left[n(\varepsilon_{r1} - 1) \frac{k_z k_0}{k_\rho^2} \right] \end{aligned} \quad (\text{B-29})$$

where α_ρ , k_ρ and k_z are related through (B-24) and (B-25). For $\varepsilon_{r1} = 1$, two separate modes are defined as the *HE* and *EH* hybrid modes

$$\frac{J_{n+1}(k_\rho a)}{k_\rho a J_n(k_\rho a)} = \frac{K_{n+1}(\alpha_\rho a)}{\alpha_\rho a K_n(\alpha_\rho a)} \quad EH_{nm} \quad (\text{B-30})$$

$$\frac{J_{n-1}(k_\rho a)}{k_\rho a J_n(k_\rho a)} = \frac{K_{n-1}(\alpha_\rho a)}{\alpha_\rho a K_n(\alpha_\rho a)} \quad HE_{nm} \quad (\text{B-31})$$

By solving (B-29), all the unknown coefficients are defined according to only one constant. After mathematical simplifications by using recurrence formulas for the Bessel function, electric and magnetic field components are rewritten as follows

$\rho < a$:

$$E_{\rho 1} = jk_z k_\rho A \left[\frac{1 + S_n}{2} J_{n+1}(k_\rho \rho) - \frac{1 - S_n}{2} J_{n-1}(k_\rho \rho) \right] e^{jn\phi} e^{-jk_z z} \quad (\text{B-32})$$

$$E_{\phi 1} = k_z k_\rho A \left[\frac{1 + S_n}{2} J_{n+1}(k_\rho \rho) + \frac{1 - S_n}{2} J_{n-1}(k_\rho \rho) \right] e^{jn\phi} e^{-jk_z z} \quad (\text{B-33})$$

$$E_{z1} = k_\rho^2 A J_n(k_\rho \rho) e^{jn\phi} e^{-jk_z z} \quad (\text{B-34})$$

$$H_{\rho 1} = -\frac{k_z^2 k_\rho A}{\omega \mu_0} \left[\frac{S_n + \frac{k^2}{k_z^2} \varepsilon_{r1}}{2} J_{n+1}(k_\rho \rho) - \frac{S_n - \frac{k^2}{k_z^2} \varepsilon_{r1}}{2} J_{n-1}(k_\rho \rho) \right] e^{jn\phi} e^{-jk_z z} \quad (\text{B-35})$$

$$H_{\phi 1} = j \frac{k_z^2 k_\rho A}{\omega \mu_0} \left[\frac{S_n + \frac{k^2}{k_z^2} \varepsilon_{r1}}{2} J_{n+1}(k_\rho \rho) + \frac{S_n - \frac{k^2}{k_z^2} \varepsilon_{r1}}{2} J_{n-1}(k_\rho \rho) \right] e^{jn\phi} e^{-jk_z z} \quad (\text{B-36})$$

$$H_{z1} = j \frac{k_z k_\rho^2 S_n}{\omega \mu_0} A J_n(k_\rho \rho) e^{jn\phi} e^{-jk_z z} \quad (\text{B-37})$$

$\rho > a$:

$$E_{\rho 2} = jk_z \alpha_\rho C \left[\frac{1 + S_n}{2} K_{n+1}(\alpha_\rho \rho) + \frac{1 - S_n}{2} K_{n-1}(\alpha_\rho \rho) \right] e^{jn\phi} e^{-jk_z z} \quad (\text{B-38})$$

$$E_{\phi 2} = k_z \alpha_\rho C \left[\frac{1 + S_n}{2} K_{n+1}(\alpha_\rho \rho) - \frac{1 - S_n}{2} K_{n-1}(\alpha_\rho \rho) \right] e^{jn\phi} e^{-jk_z z} \quad (\text{B-39})$$

$$E_{z2} = \alpha_\rho^2 A K_n(\alpha_\rho \rho) e^{jn\phi} e^{-jk_z z} \quad (\text{B-40})$$

$$H_{\rho 2} = -\frac{k_z^2 \alpha_\rho C}{\omega \mu_0} \left[\frac{S_n + \frac{k^2}{k_z^2} \varepsilon_{r2}}{2} K_{n+1}(\alpha_\rho \rho) + \frac{S_n - \frac{k^2}{k_z^2} \varepsilon_{r2}}{2} K_{n-1}(\alpha_\rho \rho) \right] e^{jn\phi} e^{-jk_z z} \quad (\text{B-41})$$

$$H_{\phi 2} = j \frac{k_z^2 \alpha_\rho C}{\omega \mu_0} \left[\frac{S_n + \frac{k^2}{k_z^2} \varepsilon_{r2}}{2} K_{n+1}(\alpha_\rho \rho) - \frac{S_n - \frac{k^2}{k_z^2} \varepsilon_{r2}}{2} K_{n-1}(\alpha_\rho \rho) \right] e^{jn\phi} e^{-jk_z z} \quad (\text{B-42})$$

$$H_{z2} = -j \frac{k_z \alpha_\rho^2 S_n}{\omega \mu_0} C K_n(\alpha_\rho \rho) e^{jn\phi} e^{-jk_z z} \quad (\text{B-43})$$

where

$$C = -\frac{Ak_{\rho}^2 J_n(K_{\rho} \rho)}{\alpha_{\rho}^2 K_n(\alpha_{\rho})} \quad (\text{B-44})$$

$$S_n = \frac{n \left[\frac{1}{(k_{\rho} a)^2} + \frac{1}{(\alpha_{\rho} a)^2} \right]}{\left[\frac{J_n'(k_{\rho} a)}{(k_{\rho} a) J_n(k_{\rho} a)} + \frac{K_n'(\alpha_{\rho} a)}{(\alpha_{\rho} a) K_n(\alpha_{\rho} a)} \right]} \quad (\text{B-45})$$

Appendix C

Asymptotic Values and Cut-Off Conditions of a Dielectric Cylinder

Understanding the behavior of the dispersion equation of a dielectric cylinder, operating in the hybrid mode, is not easy when it is expressed in the form of (B-29). The quadratic form of (B-29) can be written as

$$\left[\frac{J'_n(k_\rho a)}{(k_\rho a)J'_n(k_\rho a)} \right]^2 + \left[\frac{\mu(\varepsilon_1 + \varepsilon_2)}{\mu\varepsilon_1} \frac{K'_n(\alpha_\rho a)}{(\alpha_\rho a)K'_n(\alpha_\rho a)} \right] \frac{J'_n(k_\rho a)}{(k_\rho a)J'_n(k_\rho a)} + \frac{\varepsilon_2}{\varepsilon_1} \left[\frac{K'_n(\alpha_\rho a)}{(\alpha_\rho a)K'_n(\alpha_\rho a)} \right]^2 - n^2 \left[\frac{1}{(k_\rho a)^2} + \frac{1}{(\alpha_\rho a)^2} \right] \left[\frac{1}{(k_\rho a)^2} + \frac{\varepsilon_2}{\varepsilon_1(\alpha_\rho a)^2} \right] = 0 \quad (\text{C-1})$$

The above equation has two roots as follows:

EH mode:

$$\frac{J_{n+1}(k_\rho a)}{J_n(k_\rho a)} = k_\rho a \left[\frac{(\varepsilon_1 + \varepsilon_2)}{2\varepsilon_1} \left(\frac{n}{(\alpha_\rho a)^2} - \frac{K_{n+1}(\alpha_\rho a)}{\alpha_\rho a K_n(\alpha_\rho a)} \right) + \frac{n}{(k_\rho a)^2} - \sqrt{Y} \right] \quad (\text{C-2})$$

HE mode:

$$\frac{J_{n-1}(k_\rho a)}{J_n(k_\rho a)} = k_\rho a \left[-\frac{(\varepsilon_1 + \varepsilon_2)}{2\varepsilon_1} \left(\frac{n}{(\alpha_\rho a)^2} - \frac{K_{n+1}(\alpha_\rho a)}{\alpha_\rho a K_n(\alpha_\rho a)} \right) + \frac{n}{(k_\rho a)^2} - \sqrt{Y} \right] \quad (\text{C-3})$$

where

$$Y = \left[\frac{(\varepsilon_1 - \varepsilon_2)}{2\varepsilon_1} \left(\frac{n}{(\alpha_\rho a)^2} - \frac{K_{n+1}(\alpha_\rho a)}{\alpha_\rho a K_n(\alpha_\rho a)} \right) \right]^2 + \left[\frac{n^2}{(k_\rho a)^2} + \frac{n^2}{(\alpha_\rho a)^2} \right] \left[\frac{1}{(k_\rho a)^2} + \frac{\varepsilon_2}{\varepsilon_1(\alpha_\rho a)^2} \right] \quad (\text{C-4})$$

The resultant equations for both polarizations are expressed by only one unknown parameter, k_ρ , by using the auxiliary equation,

$$\alpha_\rho a = \sqrt{\omega^2 \mu a (\varepsilon_1 - \varepsilon_2) - (k_\rho a)^2} \quad (\text{C-5})$$

(C-2) and (C-3) represent two sets of curves which can be plotted independently. The intersection of the curves for a fixed mode and in the certain frequency results in the

corresponding k_ρ . Asymptotic values of (C-2) and (C-3) provide a better understanding of their behavior. At the cut-off frequency, the k_ρ has its minimum value and consequently α_ρ is zero. To investigate different situations, three cases are studied, $n=0$, $n=1$ and $n>1$.

$n=0$:

Hybrid modes converted to TE and TM modes and two separate dispersion equations are obtained with the same cut-off value, when $\alpha_\rho a \rightarrow 0$. The cut-off frequency is calculated as below:

$$f_c = \frac{x_{0m}}{2\pi a \sqrt{\mu(\varepsilon_1 - \varepsilon_2)}}, \quad m > 0 \quad (\text{C-6})$$

where x_{0m} denotes the m^{th} root of $J_0(k_\rho a) = 0$. Interestingly, the cut-off values for the TE_{0m} and TM_{0m} modes are the same; however, they are not degenerate modes.

$n=1$:

To find the cut-off frequency of HE_{1m} and EH_{1m} modes, the left hand sides of (C-2) and (C-3), respectively, must be zero. The evaluated cut-off frequencies are as follows:

$$J_1(k_\rho a) = 0, k_{\rho c} = \frac{x_{1m'}}{a} \quad \text{when} \quad \begin{cases} m' = m & EH_{1m} \\ m' = m - 1 & HE_{1m} \end{cases} \quad (\text{C-7})$$

For EH_{1m} , the $k_\rho a \neq 0$ constraint should be considered. It is beneficial to know that the left-hand sides of (C-2) and (C-3) for $m=1$ and $k_\rho a \rightarrow \infty$, behave like $\pm \cot(k_\rho a - \frac{\pi}{4})/k_\rho a$. Also, the right-hand side of (C-2) is a monolithically increasing function of $k_\rho a$, while the right-hand side of (C-3) is a monolithically decreasing function of $k_\rho a$.

$n>1$:

The cut-off condition for EH_{nm} is similar to the case $n=1$ with the added constraint $k_\rho a \neq 0$:

$$J_n(k_\rho a) = 0, k_{\rho c} = \frac{x_{1m}}{a} \quad (\text{C-8})$$

For the EH_{nm} modes, the left-hand side of (C-2) acts like $\tan\left(k_\rho a - \frac{\pi}{4}\right)$ for n even and $-\cot\left(k_\rho a - \frac{\pi}{4}\right)$ for n odd at large values for $k_\rho a$. The cut-off condition for HE_{nm} is achieved by finding the zeros of (C-3). The following equation describes the cut-off condition, using the asymptotic expressions of the modified Bessel functions for small values and recursion relation for the Bessel functions:

$$\frac{J_{n-2}(k_\rho a)}{J_n(k_\rho a)} = \frac{\varepsilon_2 - \varepsilon_1}{\varepsilon_2 + \varepsilon_1} \quad \text{or} \quad \frac{J_{n-1}(k_\rho a)}{J_n(k_\rho a)} = \frac{\varepsilon_2 k_\rho a}{(n-1)(\varepsilon_2 + \varepsilon_1)} \quad (\text{C-9})$$

Up to this point, the minimum values of k_ρ are obtained. These values help to determine the cut-off frequencies of both the HE and EH modes. The maximum value of k_ρ does not depend on the mode number. The roots of the left hand sides of (C-2) and (C-3) provide the required maximum values for k_ρ :

$$\begin{cases} J_{n+1}(k_\rho^{max} a) = 0 & EH_{nm} \\ J_{n-1}(k_\rho^{max} a) = 0 & HE_{nm} \end{cases} \quad (\text{C-10})$$

Appendix D

Electromagnetic Field for an Image Dielectric Disc Resonator Based on Marcatili's Method

The general electric and magnetic fields for different sub-regions of an image dielectric disc resonator, shown in Fig. D-1, are obtained by defining the electric and magnetic vector potentials in each sub-region (the fields in the sub-region 4 is assumed to be zero)

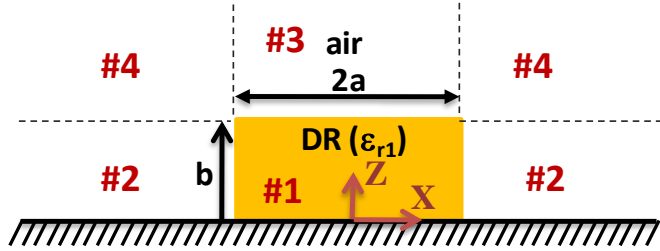


Fig. D-1. The cross view of an image dielectric disc resonator.

$$\begin{cases} \psi_{e1} = A_1 J_n(k_\rho \rho) e^{jn\phi} \cos(k_z z) \\ \psi_{h1} = B_1 J_n(k_\rho \rho) e^{jn\phi} \sin(k_z z) \end{cases} \quad (\text{D-1})$$

$$\begin{cases} \psi_{e2} = C_1 K_n(\alpha_\rho \rho) e^{jn\phi} \cos(k_z z) \\ \psi_{h2} = D_1 K_n(\alpha_\rho \rho) e^{jn\phi} \sin(k_z z) \end{cases} \quad (\text{D-2})$$

$$\begin{cases} \psi_{e3} = A_2 J_n(k_\rho \rho) e^{jn\phi} e^{-\alpha_z(z-b)} \\ \psi_{h3} = B_2 J_n(k_\rho \rho) e^{jn\phi} e^{-\alpha_z(z-b)} \end{cases} \quad (\text{D-3})$$

All the electromagnetic field components are extracted by means of (B-1)-(B-2). Then, the constants are determined by satisfying the boundary condition of each surface. After a number of mathematical calculations and simplifications, the following relations are achieved for the electric fields in each sub-region:

Region #1:

$$E_{z1} = A_1 k_\rho^2 J_n(k_\rho \rho) e^{jn\phi} \cos(k_z z) \quad (\text{D-4})$$

$$E_{\rho 1} = A_1 k_z k_\rho \left[\frac{1 + S_n}{2} J_{n+1}(k_\rho \rho) - \frac{1 - S_n}{2} J_{n-1}(k_\rho \rho) \right] e^{jn\phi} \sin(k_z z) \quad (\text{D-5})$$

$$E_{\phi 1} = -jA_1 k_z k_\rho \left[\frac{1+S_n}{2} J_{n+1}(k_\rho \rho) + \frac{1-S_n}{2} J_{n-1}(k_\rho \rho) \right] e^{jn\phi} \sin(k_z z) \quad (\text{D-6})$$

Region #2:

$$E_{z2} = A_1 k_\rho^2 \left(\frac{J_n(k_\rho a)}{K_n(\alpha_\rho a)} \right) K_n(\alpha_\rho \rho) e^{jn\phi} \cos(k_z z) \quad (\text{D-7})$$

$$E_{\rho 2} = -\frac{A_1 k_z k_\rho^2}{\alpha_\rho} \left(\frac{J_n(k_\rho a)}{K_n(\alpha_\rho a)} \right) \left[\frac{1+S_n}{2} K_{n+1}(\alpha_\rho \rho) + \frac{1-S_n}{2} K_{n-1}(\alpha_\rho \rho) \right] e^{jn\phi} \sin(k_z z) \quad (\text{D-8})$$

$$E_{\phi 2} = j \frac{A_1 k_z k_\rho^2}{\alpha_\rho} \left(\frac{J_n(k_\rho a)}{K_n(\alpha_\rho a)} \right) \left[\frac{1+S_n}{2} K_{n+1}(\alpha_\rho \rho) - \frac{1-S_n}{2} K_{n-1}(\alpha_\rho \rho) \right] e^{jn\phi} \sin(k_z z) \quad (\text{D-9})$$

Region #3:

$$E_{z3} = A_2 k_\rho^2 J_n(k_\rho \rho) e^{jn\phi} e^{-\alpha_z(z-b)} \quad (\text{D-10})$$

$$E_{\rho 3} = A_2 \alpha_z k_\rho \left[\frac{1+S_n}{2} J_{n+1}(k_\rho \rho) - \frac{1-S_n}{2} J_{n-1}(k_\rho \rho) \right] e^{jn\phi} e^{-\alpha_z(z-b)} \quad (\text{D-11})$$

$$E_{\phi 3} = -jA_2 \alpha_z k_\rho \left[\frac{1+S_n}{2} J_{n+1}(k_\rho \rho) + \frac{1-S_n}{2} J_{n-1}(k_\rho \rho) \right] e^{jn\phi} e^{-\alpha_z(z-b)} \quad (\text{D-12})$$

Appendix E

Applying the Variational Method to an Image Disc Resonator Using the Marcatili's Solution

By applying the variational method to the image dielectric disc resonator in Fig. D-1, the following stationary expression is obtained:

$$\omega_r^2 = \frac{\omega^2 \cdot \iiint_v \varepsilon E \cdot E^* \cdot dv - \iint_s (n \times E) \cdot \left(\frac{\nabla \times E^*}{\mu} \right) \cdot ds}{\iiint_v \varepsilon E \cdot E^* \cdot dv} = \omega^2 \left(1 - \frac{\sum N_s}{\sum D_v} \right) \quad (\text{E-1})$$

To calculate the surface integral of (E-1) the curl operator is applied to the conjugated electric fields in sub-regions 2 and 3:

$$\begin{aligned} \nabla \times E_3 = \hat{\rho} & \left(-j \frac{A_1 k_\rho^2}{2} \left(\frac{J_n(k_\rho a)}{K_n(\alpha_\rho a)} \right) \left[K_{n-1}(\alpha_\rho \rho) \left(\alpha_\rho - \frac{(1-S_n)k_z^2}{\alpha_\rho} \right) \right. \right. \\ & \left. \left. - K_{n+1}(\alpha_\rho \rho) \left(\alpha_\rho - \frac{(1+S_n)k_z^2}{\alpha_\rho} \right) \right] e^{jn\phi} \cos(k_z z) \right) \\ & + \hat{\phi} \left(-\frac{A_1 k_\rho^2}{2} \left(\frac{J_n(k_\rho a)}{K_n(\alpha_\rho a)} \right) \left[K_{n-1}(\alpha_\rho \rho) \left(\frac{(1-S_n)k_z^2}{\alpha_\rho} - \alpha_\rho \right) \right. \right. \\ & \left. \left. + K_{n+1}(\alpha_\rho \rho) \left(\frac{(1+S_n)k_z^2}{\alpha_\rho} - \alpha_\rho \right) \right] e^{jn\phi} \cos(k_z z) \right) \end{aligned} \quad (\text{E-2})$$

$$\begin{aligned} \nabla \times E_2 = \hat{z} & \left(-j \frac{A_2 \alpha_z k_\rho}{2} T e^{jn\phi} e^{-\alpha_z(z-b)} \right) \\ & + \hat{\phi} \left(\frac{A_2 k_\rho^2}{2} \left[J_{n-1}(k_\rho \rho) \left(\frac{(1-S_n)\alpha_z^2}{k_\rho} - k_\rho \right) \right. \right. \\ & \left. \left. - J_{n+1}(k_\rho \rho) \left(\frac{(1-S_n)\alpha_z^2}{k_\rho} - k_\rho \right) \right] e^{jn\phi} e^{-\alpha_z(z-b)} \right) \end{aligned} \quad (\text{E-3})$$

where,

$$T = \frac{J_{n-2}(k_\rho \rho)(1 - S_n)k_\rho}{2} + \frac{J_{n-1}(k_\rho \rho)(1 - S_n)(1 - S_n)}{\rho} + J_n(k_\rho \rho)S_n k_\rho + \frac{J_{n+1}(k_\rho \rho)(1 + S_n)(1 + S_n)}{\rho} - \frac{J_{n+2}(k_\rho \rho)(1 + S_n)k_\rho}{2} \quad (\text{E-4})$$

After mathematical calculations, the following expressions are obtained for the surface integrals of (E-1):

$$\sum N_s = N_H + N_V \quad (\text{E-5})$$

$$N_H = \int_0^{2\pi} \int_a^\infty (n \times E_3) \cdot \left(\frac{\nabla \times E_3^*}{\mu} \right) \cdot \rho d\rho d\phi|_{z=b}$$

$$= \frac{\pi k_\rho^4 A_1^2}{\mu} \left(\frac{J_n(k_\rho a)}{K_n(\alpha_\rho a)} \right)^2 \frac{k_z}{\alpha_\rho} \left[\left(\frac{(1 - S_n)k_z^2}{\alpha_\rho} - \alpha_\rho \right) (1 - S_n) P_{k,n-1} + \left(\frac{(1 + S_n)k_z^2}{\alpha_\rho} - \alpha_\rho \right) (1 + S_n) P_{k,n+1} \right] \sin(k_z z) \cos(k_z z) \quad (\text{E-6})$$

$$N_V = \int_0^{2\pi} \int_b^\infty (n \times E_2) \cdot \left(\frac{\nabla \times E_2^*}{\mu} \right) \cdot \rho dz d\phi|_{\rho=a}$$

$$= \frac{-\pi a k_\rho^4 A_2^2}{2\alpha_z \mu} J_n(k_\rho \rho) \left[J_{n-1}(k_\rho \rho) \left(\frac{(1 - S_n)\alpha_z^2}{k_\rho} - k_\rho \right) - J_{n+1}(k_\rho \rho) \left(\frac{(1 - S_n)\alpha_z^2}{k_\rho} - k_\rho \right) \right] e^{-2\alpha_z(z-b)}$$

$$+ \frac{\pi a k_\rho^2 A_2^2 \alpha_z}{4\mu} T \left((1 - S_n) J_{n-1}(k_\rho \rho) + (1 + S_n) J_{n+1}(k_\rho \rho) \right) e^{-2\alpha_z(z-b)} \quad (\text{E-7})$$

where,

$$P_{k,n} = \frac{a^2}{2} \left(K_{n-1}(\alpha_\rho a) K_{n+1}(\alpha_\rho a) - K_n^2(\alpha_\rho a) \right) \quad (\text{E-8})$$

The volume integral of (E-1) is calculated as:

$$\sum D_v = D_1 + D_2 + D_3 \quad (\text{E-9})$$

$$D_1 = \int_0^{2\pi} \int_0^h \int_0^a \varepsilon_0 \varepsilon_{r1} |E_1|^2 \rho d\rho dz d\phi = 2\pi \varepsilon_0 \varepsilon_{r1} A_1^2 k_\rho^4 \left[P_c P_{J,n} + \left(\frac{k_z}{k_\rho} \right)^2 P_s \hat{P}_{J,n} \right] \quad (\text{E-10})$$

$$\begin{aligned} D_2 &= \int_0^{2\pi} \int_0^h \int_a^\infty \varepsilon_0 \varepsilon_{r1} |E_2|^2 \rho d\rho dz d\phi \\ &= 2\pi \varepsilon_0 \varepsilon_{r1} A_1^2 \left(\frac{J_n(k_\rho a)}{K_n(\alpha_\rho a)} \right)^2 k_\rho^4 \left[P_c P_{K,n} + \left(\frac{k_z}{\alpha_\rho} \right)^2 P_s \hat{P}_{K,n} \right] \end{aligned} \quad (\text{E-11})$$

$$D_3 = \int_0^{2\pi} \int_h^\infty \int_0^a \varepsilon_0 \varepsilon_{r1} |E_3|^2 \rho d\rho dz d\phi = \frac{\pi \varepsilon_0 \varepsilon_{r1} A_2^2}{\alpha_z} \left(\frac{J_n(k_\rho a)}{K_n(\alpha_\rho a)} \right)^2 k_\rho^4 \left[P_{J,n} + \left(\frac{\alpha_z}{k_\rho} \right)^2 P_s \hat{P}_{J,n} \right] \quad (\text{E-12})$$

where,

$$P_{J,n} = -\frac{a^2}{2} (J_{n-1}(k_\rho a) J_{n+1}(k_\rho a) - J_n^2(k_\rho a)) \quad (\text{E-13})$$

$$\hat{P}_{K,n} = \frac{(P_{k,n-1}(1 - S_n)^2 + P_{k,n+1}(1 + S_n)^2)}{2} \quad (\text{E-14})$$

$$\hat{P}_{J,n} = \frac{(P_{J,n-1}(1 - S_n)^2 + P_{J,n+1}(1 + S_n)^2)}{2} \quad (\text{E-15})$$

Appendix F

Deep Reactive Ion Etching (DRIE) Technique for SOG Fabrication

The SOG structures, introduced in this thesis, are fabricated using the DRIE/lithography recipe, developed in CIARS. The fabrication process steps are depicted in Fig. F-1. The corresponding fabrication phases can be described as follows:

1. After RCA-1 cleaning process, thin layers of gold (Au) and chromium (Cr) are sputtered on Pyrex to form a hard mask for HF wet etching. Then the Au layer is patterned using the mask-1, by lithography process (refer to Fig. F-1(a)).
2. The Pyrex wafer is etched, using the HF etchant, to form the grating cavity inside the Pyrex. Then the remaining Au is removed (refer to Fig. F-1(b)).
3. The HRS wafer is bonded, using anodic bonding, to the structured Pyrex (refer to Fig. F-1(c)).
4. The top surface of HRS is coated by a thick, $\sim 10 \mu\text{m}$, Photo-Resist (PR) (AZ P4620), and then the PR layer is patterned using the mask-2, by lithography process (refer to Fig. F-1(d)).
5. The HRS wafer is etched using the DRIE Bosch process. As a result the waveguide structure is shaped, while it is placed on etched Pyrex (refer to Fig. F-1(e)).
6. Finally, the PR is removed using acetone and O_2 plasma. And then, the unwanted parts of the structure are taken out by the Dicing process (refer to Fig. F-1(f)).

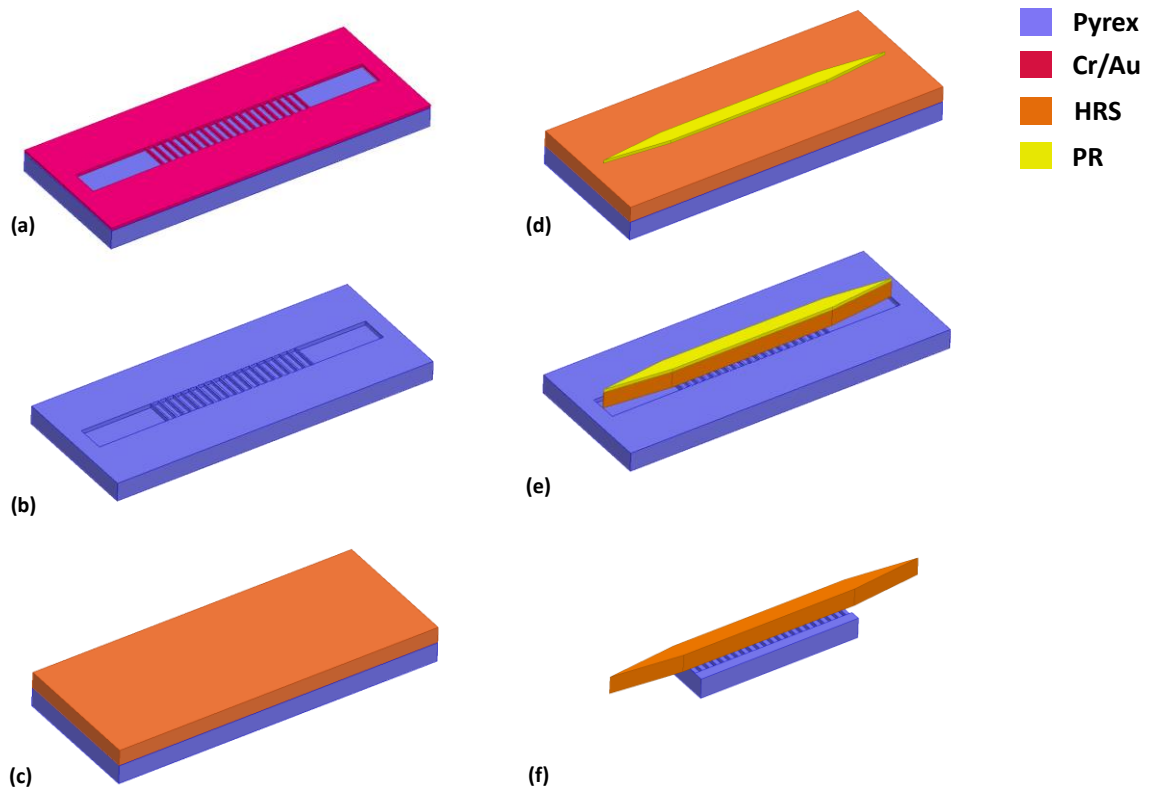


Fig. F-1: The SOG fabrication process: a) Coating the Pyrex with Cr/Au layers, and photolithography with mask-1 ,b) wet etching the Pyrex ,c) anodic bonding the HRS wafer to the etched Pyrex, d) Coating the HRS with PR, and photolithography with mask-2, e) DRIE process to form waveguide structure, and f) Dicing the Pyrex.

Appendix G

The Developed Recipe for Laser Machining the SIG Structures

A LPKF pulse UV laser machine [166], working at 355 nm wavelength, is used for fabricating the SIG structures. In order to reach a clean and smooth edge, all the parameters of the laser process should be optimized and tuned precisely. Cutting a 500 μm thick HRS wafer is achieved by following a “multi-task” laser process, in which a 15 μm laser beam cuts the HRS wafer in sequencing tasks with ascending focal point. Table G-1 lists the main laser parameters, which are used for cutting and shaping a 500 μm thick HRS wafer.

Table G-1: The developed laser machining fabrication recipe for cutting and shaping a 500 μm thick HRS wafer.

Laser Parameters	Task #1	Task #2	Task #3	Task #4
Output power (W)	5.4	5.4	5.4	4
<i>Frequency (KHz)</i>	30	30	30	45
<i>Laser beam speed (mm/s)</i>	40	60	60	200
<i>Number of repeat ion</i>	10	15	8	5
<i>Laser beam focal point in respect to the top surface of the wafer(μm)</i>	0	250	500	0

In addition to the cutting process, the laser machine is optimized for making pockets inside the silicon with minimal roughness and inaccuracy. To accomplish this, a predefined silicon area is machined in an optimized speed in a latticed pattern. The optimized laser parameters for making a 200 μm pocket inside a 500 μm silicon wafer are listed in Table G-2.

For validating the developed recipe, three pockets with the depth of 200 μm , 100 μm , and 50 μm and with identical widths of 200 μm were fabricated and evaluated by a Dektak 8 stylus profilometer. The obtained plot is shown in Fig. G-1. The results imply that the height of the desired 200 μm groove varies within the range of 200 ± 5 μm .

Table G-2: The developed laser machining recipe for making a 200 μm pocket inside the silicon.

Laser Parameters	Task #1	Task #2
Output power (W)	4	4
Frequency (KHz)	45	45
Laser beam speed (mm/s)	400	800
Number of repeat ion	18	9
Laser beam focal point in respect to the top surface of the wafer(μm)	0	200

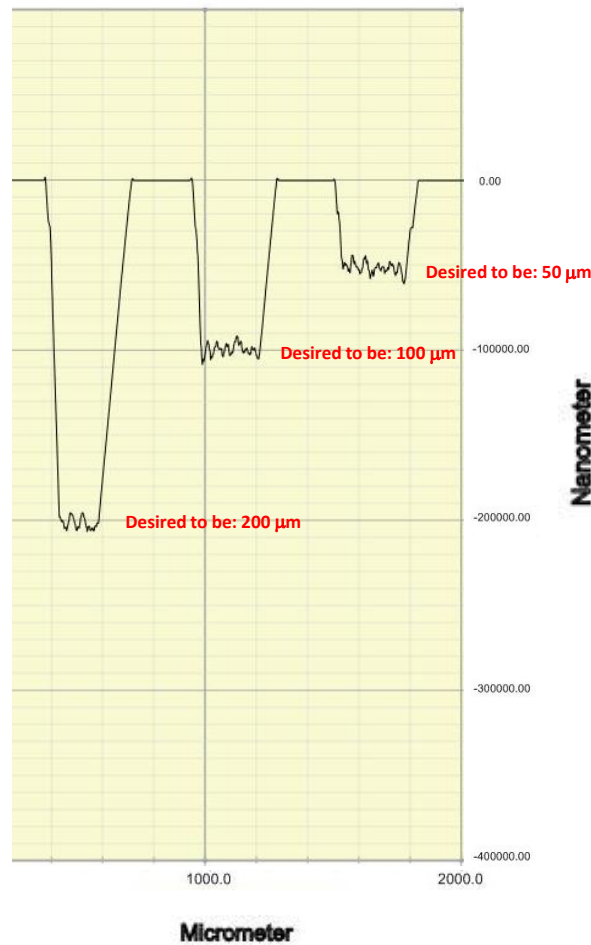


Fig. G-1: The surface profile of the laser machined grooves by means of the Dektak 8 stylus profilometer.

Bibliography

- [1] Y.Kado and T.Nagatsuma, "Exploring sub-THz waves for communications, imaging, and gas sensing," in *PIERS*, Beijing, 2009.
- [2] T.W.Crow, T.Globus, D.L.Woolard, and J.L.Hesler, "Terahertz sources and detectors and their application to biological sensing," *Phil. Trans. R. Soc.A*, vol. 362, no. 1815, pp. 365-377, 2004.
- [3] S.M.Kim, F.Hatami, and J.S.Harris, "Biomedical terahertz imaging with a quantum cascade laser," *Appl. Phys. Lett.*, vol. 88, 2006.
- [4] C.K.Walker and C.A.Kulesa, "Terahertz astronomy from the coldest place on earth," in *Infr. and Millimeter Waves*, 2006.
- [5] M.R.Kutteruf, C.M.Brown, L.K.Iwaki, M.B.Campbell, T.M.Koter, and E.J.Heilweil, "Terahertz spectroscopy of short chain polypeptides," *Chem. Phys. Lett.*, p. 337, 2003.
- [6] "IEEE 802.15 WPAN Terahertz Interest Group (IGthz)," 2003.
- [7] K.Kawasa, "Terahertz imaging for drug detection and large-scale integrated circuit inspection," *Optics and Photonics*, vol. 15, no. 10, pp. 34-39, 2004.
- [8] V.P.Wallace, E.MacPherson, J.A.Zeitler, and C.Reid, "Three-dimensional imaging of optically opaque materials using nonionizing terahertz radiation," *JOSA*, vol. 25, no. 12, pp. 3120-3133, 2008.
- [9] B.B.Hu and M.C.Nuss, "Imaging with terahertz waves," vol. 20, no. 16, pp. 1716-1721, 1995.
- [10] K.J.Siebert, T.Loffler, H.Quast, M.Thomason, T.Bauer, R.Leonhardt, S.Czasch, and H.G.Roskos, "All optoelectronic continuous wave THz imaging for biomedical applications," vol. 47, no. 21, pp. 3743-3748, 2002.
- [11] M.C.Kemp, "Detecting hidden objects: security imaging using millimeter-waves and terahertz," in *Advanced Video and Signal Based Surveillance*, 2007.
- [12] Y.S.Lee, *Principles of terahertz science and technology*, Springer, 2009.
- [13] A. W.Blain, I. Smail, R.J. Ivison, J.P. Kneib, and D.T. Frayer, *Submillimeter galaxies*, vol. 369, no. 2, pp. 111-176, 2002.
- [14] [Online]. Available: http://www.gore.com/en_xx/products/cables/index.html.
- [15] T. Itoh, *Planar transmission line structures*, IEEE, 1987.

- [16] 2014. [Online]. Available: <http://vadiodes.com/index.php/en/products>.
- [17] H. Uchimura, T. Takenoshita, and M. Fujii, "Development of a "laminated waveguide"," *IEEE Transactions on Microwave Theory and Techniques*, vol. 46, no. 12, pp. 2438-2443, 1998.
- [18] D. Deslandes, and K. Wu, "Integrated transition of coplanar to rectangular waveguides," in *IEEE MTT-S International Microwave Symposium Digest*, 2001.
- [19] K. Wu, "Substrate Integrated Circuits (SiCs)—A new paradigm for future Ghz and Thz electronic and photonic systems," *IEEE Circuits and Systems Society Newsletter* , vol. 3, no. 2, 2009.
- [20] K.Wu, "Towards the development of terahertz substrate integrated circuit technology," in *Silicon Monolithic Integrated Circuits in RF Systems (SiRF)*, 2010.
- [21] S.W. Wong, K. Wang, Z.N. Chen, and Q.X. Chu, "Electric Coupling Structure of Substrate Integrated Waveguide (SIW) for the Application of 140-GHz Bandpass Filter on LTCC," *IEEE Transactions on Components Packaging and Manufacturing Technology*, vol. 4, no. 2, pp. 316-322, 2014.
- [22] C. E. Collins, R. E. Miles, J. W. Digby, G. M. Parkhurst, R. D. Pollard,, "A new micro-machined millimeter-wave and terahertz snaptogether rectangular waveguide technology," *IEEE Microw. Guided Wave Lett*, vol. 9, no. 2, pp. 63-65, 1999.
- [23] C. H. Smith, A. Sklavonuos, and N. S. Barker, "SU-8 micromachining of millimeter and submillimeter waveguide circuits," in *n Proc. Int. Microwave Symp. Dig.*, 2009.
- [24] C. E. Colins, R. E. Miles, G. M. Parkhurst, J. W. Digby, H. Kazemi, and J. M. Chamberlain, "Use of novel photoresits in the production of submilimetre wave integrated circuits," *SPIE Millimeter and Submillimeter Waves* , vol. 164, pp. 164-168, 1998.
- [25] W.H.Chow,A.Champion, and D.P Steenson, "Measurements to 320 GHz of millimetre-wave waveguide components made by high precision and economic micro-machining techniques," in *High Frequency Postgraduate Student Colloquium*, 2003.
- [26] T.J. Reck, C. Jung-Kubiak, J. Gill, and G. Chattopadhyay, "Measurement of Silicon Micromachined Waveguide Components at 500–750 GHz," *IEEE Transactions on Terahertz Science and Technology*, vol. 4, no. 1, pp. 33-38, 2014.
- [27] G.Chattopadhyay, T. Reck, C.J-Kubiak , J.V.Siles, .hoonsup , and ehdi, "Silicon micromachining for terahertz component development," in *2013 IEEE MTT-S International Microwave and RF Conference*, 2013.
- [28] G. Gentile, R. Dekker, P. de Graaf, M. Spirito, M. J. Pelk, L. C. N.de Vreede, and B. Rejaei, "Silicon filled integrated waveguides," *IEEE Microw. Wireless Compon. Lett.*,

vol. 20, no. 10, pp. 536-538, 2010.

- [29] G.Gentile,V. Jovanovic, M.J. Pelk, Lai Jiang, R. Dekker, P.de Graaf.B. Rejaei, L.C.N.de Vreede,L.K. Nanver, M. Spirito, "Silicon-Filled Rectangular Waveguides and Frequency Scanning Antennas for mm-Wave Integrated Systems," *IEEE Transactions on Antennas and Propagation*, vol. 61, no. 12, pp. 5893-5901, 2013.
- [30] D. Hondros and P.Debye, "Elektromagnetische Wellen an dielektrischen Drähten," *Ann. Phys.*, vol. 32, no. 8, pp. 465-476, 1910.
- [31] G.C.Southworth, "Hyper-Frequency Wave Guides—General Considerations and Experimental Results," *Bell System Technical Journal* , vol. 15, no. 2, pp. 284-309, 1936.
- [32] D.D.King, "Dielectric image lines," *J. Appl. Phys.*, vol. 23, pp. 699-700, 1952.
- [33] D. D. King, "Properties of dielectric image lines," *IEEE Trans. Microwave Theory and Tech.*, vol. 3, no. 2, pp. 75-81, 1955.
- [34] M.T.Weiss and E.M.Gyorgy, "Low loss dielectric waveguides," *IRE Trans. Microwave Theory and Thech.*, pp. 38-44, 1954.
- [35] J.Wiltse, "Some characteristics of dielectric image lines at millimeter wavelenghts," *IRE Trans. Microwave Theory and Tech.*, vol. 7, pp. 65-70, 1959.
- [36] T. Itoh, "Dielectric waveguide-type millimeter-wave integrated circuits," in *Infrared and Millimeter Waves*, Academic Press, 1981.
- [37] F.Sobel, F.L. Wentworth, and J.C.Wiltse, "Quasi optical surface waveguide and other components for the 100-300 Gc Region," *IRE Trans. Microwave Theory Tech.*, vol. 9, pp. 512-518, 1961.
- [38] R.M.Knox and P.P. Toullos, "Integrated circuits for millimeter through optical frequency range," Newyork, 1970.
- [39] T. Yoneyama and S. Nishida, "Nonradiative dielectric waveguide for millimeter-wave integrated circuits," vol. 29, no. 11, pp. 1188-1192, 1981.
- [40] A.Hofmann, E.orster, J. Weinzierl , L.Schmidt,and H. Brand, "Flexible Low-Loss Dielectric Waveguides for THz Frequencies with Transitions to Metal Waveguides," in *33rd European Microwave Conference*, 2003.
- [41] A.Patrovsky and K.Wu, "Substrate integrated image guide (SIIG)-a planar dielectric waveguide technology for millimeter-wave applications," *IEEE Transactions on Microwave Theory and Techniques*, vol. 54, no. 6, pp. 2872-2879, 2006.
- [42] A. Patrovsky and K. Wu, "94-GHz planar dielectric rod antenna with substrate integrated image guide (SIIG) feeding," *IEEE Antennas Wireless Propag. Lett.*, vol. 5,

p. 435–437, 2006.

- [43] Y.J.Cheng, Y.B. Xiao, and X.G.Yong, "LTCC-Based Substrate Integrated Image Guide and Its Transition to Conductor-Backed Coplanar Waveguide," *IEEE Microwave and Wireless Comp. Lett.*, vol. 23, no. 9, pp. 450-452, 2013.
- [44] A. Malekabadi, S.A.Charlebois, D.Deslandes, and F.Boone, "High-Resistivity Silicon Dielectric Ribbon Waveguide for Single-Mode Low-Loss Propagation at F/G-Bands," *IEEE Trans. on Terahertz Science and Tech.*, vol. 4, no. 4, pp. 447-453, 2014.
- [45] M. Basha, A. Samir, S. Safavi Naeini¹, B. Biglarbegan, and S. Gigoyan, "Novel D-Band Si-Based Integrated Platform for Millimeter Wave," in *EUMW2014*, Rome, 2014.
- [46] S. Atakaramians, S.Afshar, T.M. Monro, and D.Abbott, "Terahertz dielectric waveguides," *Advances in Optics and Photonics*, vol. 5, p. 169–215, 2013.
- [47] S.K.Koul, Millimeter wave and optical dielectric integrated guides and circuits, J.Wiley, 1997.
- [48] T.N. Trinh, J.A. Malherbe, and R. Mittra, "A Metal-to-Dielectric Waveguide Transition with Application to Millimeter-Wave Integrated Circuits," in *IEEE MTT-S International Microwave Symposium Digest*, 1980.
- [49] M.Dydyk, "Image guide: a promising medium for EHF circuits," *Microwaves*, pp. 72-80, 1980.
- [50] M.Naftaly and R.E.Miles, "Terahertz time-domain spectroscopy: a new tool for the study of glasses in the far infrared," *J. of Non-Crystalline Solids*, vol. 351, pp. 3341-3346, 2005.
- [51] N. Ranjkesh, M. Basha, A. Taeb, and S. Safavid-Naieni, "Silicon-on-Glass Dielectric Waveguide, Part A: for Millimeter-Wave Integrated Circuits," *IEEE Transactions on Terahertz Science and Technology*, 2014 (accepted).
- [52] A.Taeb, S. Gigoyan, G. Rafi, M. Basha, and S. Safavi-Naeini, "A g-band dielectric waveguide WGM resonator based on Silicon-On-Glass technology," in *7th European Microwave Integrated Circuits Conference (EuMIC)*, 2012.
- [53] N. Ranjkesh, A. Taeb, A. Abdellatif, S. Gigoyan, M. Basha, and S. Safavi-Naeini, "Millimeter-Wave Silicon-On-Glass Integrated Technology," in *IMaRC2014*, 2014.
- [54] R. G. Hunsperger, *Integrated Optics Theory and Technology*, 6th ed., Springer, 2009.
- [55] F. Ladouceur and P. Labeye, "A New General Approach to Optical Waveguide Path Design," *J. of Lightwave and Tech.*, vol. 13, no. 3, pp. 481-492, 1995.
- [56] H.Sasaki, I.Anderson, "heoretical and experimental studies on active Y-junctions in

- optical waveguides," *IEEE Journal of Quantum Electronics*, vol. 14, no. 11, pp. 883-892, 1978.
- [57] N. Riesen and J. D. Love, "Design of mode-sorting asymmetric Y-junctions," *Applied optics*, vol. 51, no. 15, pp. 2778-2783, 2012.
- [58] K. Ogusu, "Experimental study of dielectric waveguide Y-junctions for millimeter-wave integrated circuits," *IEEE Transactions on Microwave Theory and Techniques*, vol. 33, no. 6, pp. 506-509, 1985.
- [59] D. Pozar, *Microwave Engineering*, 4th ed., John Wiley, 2011.
- [60] K. OKAMOTO, *Fundamentals of Optical Waveguides*, 2nd ed., Elsevier, 2006.
- [61] K. Solbach, "The Calculation and the Measurement of the Coupling Properties of Dielectric Image Lines of Rectangular Cross Section," *IEEE Transactions on Microwave Theory and Techniques*, vol. 27, no. 1, pp. 54-58, 1979.
- [62] L.B. Soldano and E.C.M. Pennings, "Optical multi-mode interference devices based on self-imaging: principles and applications," *Journal of Lightwave Technology*, vol. 13, no. 4, pp. 615-627, 1995.
- [63] P. Besse, M. Bachmann, H. Melchior, L.B. Soldano, and M.K. Smit, "Optical bandwidth and fabrication tolerances of multimode interference couplers," *Journal of Lightwave Technology*, vol. 12, no. 6, pp. 1004-1009, 1994.
- [64] S. Kobayashi, R. Mittra, and R. Lampe, "Dielectric tapered rod antennas for millimeter-wave applications," *IEEE Trans. Antennas Propag.*, vol. 30, no. 1, pp. 54-58, 1982.
- [65] J. Patrik Pousi, D. V. Lioubtchenko, S. N. Dudorov, and A. V. Räsänen, "High permittivity dielectric rod waveguide as an antenna array element for millimeter waves," *IEEE Trans. Antennas. Propag.*, vol. 58, no. 3, p. 714–719, 2010.
- [66] S. A. Yahaya, M. Yamamoto, K. Itoh, and T. Nojima, "Dielectric rod antenna based on image NRD guide coupled to rectangular waveguide," *Electron. Lett.*, vol. 39, no. 15, p. 1099–1101, 2003.
- [67] P. Mondal and K. Wu, "A Leaky-Wave Antenna in Substrate Integrated Non-Radiative Dielectric (SINRD) Waveguide With Controllable Scanning Rate," *IEEE Transactions on Antennas and Propagation*, vol. 61, no. 4, pp. 2294-2297, 2013.
- [68] A. Patrovsky and K. Wu, "94-GHz planar dielectric rod antenna with substrate integrated image guide (SIIG) feeding," *IEEE Antennas Wireless Propag. Lett.*, vol. 5, p. 435–437, 2006.
- [69] N. Ranjkesh, A. Taeb, S. Gigoyan, S. Safavi-Naeini, M.A. Basha, "High-gain integrated tapered dielectric antenna for millimeter-wave applications," in *Antennas and*

Propagation Society International Symposium (APSURSI2013), 2014.

- [70] A. Taeb, A. Abdellatif, A. Zandieh, G.Z. Rafi, S. Gigoyan, and S. Safavi-Naeini, "Millimeter-wave high gain parasitic tapered antenna made of high-resistivity silicon image-guide,," in *Antennas and Propagation Society International Symposium (APSURSI)*, 2013.
- [71] D. R. Jackson and A. A. Oliner, " Leaky-Wave Antennas," in *Modern Antenna Handbook*, John Wiley, 2007.
- [72] F. Xu and K. Wu, "Understanding Leaky-Wave Structures: A Special Form of Guided-Wave Structure," *IEEE Microwave Magazine*, vol. 14, no. 5, pp. 87-96, 2013.
- [73] L.Liu, C.Caloz, and T. Itoh, "Dominant mode leaky-wave antenna with backfire-to-endfire scanning capability," *Electronics Letters* , vol. 38, no. 23, pp. 1414-1416, 2002.
- [74] F. Schwering and S. T. Peng, "Design of dielectric grating antennas for millimeter-wave applications," *IEEE Trans. Microwave Theory Tech*, pp. 199-209, 1983.
- [75] A. Zandieh, A.S. Abdellatif, A. Taeb,and S. Safavi-Naeini, "Low-cost and high-efficiency antenna for millimeter-wave frequency-scanning applications," *IEEE Antennas and Wireless Propagation Letters*, vol. 12, pp. 116-119, 2013.
- [76] C.T.Rodenbeck, L. Ming-Yi, K. Chang, "A novel millimeter-wave beam-steering technique using a dielectric-image-line-fed grating film," in *IEEE MTT-S International Microwave Symposium Digest*, 2001.
- [77] Y.J Cheng, Y.X. Guo,X. Bao, and K. Ng, "Millimeter-Wave Low Temperature Co-Fired Ceramic Leaky-Wave Antenna and Array Based on the Substrate Integrated Image Guide Technology," *IEEE Transactions on Antennas and Propagation*, vol. 62, no. 2, pp. 669-676, 2014.
- [78] A. Taeb, A. Abdellatif,G.Z. Rafi, S. Gigoyan, M.A.Basha, andS. S.; Safavi-Neini, S., "A low-cost silicon-based beam-steering grating antenna for G-band applications," in *IEEE Antennas and Propagation Society International Symposium (APSURSI)*, 2014.
- [79] A. Taeb, L. Chen, A. Abdellatif, G.Z. Rafi, S. Gigoyan, and S. Safavi-Naeini, "Laser machined millimeter-wave metallic grating antenna on Si waveguide," in *Radio Science Meeting (Joint with AP-S Symposium)*, 2014 USNC-URSI , 2014.
- [80] L.Rayleigh, "The problem of the whispering gallery," *Phil. Mag*, vol. 20, pp. 1001-1004, 1910.
- [81] C.V.Raman and G.A.Sutherland, "On the whispering gallery phenomenon," *Proceedings of the Royal Society of London*, vol. 100, no. 705, 1922.
- [82] X.H.Jiao, P.Guillon, L.A.Bermudez, and P.Auxemery, "Whispering gally modes of dielectric structures: Applications to millimeter-wave band-stop filters," *IEEE Trans*.

- on *Microwave Theory and Techniques*, vol. 35, no. 12, pp. 1169-1175, 1987.
- [83] N.Chen and Z.L.Sun, "Theoretical analysis of whispering gallery mode dielectric resonator in mm-wave," *Infrared and Millimeter waves*, vol. 14, no. 1, pp. 1801-1812, 1993.
 - [84] C.Vedrenne and J.Arnaud, "Whispering gallery modes of dielectric resonators," *IEE Proceedings Microwaves, Optics and Antennas*, vol. 129, no. 4, pp. 183-187, 1982.
 - [85] F.Vollmer and S.Arnold, "Whispering gallery mode biosensing:label free detection down to single molecules," *Nat. Methods*, vol. 5, pp. 591-596, 2008.
 - [86] D.Cross and P.Guillon, "Whispering gallery dielectric resonator modes for W-band devices," *IEEE Transaction on Microwave Theory and Tech.*, vol. 38, no. 11, pp. 1667-1674, 1990.
 - [87] L.K.Hady, A.A.Kishk, and D.Kajfez, "Power dividers based on dielectric resonator whispering gallery modes fed by prob or slot type of coupling," *IEEE Transaction on Microwave Theory and Tech.*, vol. 57, no. 12, pp. 3403-34-9, 2009.
 - [88] J.R.Wait, "Electromagnetic whispering gallery modes in a dielectric rod," *Radio Sci.*, pp. 1005-1017, 1967.
 - [89] C. Huanyu, "Fast method for millimeter wave dielectric resonator and antenna design," Waterloo, 2009.
 - [90] E.N.Ivanov and V.I.Kalinivichev, "Approximate analysis of disc dielectric resonators with whispering gallery modes," *Radio Tech.*, vol. 10, pp. 86-89, 1988.
 - [91] Y.Garault and P.Guillon, "Higher accuracy for the resonance frequencies of dielectric resonators," *Electronics Lett.*, vol. 12, no. 18, pp. 475-476, 1976.
 - [92] M.E.Tobar and A.G.Mann, "Resonant frequencies of higher order modes in cylindrical anisotropic dielectric resonators," *IEEE Transaction on Microwave Theory and Tech.*, vol. 39, no. 12, pp. 2077-2081, 1991.
 - [93] S.B.Chon, "Microwave banpass filter containing high Q dielectric resonators," *IEEE Transaction on Microwave and Theory Tech.*, vol. 16, pp. 218-227, 1968.
 - [94] E.A.J.Marcatili, "Dielectric rectangular waveguide and directional coupler for integrated optics," *Bell Sys. Tech. J.*, pp. 2071-2102, 1969.
 - [95] K.Ogusu, "Numerical analysis of the rectangular dielectric waveguide and its modifications," *IEEE Trans. on Microwave Theory and Techniques*, vol. 25, pp. 874-885, 1977.
 - [96] T.Itoh and R.S.Rudokas, "New method for computing the resonant frequencies of dielectric resonators," *IEEE Trans. on Microwave Theory and Techniques*, vol. 25, no.

- 1, pp. 52-54, 1977.
- [97] P.Guillon and Y.Garault, "Accurate resonant frequencies of dielectric resonators," *IEEE Transaction on Microwave Theory and Tech*, vol. 25, pp. 916-922, 1977.
- [98] R.K.Mongia and b.Bhat, "Accurate resonant frequencies of cylindrical dielectric resonators using a simple analytical technique," *Electronics Lett.*, vol. 21, pp. 479-480, 1985.
- [99] K.Okamoto, *Fundamentals of optical waveguides*, 2nd edition ed., Elsevier, 2006.
- [100] R.K.Mongia, "Resonant frequency of cylindrical dielectric resonator placed in an MIC environment," *IEEE Transaction on Microwave Theory and Tech.*, vol. 38, no. 6, pp. 802-804, 1990.
- [101] W.L.Gottfried, P.Remnant, J.F.Bennet, *New Essays on Human Understanding*, 1995.
- [102] R.F.Harrington, *Time-Harmonic Electromagnetic Fields*, 2nd Edition ed., J.Wiley-IEEE Press, 2001.
- [103] V.H.Rumsey, "The reaction concept in electromagnetic theory," *Phys. Rev.*, vol. 94, 1954.
- [104] A.D.Berk, "Variational Principles for electromagnetic resonators and waveguides," *IRE Transaction on Antenna and Prop.*, vol. AP4, pp. 104-111, 1956.
- [105] E. Marcatili, "Dielectric rectangular waveguide and directional coupler," *Bell Syst. Tech. J.*, vol. 48, p. 2071-2121, 1969.
- [106] C. P. C. A. Y. C. P. C. A. T. a. M. A. Yalcin, "Optical sensing of biomolecules using microring resonators," *IEEE Journal of Selected Topics in Quantum Electronics*, vol. 12, no. 1, pp. 148-155, 2006.
- [107] S. Arnold, R. Ramjit, D. Keng, V. Kolchenko, and I. Teraoka, "MicroParticle photophysics illuminates viral bio-sensing," *Faraday Discuss*, vol. 137, no. 4, pp. 1-19, 2007.
- [108] B. M. Fischer, M. Walther, and P. Uhd Jepsen, "Far-infrared vibrational modes of DNA components studied by terahertz time-domain spectroscopy," *Phys. Med. Biol.*, vol. 47, p. 3807-3814, 2002.
- [109] M. P. Abegaonkar, R. N. Karekar, and R. C. Aiyer, "A microwave microstrip ring resonator as a moisture sensor for biomaterials: application to wheat gains," *Meas. Sci. Technol*, vol. 10, p. 195-200, 1999.
- [110] M. Baaske and F. Vollmer, "Optical resonator biosensors: molecular diagnostic and nanoparticle detection on an integrated platform," *ChemPhysChem*, vol. 13, no. 2, p. 427-436, 2012.

- [111] J. D. Suter, I. M. White, H. Zhu, H. Shi, C. W. Caldwell, and X. Fan, "Label-free quantitative DNA detection using the liquid core optical ring resonator," *Biosens. Bioelectron.*, vol. 23, no. 7, p. 1003–1009, 2008.
- [112] K. De Vos, P. De Backere, R. Baets, and P. Bienstman, "Label-free biosensors on silicon-on-insulator optical chips based on microring cavities and surface plasmon interferometry," *Transparent Optical Networks. ICTON*, p. 88–91, 2008.
- [113] N.M.Hanumegowda, I. M.White, H.Oveys, and X.Fan, "Label-free protease sensors based on optical microsphere resonators," *Sensors Letter*, vol. 3, pp. 1-5, 2005.
- [114] N.Skivesen, A.Tetu, M.Kristensen, J.Kjems, L.H.Frandsen, and P.I.Borel, "Protein detection with a planar photonic-crystal sensor," in *CLEOE-IQEC 2007*, Munich, 2007.
- [115] X.Liu, C.Xue, S.Yan, J.Xiong, and W.Zhang, "Integrated high sensitivity displacement sensor based on micro ring resonator," in *NEMS2009*, 2009.
- [116] E.N.Shaforost, N.Klein, S.A.Vitusevich, A.Offenhäusser, and A.A.Barannik², "Nanoliter liquid characterization by open whispering-gallery mode dielectric resonators at millimeter wave frequencies," *JOURNAL OF APPLIED PHYSICS*, vol. 104, pp. 1-6, 2008.
- [117] S.Blair and Y.Chen, "Resonant-enhanced evanescent-wave fluorescence biosensing with cylindrical optical cavities," *Applied Optics*, vol. 40, pp. 570-582, 2001.
- [118] M.Noto, D.Keng, I.Teraoka, and S.Arnold, "Detection of Protein Orientation on the Silica Microsphere Surface Using Transverse Electric/Transverse Magnetic Whispering Gallery Modes," *Biophys J.*, vol. 92, no. 12, p. 4466–4472, 2007.
- [119] G.Annino, D.Bertolini, M.Cassettari, M.Fittipaldi, I.Longo, and M.Martinelli, "Dielectric properties of materials using whispering gallery dielectric resonators: Experiments and perspectives of ultra-wideband characterization," *JOURNAL OF CHEMICAL PHYSICS*, vol. 112, no. 5, pp. 2308-2314, 2000.
- [120] J.Krupka, D.Mouneyrac, J.G.Hartnett, and M.E.Tobar, "Use of whispering-gallery modes and quasi-TE_{0np} modes for broadband characterization of bulk gallium arsenide and gallium phosphide samples," *IEEE Trans. Microw. Theory*, vol. 56, pp. 1201-1206, 2008.
- [121] Y.Kogami, H.Tamura, and K.Matsumura, "Characterization of low loss dielectric materials in millimeter wave region using a whispering-gallery mode resonator," in *13th Int. Conf. on Microwave, Radar and Wireless Communications*, 2000.
- [122] A. Taeb, M. Neshat, S. Gigoyan, and S. Safavi-Naeini, "A gallery mode oscillator for the low cost millimeter-wave active antenna array," in *Antennas and Propagation Society International Symposium (APSURSI)*, 2010.

- [123] A. Taeb, S. Gigoyan, G. Rafi, S. Safavi-Naeini, M. Neshat, "A low cost and sensitive sensor based on the Whispering Gallery Mode at D-band," *41st European Microwave Conference (EuMC)*, pp. 619-622, 2011.
- [124] A. Taeb, M. Neshat, S. Gigoyan, and S. Safavi-Naeini, "A low-cost millimeter-wave whispering gallery-mode based sensor: design considerations and accurate analysis," *Int. J. Microw. Wireless Tech.*, vol. 4, no. 3, pp. 341-348, 2012.
- [125] J. Krupka, K. Derzakowski, A. Abramowicz, M. E. Tobar, and R. G. Geyer, "Use of whispering gallery modes for complex permittivity determinations of ultra low loss dielectric materials," *IEEE Trans. on Microwave Theory and Techniques*, vol. 47, no. 6, pp. 752-759, 1999.
- [126] J. C. Pickup, F. Hussain, N. D. Evans, O. J. Rolinsky, and D. J. Birch, "Fluorescence-based glucose sensors," *Biosensors Bioelectronics*, vol. 20, pp. 2555-2565, 2005.
- [127] B. Feldman and A. Heller, "Electrochemical glucose sensors and their," *Chem. Rev.*, vol. 108, p. 2482-2505, 2008.
- [128] M. R. Stratton, P. J. Campbell, and P. A. Futreal, "The cancer genome," *Nature*, vol. 458, no. 7239, pp. 719-724, 2009.
- [129] S. Cagnin, M. Caraballo, C. Guiducci, P. Martini, M. Ross, M. Santaana, D. Danley, T. West, and G. Lanfranchi, "Overview of electrochemical DNA biosensors: new approaches to detect the expression of life," *Sensors (Basel)*, vol. 9, no. 4, pp. 3122-3148, 2009.
- [130] M. Neshat, D. Saeedkia, and S. Safavi-Naeini, "A THz transducer for on chip label-free DNA sensing," in *Proc. of OSA Optical Terahertz Science and*, 2007.
- [131] M. Nagel and H. Kurz, "Corrugated waveguide based genomic biochip for marker-free THz read-out," *Int. J. Infrared Millim. Waves*, vol. 27, no. 4, pp. 517-529, 2006.
- [132] A. Taeb, M. A. Basha, S. Gigoyan, M. Marsden and S. Safavi-Naeini, "Label-free DNA sensing using millimeter-wave silicon WGM resonator," *Optics express*, vol. 21, no. 17, pp. 19467-19472, 2013.
- [133] M. Basha, B. Biglarbegian, M. Neshat, S. Gigoyan, and S. Safavi-Naeini, "Low-cost, monolithic and integrated whispering gallery mode ring resonator for sensing applications," in *41st European Microwave Conference (EuMC)*, 2011.
- [134] D. Kajfez, *Q factor measurements using MATLAB*, Artech House, 2011.
- [135] M. S. Kheir, H. F. Hammad, and A. Omar, "Graphical representation and evaluation of attenuation and coupling parameters of whispering-gallery-mode resonators," *IEEE Trans. Instrumentation and Measurement*, vol. 60, no. 8, pp. 2942-2950, 2011.
- [136] J. Uher and W. J. Hofer, "Tunable microwave and millimeter-wave band-pass filters,"

- IEEE Trans. on Microwave Theory and Techniques*, vol. 39, no. 4, pp. 643-653, 1991.
- [137] A.R. Brown and G.M. Rebeiz, "A varactor-tuned RF filter," *IEEE Trans. on Microwave Theory and Techniques*, vol. 48, no. 9, pp. 1157-1160, 2000.
- [138] R.R. Mansour, H. Fengxi, S.Fouladi, W.D. Yan, M. Nasr, "High-Q Tunable Filters: Challenges and Potential," *IEEE Microwave Magazine*, vol. 15, no. 5, pp. 70-82, 2014.
- [139] H. Joshi, H. Sigmarsson, D. Peroulis, and W.J. Chappell, "Highly Loaded Evanescent Cavities for Widely Tunable High-Q Filters," in *IEEE MTT-S International Microwave Symposium*, 2007.
- [140] A.B. Matsko, W. Liang, A. Savchenkov, V. Ilchenko, D. Seidel, and L. Maleki, "Multi-octave tunable agile RF photonic filters," in *International Topical Meeting on Microwave Photonic (MWP)*, 2012.
- [141] M. Neshat, D. Saeedkia, S. Gigoyan, and S. Safavi-Naeini, "Mode selective dielectric resonator coupled to dielectric image waveguide for sensing applications," in *15th International Conference on Terahertz Electronics. IRMMWTHz*, 2007.
- [142] A. Taeb, S. Gigoyan, M. Basha, and S. Safavi-Naeini, "Whispering Gallery Mode Resonance Structure for Millimeter-Wave/Sub-THz Applications," in *IEEE European Microwave Week (EUMW2014)*, 2014.
- [143] Y.Sun and C.J.Scheytt, "A 360 degree phase shifter for 60GHz application in SiGe BiCMOS technology," in *IEEE International Conference on Microwaves, Communications, Antenna and Electronics*, 2009.
- [144] D.W.Kang and S.Hong, "A 4-bit CMOS phase shifter using distributed active switches," *IEEE Transaction Microwave Theory and Tech.*, vol. 55, no. 7, pp. 1476-1483, 2007.
- [145] F.Ellinger, U.Jorges, U.Mayer, and R.Eickhoff, "Analysis and compensation of phase variations versus gain in amplifiers verified by SiGe HBT cascode RFIC," *IEEE Transaction on Microwave Theory and Tech.*, vol. 57, no. 8, p. 1885-1894, 2009.
- [146] N.S.Barker and G.M.Rebeiz, "Optimization of distributed MEMS transmission-line phase shifters-U-band and W-band designs," *IEEE Transaction on Microwave Theory Tech.*, vol. 48, p. 1957-1966, 2000.
- [147] A.Kozyrev, A.Ivanov, O.Soldatenkov, A.Tumarkin, S.Ivanova, T.Kaydanova, J.D.Perkins, J.Alleman, D.S.Ginley, L.Sengupta, L.Chiu, and X.Zhang, "Millimeter-wave loaded line ferroelectric phase shifters," *Integrated ferroelectrics*, vol. 55, no. 1, pp. 847-852, 2003.
- [148] A. Franc, O.H.Karabey, and G. Rehder, "Compact and Broadband Millimeter-Wave Electrically Tunable Phase Shifter Combining Slow-Wave Effect With Liquid Crystal Technology," *IEEE Transactions on Microwave Theory and Tech.*, vol. 61, no. 11,

2013.

- [149] M. J. Aylward and N. Williams, "Feasibility studies of insular guide millimeter wave integrated circuits," in *AGARD Millimeter and Submillimeter Wave Propagation and Circuits*, 1979.
- [150] H. Jacobs and M.M. Chrepta, "Electronic Phase Shifter for Millimeter-Wave Semiconductor Dielectric Integrated Circuits," *IEEE Transactions on Microwave Theory and Techniques*, vol. 22, no. 4, pp. 411-417, 1974.
- [151] M.i Li and K. Chang, "New Tunable Phase Shifters Using Perturbed Dielectric Image Lines," *IEEE Transactions on Microwave Theory and Techniques*, vol. 46, no. 9, 1998.
- [152] D.Chicherin, M.Sterner, J.Oberhammer, S.Dudorov, D.Lioubtchenko,A.J.Niskaen, V.Ovchinnikov and A.V.Raisanen, "MEMS based high-impedance surface for millimeter wave dielectric rod waveguide phase shifter," in *EuMA*, Paris, 2010.
- [153] A.S. Abdellatif, N. Ranjkesh, M. Fahimnia, A. Taeb, A., S. Gigoyan, and S. Safavi-Naeini, "Low insertion loss variable phase shifter for emerging millimeter-wave communication systems," in *IEEE MTT-S International Microwave Symposium (IMS)*, 2014.
- [154] A. S. Abdellatif,M. Faraji-Dana, N. Ranjkesh, A. Taeb, M. Fahimnia, S. Gigoyan, and S. Safavi-Naeini, "Low Loss, Wide-band, and Compact CPW-based Phase Shifter for Millimeter-Wave Applications," *IEEE Trans. on Microwave and theory Tech.*, 2014.
- [155] A. Bhattacharyya, "Beam Forming Networks in Multiple-Beam Arrays," in *Phased Array Antennas: Floquet Analysis, Synthesis, BFNs and Active Array Systems*, John Wiley & Sons, 2006.
- [156] R. Hansen, *Phased Array Antennas*, New Jersey: John Wiley, 2009.
- [157] S.J Ajioka. and J. L. McFarland, "Beam-forming feeds," in *Antenna Handbook; Theory, Applications and Design*, New York, John Wiley, 1998.
- [158] J. Butler and R. Lowe, "Beam-Forming Matrix Simplifies Design of Electronically Scanned Antennas," *Electronic Design*, vol. 9, pp. 170-173, 1961.
- [159] C. Tseng, C. Chen, and T. Chu, " Low-Cost 60-GHz Switched-Beam Patch Antenna Array With Butler Matrix Networ," *IEEE Antennas and Wireless Propagation Letters*, vol. 7, pp. 432-435, 2007.
- [160] S. Yamamoto, J. Hirokawa, and M. Ando, "A beam switching slot array with a 4-way Butler matrix installed in a single layer post-wall waveguide," in *IEEE Antennas Propag. Soc. Int. Symp*, 2002.
- [161] C. J. Chen and T. H. Chu, "Design of a 60-GHz substrate integrated waveguide Butler matrixVA systematic approach," *IEEE Trans. Microw. Theory Tech.*, vol. 58, no. 7, pp.

1724–1733,, 210.

- [162] A. Alphones and M. Tsutsumi, "Optical control of millimeter wave in silicon rib guides," in *IEICE*, Japan, 1991.
- [163] R. Simons, *Optical control of microwave devices*, Norwood: Artech House, 1990.
- [164] B. Biglarbegian, M. Basha, A. Taeb, S. Gigoyan, and S. Safavi-Naeini, "Silicon-based integrated millimeter-wave CPW-to-dielectric image-guide transition," *International Journal of RF and Microwave Computer-Aided Engineering*, vol. 24, no. 4, pp. 490-497, 2014.
- [165] C. Yeh and F. I. Shimabukuro, *The Essence of Dielectric Waveguides*, Springer, 2008.
- [166] "LPKF Laser & Electronics," 2014. [Online]. Available: <http://www.lpkf.com/products/rapid-pcb-prototyping/laser-circuit-structuring/laser-micromaterial-processing.htm>.